VALORIZATION OF BIOMASS USING NOVEL CATALYTIC AND ELECTROCATALYTIC PROCESSES

By

Manali Dhawan

A DISSERTATION

Submitted to
Michigan State University
in partial fulfillment of the requirements
for the degree of

Chemical Engineering – Doctor of Philosophy

2021

ABSTRACT

VALORIZATION OF BIOMASS USING NOVEL CATALYTIC AND ELECTROCATALYTIC PROCESSES

By

Manali Dhawan

Increasing energy requirements and environmental pollution, along with predicted shortages of fossil fuels in the near future, have accelerated the search for alternative renewable energy sources. Biomass is a promising renewable resource for the production of value-added fuels and chemicals. In this work, triglycerides, furfural and 5-hydroxymethylfurfural (HMF) are used as bio-derived feedstock chemicals for chemo- or electro-catalytic conversion to valuable chemicals that find applications in fuels, polymer, perfumery and pharmaceutical industries.

Chemical interesterification of triglycerides was conducted with methyl acetate, as an alternative to transesterification, to co-produce biodiesel and a higher value-added compound, triacetin, instead of glycerol. Conversion of waste methyl acetate in terephthalic acid production industry using triglyceride into two valorized products biodiesel and triacetin is a novel idea. Biodiesel is a well-known renewable fuel and triacetin can be used as a fuel additive. Amongst various base catalysts screened, calcined Mg-Al hydrotalcite (Mg:Al mole ratio – 3:1) was found to have the best activity in terms triglyceride conversion and triacetin selectivity.

We also studied the etherification of HMF with ethylene glycol to produce 5-(2-hydroxyethoxymethyl) furfural (HEMF), which finds application as a fuel additive. Metal substituted heteropoly acid catalysts were identified as a chemo-selective catalyst that favored etherification of HMF over acetalization reaction. Aluminum substituted dodecatungsto-phosphoric acid achieved the highest HMF conversion and HEMF selectivity, which was attributed to the combined role of the catalyst's Lewis and Bronsted acidity.

Further, electrocatalytic hydrogenation (ECH) of furfural using zinc as a novel metal catalyst was studied to produce furfuryl alcohol and 2-methylfuran, which have applications in pharmaceutical, polymer and fuel industries. The effect of metal catalyst and electrolyte pH on the yield and Faradaic efficiency (FE) of the desired products was studied. Electrolysis at neutral pH (pH 6 to 8) exhibited increased yields and FE as compared to acidic and basic pH. FE for ECH of furfural with Zn was remarkably higher as compared to Cu and Ni.

However, during ECH of furfural, the total yield of the desired products was low compared to the conversion of furfural which was due to electrodimerization reactions. Thus, zinc metal nanoparticles were synthesized by electrodeposition to achieve higher activity for furfural ECH as compared to bare zinc metal due to high surface area and roughness. Furfural electrolysis in 0.5 M bicarbonate electrolyte at -0.6 V/RHE yielded higher conversion, yield and FE as compared to bare zinc. Catalyst characterization revealed the presence of surface zinc oxide species post-electrolysis, which could have a role in reaction mechanism.

Overall, this work contributes to the field of biomass valorization, by identifying new selective catalysts and processes to produce value-added chemicals using renewable bio-derived feedstocks. Catalyst synthesis, reaction engineering and process optimization studied for biomass conversion processes in this work will aid in future process intensification of such processes.

Dedicated to Mommy, Megha, Ravi, Masi and Shivam

ACKNOWLEDGEMENTS

I take this opportunity to express my deepest gratitude to the almighty God who always helped me in every life endeavour no matter how tough they were. He continues to make me strongly believe and realize that whatever happens in life is for the ultimate best through every decision that I took.

I would like to express my sincere gratitude to my advisors, Dr. Ganapati D. Yadav, Institute of Chemical Technology (ICT), India and Dr. Scott Calabrese Barton, Michigan State University (MSU), USA for providing me with Dual Ph.D. degree opportunity as part of collaboration between ICT and MSU to pursue Ph.D. in Green Technology and Chemical Engineering. I am honoured to be the first student to complete this Dual Ph.D. program. It was my pleasure working under such eminent scientists. They always motivated me to work hard, smart, be creative and keep work standards high. Motivating quotes by Dr. Yadav, “Failure is temporary, but success is autocatalytic” and “If research would be a one-day thing, why would you be given a year” motivated me a lot during my Ph.D. tenure. Also, a quote by Dr. Barton, “Ph.D. is figuring out things on and on until you find another thing to figure out” inspires me to extend my inquisitiveness on things and not give up. These quotes fall perfectly to my research work. Their support and guidance has enlightened the path of my career. I learnt a lot through the research at these universities and it helped me to expanse my research area. Prof. Yadav and Prof. Barton helped me to grow in terms of both personal and professional development. They provided me with knowledge and professional experience which helped me tailoring my life and career.

I would like to thank Dr. Yadav for providing me Ph.D. Research Fellowship under his J. C. Bose National Fellowship of Department of Science and Technology, Govt. of India. I also acknowledge Prof. Barton for supporting me with Teaching Assistantship opportunity on CHE

431 course and Research Assistantship provided through Department of Chemical Engineering and Materials Science, MSU.

I would also like to acknowledge my committee members, Dr. Christopher Saffron, Dr. Ramani Narayan, Dr. Robert Ferrier, Dr. Laxmi Kantam Mannepalli and Dr. Sanjay Mahajani for providing their valuable feedback on our work. I would like to thank Prof. Carl Lira, Dr. Iman Nezam, Dr. Lars Peereboom for providing me access to gas chromatography instrument in their laboratory and helping me set my method up. I would thank Mindy Lee for collaborating and helping me with SEM analysis of zinc particles. I thank Meheryar Kasad for his help with GC-MS analysis of reaction samples.

These five years of research work were full of learning, and I just can't move further without expressing my gratitude to my MSU lab mates, who were very welcoming when I joined the group and helped me in learning new field of electrochemistry. Thanks to Alex for bearing with me and always answering my numerous inquisitive questions, sorry to bug you. Thanks to Kanchan for making me feel homely in USA and being my guiding sister far from home. Thanks to Yan for always helping me readily on Python. I want to thank Sonam for helping me in managing documentation work at ICT while my stay at MSU, even during the pandemic time and also for always cheering me up through my homesick days at USA. Thanks to Manish for answering my endless kinetics questions and research help. I want to thank my ICT lab mates for their help in making me learn lab experimental set-up and methods. Specially, I would like to thank Manish, Sonam, Deepak, Radhika, Harshada, Shivaji, Surbhi, Godfree, Gunjan, Shalaka, Ashly, Poonam, Venus, Kalidas, Jayaram, Manoj, Nikhil and Swanand, for their valuable help.

I thank my Bachelor's friends (Shriraj, Suraj, Aditi, Chiranjiv, Darshan, Kiran, Avishkar, Santosh, Nilesh), Master's friends (Prajakta, Rutuja, Swapnil, Dhananjay, Ankita, Venus, Apurv,

Chetan), Ph.D. friends (Sonam, Manish, Surbhi, Ankita Asati, Radhika, Harshada, Shalaka) for great parties. I missed coffee jokes, talks and laughs with Manish, Sonam and Surbhi in USA. I thank my USA friends (Gouree, Sejal, Karthik, Avni, Rashmi, Akash, Apoorva, Aditya, Sneha) for being my family away from home and making this journey easier to go through with trips and parties. There are lot of memories and experiences which I cannot put into words.

Most importantly, I thank and dedicate this thesis to my mother, Mrs. Geeta Dhawan, my aunt, Neeta Bose, my sweet sister, Megha Dhawan, my soon to be husband, Ravikumar Nalawade, and my brother, Shivam Dhawan for their immense support, care and love from miles way. Words will fall short in describing their contribution towards my life. They supported my decision to move to USA and bore the pain to stay away from me over these three years. Nothing can match it. I love you all!

Manali Dhawan

TABLE OF CONTENTS

LIST OF TABLES

LIST OF FIGURES

LIST OF SCHEMES

KEY TO SYMBOLS

α	Anodic or cathodic transfer coefficient
b	Tafel slope
C_5	Pentose
C_6	Hexose
C_i	Concentration of any species 'i' (mol/L)
C_S	Concentration of vacant sites (mol/g)
C_T	Total concentration of sites (mol/g)
E_a	Activation energy (kcal/mol)
E°_{cell}	Equilibrium cell potential
F	Faraday's constant
G	Gibbs free energy
i	Current density
i_a	Anodic current density
i_c	Cathodic current density
i_0	Exchange current density
k	Rate constant (L^2/(mol.g.s))
k_0	Pre-exponential factor
k_i	Forward adsorption or desorption rate constant of any species 'i' (L^2/mol/g/s)
K_i	Adsorption or desorption equilibrium constant of any species 'i' (L/mol)
k_s	Forward surface reaction rate constant (L^2/mol/g/s)
M	Methyl acetate
η	Overpotential

n	number of electrons transferred
Q	Charge
r_i	Rate of consumption or formation of any species 'i' (mol/L/s))
R	Gas constant
S	Surface catalytic acid sites
t	Time
T	Triglyceride
T_0	Reference temperature
U°_{cell}	Equilibrium cell potential
U°_{c}	Cathodic equilibrium reduction potential
U°_{a}	Cathodic equilibrium reduction potential
U	Equilibrium potential
V	Working electrode potential
w	Catalyst loading (g/L)
X	Fractional conversion of HMF

KEY TO ABBREVIATIONS

ABM	2-(4-aminobenzylidene)-malononitrile
ACC	Activated carbon cloth
ACF	Activated carbon fiber
ACN	Acetonitrile
AMF	5-alkoxymethylfurfural
BET	Brunauer-Emmett-Teller
CE	Counter electrode
CH	Chemical hydrogenation
CHT	Calcined hydrotalcite
CN	Cetane number
CV	Cyclic voltammetry
DA	Diacetinmonoglyceride
DHMF	2,5-dihydroxymethylfuran
DHMTHF	2,5-dihydroxymethyltetrahydrofuran
DFF	2,5-diformylfuran
DMF	2,5-dimethylfuran
DTP	Dodecatungstophosphoric acid
ECH	Electrochemical/Electrocatalytic hydrogenation
EDAX/EDS	Energy Dispersive Spectroscopy
EMF	5-ethoxymethylfurfural
ER	Electroreduction
HMS	Hexagonal mesoporous silica

FA	Furoic acid
FAL	Furfuryl alcohol
FAME	Fatty acid methyl ester
FDCA	2,5-furandicarboxylic acid
FE	Faradaic efficiency
FFCA	5-formylfurancarboxylic acid
FTIR	Fourier Transform Infrared Spectroscopy
GC	Gas Chromatography
GVL	gamma-valerolactone
HT	Hydrotalcite
HD	2,5-hexanedione
HER	Hydrogen evolution reaction
HEMF	5-(2-hydroxyethoxymethyl) furfural
HPA	Heteropolyacid
HMF	5-hydroxymethylfurfural
HMFA	5-hydroxymethylfurfural ethylene acetal
HPLC/LC	High Performance Liquid Chromatography
HT	Hydrotalcite
IS	Internal standard
LA	Levulinic acid
LHHW	Langmuir-Hinshelwood-Hougen-Watson
MA	Monoacetindiglyceride
MF	2-methylfuran

5-MF	5-methylfurfural
MMF	5-methoxymethylfurfural
MOF	Metal organic framework
MS	Mass Spectroscopy
MTHF	2-methyltetrahydrofuran
NBM	2-(4-nitrobenzaldehyde)malononitrile
OCV	Open-circuit potential
RE	Reference electrode
RVC	Reticulated vitreous carbon
SEM	Scanning Electron Microscopy
SV	Staircase voltammetry/Steady state voltammetry
TA	Triacetin
TEM	Transmission Electron Microscopy
TGA	Thermogravimetric analysis
THFA	Tetrahydrofurfuryl alcohol
TPD	Temperature Programmed Desorption
WE	Working electrode
XRD	X-ray diffraction
ZIF-8	Zeolitic imidazolate framework-8

Chapter 1

Introduction

The World population is rapidly growing, with the current numbers already exceeding 7.7 billion, which would consequently lead to increase in material and energy consumption [1]. According to the U.S. Energy Information Administration, International Energy Outlook 2019 report projects that the world energy consumption is expected to rise nearly 50 % by 2050, wherein most of this growth is driven by developing countries (particularly Asia), fast-paced economic growth and increased standard of living [2]. Non-renewable fossils fuels such as coal, oil and natural gas remain the most used fuel source, but these sources are depleting as indicated by their reserve to production ratio. Reserves-to-production ratio measures the number of years of global coal, oil and natural gas production left based on the known reserves and current annual production levels. In 2019, the oil reserves accounted for 50 years of current production, with coal and gas standing at 132 and 49.8 years, respectively [3]. It is well known that burning of these fossil fuels lead to increased carbon dioxide (greenhouse gas) emission, which contributes to global warming and climate change [3,4]. Interest in production of fuels and chemicals from renewable resources continues to grow, as costs decrease [5,6] and the environmental impact of fossil resources becomes more apparent [7,8]. Thus, there has been a growing need to investigate alternative promising renewable energy sources. According to BP Statistical Review of World Energy 2020, renewable energy recorded 40 % growth in primary energy consumption in 2019, the largest increment as compared to other energy source consumption. It also increased its share in global electricity generation to 10 %, surpassing nuclear energy for first time. Renewable energy accounted for a total share of 5 % in the energy mix, inclusive of wind (2.4 %), solar (2 %), geothermal, biomass and biofuels total accounting for (0.6 %) [3]. Biomass is the only carbon-

based, naturally abundant energy source, a large portion of which is usually managed as waste [9–11]. Thus, an intriguing research question is how to find value in biomass waste, which can be answered using various sustainable pathways.

Biomass is a promising renewable resource that has an immense potential for the production of value-added and carbon neutral biofuels and fine chemicals, which have similar or superior properties in comparison to fossil fuel derived chemicals [12–14]. A critical analysis of crude oil versus biomass has been presented, which prioritizes the development of catalytic and biocatalytic lignocellulosic biomass conversion processes, methane to olefin conversion technologies, and use of hydrogen for CO_2 valorization to fuels and chemical, in order to achieve a carbon-neutral economy [15].

Green chemistry utilizes a set of principles that reduces or eliminates the use or generation of hazardous substances in the design, manufacture and application of chemical products [16]. The twelve principles of green chemistry can be underlined as: 1) Prevention, 2) Atom economy, 3) Less hazardous chemical synthesis, 4) Designing safer chemicals, 5) Safer solvent and auxiliaries, 6) Design for energy efficiency, 7) Use of renewable feedstocks, 8) Reduce derivatives, 9) Catalysis, 10) Design for degradation, 11) Real-time analysis for Pollution Prevention, 12) Inherently safer chemistry for accident prevention. The process of biomass utilization to valuable products should be based on maximum utilization of green chemistry principles as possible, in order to call it a greener process. Catalysis is one of an important principle of green chemistry which can be used to develop green processes to obtain products with high selectivity, atom economy (total mass of reactants that are converted to desired products) and lower E-factor (mass of waste per mass of desired products). In our work, in addition to catalysis, we have also applied

some other principles of green chemistry such as waste prevention, use of renewable feedstocks, less hazardous chemical synthesis, safer solvents and design for energy efficiency [16–18].

1.1 Biomass

Biomass can be described as any hydrocarbon material primarily consisting of carbon, hydrogen, oxygen, nitrogen with minor traces of sulfur and inorganic species [10,19,20]. The sources of biomass are abundant, and are 60 % terrestrial (woods, herbs, crops, bagasse, food and feed crops, agricultural and industrial residues, sawdust, grass, pulp/paper waste, municipal waste, food, oil, animal wastes, etc.) and 40 % aquatic (aquatic plants, algae) [10,11,20]. Biomass comprises 75 % carbohydrates (lignocellulose) and 20 % lignin, with the remainder consisting of

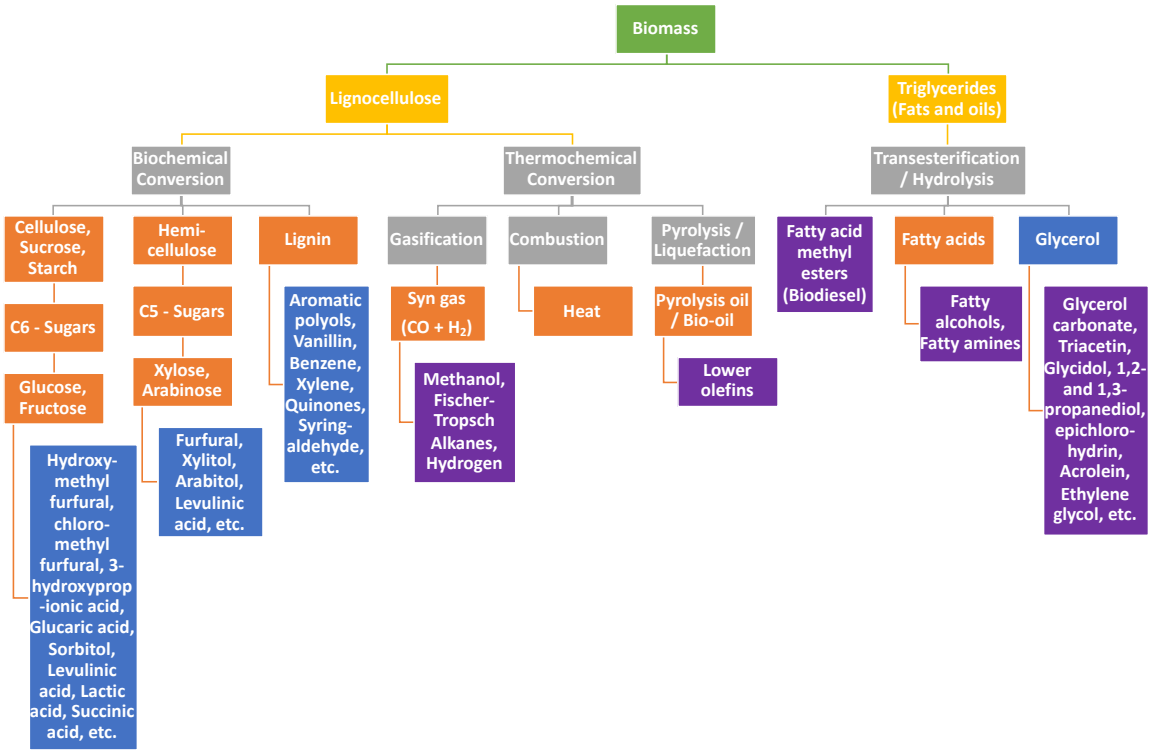

Figure 1.1 Biomass conversion processes to platform and value-added chemicals [11,19,22,37,52]

triglycerides, proteins, and terpenes [11]. The constituents of lignocellulosic feedstock can be divided into three categories: cellulose (40 - 50 %), hemicellulose (25 - 35 %) and lignin (15-20 %) (Figure 1) [9,11,20–23]. Cellulose is a linear, unbranched polysaccharide that is composed of hexose (D-glucose) subunits and has the general formula of $(C_6H_{10}O_5)_n$ [20,22]. Hemicellulose (general formula: $(C_5H_8O_4)_n$) is a relatively complex polysaccharide consisting of branched chains made of hexose (D-glucose, D-mannose, D-galactose) as well as pentose (D-xylose, L-arabinose) subunits [20,22]. Lignin is fibrous, highly branched biopolymer containing cinnamyl alcohol monomers [11,19,20].

1.2 Platform chemicals from biomass

Bio-derived platform chemicals are intermediate molecules in the production of value-added biofuels, specialty and commodity chemicals [10,11,19,24]. Oil seeds, vegetable oils and animal fats are an important triglyceride derived biomass source of biofuels [25,26]. Triglyceride based feedstocks can be converted to fatty acids and glycerol via hydrolysis, which can be further valorized to biodiesel and glycerol derived chemicals [10,11,27,28]. Biodiesel can be also obtained by direct transesterification or interesterification of triglycerides with alcohol and acetates, respectively [29–32].

Lignocellulosic feedstocks such as agricultural residues (sugarcane bagasse, corn cobs, corn stover, rice husks, orange peel, oat hulls, wheat straw, etc.), forest residues, wood waste, municipal solid organic waste, etc. are classified as second-generation bio-based platform chemicals, which offer an advantage over first generation feedstocks (food crops such as sugarcane, corn, starches, vegetable oils and oil seeds) due to their inedibility. The production of fuels and chemicals from second generation inedible feed crops and oil seeds is desired to avoid competition with food supply required to feed the growing population [11,24,26,33]. However, lignocellulose, due to its

complex polymeric structure containing high content of strongly bound cellulose, hemicellulose and lignin, is difficult to defragment and be directly utilized to produce chemicals [9,11,19,34]. It must be pretreated, depolymerized and partially deoxygenated to produce sugars, which can then be chemically converted to a variety of platform molecules serving as feedstocks for the synthesis of fuels and chemicals [9–11,19,22].

The pathways to deconstruct lignocellulosic biomass include thermochemical (pyrolysis and gasification) and biochemical (hydrolysis) processes [10,11,24] (Figure 1). Pyrolysis is the thermal degradation of biomass in the absence of oxygen to give pyrolysis oil (bio-oil), charcoal, syn gas [11,20,24,35,36]. Biomass gasification in the presence of oxygen yields syngas ($CO + H_2$) [9,11,22,24]. Biochemical hydrolytic processes involve pretreatment of lignocellulosic biomass using mineral acids or enzymes to fractionate lignin, cellulose, and hemicellulose [9,11,24]. The cellulose and hemicellulose can be further hydrolyzed to produce pentose (C_5) and hexose (C_6) sugars [11,22,24]. The pentose (xylose, arabinose) and hexose (glucose, fructose) sugars can be further converted by: fermentation to produce acids (succinic acid, 3-hydroxypropionic acid, glutamic acid, etc.) [10,11]; hydrogenation to produce mannitol, sorbitol and xylitol [22,37]; dehydration to produce furfural, levulinic acid, 5-hydroxymethylfurfural (HMF) [10,11,22,23], which are some of the important platform materials to produce biofuels and chemicals [10,11,14,15,22,38]. Thermochemical lignin conversion processes yield platform chemicals such as benzene, toluene, xylene, quinones, phenols, guaiacol, catechol, eugenol, cresols, syringol, vanillin, syringaldehyde), etc., which can be chemically converted to a variety of value-added fuels and chemicals [19,34,39,40].

1.3 Value added chemicals from biomass-derived platform chemicals

Bio-derived platform chemicals can be converted by enzymatic, supercritical, chemical, or electrochemical reactions to various value-added chemicals, which find applications in fuel, fuel additives, polymer, solvents, perfumery, pharmaceutical industries, etc. [38,41–46]. Bio-oil obtained from biomass pyrolysis can be stabilized by hydrogenation of constituent unsaturated oxygenates such as aldehydes, ketones, phenols to saturated alcohols and polyols, and can then be utilized for production of transportation fuels [36,47]. Syngas ($CO + H_2$) obtained from biomass gasification can be valorized to hydrocarbon fuels and chemicals by Fischer-Tropsch or methanol synthesis [11,48,49].

In 2004, US Department of Energy identified a list of top 12 chemical candidates derived from sugars that can be used as potential platform chemical to obtain diversity of high value-added products [50]. In 2010, Bozell and Petersen revisited this list and presented an updated list of platform chemicals based on research advances made since 2004, to include some of the previous identified platform chemicals along with some new compounds [51]. The updated list of platform chemicals along with their annual production volumes includes glycerol (1500 kt), lactic acid (>600 kt), 3-hydroxypropanoic acid (800 kt), levulinic acid (2-3 kt), succinic acid (34 kt), sugars (sorbitol (1800 kt), xylitol (190 kt)), furans (furfural (360 kt), HMF, 2,5-furandicarboxylic acid (FDCA)), bio-hydrocarbons (800 kt) and ethanol (86000 kt) [51–53].

Examples of value-added chemicals obtained from some of the aforementioned C_5 and C_6 sugar derived platform chemicals are: 1) gamma-butyrolactone, tetrahydrofuran, 1,4-butanediol by hydrogenation of succinic acid [37,52,54]; 2) 1,3-propanediol and acrylic acid by dehydration and reduction of 3-hydroxypropionic acid, respectively [37]; 3) polylactic acid by polymerization of lactic acid [37,55]; 4) propylene glycol, ethylene glycol, glycerol by hydrogenolysis of sorbitol

and xylitol [37,56]; 5) levulinic acid esters by esterification, 1,4-pentanediol by reduction, gamma-valerolactone by reduction cyclisation of levulinic acid [37,57]; 6) furfuryl alcohol, tetrahydrofurfuryl alcohol, 2-methyl furan and 2-methyltetrahydrofuran by hydrogenation of furfural [37,43,58,59]; 7) 2,5-dimethylfuran and FDCA by hydrogenation and oxidation of HMF [37,43,57], etc. The applications of some value-added chemicals are given in Figure 2.

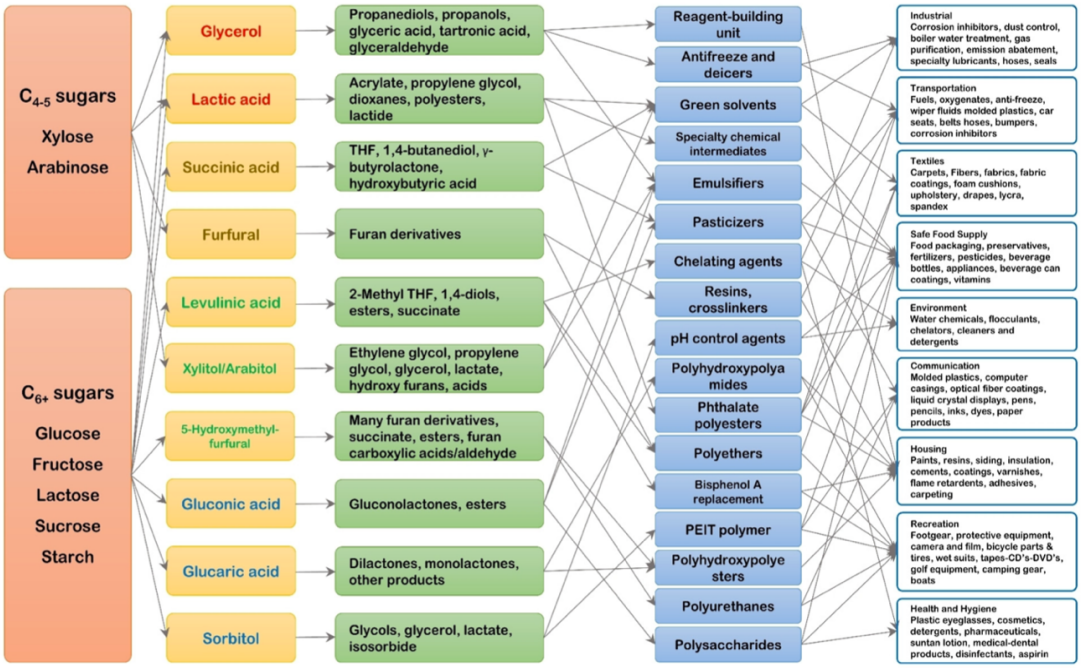

Figure 1.2 Applications of value-added chemicals obtained from bio-derived feedstock chemicals (Reproduced from [211])

Recently, Shanks and Keeling [60] introduced the concept of bioprivileged molecules as a new paradigm for biobased chemical development. They are defined as "biology-derived chemical intermediates that can be efficiently converted to a diversity of chemical products including both novel molecules and drop-in replacements". The examples of bioprivileged intermediate molecules discussed were muconic acid, HMF and triacetic acid lactone, which can be converted to various products with few catalytic steps [60]. It emphasizes the use of forward diversity-oriented synthesis approach to integrate biological and chemical processes to develop new

intermediate chemicals as platform chemicals, which can then be used for catalytic valorization to target value-added molecules, which have been efficiently explored by computational tools [61].

Some of the value-added chemicals obtained from bio-derived platform chemicals are discussed in detail as follows:

1.3.1 Triglycerides

Vegetable oils and animal fats are triglycerides consisting of different fatty acids attached to a glycerol backbone [62,63]. Biodiesel (fatty acid alkyl esters) is a renewable fuel conventionally produced by transesterification of triglycerides with alcohols, usually methanol and ethanol [32,62] (Figure 3, pathway a). The renewable oil feedstocks are soybean oil, palm oil, rapeseed oil, cotton seed oil, sunflower seed oil, etc [62,63]. Non-edible oils like those derived from jatropha, pongamia or jojoba can also be used [32,63]. Likewise, waste cooking oil is considered an economic resource for biodiesel production [63].

Biodiesel possesses superior properties compared to petroleum-based fuels, including biodegradability, low sulfur content, small carbon footprint, less carbon dioxide emissions, higher flash point and cetane number (CN) (measure of fuel ignition property calculated as percentage by volume of n-hexadecane (cetane) in a mixture of n-hexadecane (100CN) and heptamethylnonane (15CN) that has the same ignition quality when tested in the same engine under same conditions as the fuel in question) [10,64–66]. Thus, pure biodiesel or biodiesel blends can be used in conventional compression-ignition engines without the need for engine modifications [62].

Transesterification of triglycerides is aided by enzymatic [67] as well as chemical alkali or acid catalyzed processes [62,68–71] or by non-catalytic supercritical processes [72]. Homogeneous base catalysts such as alkali metal carbonates, hydroxides and alkoxides are widely used in commercial processes because they are cost-effective and result in high activity at mild reaction

conditions [69,73]. However, these processes require additional steps for recovery of glycerol and purification of waste streams [62]. Thus, many heterogeneous base and acid catalysts such as alkaline metal oxides, hydroxides, hydrotalcites [70,74,75], heteropoly acids [71] and solid superacid [76] catalysts were developed and evaluated for biodiesel production processes, since they could be easily removed from the reaction mixture with no polluting by-products formed, making the purification step easier.

However, 10% w/w glycerol is co-produced in the biodiesel production process, which reduces the process efficiency [77–80]. Increasing demand of biodiesel has led to an increase in the glycerol production simultaneously [77,80]. Glycerol has many applications in the textile, cosmetics, pharmaceuticals, and food industries, but it stills remains an excessively supplied chemical in the market [79,81,82]. Glycerol can be utilized as a platform chemical in large scale plants to produce several value-added chemicals, but this requires further rigorous purification procedures [78]. Biodiesel production is not economical vis-à-vis petro-diesel unless the co-product glycerol is valorized.

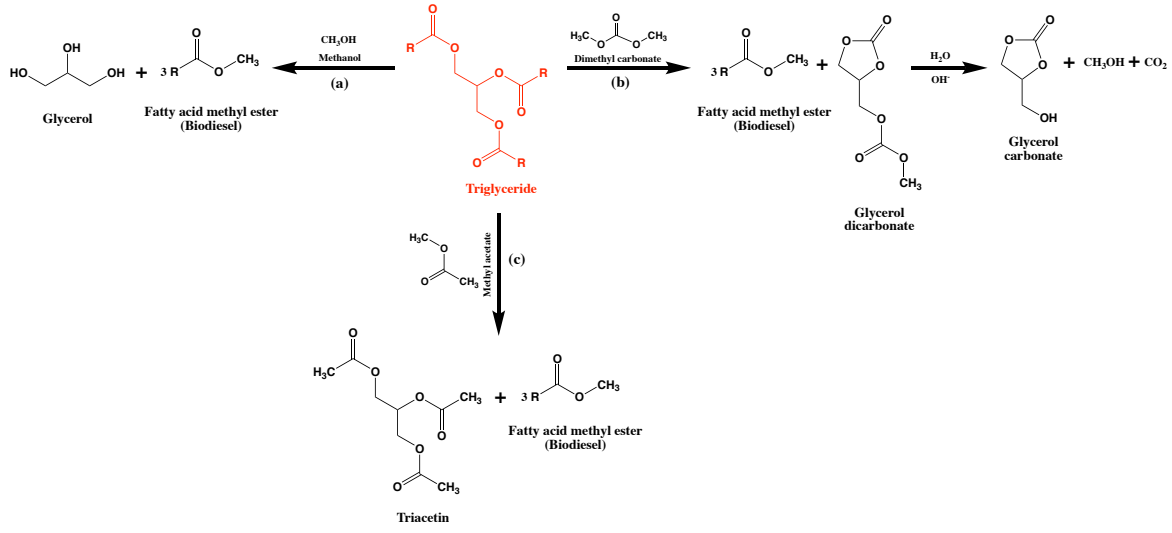

Figure 1.3 Valorization pathways of triglycerides to biodiesel, glycerol and glycerol derivatives using different acyl acceptors (Adapted from [324])

One of the ways to increase the efficiency of biodiesel process is to utilize product glycerol in-situ to produce another value-added chemical simultaneously, by one-pot cascade synthesis [29]. For example, valorization of glycerol to produce glycerol carbonate by chemical, enzymatic and supercritical methods has been extensively researched over the years [83–88]. Glycerol carbonate has varied applications such as polymer synthesis, surfactants, solvents, gas separation membranes, and as a green substitute for propylene carbonate and ethylene carbonate, etc. [89]. The one-pot simultaneous catalytic coproduction of biodiesel and glycerol carbonate using triglycerides with dimethyl carbonate as reactant is an efficient pathway to increase the biodiesel process efficiency (Figure 3, pathway b) [29,87,90–92].

Another possibility to increase the efficiency of biodiesel production is to avoid glycerol formation as a co-product. The formation of glycerol esters: glycerol triacetate (triacetin), glycerol diacetate (diacetin), glycerol monoacetate (monoacetin), which are used as fuel additives, by esterification and transesterification of glycerol with acetic acid and methyl acetate, respectively has been reported in the literature [93–95]. Chemical interesterification of triglycerides with methyl acetate is a good alternative as compared to transesterification, as it yields a higher value-added compound, triacetin, as a co-product instead of the already abundant commodity, glycerol [30,96–98] (Figure 3, pathway c). Methyl acetate is produced as a major waste byproduct in the terephthalic acid manufacture wherein air oxidation of p-xylene in acetic acid is conducted in the presence of Co-Mn-Br catalyst in liquid phase [99].

1.3.2 Furfural

Furfural is bio-derived feedstock obtained by the dehydration of pentose sugars such as xylose [22,23,100,101]. It can be valorized by hydrogenation, oxidation, hydrogenolysis, etherification, esterification and decarboxylation processes to value-added C4 and C5 chemicals, which can be

used to produce fuels, fuel additives and chemicals [23,37,102–104]. Figure 1 depicts some of the pathways for furfural valorization. Some of the valuable C4 and C5 chemicals obtained from furfural are furfuryl alcohol (FAL), 2-methylfuran (MF), tetrahydrofurfuryl alcohol (THFA), 2-methyltetrahydrofuran (MTHF), furan, tetrahydrofuran, furanone, levulinic acid, gamma-valerolactone, alkyl levulinates, pentanediols, furoic acid (FA), furfuryl acetate, furfuryl ethers, liquid alkanes, etc. (Figure 4) [22,23,37,102,103,105]. These chemicals find applications in solvents, resins, perfumery, agrochemical, and pharmaceutical industries [23,102,103,105].

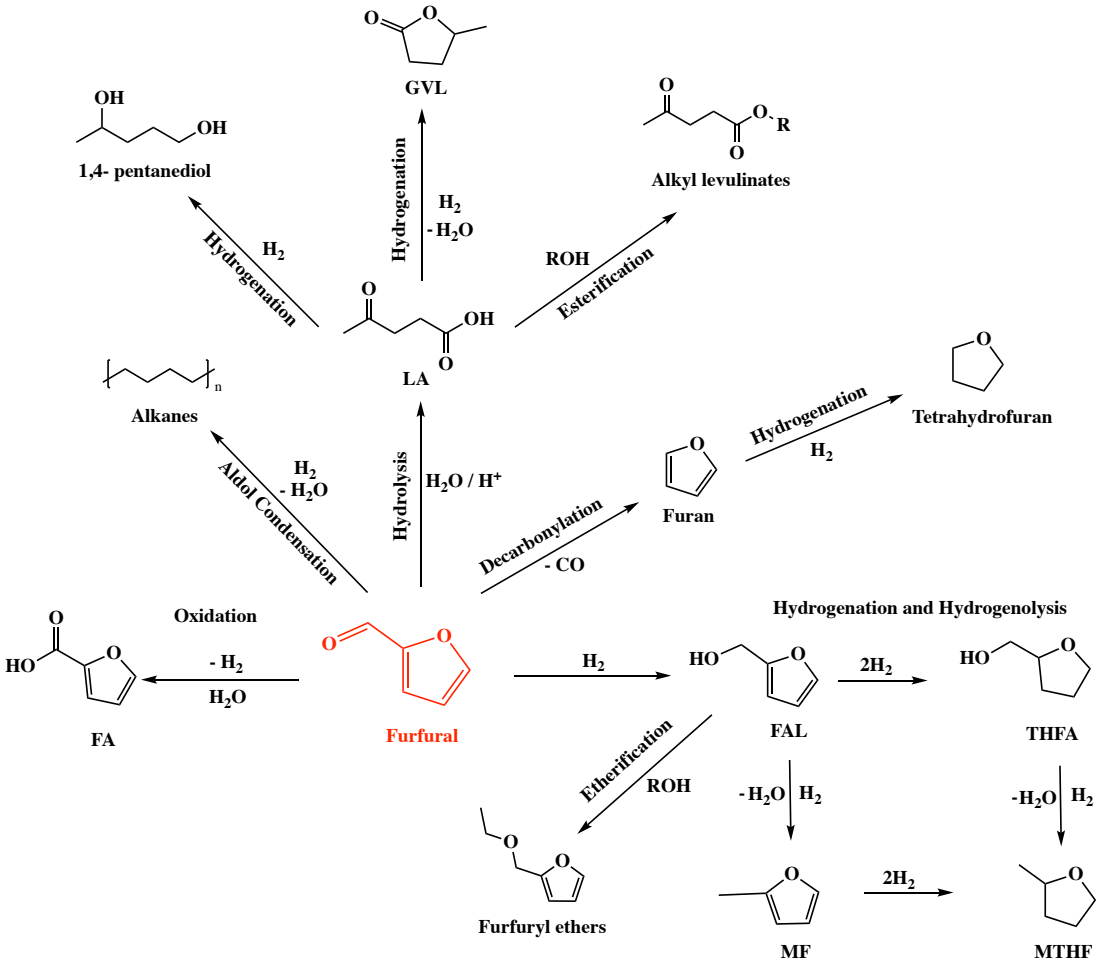

Figure 1.4 Catalytic conversion pathways of furfural to value-added fuels and chemicals [11,23,102,103,105]

Furfural can be converted by hydrogenation to form FAL and MF [22,23,59,101]. FAL is used as a solvent, for the production of thermostatic resins, in adhesives and coatings and finds applications in perfumery, polymer and pharmaceutical industries [8,101,106–109]. MF can be used biofuel or fuel additive because of low water solubility, high octane number and energy density [8,101,106–110]. Further reduction of FAL and MF yields THFA, a green solvent, and MTHF, a fuel additive, respectively [23,59,100]. Oxidation of furfural yields FA [111]. FA is a valuable intermediate in the perfumery and pharmaceutical industries [37,111].

1.3.3 5-Hydroxymethylfurfural

5-Hydroxymethylfurfural (HMF) is an important bio-derived feedstock chemical, which is obtained by the dehydration of hexose (glucose, fructose) sugars [112]. HMF has been named as a 'sleeping giant' in the field of intermediate chemicals [51,113]. HMF is a versatile carbonyl compound with sensitive functional groups that can be converted to a variety of value-added compounds by undergoing oxidation, hydrogenation, hydrogenolysis, etherification, aldol condensation, dehydration, etc. [11,45,101,114–117]. Some of the pathways of HMF valorization to value added biofuels and chemicals are given in Figure 5. HMF can be converted to 2,5-dihydroxymethylfuran (DHMF), 2,5-dihydroxymethyltetrahydrofuran (DHMTHF), 2,5-hexane-dione (HD), 2,5-dimethylfuran (DMF), 5-methylfurfural (5-MF), etc. by reduction [37,43,114,115] and to 2,5-diformylfuran (DFF), 5-formylfurancarboxylic acid (FFCA) and 2,5-furandicarboxylic acid (FDCA), etc. by oxidation [22,37,43,116]. HMF derivatives are of great interest and find applications as fuel and fuel additives, as monomers of plastics, and in polymer and pharmaceutical industries [115,118–121]. DFF [115,122–124], ethyl levulinate [119,125], levulinic acid (LA) [120,126], and FDCA [127,128], liquid alkanes [103,105], gamma-valerolactone (GVL) [105], 1,6-hexanediol [52,105], caprolactam [52,105], are some of the high-

quality fuels and chemicals obtained from HMF. DHMF has applications in many of the industrial polymerization and etherification processes [118,129,130]. HD is used for the production of fuel additives such as 3-methylcyclopentanol and methylcyclopentane [114,131]. FDCA acts as a monomer to produce a renewable polymer with enhanced properties as compared to polyethylene terephthalate polymers [132].

HMF can be also be etherified to 5-alkoxymethylfurfural (AMF) [45,121,129,133–135]. 5-Alkoxymethylfurfurals (AMFs) serve as promising fuel additives due to their high energy density

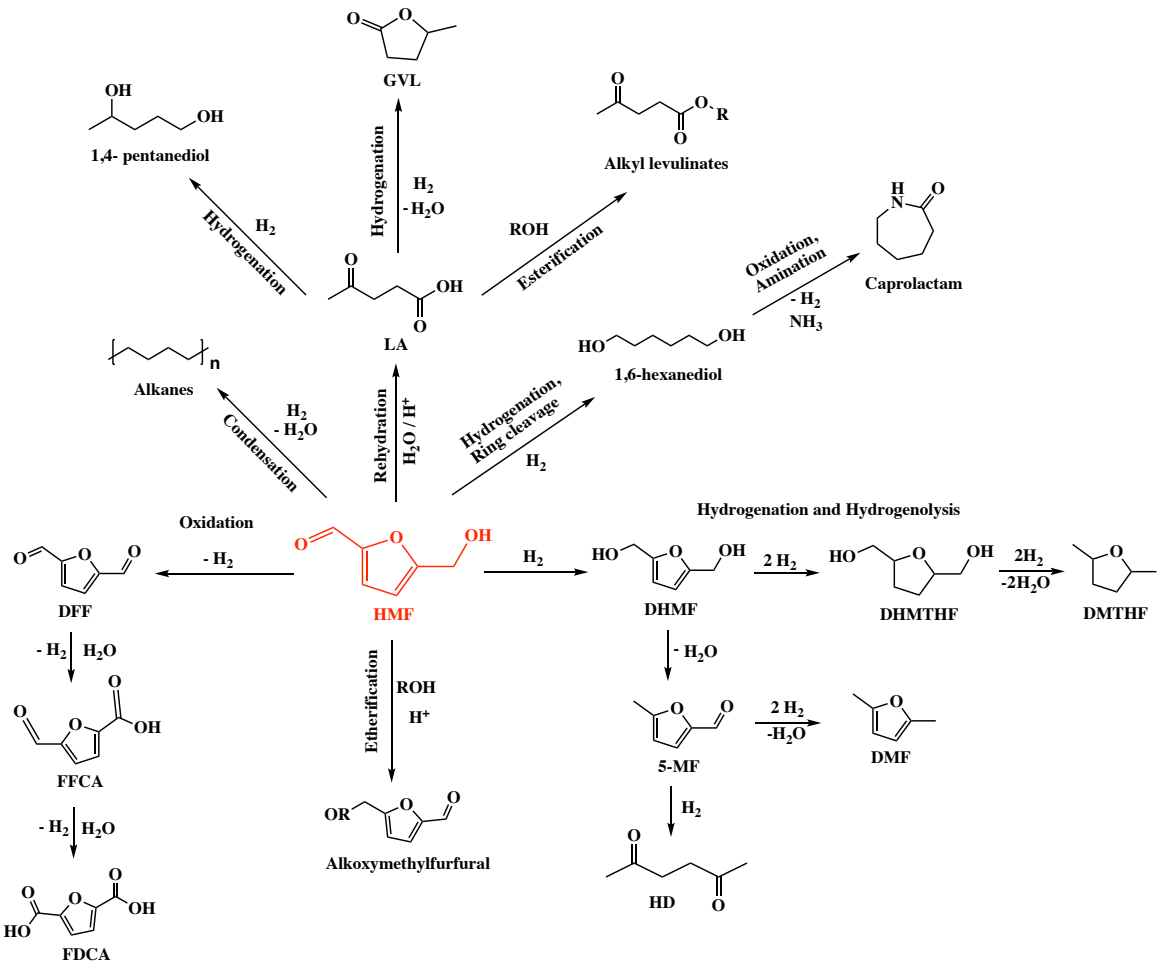

Figure 1.5 Catalytic conversion pathways of HMF to value-added fuels and chemicals [11,102,103,105]

[45,121,136]. Amongst AMFs, 5-methoxymethylfurfural (MMF) and 5-ethoxymethylfurfural

(EMF) produced by etherification of HMF with monohydroxy alcohols, such as methanol and ethanol, respectively, are some of the well-known and extensively studied fuel candidates [45,121,129,137]. EMF has been reported to be an excellent fuel additive with energy density of 8.7 kWh/L, which is close to that of diesel (9.7 kWh/L) and gasoline (8.8 kWh/L) [138]. AMF fuel additives with better blending abilities can be produced using di- or tri-hydroxy alcohols such as 5-(2-hydroxyethoxymethyl)furfural (HEMF) obtained by HMF etherification with ethylene glycol [139,140].

1.4 Catalysis

A catalyst is a substance that increases the rate of the reaction by decreasing the activation energy required for the conversion of reactants to products. It remains unchanged after participation in a chemical reaction and can be continuously utilized during the reaction. Catalysis is the application of catalysts and catalytic processes [17,18,141,142]. It is advantageous in achieving process intensification with maximum energy efficiency by developing one pot catalytic cascade reactions using multifunctional catalysts [17].

1.4.1 Types of Catalytic Processes

Depending on the type of catalyst used in the process, catalysis can be broadly divided into homogeneous catalysis [143], heterogeneous catalysis [143,144], electrocatalysis [43,145–147], photocatalysis [148], and bio-catalysis [149]. Catalysts may be supplied in several physical forms, *e.g.* powders, granules, pellets or extrudes, depending upon the type of the catalyst, the reaction and the reactor type to be employed [18,141].

1.4.1.1 Homogeneous Catalysis

Homogeneous catalysis involves the presence of catalyst and reactants in the same phase, usually liquid. Homogeneous catalysts are soluble/miscible in the reaction mixture. They can be

acid, base, transition metal complexes, metal ions, etc. depending on the type of reaction desired. Homogeneous catalysts, being well dissolved in the reaction mixture and typically possessing a single active site, are often more active and selective than heterogeneous catalysts. High activity may also arise since pore diffusion limitations are absent but bulk heat and mass transfer limitations may exist if sufficient agitation is not provided, particularly in viscous systems. Homogeneous catalysts are not thermally stable and thus, cannot be used for high temperature reactions [18]. Since, they are completely miscible, recovery of the catalyst at the end of reaction is not possible, and hence they are not reusable [18,143]. Additionally, product extraction procedures are tedious as they require neutralization of the acid/base catalyst, to separate the product efficiently [18]. This makes the process expensive, leads to large amount of waste generation, and is environmental unfriendly [143]. Thus, the E-factor for homogeneously catalyzed processes is high [11]. However, still many bulk and fine chemicals and pharmaceuticals are being synthesized using homogeneous catalysts which are based on transition metal complexes [9,11]. Homogeneously catalyzed reaction mechanisms are often well understood in terms of specific reactant-catalyst interaction and transition states [143].

1.4.1.2 Heterogeneous Catalysis

Heterogeneous catalysis involves the presence of catalyst and reactants in distinct phases, wherein catalyst is usually solid and the reactants/products are liquid or gas [18,141]. The catalyst is insoluble in the reaction mixture, and it must be well dispersed and porous to allow large interfacial area at which the reaction can occur efficiently [141]. Insolubility leads to the presence of bulk mass transfer and pore diffusion limitations, which must be ameliorated by applying agitation, increasing pore volume among many techniques [18,141]. High temperature conditions are often desired to achieve high activity, which is possible if a catalyst displays high thermal

stability [18]. Additionally, heterogeneous catalysts can be easily separated at the end of the reaction by filtration from a batch reactor and can be re-used multiple times after washing and pretreatment. In packed and fluidized bed reactors, spent catalysts can be regenerated using water, oxygen, steam, or heat in situ or at an off-site [150,151]. This makes the process green, environmental benign and economical [17,141,143,144].

Some common heterogeneous chemical catalysts used in industrial processes include metals, metal oxides, zeolites, clays, heteropolyacids, hydrotalcites, etc. [18,144]. Some heterogeneous catalysts such as clays, zeolites etc. are advantageous in that they offer high chemical selectivity due to pore shape and structure allowing only desired reactants to undergo reaction [141]. These catalysts can either be used in their bulk form or as supported catalysts by dispersing them on a high surface area substrate such as hydrotalcite supported on hexagonal mesoporous silica, Pt/alumina, heteropolyacid supported on clays [18,152,153]. Solid catalysts can be easily scaled up to design continuous processes, which makes them economic at industrial scale [143]. Catalyst reusability and efficient product separation leads to lower E-factor for heterogeneously catalyzed processes [18,144]. Thus, heterogeneous catalysts are highly utilized in processes used for bulk chemical manufacture and fuel synthesis in petrochemical industries [18,143,144].

Heterogeneous catalytic reactions occur at the fluid-solid interface, and the mechanism typically involves five steps: 1) Diffusion of reactants from the bulk phase to the catalyst surface, 2) Adsorption of reactants on the catalyst surface, 3) Surface reaction on the catalytic active sites to form the product, 4) Desorption of products from the catalyst surface, 5) Diffusion of products from the catalyst surface to bulk phase [18,141]. The surface reaction can occur by Langmuir-Hinshelwood-Hougen-Watson (LHHW) mechanism or Eley-Rideal mechanism. The LHHW model involves surface reactions either with a single site mechanism, wherein a reactant adsorbed

at only one site is involved in the reaction, or a dual site mechanism, wherein a reactant adsorbed at one site reacts with another similar/different type of site, which could be vacant or populated with another reactant to form a product [141]. The Eley-Rideal mechanism involves reaction between an adsorbed molecule and another molecule in the liquid/gas phase, the latter being near the catalyst surface having an adsorbed species but the second species not being adsorbed [141].

1.4.1.3 Electrochemical Catalysis

Electrocatalysis employs the use of an electrode as a catalyst to accelerate an electrochemical (electron transfer) reaction [154,155]. Electrocatalytic conversion is a green pathway to convert biomass-derived platform chemicals into value-added fuels and chemicals by using hydrogenation and oxidation processes [156–161]. Electrochemical reactions are conducted in aqueous solutions using water as the hydrogen/oxygen source and at ambient conditions, thus fulfilling the major principles of green chemistry [36,101]. With decreasing electricity prices and increasing production from renewable sources such as solar and wind, electrocatalytic reactions provide a sustainable way to store the energy derived from renewable feedstocks into liquid biofuels [100]. As with temperature in chemical catalysis, the two additional parameters which can be controlled in an electrocatalytic system are electrode potential and/or faradaic current. These parameters are helpful in tuning the reaction rate and selectivity [162]. The direction of the reaction can be changed just by reversing the current [162].

An overall electrochemical reaction can be written as the sum of two half reactions, oxidation and reduction, each of which has an equilibrium reduction potential. Oxidation occurs at the anode and involves loss of electrons (e.g. zinc oxidation, equation 1.1) while reduction occurs at the cathode involving gaining electrons (e.g. copper reduction, equation 1.2). Zinc oxidation and copper reduction are examples of two half-cell reactions in a Daniel cell, wherein copper metal is

reduced at the cathode using the electrons from zinc oxidation at anode, thus, the full-cell electrochemical reaction can be written as in equation 1.3 [162].

$$\mathrm{Zn}_{(s)} \rightarrow \mathrm{Zn}^{2+}_{(aq)} + 2e^- \tag{1.1}$$

$$\mathrm{Cu}^{2+}_{(aq)} + 2e^- \rightarrow \mathrm{Cu}_{(s)} \tag{1.2}$$

$$\mathrm{Zn}_{(s)} + \mathrm{Cu}^{2+}_{(aq)} \rightarrow \mathrm{Zn}^{2+}_{(aq)} + \mathrm{Cu}_{(s)} \tag{1.3}$$

The higher the equilibrium reduction potential of a chemical ion/compound, easier it is to reduce it. The two half reactions are connected via a salt bridge or an ion exchange membrane to conduct ions. The electrons travel through the circuit and can either do electrical work (galvanic cell) or take up electrical energy (electrolytic cell) [163]. Electrochemical reactions can be conducted using a two or three electrode system. In a three-electrode system (Figure 6), the reaction of interest (oxidation/reduction) occurs on the working electrode (WE), the corresponding half reaction occurs at the counter electrode (CE), which is required for charge neutrality. The potential of WE is measured with respect to a reference electrode (RE), whose equilibrium potential is known such as reversible hydrogen electrode, silver/silver chloride electrode, saturated calomel electrode, etc. [162]. Electrolytic cells can be operated in two modes: galvanostatic (constant current) and potentiostatic (constant potential), the latter being more reliable to study the kinetics of the system [162].

Equilibrium cell potential ($U^{\circ}_{\mathrm{cell}}$) of an electrochemical system are calculated from the standard equilibrium reduction potential difference between two half reactions: cathodic ($\mathrm{U}^{\circ}_{\mathrm{c}}$) and anodic ($U^{\circ}_{\mathrm{a}}$) (equation 1.4).

$$U^{\circ}_{\mathrm{cell}} = U^{\circ}_{\mathrm{c}} - U^{\circ}_{\mathrm{a}} \tag{1.4}$$

The cell potential can be used to calculate the change in Gibbs free energy (G) of the reaction given by:

$$\Delta G = -nFU^{\circ}_{\text{cell}} \tag{1.5}$$

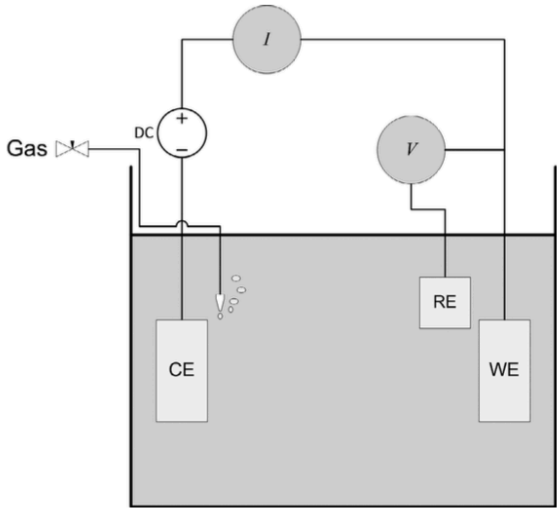

Figure 1.6 Schematic of a three-electrode electrochemical system (Reproduced from [162])

Where, n = number of electrons transferred in an overall reaction, F = Faraday's constant (96485 C/mol of electrons) and E°_{cell} is the equilibrium cell potential. Negative standard Gibbs free energy indicates a spontaneous reaction [162].

The equilibrium reduction potential of a half reaction can also be referenced as the open circuit potential, which is when the forward and reverse reactions are at equilibrium and the net current is zero. Overpotential (η) is the driving force for any electrochemical reaction and it can be calculated as the difference between the working electrode potential (V) and the equilibrium potential (U) relative to same RE.

The current obtained for a given overpotential is determined by the kinetics of the reaction and mass transfer effects. Current density is a more useful aspect in assessing an electrochemical

reaction as compared to current and it can be calculated as current per unit geometric surface area/electrochemical surface area or per unit mass [162].

The Faradaic kinetics of a system can frequently be described by the Butler-Volmer equation, wherein the total current density (i) can be written in terms of anodic (i_a) and cathodic (i_c) current density terms:

$$i = i_a + i_c \tag{1.6}$$

$$i = -i_0 \left\{ \exp\left(\frac{\alpha_a F \eta}{RT}\right) - \exp\left(\frac{-\alpha_c F \eta}{RT}\right) \right\} \tag{1.7}$$

Where, i_0 is the exchange current density (mA/cm^2), α is the anodic or cathodic transfer coefficient, *R* is gas constant and *T* is temperature. Near equilibrium, both the anodic and cathodic current density terms must be considered but if the reaction is far away from equilibrium, only one of the anodic/cathode reactions dominate and we can reduce Butler-Volmer equation to Tafel equation, which is given by [162]:

$$i_a = i_0 \exp\left(\frac{\alpha_a F \eta}{RT}\right) \quad \text{(Anodic Tafel)} \tag{1.8}$$

$$i_c = -i_0 \exp\left(\frac{-\alpha_c F \eta}{RT}\right) \quad \text{(Cathodic Tafel)} \tag{1.9}$$

The Tafel equation can be simplified to get a relationship for overpotential as a function of current density, which can be used to calculate charge transfer coefficient (fraction of total potential energy that imparts activation energy for an electrochemical reaction) (*via* α) and Tafel slope (slope of the plot of overpotential vs log of current density indicating overpotential required to increase reaction rate by an order of magnitude) (b, mV/decade) as:

$$\eta = -\frac{RT}{\alpha_C F}\ln(-i) + \frac{RT}{\alpha_C F}\ln(i_0) \tag{1.10}$$

$$\eta = -\,\mathrm{b}\ln(-i) + \alpha \ln(i_0) \tag{1.11}$$

The efficiency of an electrocatalyst can be described by its exchange current density (equilibrium anodic and cathodic current density, mA/cm^2), Tafel slope (mV/decade), current density for a given overpotential (mA/cm^2) and overpotential required to reach a desired current density (Volts). Catalyst efficiency is primarily measured in terms of Faradaic efficiency, which quantifies the fraction of total current that drives the desired reaction [162]. Some important electrochemical reactions that are extensively researched include proton/water reduction to hydrogen gas, oxygen reduction to water, CO_2 reduction to hydrocarbons and nitrogen reduction to ammonia. These reactions have applications in fuel cells, batteries and wastewater treatment as well as biomass and carbon dioxide upgrading to fuels and chemicals [43,147,164–166].

Electrochemical processes have been used commercially for high scale production of chemicals for e.g. electrohydrodimerization of acrylonitrile to adiponitrile, production of chlorine and sodium hydroxide by Chlor-Alkali process, aluminum metal production, winning and refining processes to produce Cu, Ni, Mg, Ti and Zn [167–169]. Adiponitrile is used for the synthesis of hexamethylenediamine, which is a raw material for the production of nylon-6,6 polymers. Nearly 30 % of the world's total adiponitrile production is by electrochemical route, led by producers such as Solutia, Asahi Chemical and BASF. Chlor-Alkali products also act as a precursor for the manufacture of specialty chemicals used as adhesives, plastics, paints, cosmetics, lubricants, polymers, etc. Some other chemicals that are produced by electro-organic synthesis include fluorination of alkyl substrates to perfluorinated hydrocarbons (3M, Bayer, Clariant), hydrodimerization of formaldehyde to ethylene glycol (Hydro Quebec), epoxidation of propylene to propylene oxide (Kellog, Shell), reduction of maleic acid to succinic acid (CECRI), reduction of nitrobenzene to azobenzene (Johnson Matthey), hydrogenation of naphthalene to 1,4-dihydronaphthalene (Clariant).

1.4.2 Electrochemical vs Chemical Hydrogenation

Electrochemical/Electrocatalytic hydrogenation (ECH) reactions are emerging as a green alternative to chemical/chemo-catalytic hydrogenation (CH) reactions for the production of fuels and chemicals, as they are carried out at room temperature, atmospheric pressure and in the presence of aqueous solvents. Additionally, ECH uses the protons generated at the anode by water splitting as a source of atomic hydrogen, thereby lowering the operation and energy cost of the cell and thus increasing efficiency [170]. This also replaces the transportation, storage, usage of molecular H_2 as required in the chemical hydrogenation reaction.

CH and ECH pathways differ in their ways to generate atomic hydrogen. In the CH process, there is splitting of the externally supplied molecular hydrogen gas to atomic hydrogen, whereas ECH uses electrons generated by water oxidation (1.12) to reduce protons/hydronium ions from the electrolyte to atomic adsorbed hydrogen on the cathodic surface by Volmer reaction (1.13) [170].

$$\text{Water oxidation:} \qquad 2\ H_2O \rightarrow 4\ H^+ + 4\ e^- + O_2 \tag{1.12}$$

$$\text{Volmer reaction:} \qquad H^+ + e^- + M \rightarrow (H_{ads})M \tag{1.13}$$

In ECH, the kinetic barriers required for H_2 activation are not required and thus, the reactions demanding high temperatures and pressures in a chemo-catalytic pathway can take place at ambient conditions in the electrochemical pathway because of the applied voltage [171].

Electrochemical reaction mechanisms can be distinguished as inner and outer sphere electron transfer processes. In an inner sphere electron transfer process, reactions occur in an inner Helmholtz plane (position of centers of ions or molecules directly adsorbed on electrode surface), wherein a common electroactive metal complex ligand is adsorbed on the electrode surface which acts as a bridge for electron transfer from the electrode to the electroactive species. Inner sphere

reactions are highly dependent on the nature of electrode material. In an outer-sphere process, electroactive species is present in the outer Helmholtz plane (plane of closest approach for solvated ions preventing adsorption) and electron transfer takes place with primary coordination spheres remaining intact. The nature of electrode material might be expected to be less important for such reactions [162,172].

ECH mechanisms involve inner sphere electron transfer processes characterized by strong adsorptive interactions of the reactant with the electrode surface [162]. Some carbonyl compounds (aldehydes and ketones) have also been reported to be hydrogenated through electroreduction routes (ECR), which do not involve adsorbed hydrogen and thus, surface reaction. Electroreduction mechanisms can be classified as outer sphere electron transfer reactions since the reactants do not interact with the electrode surface [162]. In electroreduction pathway, electrons (e^-) are still provided by the catalytic electrode, however, the protons (H^+) required for reduction are taken directly from the electrolyte. This results in the formation of a radical intermediate (C•-OH) from reaction of carbonyl reactant with H^+/e^- pair, which can be further reduced to alcohol by uptake of another H^+/e^- pair or be dimerized to a pinacol product (Figure 7). This electrodimerization reduces the Faradaic efficiency (FE) of the desired electroreduction or ECH product [106,159,173].

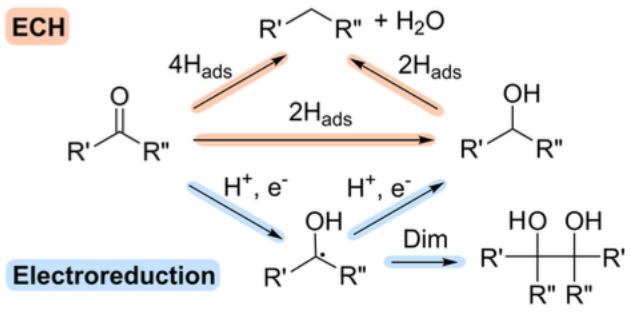

Figure 1.7 Proposed pathways of ECH and ECR of carbonyl compounds (Reproduced from [106])

The preference for ECH or ECR is determined by the overpotential required for the formation of adsorbed hydrogen (H_{ads}) and radical intermediate (C•-OH). Thus, ECH is preferred on low hydrogen overpotential electrodes (Pt, Pd, Ru, Rh) and ECR is favorable on high hydrogen overpotential electrodes (Pb, Cd, graphite). Medium hydrogen overpotential electrodes (Cu, Ni, Fe, Co, Au) would involve both ECH and ECR in competition [106].

Metals with high, medium, and low hydrogen overpotential are depicted by the ascending curve of the volcano plot shown in Figure 8 for hydrogen evolution reaction in acidic solutions. It shows plot of log of exchange current density against strength of metal-hydrogen bond formed during an electrochemical reaction. Low hydrogen overpotential electrodes (Pt, Pd, Ru) fall near the top of the volcano plot, where M-H bond is strong enough to adsorb H atoms but not so strong that H_2 gas could not evolved. Thus, their hydrogen adsorption energy is close to zero ($\Delta G^0 \approx$

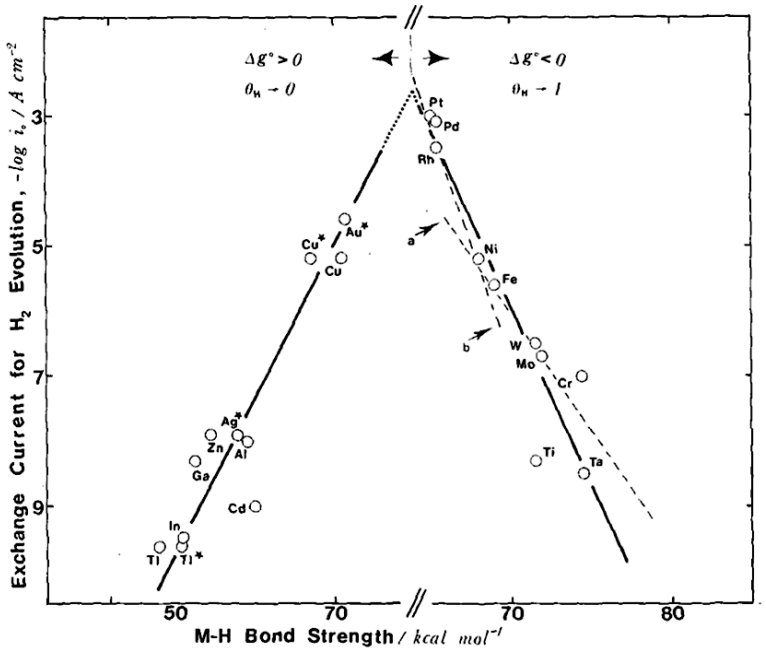

Figure 1.8 Exchange current density for HER vs strength of metal-hydrogen bond (ΔG^0 is standard free energy of hydrogen adsorption and θ_H is surface coverage with atomic hydrogen (Reproduced from [325])

0) and they possess the highest catalytic activity for HER. High hydrogen overpotential electrodes (Pb, Cd, graphite) adsorb hydrogen very weakly ($\Delta G^0 > 0$)and this suggests favoring of ECR mechanism on such electrodes.

The selectivity for ECH/ECR is also often limited by competitive hydrogen evolution reaction (HER), which consumes protons to produce H_2. This can occur by by Tafel or Heyrovsky reactions and this lowers the electrochemical efficiency of the cell [8,101,106].

$$\text{Tafel reaction: } 2\,(H_{ads})M \rightarrow H_2 + 2\,M \tag{1.14}$$

$$\text{Heyrovsky reaction: } H^+ + e^- + (H_{ads})M \rightarrow H_2 + M \tag{1.15}$$

As an example, HER and ECR reactions have been reported to decrease the Faradaic efficiency of ECH of furfural. ECR leads to the formation of dimerized product, hydrofuroin, as opposed to the desired product, FAL, which can be formed by either ECH or ECR [100,106]. Thus, selective metal catalysts are desired that have high FE for ECH and desired ECR as compared to HER, which will help to maximize the efficiency of the reaction.

1.4.3 Types of catalyst

The catalyst utilized in a process could be monofunctional or multifunctional. Monofunctional catalysts possess one type of functionality and can be acid, base or redox metal catalyst [18,144,174]. Multifunctional catalysts contain a mixture of materials possessing different combinations of acid, base and metal catalyst functional moieties [18,144,175,176]. These functionalities can be supported on high surface area mesoporous materials such as incorporation of metals into solid acid or base catalyst or a combination thereof to achieve novel heterogenous catalysts [18,175]. One-pot catalytic cascade reactions usually require multifunctional catalysts to achieve selective intermediate, product and co-product synthesis, without requiring separation and purification of intermediates. Cascade reaction mechanisms with multifunctional catalysts involve

two or more sequential or parallel reactions, which are catalyzed by two or more different active sites from different catalytic functionalities [160,174–180]. For example, metal organic frameworks (MOF) can be designed to incorporate acid and basic active sites in their backbone or to have different metal centers forming bimetallic MOF [175,177]. A representative cascade reaction is one-pot synthesis of 2-(4-aminobenzylidene)-malononitrile (ABM) catalyzed by metal-base bifunctional core-shell Pd nanoparticles surrounded by amino functionalized MOF, where basic MOF catalyzes Knoevenagel condensation of 4-nitrobenzaldeyde and malononitrile to 2-(4-nitrobenzaldehyde)malononitrile (NBM) and Pd metal nanoparticles selectively hydrogenate NO_2 group of NBM to ABM [175]. Similarly, carbon supported bimetallic Au and Pd nanoparticles have been used for electrocatalytic oxidation of HMF to FDCA via DFF and FFCA intermediate formation, where Pd/C effectively hydrogenates HMF to DFF and DFF to FFCA and Au/C rapidly hydrogenates FFCA to FDCA [160]. Such processes would be more sustainable in terms of process efficiency, waste minimization, resource use and environmental friendliness [174,176].

1.4.3.1 Base catalyst

Some common reported heterogeneous base catalysts include bare and supported: clay minerals (*e.g.* Mg-Al, Cu-Al, La-Al hydrotalcites, sepiolite, chrysolite), alkali metal hydroxides (*e.g.* KOH/Al_2O_3), alkaline (*e.g.* MgO, CaO) and rare earth metal oxides (e.g. La_2O_3), ZrO_2, bimetallic metal oxides (e.g. $ZnO\text{-}Al_2O_3$, $MgO\text{-}TiO_2$), alkali ion-exchanged (*e.g.* Cs-X, Na-X), zeolites, supported alkali metal compounds (*e.g.* Na/Al_2O_3), non-oxides (*e.g.* KF/Al_2O_3), hydroxyapatites, etc. [144,181–188]. Some of the solid base catalyzed reactions include alkylation, isomerization, aldol condensation, esterification, transesterification, interesterification, etc. [144,181–183]. Base catalysts are widely used in industries for fine chemical synthesis [144,182].

1.4.3.1.1 Hydrotalcite

Hydrotalcites (HT - hydroxycarbonates of magnesium and aluminum) are minerals belonging to the family of anionic clays, containing anionic species in the interlamellar space [189]. Hydrotalcite like compounds have a general formula of $M^{2+}_{1-x}M_x^{3+}(OH_2)^{x+}(A_{x/n})^{n-}.yH_2O$ where M^{2+} (Al, Fe, Cr) and M^{3+} (Mg, Ni, Co, Zn, Cu, Ca) are divalent and trivalent metal cations respectively, $A^{n-}(CO^{3-}, SO_4^{2-}, Cl^-, NO^{3-})$ is an n-valent anion, and x usually has a value between 0.25 and 0.33 [189–191]. Mg-Al hydrotalcites are also known as layered double hydroxides with brucite-like ($Mg(OH)_2$) layers containing octahedrally coordinated M^{2+} and M^{3+} ions with positive charge compensated by interlayer anions [189,192] (Figure 9).

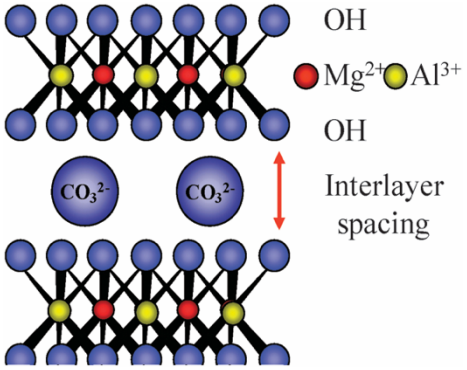

Figure 1.9 Schematic of Mg-Al hydrotalcite structure (Reproduced from [193])

A coprecipitation method is conventionally used for the synthesis of HTs [153,194]. Decomposition of HTs gives a high surface area with strong Lewis base sites and weak acid sites [189,192]. They exhibit memory effects, and rehydration of heat-treated HT recovers their structure and can form Bronsted base sites by the replacement of anions by hydroxyls [189,192]. Calcination of hydrotalcite is well known to achieve a mixed oxide that possesses Lewis basicity [153,192,194]. This thermal treatment removes the water molecules, the interlayer charge compensation anions and other volatile species introduced during coprecipitation. The acidic and basic properties in the HT can be adjusted with changes in metal and metal composition [189].

1.4.3.2 Acid catalyst

Heterogeneous acid catalyzed reactions are widely used in industries for reaction processes such as Friedel Crafts acylation and alkylation, etherification, esterification, transesterification, dehydration, cyclization, nitrations, halogenations etc. [144,195,196]. Acid catalysts are characterized by their Lewis and Bronsted acidity or a combination thereof. The strength and number of the Lewis/Bronsted acid sites determines product selectivity [195]. Lewis acids such as aluminum chloride need to be supported on a high surface area support such as zeolites, carbon, silica, zirconia, clays for use as heterogenous catalysts [195,196]. Several Bronsted acid catalysts have been described in the literature: sulfated zirconia, sulfated titania, zeolites, heteropolyacids, clays, etc. They can either used in bare form or be supported for high dispersion and better thermal stability [144,195].

1.4.3.2.1 Heteropolyacid

Heteropolyacid (HPA) catalysts have gained a great deal of interest as they show excellent Bronsted acidity [197–199]. There acidity approaches the super acid region (Hammett acid strength = -13.2) leading to high catalytic activity [200,201]. HPAs are composed of protons as counter cations bound to heteropoly anions having metal-oxygen octahedra as a basic unit. Keggin-type HPAs have been widely used because of their ease of preparation. An example HPA catalyst, dodecatungstophosphoric acid (DTP, $H_3PW_{12}O_{40}$) possessing Keggin structure is formed by the condensation of phosphate ion with tungstate ion.

$$PO_4^{3-} + 12\ WO_4^{3-} + 27\ H^+ \rightarrow H_3PW_{12}O_{40} + 12\ H_2O \qquad (1.16)$$

Here, phosphorous (P) is the heteroatom, which is located at the center of HPA molecule. The other atoms, known as polyatoms or addenda atom are bound to central P heteroatom through oxygen atoms. In the DTP structure, a Keggin unit consists of a central PO_4 tetrahedron, and 12

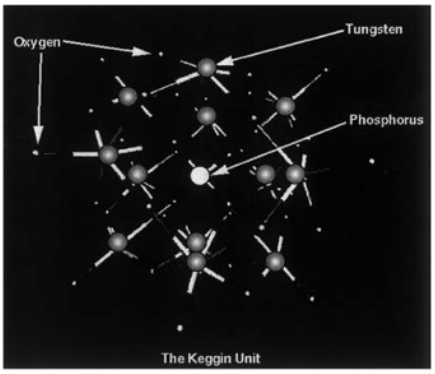

Figure 1.10 Schematic of Keggin structure of DTP (Reproduced from [199])

terminal and 24 bridged oxygen atoms that form twelve octahedra of addenda atoms, W, surrounding it [199,200] (Figure 10).

Typical HPAs used are $H_3PW_{12}O_{40}$, $H_4SiW_{12}O_{40}$, $H_3PMo_{12}O_{40}$ and $H_4SiMo_{12}O_{40}$. The acid strength and thermal stability of HPAs change with the heteroatom and polyatom (Table 1) and follow the order as: $H_3PW_{12}O_{40} > H_4SiW_{12}O_{40} \geq H_3PMo_{12}O_{40} > H_4SiMo_{12}O_{40}$. As compared to other HPAs, the highest acidity and thermal stability is possessed by DTP ($H_3PW_{12}O_{40}$), and acid strength decreases according to the support type, $SiO_2 > Al_2O_3 >$ carbon [199,200,202]

Table 1.1 Acid strength and thermal stability of HPAs [200,203]

Acid	**Dissociation constants of HPAs in acetone at 25 °C**			**Decomposition Temperature (°)**
	pK_1	**pK_2**	**pK_3**	
$H_3PW_{12}O_{40}$	1.6	3	4	465
$H_4SiW_{12}O_{40}$	2	3.6	5.3	445
$H_3PMo_{12}O_{40}$	2	3.6	5.3	375
$H_4SiMo_{12}O_{40}$	2.1	3.9	5.9	350

However, HPAs suffer from low surface area, poor stability due to leaching and are highly soluble in the presence of polar solvents such as alcohol and water. Hydrated conditions lead to

the decrease in the catalytic activity [204]. Due to their instability and leaching in protonic form during liquid phase reactions, they tend to have a homogeneous catalytic nature in reaction media and suffer from poor catalyst recyclability [199].

These problems have been solved by using HPAs supported on mesoporous material such as mesoporous silica, mesoporous aluminosilicates, alumina, metal oxide, carbon, K-10 clay, etc. and replacing the protons in HPA with metal ions such as Cs^{+}, Al^{3+}, Fe^{3+}, Ca^{2+}, Co^{2+}, Sn^{4+}, Ru^{3+}, Fe^{3+}, Zr^{4+}, etc. [104,152,209,197–199,202,205–208]. Some polyvalent metal ions such as Al^{3+}, Fe^{3+}, Ru^{3+}, etc. generate Lewis acid sites in the catalyst, which combined with DTP's Bronsted acidity results in higher acidity that the parent DTP [208,210].

1.4.3.3 Metal catalyst:

Metal catalysts are generally used for reduction and oxidation reactions in chemical/electro-chemical reactions [38,158,211–215]. The various examples of metal catalysts include precious/noble metals (platinum, rhodium, palladium, ruthenium, gold, silver), transition metals (nickel, cobalt, iron, copper, etc.), zinc, lead, etc. [36,106,217–220,114,158,165,211,213–216]. These catalysts can be used in different forms such as bare metal (powders, wires, pellets, foils), metal oxides (copper oxide, manganese oxide, titania, zinc oxide), metal alloys (Raney nickel), or supported forms (Pt/C, Ni/C, Pt/alumina), etc. [211,213,215,221]. Single atom catalysts such as metal nitrogen carbon catalysts synthesized by pyrolysis of nitrogen and carbon based precursors have served as a promising catalyst for oxygen reduction reactions due to high porosity and atomically dispersed active sites [222–225]. In a chemo- or electro-catalytic reaction, a bare metal catalyst exhibiting high conversion, yield and FE for a desired reaction can be used for synthesizing high surface area and selective metal nanoparticle catalysts [211]. Metal nanoparticle catalysts can help in achieving higher activity, yield, selectivity and FE of the desired products as compared to

the bulk metal due to high surface area to volume ratio [158,165,226–228]. For example, during ECH of furfural, electrodeposited copper catalysts exhibited increased yields for FAL and MF production by 40 and 20 μmol/cm^2, as compared to the bare copper catalysts [158]. Higher FE and product selectivities have been achieved with zinc metal nanoparticle catalysts over bare zinc metal for CO_2 reduction reactions [165,226–228]. In the following sections, we discuss various substrates that can be used for supporting metal nanoparticle catalysts and synthesis of nanoparticle catalysts by electrodeposition.

1.4.3.3.1 Supports for metal nanoparticle catalysts

There are numerous substrates reported in the literature to support nanoparticle catalysts [47,223,229,230]. Reticulated vitreous carbon (RVC) has been used as a porous carbon support for adsorption of catalysts such as Pd/C, Rh/C, Pt/C. RVC provides a high surface area with good strength and conductivity [229,231]. Carbon felt has been utilized as an efficient catalyst support in flow cell batteries due to its high mass transfer coefficient, flow permeability, and specific surface area [230].

Activated carbon cloth (ACC) has been used as a microporous catalyst support for the adsorption of metals on its surface. Ruthenium has been supported as a catalyst on ACC by incipient wetness impregnation followed by reducing the impregnated catalyst under H_2 stream in an autoclave [36,47].

MOF have gained attention as highly porous support material for catalyst due to high surface area, uniform morphology, and tunable chemical composition. Zeolitic imidazolate framework-8 (ZIF-8) is a MOF that contains a zinc ion bound to 2-mehtylimidazole ligands. ZIF-8 and bimetallic Co-Zn-ZIF, Fe-Co/Zn ZIF have emerged as excellent catalysts for oxygen and CO_2

reduction reactions due to high specific surface area and pore structure which allow adsorption of the reactants [232–237].

Apart from these substrates, the bulk metal itself has been used as a substrate for the growth of nanoparticle catalysts by various techniques [165,226–228,238].

1.4.3.3.2 Zinc metal nanoparticles

Zinc metal is a widely used metal reductant. It can serve as practical catalyst because it's cost-effective and abundantly available on earth as compared to other precious metal catalysts. In chemical reactions, it is mainly used in the form of zinc dust or mossy zinc [215]. In electrochemical reactions, zinc has been used as a bare metal electrode or as metal nanoparticles with different morphologies. The different forms of zinc that have been used include zinc nanoparticles [238], porous zinc [226,227], dendritic zinc [228], hexagonal Zn [165], etc.

Electrodeposition is the most extensively used method to make metallic zinc nanoparticles [165,226–228,239]. There is also a report on zinc nanoparticles synthesis using inverse micelle encapsulation in poly(styrene)-block-poly(2-vinylpyridine) diblock copolymer with uniform size distribution varying from 1.7 to 6.8 nm [238]. Zinc metal nanoparticles synthesis by electrodeposition has been discussed in the following section.

1.4.3.3.3 Electrodeposition

Electrodeposition or electrolytic deposition refers to the deposition of metals on the target electrode (cathode) using an electrolytic cell containing corresponding metal electrolyte [162]. There have been numerous reports on zinc electrodeposition from various electrolyte baths with different morphologies [165,226,245,227,228,239–244]. It has been observed that the choice of zinc precursor, applied potentials, halt time at each potential and number of applied cycles greatly affects the morphology of electrodeposited zinc nanoparticles.

Lu et al. electrodeposited Zn on Zn foil from zinc nitrate solution by applying different multistep potentials of -1 V, -2 V, -2.5 V (vs. Ag/AgCl) each of 0.3-6 s for 30-90 cycles. The electrodeposited zinc was found to have a porous network of nanoparticles of size ranging from 30 – 70 nm [227]. Won et al. observed the formation hexagonal zinc particles when zinc chloride was used as a precursor for electrodeposition on zinc foil by applying multi-step potential of – 2 and -2.5 V/SCE of 3 s each for 30 cycles (Figure 11). The size of the particles was found to be in the range of 400 nm to 1.5 µm [165].

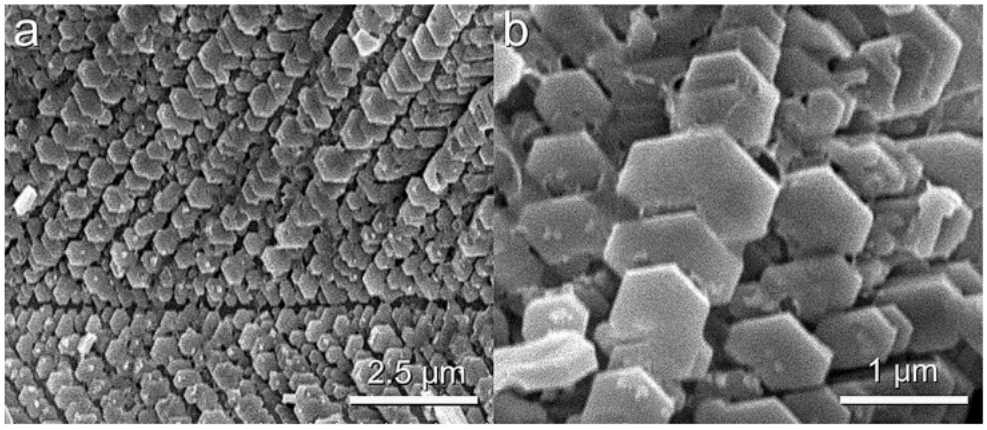

Figure 1.11 SEM morphology of electrodeposited hexagonal zinc particle [165]

The formation of porous hexagonal zinc oxide was also observed when hexamethylenetetramine and ammonium chloride were used as additives, in addition to zinc nitrate and hydrogen peroxide, as precursor of zinc and oxygen, respectively. The ZnO oxide particles were allowed to grow for 2 h on Zn foil at a potential of -0.8 V vs Ag/AgCl electrode. The electrodeposited ZnO was reduced by using cyclic voltammetry from -0.77 to -1.27 V/RHE at a scan rate of 50 mV/s for 15 min [226].

Zinc dendrites were observed when zinc oxide dissolved in potassium hydroxide was used as a precursor for electrodeposition. ZnO was electrochemically reduced to metallic Zn on Zn foil using chronoamperometry at -1 A/cm^2 for 60 s. The effect of deposition rate on the morphology

of Zn electrode was studied. It was found that at low and moderate deposition rates of 10 and 20 mA/cm^2, fragile and bulky electrodes are formed, respectively. A very high deposition rate of 1A/cm^2 was required to form uniformly coated Zn dendrite nanostructures with thickness layer of around 50-100 μm [228].

1.5 Reaction Metrics

The variables used to assess the activity of the catalyst for a particular reaction were calculated using the following equations:

$$Conversion = \frac{{C_A}^0 - {C_A}^t}{{C_A}^0} \tag{1.17}$$

$$Yield = \frac{{C_B}^t}{{C_A}^0} \tag{1.18}$$

$$Selectivity = \frac{{C_B}^t}{C^t} \tag{1.19}$$

$$Faradaic\ efficiency = \frac{{C_B}^t F\, n_i}{Q} \tag{1.20}$$

where, ${C_A}^0$ is the initial concentration of reactant, ${C_B}^t$ is the concentration of the desired product, C^t is the total concentration of the products (desired and undesired) formed at any time 't'; F is the Faraday's constant; n_i is the electron transfer coefficient for a given product and Q is the total charge passed during electrolysis.

1.6 Overview of work

This work aimed to valorize biomass derived platform chemicals – triglycerides, furfural and HMF, to produce value-added fuels and chemicals by using catalytic and electrocatalytic processes (Figure 12).

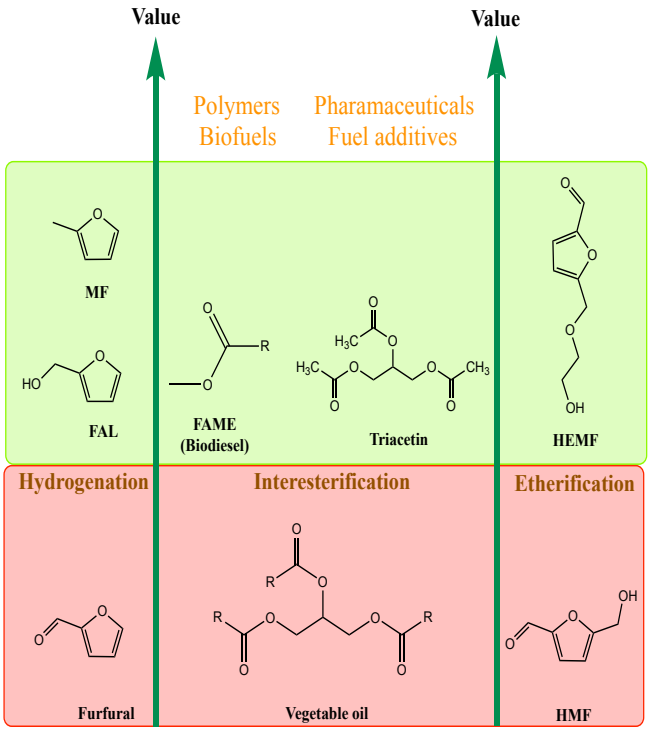

Figure 1.12 Value-added chemicals from vegetable oil triglycerides, furfural and HMF

The dissertation involves the following projects:

In Chapter 2, chemical interesterification of triglycerides with methyl acetate was conducted to co-produce value added chemicals: biodiesel and triacetin. Various base catalysts were screened for their activity in terms triglyceride conversion and triacetin selectivity. The virgin and the reused catalyst were characterized to understand their role in activity and verify stability. The reaction parameters were optimized, and the concentration data of the reaction species recorded at different temperatures were used to model reaction kinetics. (Figure 1.13a)

In Chapter 3, chemo-selective etherification of HMF was conducted with ethylene glycol to obtain 5-(2-hydroxyethoxymethyl)furfural (HEMF) - a fuel additive with high conversion and selectivity. Metal substituted dodecatungstophosphoric acid supported on K-10 clay catalysts were found to be selective for the synthesis of etherified product (HEMF) over the acetalized product (5-hydroxymethylfurfural ethylene acetal). All the catalysts were characterized, and high acidity

of Al substituted DTP/K10 containing Lewis as well as Bronsted acid sites suggested to a play a role in highest HEMF selectivity. The effect of various experimental reaction parameters was studied, and reaction kinetics were deduced. (Figure 1.13b)

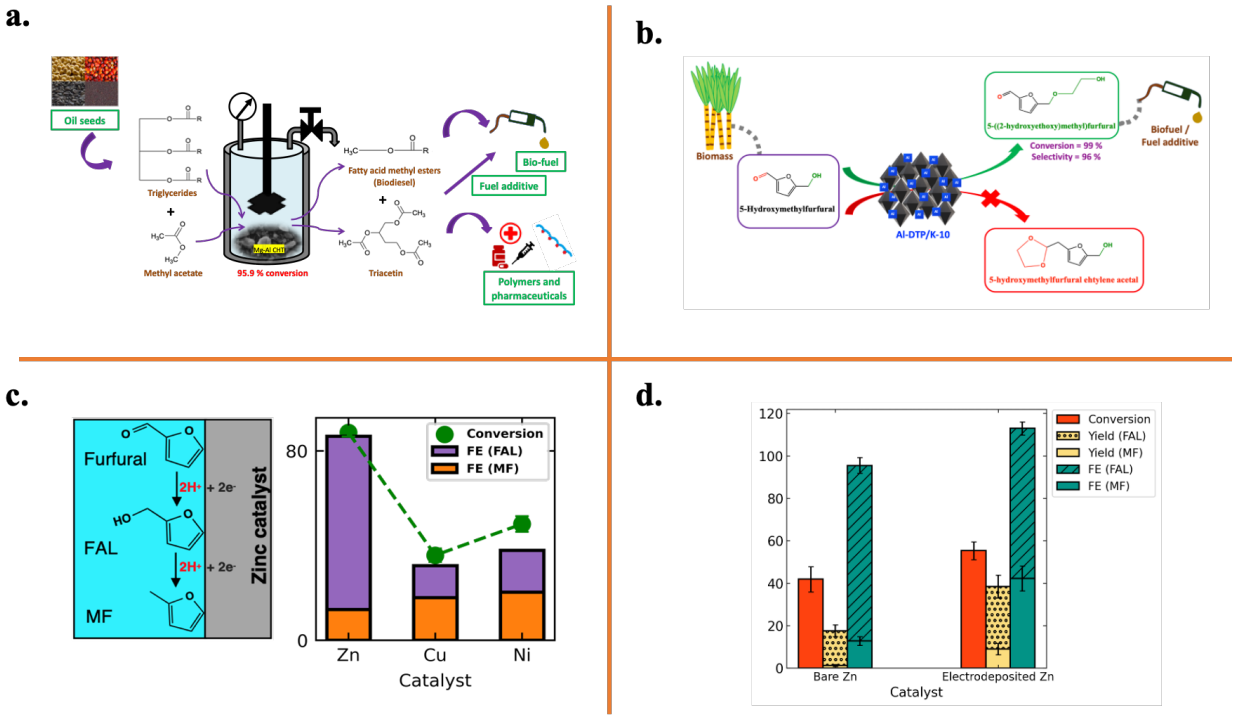

Figure 1.13 Overview of the work. a) Interesterification of triglycerides with methyl acetate to coproduce biodiesel and triacetin using calcined hydrotalcite catalyst, b) Chemo-selective etherification of HMF with ethylene glycol to 5-(2-hydroxyethoxy)methyl furfural using Al substituted dodecatungstophosphoric acid supported on K-10 catalyst, c) Electrocatalytic hydrogenation of furfural to furfuryl alcohol and 2-methylfuran using copper, nickel and zinc bare metal catalyst, d) Activity comparison of bare and electrodeposited zinc metal catalyst for electrocatalytic hydrogenation of furfural

In Chapter 4, electrocatalytic hydrogenation (ECH) of furfural was conducted to produce furfural alcohol and 2-methyl furan. This work establishes the use of zinc as a novel metal catalyst for the ECH of furfural. Yield and FE of furfural ECH was studied for varying electrolyte pH, which was found to significantly affect FE and product profile. At near-neutral pH, zinc stood out as an active catalyst as compared to well-studied copper and nickel catalysts for furfural ECH in terms of conversion, yield and Faradaic efficiency (FE). Oxidation of zinc was observed during

electrolysis, only in the presence of furfural, suggesting that oxidized zinc may play a role in the reaction mechanism. (Figure 1.13c)

In Chapter 5, supported zinc metal nanoparticles were used for the ECH of furfural to achieve higher conversion, yield and FE of FAL and 2-MF products as compared to bare zinc metal due to high surface area and porosity. Zinc metal nanoparticles helped in increasing the reaction rate for the conversion of intermediate radicals in ECH of furfural to FAL and MF instead of forming dimerized furfural product. (Figure 1.13d)

Chapter 2

Interesterification of triglycerides with methyl acetate for the co-production biodiesel and triacetin using hydrotalcite as a heterogenous base catalyst[1]

2.1 Introduction

As discussed in Chapter 1, formation of glycerol esters such as triacetin is a means to valorize glycerol formed in addition to biodiesel in the conventional transesterification process [62,67,77,78,246–248]. Triacetin finds application as a plasticizer and gelatinizing agent in polymers, explosives, as an additive in cosmetics and pharmaceutical industries [42,249]. It has also been recognized that triacetin can be successfully used as valuable fuel additive to biodiesel up-to 10 wt. %. The final fuel mixture thus obtained possesses improved cold, combustion and viscosity properties, and also meets the ASTM D6451 and EN 14214 quality standards [250]. These aforementioned fuel additives are generally produced by esterification and transesterification of glycerol with acetic acid and methyl acetate, respectively [93–95]. However, these procedures require the isolation and purification of glycerol after biodiesel synthesis. As a result, these two consecutive processes are being carried out independently in two separate reactors.

There exists a possibility of combining the two reactions in a single one-pot reaction by conducting interesterification reaction of triglycerides with methyl acetate, where triacetin is formed as a valuable co-product with fatty acid methyl ester (FAME) instead of glycerol. Interesterification is highly reversible and leads to the presence of value-added intermediate compounds, monoacetin-diglycerides and diacetinmonoglycerides, in high quantities in the

[1]This work is published as M.S. Dhawan, S.C. Barton, G.D. Yadav, Interesterification of triglycerides with methyl acetate for the co-production biodiesel and triacetin using hydrotalcite as a heterogenous base catalyst, Catal. Today. (2020). doi:10.1016/j.cattod.2020.07.056.

reaction mixture [251]. Their separation using vacuum distillation has been investigated in the literature [252,253]. Since all the intermediates, and co-products (biodiesel and triacetin) are value-added chemicals, the atom economy of this process is 100 %. The co-production process leads to less waste generation as glycerol is not formed and further purification procedures for its valorization are not required. The only waste generated will be of unreacted triglycerides, methyl acetate, and waste solvents generated during the desired product purification. Overall, this co-production process will lead to waste prevention and thus, low E-factor. Also, with the use of triglycerides, heterogeneous catalyst and co-production process of two products, it satisfies the green chemistry principles of using renewable feedstock, catalysis and design for energy efficiency.

This reaction has been mostly studied using chemical homogenous catalysts, enzymes or under supercritical conditions. Lipases have been extensively studied to successfully catalyze the interesterification of triglycerides giving nearly quantitative yield of FAME with minimum loss in activity upon reuse. However, the quantitative production of triacetin was not explored in detail. Enzyme catalyzed reactions offer the advantages of conducting reactions at mild conditions and catalyst reusability but fail to achieve higher yields in short reaction times [42,254–257]. There are reports on the co-production of biodiesel and triacetin under supercritical conditions, but high reaction temperatures and pressures are required to achieve high yields, which reduces the scalability of the process [98,258–260]. Casas et al. explored the chemical interesterification of triglycerides with methyl acetate using potassium methoxide as a homogeneous catalyst. This reaction can absolutely be achieved with milder reaction conditions and lower operating cost, but it suffered lower yields due to insolubility of the catalyst in the reaction system and high reversibility of the reaction. In a further study to solve the solubility issues, they studied the same

reaction using methanolic potassium methoxide as a catalyst, which increased the reaction rate due to homogeneity of the process [31]. However, enhanced side reactions were observed due to the presence of methanol, leading to the production of monoacetin, diacetin and glycerol as side products [97]. There has been a study on the interesterification reaction of triglycerides using tert-butoxide in tert-butanol as a catalyst which reduced the side reactions, thereby achieving 73.2 wt. % and 16.6 wt. % content of biodiesel and triacetin, respectively [96].

We aimed to use a heterogeneous base catalyst for the interesterification reaction which can achieve good conversion of triglycerides and high selectivity of intermediates and products. In our previous work, we carried out simultaneous co-production of biodiesel and glycerol carbonate using calcined hydrotalcite as a catalyst and achieved good conversions [29]. Thus, in the present work, we intended to use the calcined hydrotalcite as a heterogeneous base catalyst to achieve the interesterification of triglycerides with methyl acetate to co-produce biodiesel and triacetin. The effect of different Mg to Al mole ratios in the calcined Mg-Al hydrotalcite catalyst was studied. These calcined Mg-Al hydrotalcites were screened with their respective metal oxides (MgO, Al_2O_3) to assess their individual effect on the reaction. The activity of calcined Mg-Al hydrotalcite supported on hexagonal mesoporous silica (CHT-HMS) was also screened for this reaction. Additionally, it was thought to study the effect of Ca-Al hydrotalcite on the interesterification reaction as it has served good activity for the transesterification of vegetable oil in the literature [261–263]. The reaction kinetics was derived on the basis of the mean concentration profile of the reactant, product and intermediate species. The virgin and the reused catalysts were fully characterized.

2.2 Materials and Methods

2.2.1 Chemicals

Refined soybean oil was obtained from a local market. The average molecular weight of soybean oil was 874 g/mol and it was of the same fatty acid composition as reported in our previous study [29]. The following chemicals were obtained from recognized vendors and used as received: methyl acetate, sodium hydroxide, sodium carbonate (all from S.D. Fine Chemicals Ltd, Mumbai), magnesium nitrate hexahydrate, aluminum nitrate nonahydrate, calcium nitrate tetrahydrate, triacetin, methanol High Performance Liquid Chromatography (HPLC) grade, isopropyl alcohol HPLC grade, n-hexane HPLC grade (all from Thomas Baker, Mumbai), methyl palmitate (97%), methyl oleate (96%), methyl stearate (99%), methyl linoleate (all from Alfa Aesar, Mumbai), hexadecyl amine (Otto Chemie Pvt. Ltd., Mumbai), tetraethyl orthosilicate (Sigma–Aldrich, USA).

2.2.2 Catalyst synthesis

2.2.2.1 Preparation of calcined Mg-Al Hydrotalcite (Mg-Al CHT)

Hydrotalcite of varying Mg-Al ratios (1:1, 2:1, 3:1) was synthesized by a co-precipitation method. A solution containing 3 - x moles of magnesium nitrate hexahydrate and x moles of aluminum nitrate nonahydrate for a ratio x/3 = 0.25, 0.33, 0.5 was dissolved in 150 mL distilled water. Solution of 6 + x moles of sodium hydroxide and 2 mol of anhydrous sodium carbonate was prepared in 150 mL distilled water. Both the solutions were co-added under mechanical stirring (speed of agitation = 600 rpm) to the round bottom flask (500 mL) maintained at a temperature of 30˚C. The pH of the solution was between 9 and 10. The white precipitate of hydrotalcite obtained was digested at 60˚C for 12 h. Hydrotalcite was washed with distilled water until neutral pH and

then dried at 100˚C for 24 h. Dried hydrotalcite was crushed to fine powder and calcined at 500 ˚C for 6 h to obtain calcined Mg-Al hydrotalcite (Mg-Al CHT) [153,264,265].

2.2.2.2 Preparation of calcined Ca-Al Hydrotalcite (Ca-Al HT)

Ca-Al HT of mole ratio 3:1 was prepared by co-precipitation. A solution of calcium nitrate tetrahydrate (0.09 mol) and aluminum nitrate nonahydrate (0.03 mol) was prepared in 150 mL distilled water. This solution was co-precipitated by co-adding it with a solution of sodium hydroxide (0.18 mol) and anhydrous sodium carbonate (0.06 mol) prepared in 150 mL distilled water. The rest of the procedure was followed in a similar manner as described above for Mg-Al hydrotalcite. The Ca-Al HT catalyst was calcined at 500 ˚C for 6 h.

2.2.2.3 Preparation of 10 % w/w Mg-Al CHT supported on hexagonal mesoporous silica (CHT-HMS)

HMS was prepared by a protocol reported in literature [153,265,266]. CHT-HMS of Mg-Al mole ratio 3:1 was synthesized by co-precipitation. A solution containing magnesium nitrate hexahydrate (0.009 mol) and aluminum nitrate nonahydrate (0.003 mol), and a solution of sodium hydroxide (0.027 mol) and anhydrous sodium carbonate (0.008 mol) were each prepared separately in 50 mL distilled water. To 5 g of HMS, the above solutions were added simultaneously under mechanical stirring (600 rpm) in an oil bath maintained at 30˚C. The rest of the procedure was followed in a similar manner as described above for Mg-Al hydrotalcite. The fine powder was calcined at 500 ˚C for 6 h to obtain 10 % w/w CHT-HMS.

2.2.2.4 Preparation of MgO and Al_2O_3

MgO and Al_2O_3 were synthesized by co-precipitation procedure. A 150 ml solution of magnesium nitrate hexahydrate (0.5 M) was co-added with a 150 ml solution of sodium hydroxide (0.5 M) in a round bottom flask under mechanical stirring to obtain white precipitates of $Mg(OH)_2$.

Similarly, a solution of aluminum nitrate nonahydrate (0.5 M) was co-added to the same concentration of sodium hydroxide solution to obtain $Al(OH)_3$. The neutralization, washing, filtration and drying procedures were carried out in the same way as described above (Section 2.2.1). The calcination was performed at 500 ˚C for 6 h to get MgO and Al_2O_3 catalyst.

2.2.3 Catalyst characterization techniques

The fresh and reused catalyst was characterized by various techniques such as TPD, XRD, FT-IR, SEM, N_2 adsorption-desorption for BET surface area and DSC-TGA. The characterization protocol is given here.

TPD analysis was conducted using a Micromeritics AutoChem II 2920 chemisorption analyzer in which NH_3 and CO_2 was used as probe molecule for finding acidity and basicity of samples, respectively from temperature 50-500°C at ramp rate of 10 ºC per min. The catalyst was taken in a quartz tube and was pre-treated with helium at 350 ºC for 30 min. The temperature is then brought down to 50 ºC under the constant flow of helium. Then 10 % NH_3/CO_2 in helium as preparation gas was passed through the tube for 60 min. Then, the sample was flushed with helium for 30 min to remove any physisorbed ammonia molecules on the catalyst surface. The temperature was then increased gradually to 500 ºC and the amount of desorbed ammonia molecules were detected by a TCD detector and quantified by calibration.

XRD analysis was done on a Bruker AXS diffractometer using Cu Kα radiation (1.5406 A°) at 40kV and 100Ma. Measurements were taken in steps of 0.010º in 17.7s step time from 2θ = 5–80º.

FTIR patterns were recorded on Bruker vortex 80V spectrophotometer and analysis was carried out from 4000-400 cm^{-1} using KBr Pellets. A blank KBr pellet was taken as reference

against each sample. KBr and samples were mixed in 100:1 ratios (approximately) and pressed to make pellets.

Surface area and pore size distribution measurements were measured by N_2 adsorption-desorption process at −196˚C on ASAP 2010 instrument, Micromeritics, USA. The measurements were made after subjecting the sample to degassing under high vacuum at 200 ˚C for 4 h.

The surface morphology and elemental analysis of the catalyst was done using SEM and EDAX (JEOL-JSM 6380 LA, Japan). The dried samples were mounted on specimen studs and sputter coated with thin film of platinum to prevent charring.

DSC-TGA analysis was conducted using a Shimadzu DTG-60H differential thermal gravimetric analyser in which measurements were carried out from 30-500°C with ramp rate of 10°C per min in nitrogen atmosphere.

2.2.4 Reaction Procedure

The interesterification reactions were performed in a 100 cm^3 high pressure autoclave (Amar Equipments Pvt. Ltd., Mumbai) equipped with pitched bladed turbine impellor, temperature controller and pressure indicator. Soybean oil triglycerides acted as a limiting reagent. Methyl acetate was utilized as reactant as well as solvent. The control reaction was conducted using 0.008 mol soybean oil, 0.4 mol methyl acetate (1:50 molar ratio) (total volume = 40 cm^3) and catalyst loading 0.04 g/cm^3 (1.6 g) at an agitation speed of 1000 rpm at 200 °C. The samples were collected periodically using sampling valve till 4 h and the catalyst particles present in the sample were removed by filtration.

2.2.5 Reaction Analysis

The conversion of soybean oil triglycerides and selectivity of intermediates as well as triacetin was analyzed by HPLC (Agilent 1200 Infinity series) using Agilent C18 reverse phase column

(250 mm x 4.6 mm, 5 µm) with gradient elution of methanol and isopropyl alcohol-hexane (5:4, v/v), as reported in our previous study [29] and also in literature [267]. The compounds were analyzed using a UV detector at a wavelength 205 nm with a column temperature of 40 ºC, injection volume of 10 µL, phase flow rate of 1.0 ml min^{-1}. The details of the analytical methodology (Table A2.1) and chromatogram of reaction mixture (Figure A2.1) are given in the Appendix. Product confirmation was done by GC-MS (Thermo Scientific Trace 1300 Gas Chromatograph equipped with an ISQL LT single quadrupole Mass Spectrometer) using TG-5MS capillary column (150 mm x 0.25 mm, 0.25 µm) (Figure A2.2-A2.7).

The conversion calculations were done using soybean oil triglycerides (T) as the limiting reactant (2.1). The total area under the peaks of soybean oil triglyceride, monoacetindiglycerides (MA), diacetinmonoglycerides (DA) were used to calculate conversion and selectivity. The selectivity of triacetin was calculated by taking into account MA, DA and triacetin (TA) (1.2).

$$Conversion = \frac{{C_T}^0 - {C_T}^t}{{C_T}^0} \quad (2.1)$$

$$Selectivity\ (Triacetin)\ = \frac{{C_{TA}}^t}{{C_{MA}}^t + {C_{DA}}^t + {C_{TA}}^t} \quad (2.2)$$

where, ${C_T}^0$ is the initial concentration of triglyceride and ${C_T}^t$, ${C_{MA}}^t$, ${C_{DA}}^t$, ${C_{TA}}^t$ are the concentrations of the triglyceride, MA, DA and TA at any time, 't'.

2.3 Results and discussions

2.3.1 Catalyst characterization

2.3.1.1 TPD

The different Mg:Al mole ratio in the Mg-Al CHT was suspected to have the most effect on the basicity and acidity profiles of the catalyst. Hence, TPD analysis was done for all the catalysts to determine acidity and basicity using NH_3 and CO_2 as probe molecules, respectively. TPD

analysis of all the catalysts confirmed the presence of both weak basic and acidic sites (Figure 2.1 and 2.2). The basicity and acidity of Ca-Al HT and CHT-HMS, despite containing Ca and Mg to Al in the ratio 3:1 respectively, was found to be similar to Mg-Al CHT (1:1). This means that the basic and acidic sites of Mg-Al CHT in CHT-HMS were masked by neutral HMS. Also, Ca-Al HT (3:1) imparts lower basicity to hydrotalcite as compared to Mg-Al CHT (3:1). The values of the concentration of these sites are given in Table 2.1.

Table 2.1 TPD analysis of the catalysts

Catalysts	**CO_2 TPD analysis**	**NH_3 TPD analysis**
	Basicity (mmol/g)	**Acidity (mmol/g)**
Ca-Al HT	0.62	0.24
CHT-HMS	0.69	0.55
Mg-Al CHT (1:1)	0.64	0.58
Mg-Al CHT (2:1)	0.77	0.57
Mg-Al CHT (3:1)	0.9	0.82
Reused Mg-Al CHT (3:1)	0.89	0.75

It was found that with the increase in Mg-Al mole ratio, the basicity of the Mg-Al CHT catalyst increased. Mg-Al CHT (3:1) possessed the highest basicity. The spent catalyst showed a negligible loss in the basic and acidic sites after reuse confirming the stability of the catalyst.

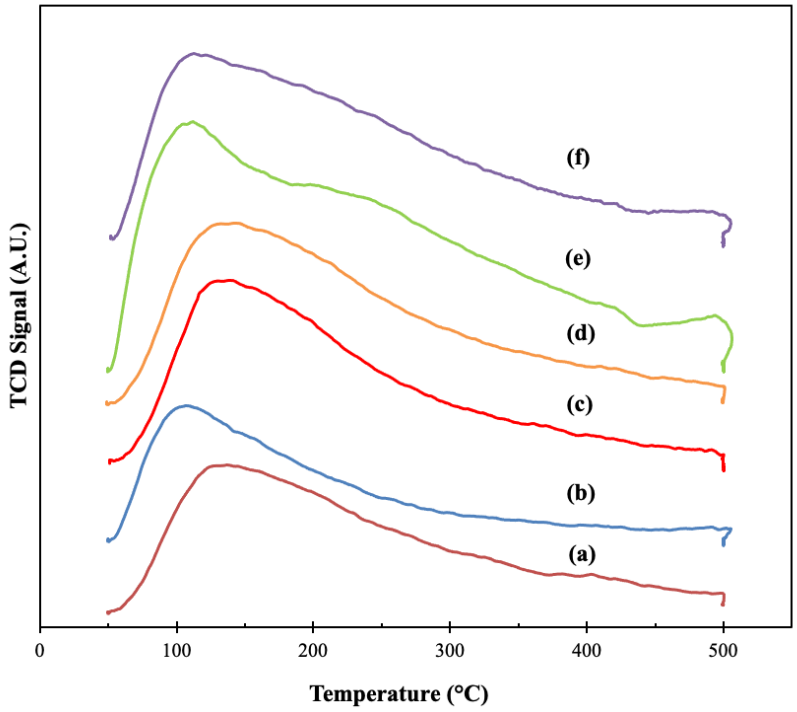

Figure 2.1 CO_2-TPD patterns of catalysts (a) Ca-Al HT (b) CHT-HMS (c) Mg-Al CHT (1:1) (d) Mg-Al CHT (2:1) (e) Mg-Al CHT (3:1) (f) Reused Mg-Al CHT (3:1)

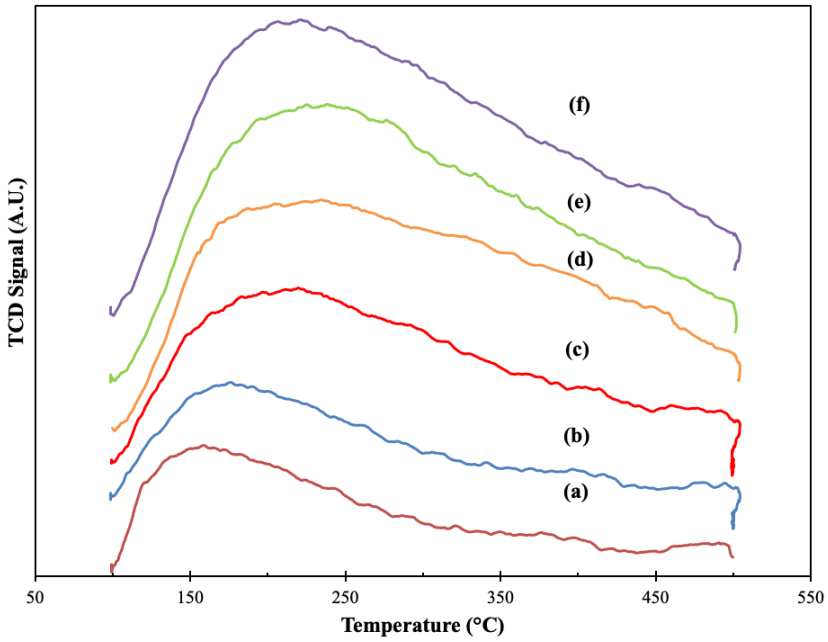

Figure 2.2 NH_3-TPD patterns of catalysts (a) Ca-Al HT (b) CHT-HMS (c) Mg-Al CHT (1:1) (d) Mg-Al CHT (2:1) (e) Mg-Al CHT (3:1) (f) Reused Mg-Al CHT (3:1)

2.3.1.2 XRD

The XRD patterns of all the catalysts are shown in Figure 2.3. XRD pattern of Ca-Al HT showed a very small peak at low Θ value (23.2°) which correspond to the conversion of the layered structure of Ca-Al layered double hydroxide to Ca-Al mixed oxide, and formation of amorphous phase (JCPDS 890460). The sharp, symmetric peak at 29.6° and broad peaks at high Θ values (35-65°) indicate the formation of a crystalline calcite phase ($CaCO_3$), which might have resulted from the non-uniform distribution of Ca and Al cations, resulting in Ca^{2+} ions agglomeration (JCPDS 72-1652). This is in accordance with the XRD results obtained by Cortez et al. [261]. 10 % w/w CHT-HMS showed a strong reflection at 21.2°, corresponding to that of amorphous SiO_2 obtained after calcination of HMS. The Mg-Al particles on the surface/pores of HMS might be too small, and thus no peak of the oxides was obtained in the XRD pattern of CHT-HMS. The XRD pattern

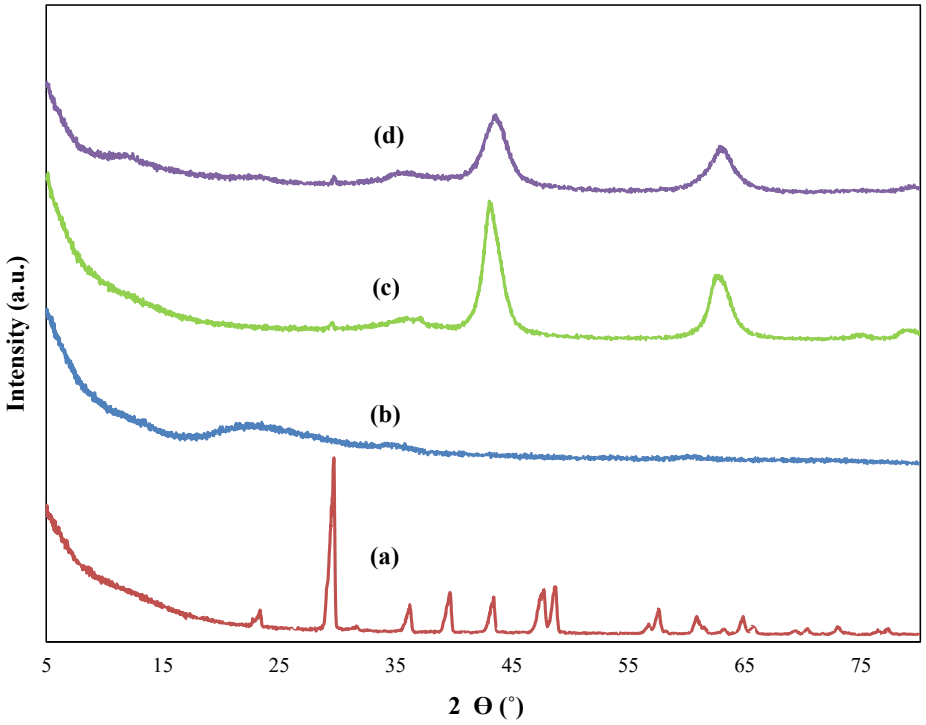

Figure 2.3 XRD of catalysts (a) Ca-Al HT (b) CHT-HMS (c) Mg-Al CHT (3:1) (d) Reused Mg-Al CHT (3:1)

of Mg-Al CHT (3:1) depicted characteristic peaks of the Mg-Al oxide at 43° and 62.4° corresponding to (200) and (220) planes (JCPDS 45-0946). This shows that after calcination, the layered double hydroxides were transformed to Mg-Al mixed oxides and the intensity of peaks signify amorphous material. The crystallite size of Mg-Al CHT (3:1) was calculated as 11.3 nm using the Scherrer equation. It increased to 16.6 nm after reuse. Reused Mg-Al CHT (3:1) showed similar reflections as Mg-Al CHT (3:1) indicating the fidelity of the catalyst.

2.3.1.3 FT-IR

FTIR patterns of all the catalysts are depicted in Figure 2.4. The FTIR spectra of Ca-Al HT showed the presence of carbonate ions at around 1420 cm^{-1} and metal oxides vibrations at 874 cm^{-1} and 711 cm^{-1}. The FTIR spectra of CHT-HMS showed broad band at 1069 cm^{-1} corresponding to Si-O-Si asymmetric stretching vibration, Si-O-Si symmetric vibration at 794 cm^{-1}, O-Si-O

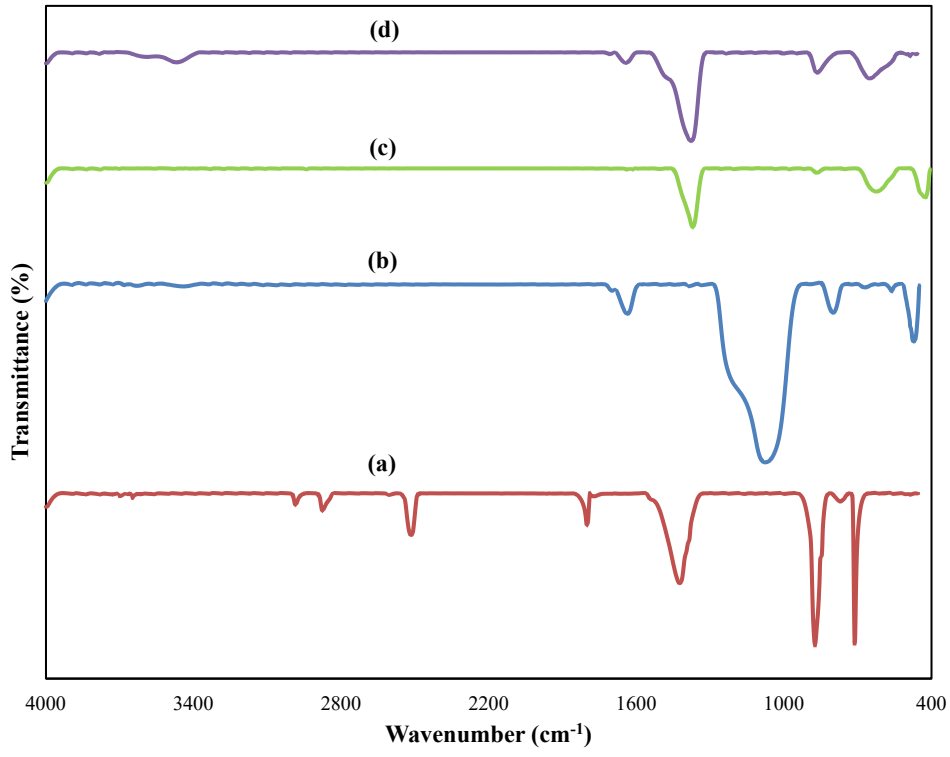

Figure 2.4 FT-IR spectra of catalysts (a) Ca-Al HT (b) CHT-HMS (c) Mg-Al CHT (3:1) (d) Reused Mg-Al CHT (3:1)

bending vibrations at 470 cm^{-1}, and a slight presence of water showing –OH stretching and bending vibration at 3438 cm^{-1} and 1639 cm^{-1}. FTIR analysis of Mg-Al CHT (3:1) showed the presence of Mg-O bands at 426 cm^{-1} and Al-O at 621 cm^{-1}. The bands of carbonates at 1250-1500 cm^{-1} were of decreased intensity as a result of their loss during calcination [192]. Reused Mg-Al CHT (3:1) showed a similar FTIR pattern as that of virgin Mg-Al CHT (3:1) along with a slight presence of H_2O molecules, depicted by their stretching vibration at 3457 cm^{-1} and bending vibration at 1633 cm^{-1}. This shows that the reused catalyst retains its structure even after reuse, which signifies the stability of the catalyst.

2.3.1.4 Surface area analysis

The BET surface area, pore volume and pore size of all the catalysts measured by nitrogen adsorption-desorption method are given in Table 2.2. Ca-Al HT showed a type III isotherm,

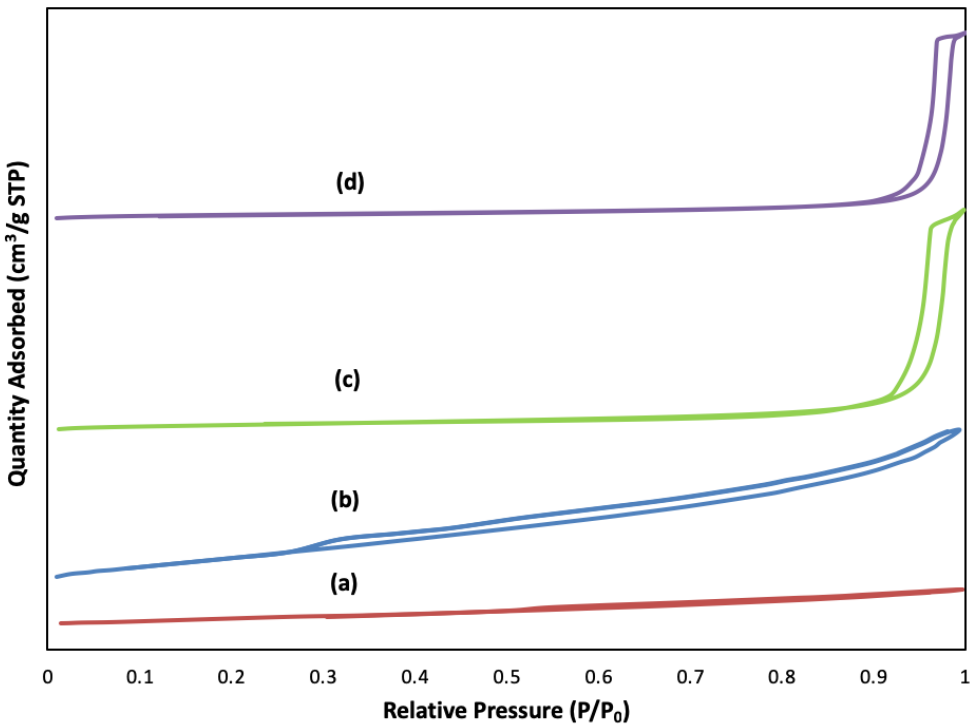

Figure 2.5 N_2 adsorption-desorption isotherms of catalysts (a) Ca-Al HT (b) CHT-HMS (c) Mg-Al CHT (3:1) (d) Reused Mg-Al CHT (3:1)

characteristic of a nonporous or macroporous solid and a little H4 type of hysteresis which indicated narrow slit-like pores and particles with internal void. CHT-HMS, virgin and reused Mg-Al CHT (3:1) showed a type IV isotherm signifying a mesoporous solid but with different types of hysteresis (Figure 2.5). CHT-HMS exhibited H3 type of hysteresis indicating slit-shaped pores and plate-like particles. The low total specific surface area of CHT-HMS after loading of Mg-Al CHT on high specific surface area HMS could be due to the blockage of the pores in HMS, which reduces the accessibility of N_2 into the pore structure. Similar findings have been reported after loading Mg-Al CHT on HMS [88,266].

Table 2.2 Surface area, pore volume and pore diameter analysis

	Ca-Al HT	**CHT-HMS**	**Mg-Al CHT (3:1)**	**Reused Mg-Al CHT (3:1)**
BET Surface Area ($m^2 g^{-1}$)	78.9	74.7	101.1	69.6
BJH Pore Volume ($cm^3 g^{-1}$)	0.7	0.7	0.9	0.4
BJH Average Pore Size (Å)	364.3	384.4	358.4	248.8

Mg-Al CHT (3:1) showed the highest surface area with a H1 type hysteresis loop, corresponding to well defined cylindrical pores open at both ends with good connectivity (according to IUPAC classification). Reused Mg-Al CHT (3:1) was found to be stable as it showed similar textural features with small losses after third re-use.

2.3.1.5 SEM

SEM images of the catalysts are depicted in Figure 2.6. The virgin as well as the reused catalyst show agglomerated particles with irregular morphology.

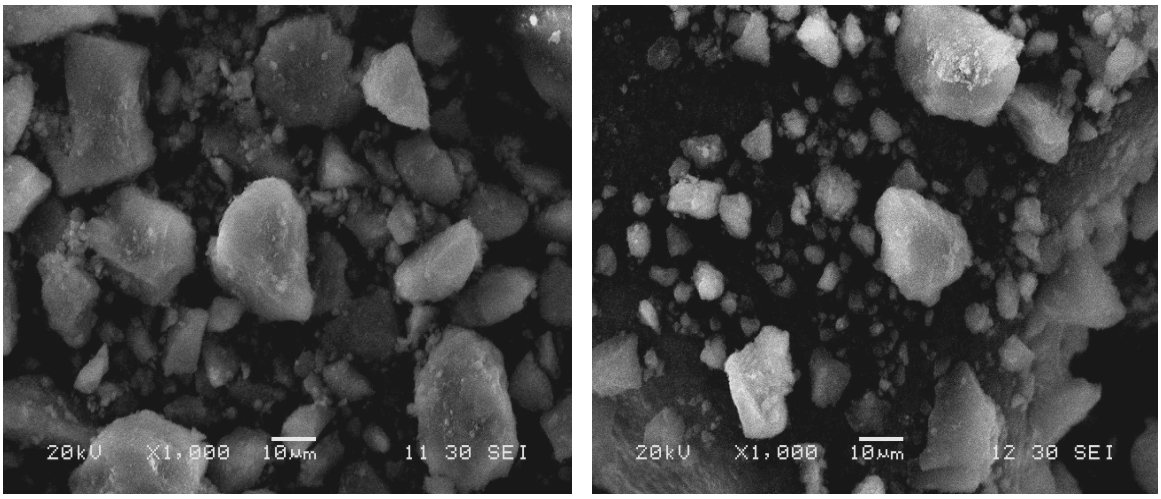

(a) **(b)**

Figure 2.6 SEM images of (a) Mg-Al CHT (3:1) (b) Reused Mg-Al CHT (3:1)

2.3.1.6 EDAX

The composition of the elements of virgin and reused Mg-Al CHT (3:1) catalyst was determined by EDAX and it showed the presence of Mg and Al in the same mole ratio as that taken theoretically for the preparation of the catalyst (Table 2.3).

Table 2.3 Elemental analysis of the catalysts

Element (mole %)	Mg-Al CHT (3:1)	Reused Mg-Al CHT (3:1)
Mg	74.9	74.1
Al	24.9	25.4
Mg:Al mole ratio	3:1	2.9:1

2.3.1.7 DSC-TGA

Thermal stability of the samples was determined by DSC-TGA analysis of the catalysts as given in Figure 2.7 and 2.8. DSC curve of both the catalysts showed an endothermic peak at around 90 °C, which is due to the loss of surface adsorbed water and decomposition of carbonates, thereby contributing to the weight loss. The TGA analysis of Mg-Al CHT (3:1) showed a total weight loss of 4.1 %, which meant that the catalyst was stable at higher temperature. Reused catalyst also showed nearly similar weight loss (7.5 %) as that of fresh catalyst.

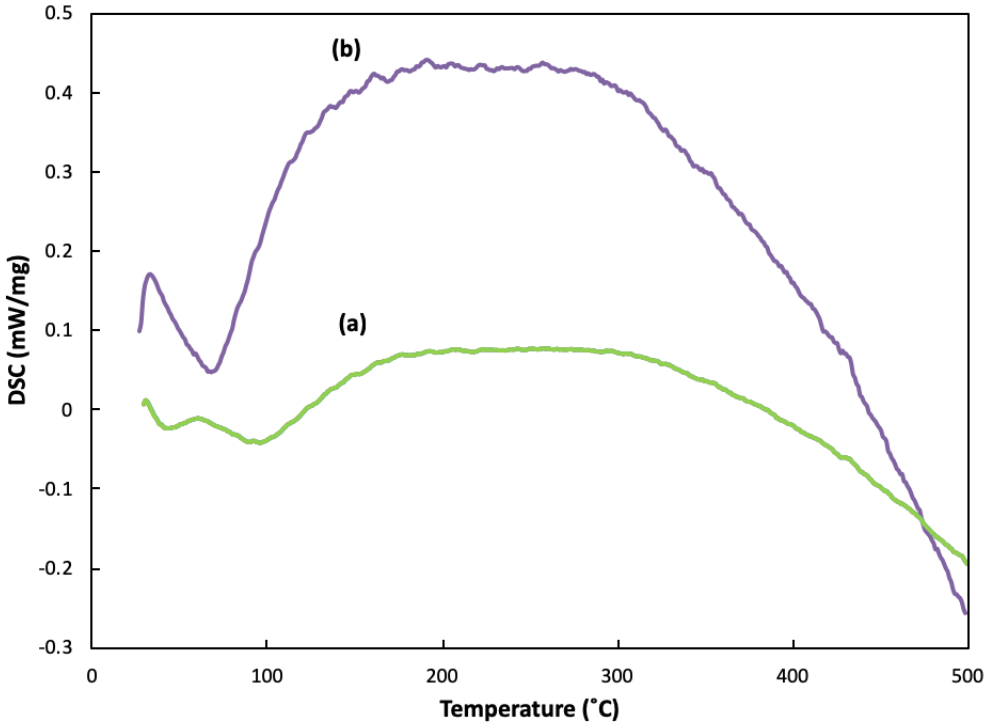

Figure 2.7 DSC analysis of catalysts (a) Mg-Al CHT (3:1) (b) Reused Mg-Al CHT (3:1)

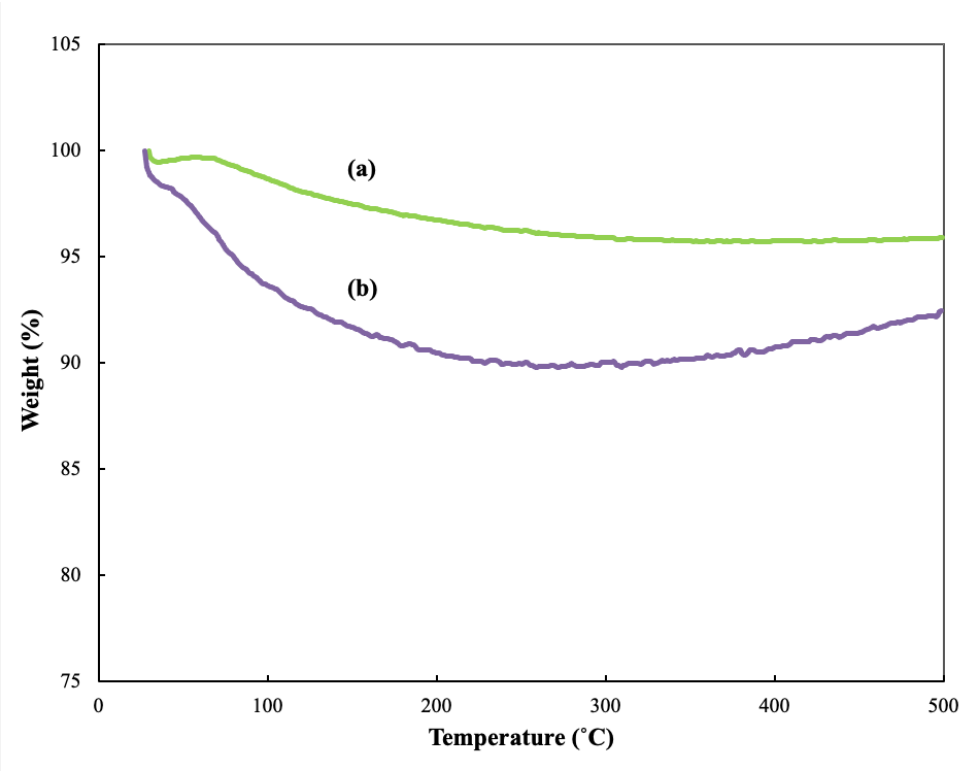

Figure 2.8 TGA analysis of catalysts (a) Mg-Al CHT (3:1) (b) Reused Mg-Al CHT (3:1)

2.3.2 Interesterification of soybean oil triglycerides with methyl acetate

Scheme 2.1 depicts the transesterification reaction of soybean oil triglycerides (T) with methyl acetate, which consists of three steps. Fatty acid methyl esters (F) are formed in each consecutive step of the reaction. Intermediates – monoacetindiglycerides (MA) and diacetinmonoglycerides (DA) are formed in step 1 and step 2, respectively, followed by formation of triacetin (TA) in step 3. The rate constants of each reversible step are mentioned on the arrow where k_1 is the rate constant of first step for conversion of T to MA and k_1' is the rate constant of the reverse reaction, and so on. The effect of various reaction parameters on the conversion of triglycerides and selectivity of triacetin were studied and plotted as a function of time.

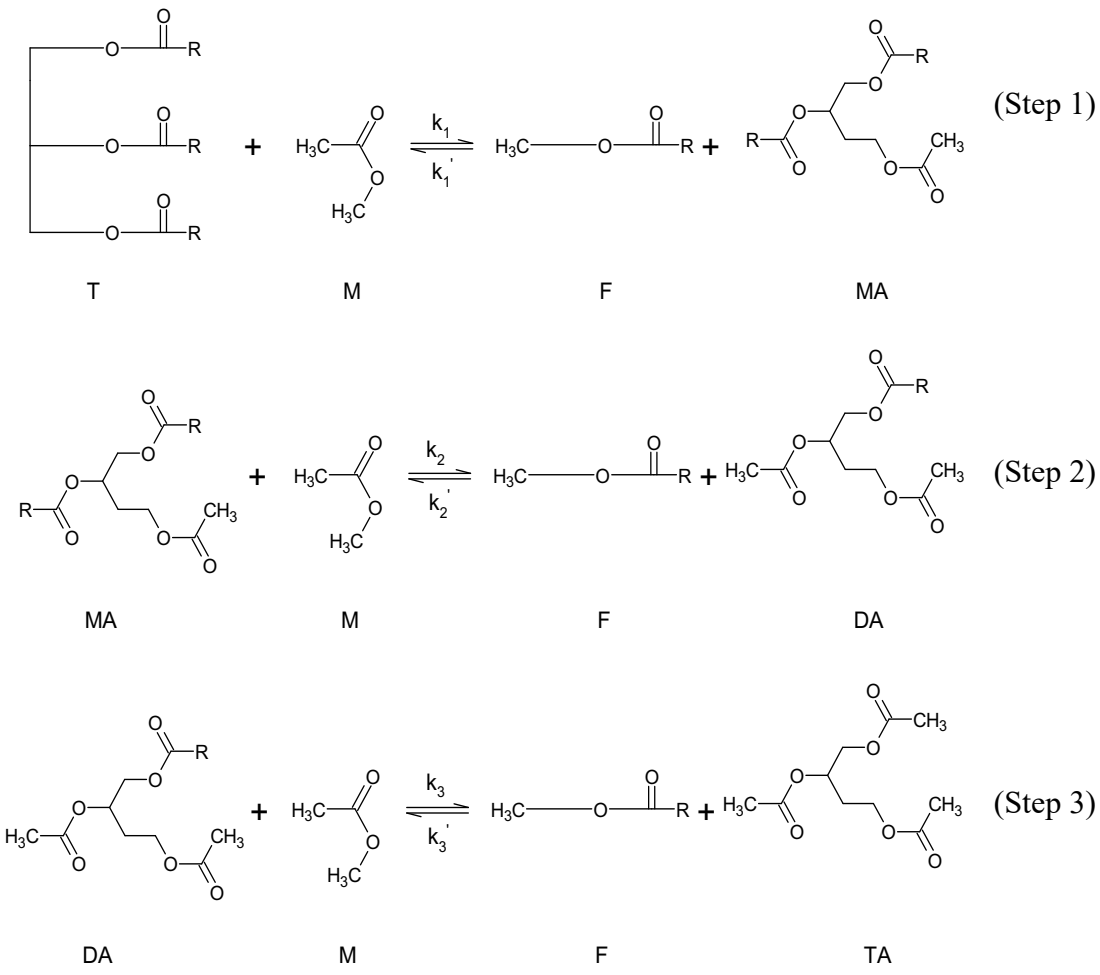

Scheme 2.1 Consecutive reactions in interesterification of soybean oil triglycerides with methyl acetate

2.3.2.1 Efficacy of various catalysts

The interesterification reaction was studied using various base catalysts such as MgO, Alumina, Ca:Al HT (3:1), CHT-HMS (Mg:Al=3:1), Mg-Al CHT (3:1), Mg-l CHT (2:1) and Mg-Al CHT (1:1). The reactions were performed for 4 h with the conditions maintained at oil to methyl acetate mole ratio of 1:50 (total volume = 40 cm^3) at 200 ^oC with agitation speed of 1000 rpm and catalyst loading of 0.04 g/cm^3. All the aforementioned catalysts had remarkable activity towards the conversion of soybean oil triglycerides but with varied selectivities towards triacetin (Figure 2.9). MgO showed good activity towards the conversion of triglycerides (85.4 %), but the selectivity of triacetin was comparatively low (2.4 %). However, the activity of alumina towards

the interesterification reaction was tremendously low with a conversion of 70.5 % and selectivity of triacetin as 1 %. This shows that both acidic and basic sites play a role in the reaction to favor the conversion of intermediates to triacetin. Thus, Mg-Al hydrotalcite was a good choice. CHT-HMS showed less activity towards the reaction (conversion: 92.7 %, selectivity of triacetin: 2.8 %) which might be due to the hinderance of basic sites by HMS, as shown by XRD analysis (Figure 3). The activity of the Mg-Al CHT catalysts with different Mg:Al mole ratios was close to each other in terms of conversion with varying selectivities towards triacetin, in the following order: Mg-Al CHT (3:1) (95.9 %, 5.3 %) > Mg-Al CHT (2:1) (92.2 %, 4.2 %) > Mg-Al CHT (1:1) (89.7 %, 3.9 %). Ca:Al HT also showed appreciable activity, with 92.5 % conversion and 4.3 % selectivity of triacetin. In all cases it was observed that, higher conversion of intermediate MA to DA, favored high selectivity to triacetin (TA). Mg-Al CHT (3:1) was found to have the highest

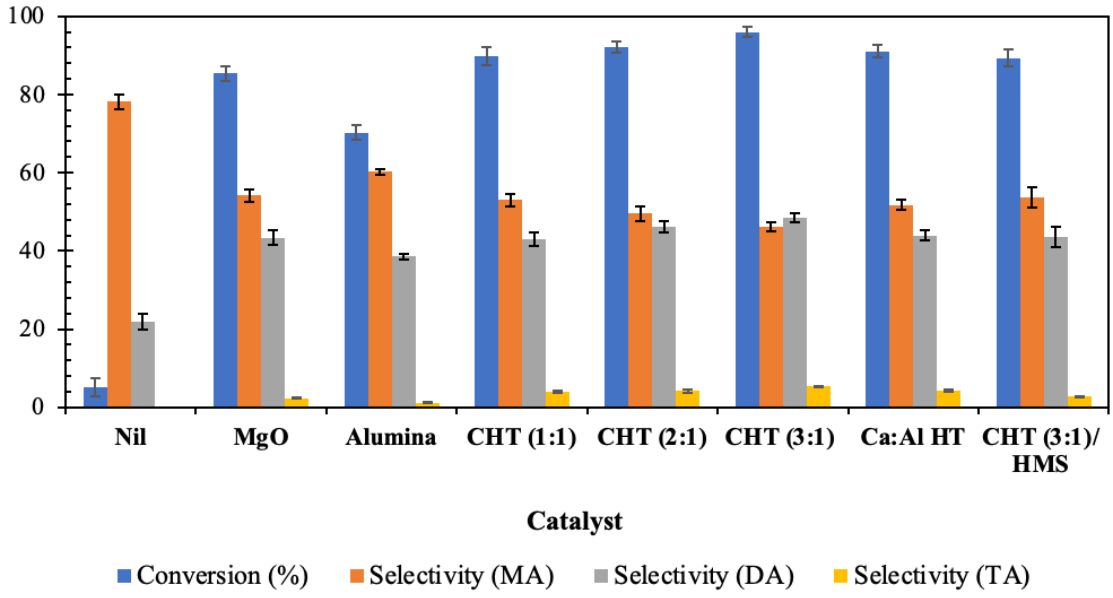

Figure 2.9 Effect of different catalysts on the conversion of soybean oil triglycerides and selectivity of intermediates and triacetin. Soybean oil: 7.0 g, soybean oil:methyl acetate mole ratio: 1:50, speed of agitation: 1000 rpm, temperature: 200 °C, catalyst loading: 0.04 g/cm^3, total volume 40 cm^3, reaction time 240 min

activity for the conversion of soybean oil triglycerides and selectivity towards triacetin. This is expected because of the high basicity of this catalyst as compared to the other catalysts, as seen in TPD analysis (Table 2.1). Hence it was used in further experimental studies and reaction optimization.

2.3.2.2 Effect of speed of agitation

The speed of agitation was varied from 600-1000 rpm with the other parameters held constant at catalyst loading of 0.04 g/cm^3, mole ratio of oil:methyl acetate at 1: 50 and temperature 200 ^{o}C (Figure 2.10). The conversion of soybean oil triglycerides and selectivity of triacetin increased from 84 % to 95.9 % and 4.1 % to 5.3 %, respectively, when the speed of agitation was increased

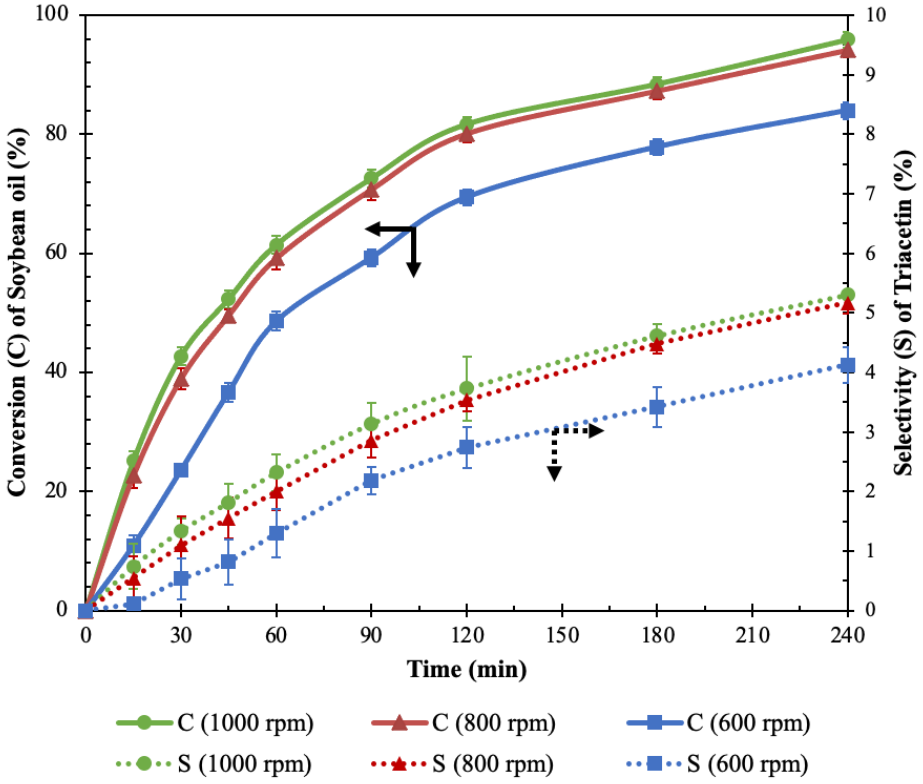

Figure 2.10 Effect of speed of agitation on conversion of soybean oil triglycerides and selectivity of triacetin. Soybean oil: 7.0 g, soybean oil:methyl acetate mole ratio: 1:50, temperature: 200 °C, catalyst loading: 0.04 g/cm^3, total volume 40 cm^3, reaction time 240 min.

from 600 to 800 rpm. There was no appreciable change in the conversion of soybean oil as well as selectivity of triacetin when the speed was increased from 800 to 1000 rpm. This signifies that at 1000 rpm, mass transfer resistance was minimal, and it was chosen as the agitation speed for further experimental studies.

2.3.2.3 Effect of catalyst loading

The effect of catalyst loading was studied in the range from 0.03 to 0.05 g/cm^3, keeping the other parameters constant. The conversion of soybean oil triglycerides was found to increase significantly from 81.2 % to 95.9 % when the catalyst loading was increased from 0.03 g/cm^3 to 0.04 g/cm^3. The selectivity of triacetin also followed the same trend with increase from 3.8 % to 5.3 % (Figure 2.11). This is due to the proportional increase in the number of catalytic sites which

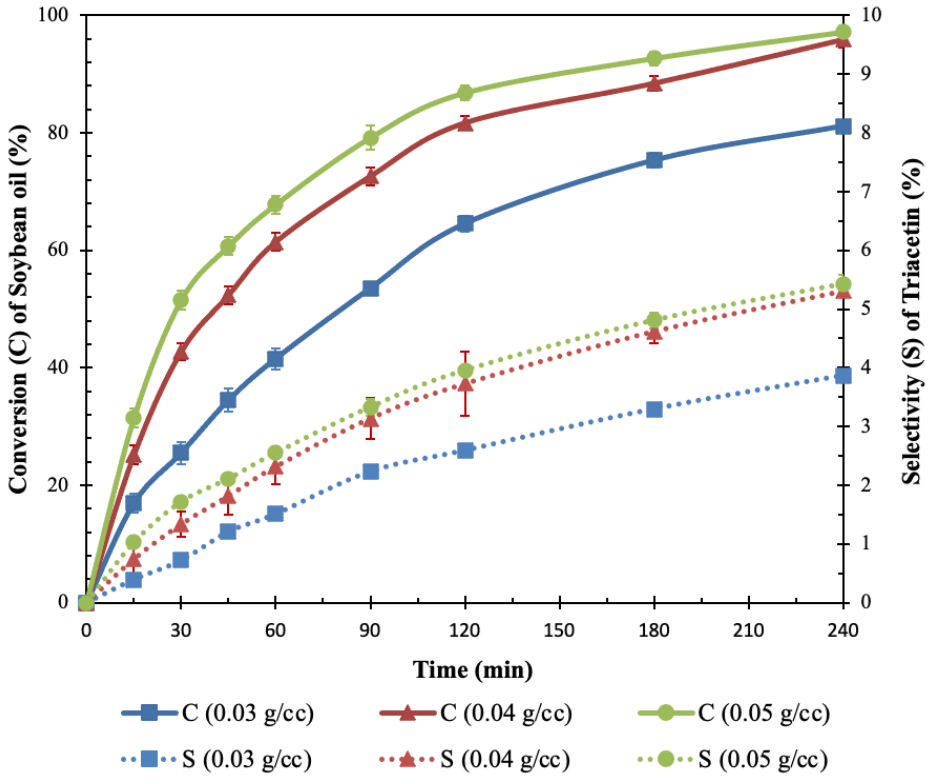

Figure 2.11 Effect of catalyst loading on conversion of soybean oil triglycerides and selectivity of triacetin. Soybean oil: 7.0 g, soybean oil:methyl acetate mole ratio: 1:50, speed of agitation: 1000 rpm, temperature: 200 °C, total volume 40 cm^3, reaction time 240 min.

can catalyze the conversion of reactants and intermediates to products with higher catalyst loading. The optimum catalyst loading was found to be 0.04 g/cm^3 as above this there was not much notable change observed in conversion and selectivity.

2.3.2.4 Effect of mole ratio of soybean oil triglycerides to methyl acetate

Soybean oil to methyl acetate mole ratio was varied from 1:30 to 1:60 with the total volume and other parameters held constant (Figure 2.12). Increasing mole ratio of soybean oil to methyl acetate not only resulted in increasing conversion of soybean oil triglycerides but also favored the reaction of intermediates with methyl acetate towards triacetin formation. The high viscosity due to the triglycerides is compensated by using excess methyl acetate. It also acted as a solvent to dissolve the intermediates and triacetin. The increase in the mole ratio from 1:30 to 1:50 lead to

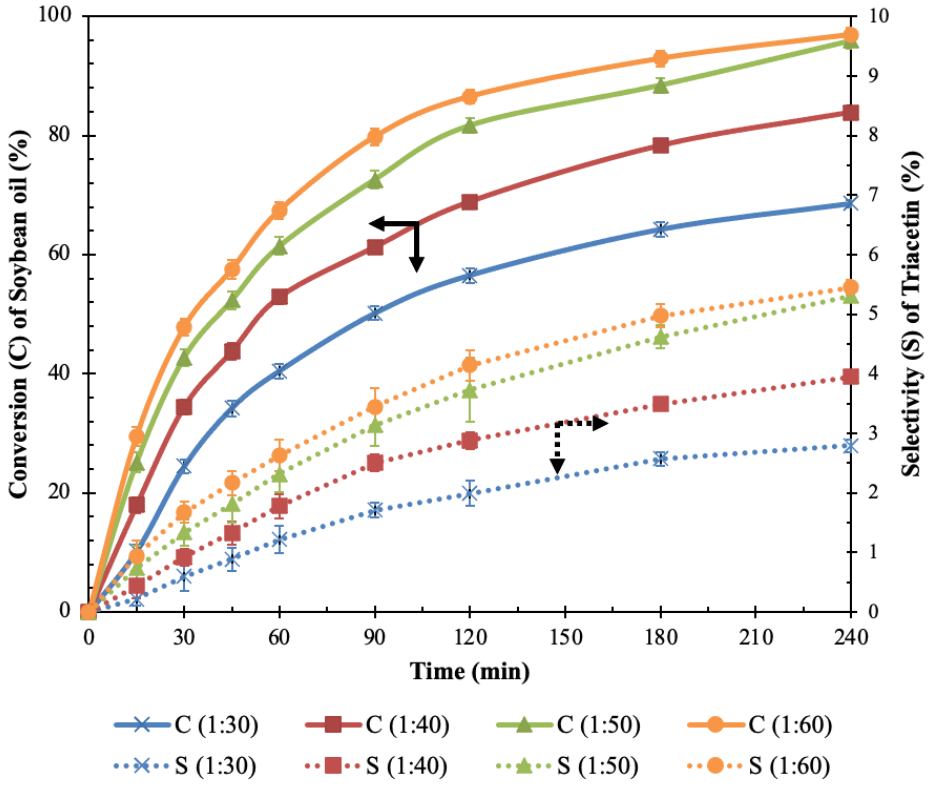

Figure 2.12 Effect of soybean oil triglycerides to methyl acetate mole ratio on conversion of soybean oil triglycerides and selectivity of triacetin. Speed of agitation: 1000 rpm, catalyst loading: 0.04 g/cm^3, temperature: 200 °C, total volume 40 cm^3, reaction time 240 min.

increase in conversion from 68.6 % to 95.9 % and selectivity of triacetin also doubled. Increase in the mole ratio from 1:50 to 1:60 did not lead to a much appreciable increase in the conversion of soybean oil or selectivity of triacetin. Hence, mole ratio of 1:50 was used for further reactions.

2.3.2.5 Effect of temperature

The effect of temperature on the interesterification reaction rate was studied in the range of 180-210 ºC with the other variables constant (Figure 2.13). An increase in reaction temperature led to a significant increase in the rate of the interesterification reaction. Higher reaction temperatures favored the conversion of triglycerides and intermediates to end product, triacetin.

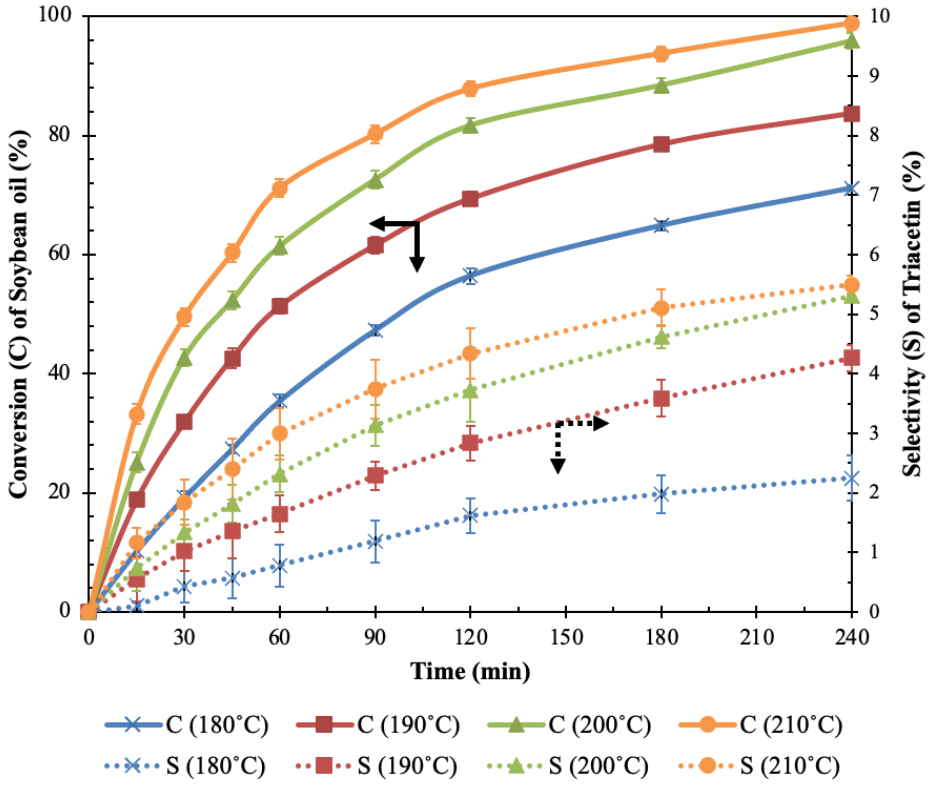

Figure 2.13 Effect of temperature on conversion of soybean oil triglycerides and selectivity of triacetin. Soybean oil: 7.0 g, soybean oil:methyl acetate mole ratio: 1:50, speed of agitation: 1000 rpm, catalyst loading: 0.04 g/cm^3, total volume 40 cm^3, reaction time 240 min.

2.3.2.6 Development of kinetic model

For a fixed catalyst loading *w*, the rates of reaction or formation can be established. The net rate of consumption of methyl acetate (M) by three parallel reactions is given by the following equation:

$$-r_M = -\frac{dC_M}{dt} = w.\{(k_1 C_M C_T + k_2 C_M C_{MA} + k_3 C_M C_{DA}) - (k_1{}' C_F C_{MA} + k_2{}' C_F C_{DA} + k_3{}' C_F C_{TA})\} \quad (2.3)$$

The rate of consumption of triglycerides (T) and the rates of formation of fatty acid methyl esters (biodiesel) (F), monoacetindiglycerides (MA) and diacetinmonoglycerides (DA), triacetin (TA) are as follows:

$$-r_T = -\frac{dC_T}{dt} = w.(k_1 C_M C_T - k_1{}' C_F C_{MA}) \quad (2.4)$$

$$r_{MA} = \frac{dC_{MA}}{dt} = w.(k_1 C_M C_T - k_1{}' C_F C_{MA} - k_2 C_M C_{MA} + k_2{}' C_F C_{DA}) \quad (2.5)$$

$$r_F = \frac{dC_F}{dt} = w.(k_1 C_M C_T - k_1{}' C_F C_{MA} + k_2 C_M C_{MA} - k_2{}' C_F C_{MA} + k_3 C_M C_{DA} - k_3{}' C_F C_{TA}) \quad (2.6)$$

$$r_{DA} = \frac{dC_{DA}}{dt} = w.(k_2 C_M C_{MA} - k_2{}' C_F C_{DA} - k_3 C_M C_{DA} + k_3{}' C_F C_{TA}) \quad (2.7)$$

$$r_{TA} = \frac{dC_{TA}}{dt} = w.(k_3 C_M C_{DA} - k_3{}' C_F C_{TA}) \quad (2.8)$$

The mean concentration profile of the reactant, intermediates and product at different temperature was used to deduce the kinetics using the integral method. The rate equations were integrated using scipy.integrate.solve_ivp in Python [268]. The concentration of T, MA, DA and TA at all studied temperatures and experimental time points were estimated by nonlinear least squares fitting of the pre-exponential factor (k_0) and activation energy (E_a), using a reference temperature (T_0) of 200 °C. The experimental and fitted concentration profile at 200 ºC is shown in Figure 2.14. The fit was found to be good, with an R^2 value of 99.96 %. The concentration profiles at other studied temperatures are provided in the Appendix (Figure A2.8). Rate constant

(k) at 200 °C (equals pre-exponential factor as T = T_0) and activation energy for each reversible interesterification step (Scheme 2.1) are given in Table 2.4. Pre-exponential factor and activation energy calculated at a reference temperature of 200 °C were used to calculate forward and reverse kinetic rate constants at each studied temperature (T) using the Arrhenius equation (2.9).

$$k = k_0 * exp\left(\frac{E_a}{R}\left(\frac{1}{T_0} - \frac{1}{T}\right)\right) \tag{2.9}$$

The Arrhenius plot was made using the values of kinetic rate constants (Figure 2.15).

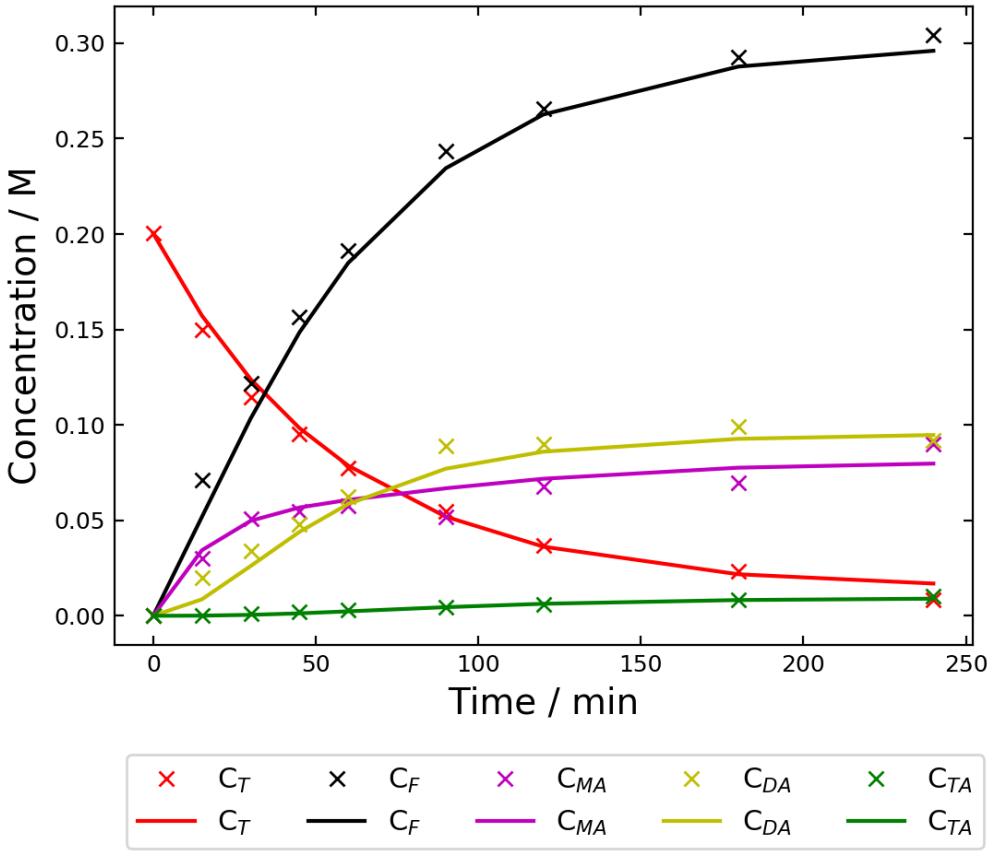

Figure 2.14 Experimental (x) and fitted (—) concentration (C) profile of soybean oil triglycerides (T), fatty acid methyl esters (F), monoacetindiglycerides (MA), diacetinmonoglycerides (DA) and triacetin (TA) as a function of time. Soybean oil: 7.0 g, soybean oil:methyl acetate mole ratio: 1:50, speed of agitation: 1000 rpm, temperature: 200 °C, catalyst loading: 0.04 g/cm^3, total volume 40 cm^3, reaction time 240 min.

Table 2.4 Rate constant at 200 °C and activation energies for the interesterification reaction

Reaction	k (L^2/mol//g/sec)	E_a (kJ/mol)
Step 1 (forward)	$6.8 \times 10^{-7} \pm 4.4 \times 10^{-11}$	61.5 ± 0.01
Step 1 (reverse)	$3.9 \times 10^{-6} \pm 2.9 \times 10^{-9}$	-92.4 ± 0.9
Step 2 (forward)	$1.3 \times 10^{-6} \pm 2.2 \times 10^{-10}$	50 ± 0.3
Step 2 (reverse)	$3.5 \times 10^{-5} \pm 8.0 \times 10^{-9}$	-12.6 ± 0.3
Step 3 (forward)	$7.1 \times 10^{-8} \pm 1.2 \times 10^{-11}$	108.1 ± 0.2
Step 3 (reverse)	$2.4 \times 10^{-5} \pm 6.3 \times 10^{-9}$	107.2 ± 0.5

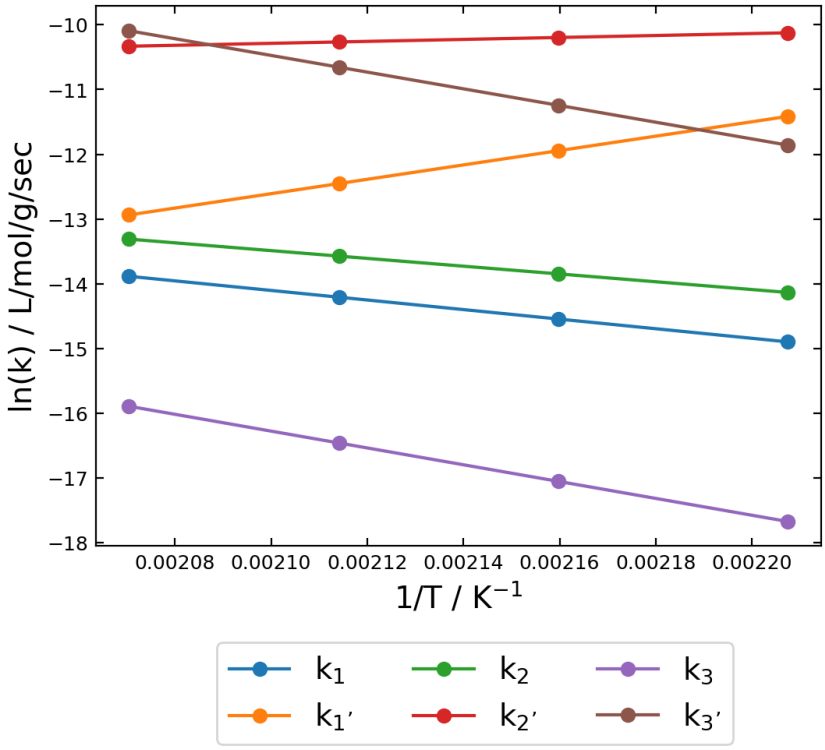

Figure 2.15 Arrhenius plot with kinetic rate constants (k) as a function of temperature (T)

The activation energy of the first two reverse reactions i.e. conversion of MA to T and conversion of DA to MA were found to be negative. The negative activation energy suggest that the first two reversible reactions are non-elementary [269], and likely consist of sub-steps wherein a pre-reactive intermediate is formed before going to final products. The overall activation energy

for the interesterification reaction can be written as the sum of individual activation energies of all steps and it was found to be positive. Thus, increasing conversion and selectivity to MA, DA and triacetin was found with increasing temperature. The rate constants of the first two reverse reactions, i.e. k_1' and k_2' were found to decrease with increase in temperature as a result of negative activation energy. This means that the reversibility of interesterification reaction increases with decreasing temperature.

2.3.2.7 Catalyst reusability

Reusability studies of the catalyst Mg-Al CHT (3:1) were conducted over three cycles (Figure 2.16). The catalyst, filtered after the completion of reaction, was washed with methanol to remove any adsorbed compounds. The catalyst was dried at 100 ºC for 12 h followed by calcination at 500 ºC for 6 h. The catalyst lost during filtration was replaced with fresh catalyst in each experiment.

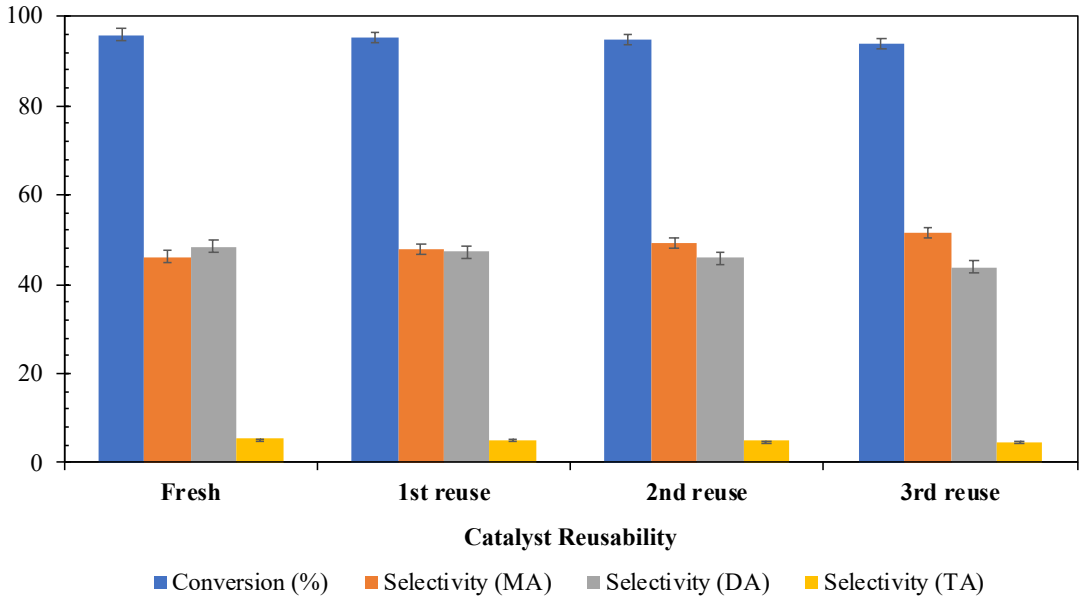

Figure 2.16 Effect of catalyst reuse on the conversion of soybean oil and selectivity of intermediates and triacetin. Soybean oil: 7.0 g, soybean oil:methyl acetate mole ratio: 1:50, speed of agitation: 1000 rpm, temperature: 200 °C, catalyst loading: 0.04 g/cm^3, total volume 40 cm^3, reaction time 240 min.

There was a marginal decrease of 1.6 % in conversion of triglycerides and 0.5 % in the selectivity

of triacetin at the end of the 3rd reuse. The reused catalyst was also characterized by various techniques as discussed earlier. The results show the stability and activity of the catalyst after three reuses.

2.4 Conclusion

The interesterification of soybean oil triglycerides with methyl acetate to co-produce biodiesel and triacetin was studied using various heterogeneous base catalysts. Mg-Al CHT (3:1) was found to be the best catalyst for the conversion of triglycerides and selectivity towards triacetin. The reaction conditions were optimized at agitation speed of 1000 rpm, a catalyst loading of 0.04 g/cm^3, oil to methyl acetate mole ratio of 1:50 and a temperature of 200 ^{o}C. Increase in temperature was found to enable the reaction towards higher triacetin formation. The kinetic model for the system was developed using concentration data and the activation energy of each step was calculated. The virgin and the reused catalyst were fully characterized to establish its structural fidelity. The catalyst was found to be stable and reusable without any significant loss in its activity.

Chapter 3

Chemo-selective etherification of 5-hydroxymethylfurfural to 5-(2-hydroxyethoxymethyl)furfural using aluminum substituted dodecatungstophosphoric acid supported on K-10 clay as catalyst [2]

3.1 Introduction

The production of AMFs by etherification of HMF with alcohols was highlighted in Chapter 1. MMF and EMF are well recognized high energy density fuel additives produced by reaction of monohydroxy alcohol with HMF [45,121,129,137]. MMF and EMF pose problems when used at higher concentration to blend with petroleum fuels or biodiesel [140]. Branched or high-molecular weight AMF have been reported to overcome these problems as they exhibit improved cold flow properties [138,270,271]. The literature is primarily limited to C1-C5 primary or branched alcohols [136,138,272,273]. It was reported that AMFs produced by reacting HMF with di- or tri-hydroxy alcohols can be used to produce better fuel additives with enhanced blending characteristics than the ethers produced from monohydroxy alcohols - methanol or ethanol [140].

5-(2-Hydroxyethoxymethyl)furfural (HEMF) is one such AMF which is obtained by etherification of HMF with ethylene glycol in the presence of an acid catalyst [139,140]. HMF possesses both alcohol and aldehyde functional groups which on reaction with ethylene glycol can give rise to ether [139,140] and/or acetals [274] depending on the catalyst and conditions used.

[2]This work is under revision as M.S. Dhawan, G.D. Yadav, S. Calabrese Barton, Chemo-selective etherification of 5-hydroxymethylfurfural to 5-(2-hydroxyethoxymethyl)furfural using aluminum substituted dodecatungsto-phosphoric acid supported on K-10 clay as catalyst, Green Chemistry (2021).

The desired reaction is depicted by Scheme 3.1, where the hydroxyl group of HMF reacts with ethylene glycol to give an ether - 5-(2-hydroxyethoxymethyl) furfural (HEMF). Water is the only co-product formed in the etherification reaction; this results in an atom economy of 90 %. If water is recycled in the process, the E-factor will be <1 %. Again, with the use of HMF as reactant and heterogeneous catalyst of the reaction, it satisfies the green chemistry principles of using renewable feedstock and catalysis. The side reaction is depicted by Scheme 3.2, where ethylene glycol instead reacts with the aldehyde group of HMF to produce undesired 5-hydroxymethylfurfural ethylene acetal (HMFA). The formation of side product HMFA will lead to a high E-factor. Ethylene glycol is used in excess to act as a reactant as well as solvent for the reaction. Unreacted HMF and ethylene glycol (if not recycled) will also contribute to high E-factor.

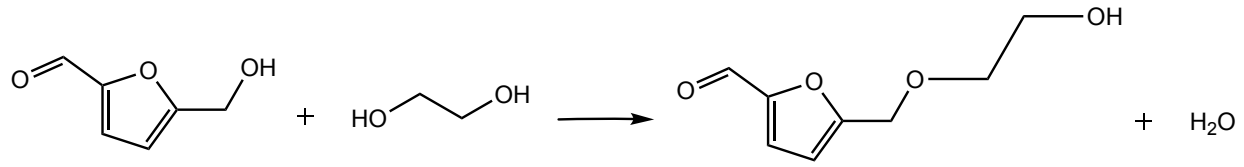

5-hydroxymethylfurfural (HMF) + Ethylene glycol → 5-((2-hydroxyethoxy)methyl)furfural (HEMF) + H_2O

Scheme 3.1 Etherification reaction of HMF with ethylene glycol to give 5-(2-hydroxyethoxymethyl) furfural

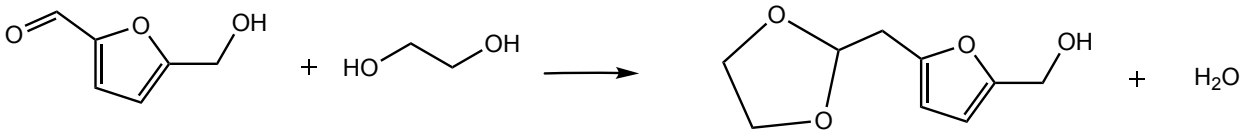

5-hydroxymethylfurfural (HMF) + Ethylene glycol → 5-hydroxymethylfurfural ehtylene acetal (HMFA) + H_2O

Scheme 3.2 Acetalization of HMF with ethylene glycol to give side product - 5-hydroxymethylfurfural ethylene acetal

HEMF was formed as a co-product with HMF as a result of direct reaction of fructose with ethylene glycol in 0.5 wt. % sulfuric acid at 85 °C [140]. Cottier et al. reported the production of HEMF using pyridine HCl as a catalyst to obtain 24 % yield at 160 °C temperature and 20 Torr pressure [139]. Pyridine HCl and sulphuric acid are homogenous acid catalysts, which are non-reusable, toxic, and environmental unfriendly [275,276]. Conversely, Hara et al. reported the formation of HMFA with 80 % spectroscopic yield by acetalization of HMF with ethylene glycol using cerium phosphate as a catalyst at reflux conditions [274]. Thus, chemo-selective acid catalysts are required to guide the reactivity of HMF with ethylene glycol towards the formation of ether.

Catalysts possessing slight Lewis and strong Bronsted acidity have been found efficacious for achieving high AMF product selectivity [138,271]. Furanix Technologies reported a patent on the etherification of HMF with di- or tri-hydroxy compounds typically in the presence of homogenous catalysts such as organic, inorganic acids, Lewis acids, to give HEMF. The temperature of the reactions was preferably said to be in the range of 150-225 °C. The inventors said that heterogeneous catalysts such as protonic, Bronsted or Lewis acids can be used for this reactions for purification reasons [140]. Lewis acidity and weak basicity in the cerium phosphate catalyst was reported to be selective for the HMFA production [274]. Thus, the aim was to find a heterogeneous strong Bronsted acid catalyst that is active for HEMF formation by reaction of ethylene glycol with Bronsted acid-sensitive hydroxyl group in HMF. In this work, etherification of HMF was studied with ethylene glycol as a reactant as well as solvent using metal supported heteropoly acid catalysts to produce HEMF.

Heteropoly acid (HPA) catalysts were chosen to serve this purpose as they show excellent Bronsted acidity in the literature [197–199]. Amongst the HPA, dodecatungstophosphoric acid

(DTP, $H_3PW_{12}O_{40}$) catalyst possessing Keggin structure has the highest acidity and thermal stability as compared to other HPAs [199,202]. Supporting HPAs on mesoporous material such as metal oxide, carbon, K-10 clay, etc. and the replacement of the protons in the HPA with metal ions such as Cs^+, Al^{3+}, Fe^{3+}, etc. has been reported to solve leaching, thermal stability and low surface area problems associated with the HPA catalyst [104,152,197,199]. Cs substituted DTP catalysts has been widely used for many acid catalyzed reactions [198,199,202,205,206]. Several metal ions such as Na^+, Sm^{3+}, Sn^{4+}, Ag^+, Ca^{2+}, Co^{2+}, Sn^{4+}, Ru^{3+}, Fe^{3+}, Zr^{4+}, and Al^{3+} substituted catalysts have been used for various reactions [207–209]. Some polyvalent metal ions such as Fe^{3+}, Sn^{4+}, Ti^{4+}, Bi^{3+} and Ru^{3+} have been reported to act as electron pair acceptors generating Lewis acid sites in the substituted heteropoly acid catalyst and possessing higher Bronsted acidity due to dissociation of coordinated water caused by the polarizing effect of the cation [208,210]. Also, Al substituted DTP catalyst has been reported to possess higher acidity than the parent DTP catalyst [152]. Thus, it was thought to study the effect of different valency metal ion substitutions on the acidity of DTP/K-10 catalyst and their activity for the etherification reaction.

3.2 Materials and Methods

3.2.1 Chemicals

HMF was obtained as a gift sample from Godavari Chemicals, Mumbai, India. The chemicals purchased from the reputed firms were as follows: ethylene glycol, dodecatungstophosphoric acid, aluminum nitrate, cupric chloride, cesium chloride (S. D. Fine Chemical Ltd., Mumbai), zirconyl nitrate, acetic acid, acetonitrile HPLC grade (Thomas Baker, Mumbai), montmorillonite K-10 clay (Sigma Aldrich, USA). All chemicals were used without further purification.

3.2.1.1 Catalyst synthesis

Four different (20 % w/w) metal substituted dodecatungstophosphoric acid catalysts (20 % w/w M_x-DTP) supported on montmorillonite K-10 clay (M_x-DTP/K-10) were prepared using incipient wetness impregnation technique, where x represents the number of metal ions [152,197,202]. The source of metals was cesium chloride for Cs, cupric chloride for Cu, aluminum nitrate for Al and zirconyl nitrate for Zr. Metals with varying valencies from 1-4 i.e. Cs, Cu, Al and Zr were exchanged with 2 hydrogens of DTP while retaining 1 hydrogen ligand, in order to study the metal valency effect on the catalyst and its activity. Thus, 20 % Cs_2-DTP/K-10**,** $Al_{0.66}$-DTP/K-10, Cu_1-DTP/K-10 and $Zr_{0.5}$-DTP/K-10 were prepared. In the case of aluminum, different variants of 20 % (w/w) aluminum exchanged DTP/K-10 were obtained - $Al_{0.66}$-DTP/K-10, $Al_{0.33}$-DTP/K-10 and $Al_{0.835}$-DTP/K-10 based on the retention of 2 and 0.5 hydrogen in DTP, respectively. At least 0.5 hydrogen was required to be maintained in the DTP to maintain its acidity.

The procedure for synthesizing the catalysts consisted of three stages: metal loading, DTP loading and calcination. For preparing 20 % (w/w) $Al_{0.66}$-DTP/K-10, K-10 was dried in oven overnight at 120 °C to remove moisture. The desired amount of aluminum nitrate was added to 5 mL of methanol and sonicated to obtain a homogenous solution. 4 g dried K-10 was taken in a beaker and 5 mL CsCl solution was added to it intermittently (approximately 1 mL each time). The mixture was mixed and crushed using pestle-mortar under ambient conditions until it was dry. The formed impregnated solid was dried in oven at 120 °C for 4 h to remove the residual methanol. The solid mixture was further impregnated with 5 mL solution of DTP in methanol intermittently as described previously to obtain a dry catalyst. The resulting mixture was again dried in oven at 120 °C for 4 h and subjected to calcination at 350 °C for 3 h to get active $Al_{0.66}$-DTP/K-10 catalyst.

Similarly, 20 % (w/w) Cu_1-DTP/K-10, $Zr_{0.5}$-DTP/K-10, Cs_2-DTP/K-10, $Al_{0.33}$-DTP/K-10, $Al_{0.835}$-DTP/K-10 and DTP/K-10 (without metal loading to serve as a blank) were prepared.

3.2.1.2 Catalyst characterization

The virgin and the reused catalysts were characterized by different techniques: XRD, FTIR, N_2 physisorption surface area and porosimetry, SEM, TPD, DSC and TGA. The details of the characterization protocol are mentioned in Chapter 2 and can also be found in the literature [30]. The methodology followed for analysis using XRD, FTIR, and SEM techniques is same as given in Chapter 2. TPD analysis was performed in the temperature range of 50-700 °C at ramp rate of 10 ºC per min to detect any strong acid sites at higher temperatures. For BET surface area and porosity analysis, the samples were degassed under high vacuum at 300 ˚C for 6 h. DSC and TGA analysis was performed in the temperature range of 50-700 °C with ramp rate of 10°C per min in nitrogen atmosphere to confirm the stability of the catalyst at high temperatures.

3.2.1.3 Reaction procedure

All etherification experiments were conducted in a 50 mL glass reactor equipped with 4 baffles and a standard 6-blade turbine impellor. The control experiment consisted of 5.95 mmol HMF, 0.178 mol ethylene glycol (1:30 molar ratio) as reactant as well as solvent with a total volume of 12 cm^3, catalyst loading of 0.03 g/cm^3 at 100 °C with a speed of agitation of 1000 rpm for 6 h. After the reaction, the reactor was cooled down and the mixture was filtered to obtain the catalyst and the product solution.

3.2.1.4 Reaction analysis

The conversion of the reactant, HMF and formation of the product, HEMF, was monitored by HPLC (Agilent 1200 Infinity series) using Agilent C8 reverse phase column (150 mm x 4.6 mm, 5 μm) maintained at a temperature of 25 °C. 0.1 % acetic acid in DI water and acetonitrile in the

ratio 80:20 v/v was used as a mobile phase with isocratic elution through the column at a flow rate of 1 mL/min. 10 μL of reaction mixture was injected in the column and analyzed using UV detector at a wavelength of 240 nm. A representative HPLC chromatogram of the reaction mixture containing HMF, HMEF and HMFA is shown in Figure A3.1. The products were confirmed using the same method by LC-MS (Agilent 1200 Infinity series equipped with 6140A single quadrupole mass spectrometer) using Agilent C8 reverse phase column (250 mm x 4.6 mm, 5 μm) (Figure A3.2).

3.3 Results and Discussion

3.3.1 Catalyst characterization

3.3.1.1 XRD

The XRD spectra of all the catalysts is shown in Figure 3.1. Montmorillonite K-10 shows amorphous nature. The K-10 showed characteristic mineral clay peaks at 20.3° and 35.1°. The sharp peaks observed at 26.8°, 50°, 59.8° are attributed to quartz impurity. This is in agreement with the results obtained by Wu et al. [38]. In Figure 1b, the DTP/K-10 shows the same peaks as K-10. The peak intensity decreases after the loading of DTP and in metal exchanged DTP catalysts. The crystalline nature of the DTP is well-substantiated in the literature with the finding that the loading of DTP on K-10 results in the loss of its crystallinity [197,277]. DTP and metal exchanged DTP catalysts do not show distinct peaks which can be due to low loading (20 % w/w) or high dispersion on the K-10 support. No significant change in the XRD pattern of all the catalysts confirms good dispersion of the catalyst on the support material. This could also have imparted

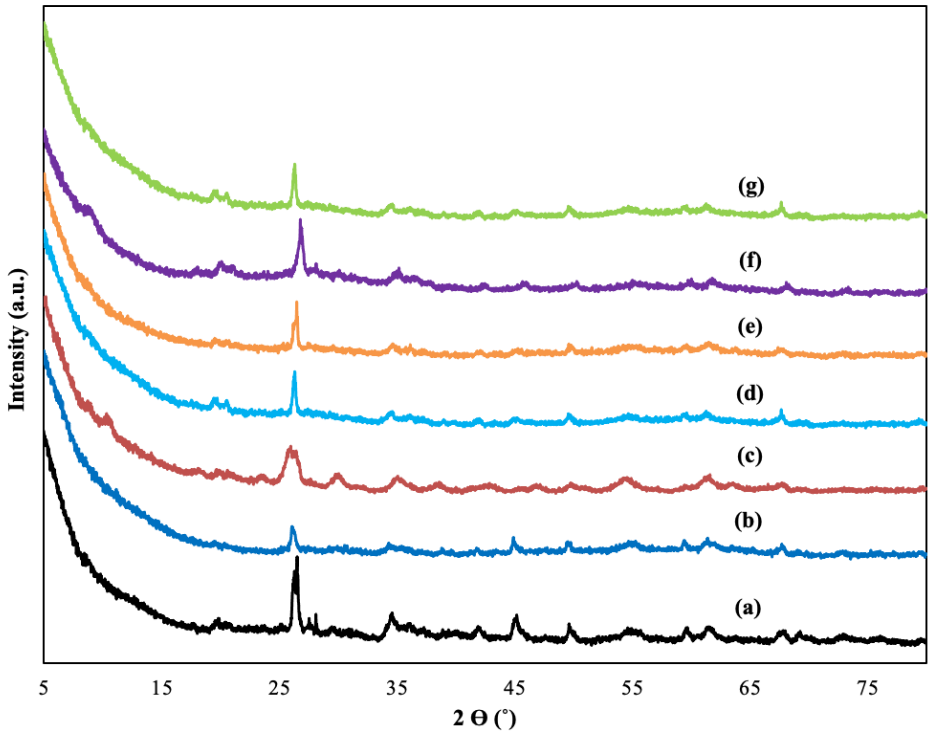

Figure 3.1 XRD of catalysts (a) K-10 (b) DTP/K-10 (c) Cs_2-DTP/K-10 (d) Cu_1-DTP/K-10 (e) $Zr_{0.5}$-DTP/K-10 (f) $Al_{0.66}$-DTP/K-10 (g) Reused $Al_{0.66}$-DTP/K-10

the amorphous nature to all the catalysts similar to K-10. The reused $Al_{0.66}$-DTP/K-10 catalyst shows similar spectra as the of fresh catalyst establishing the fidelity of the catalyst after reuse.

3.3.1.2 FT-IR

The FT-IR was done of all the catalysts to verify the retention of the Keggin structure of DTP after metal exchanging and loading on the K-10 support (Figure 3.2). In Fig. 2a, the broad peak shown by K-10 at around 1049 and 523 cm^{-1} is attributed to Si-O stretching and bending vibration, respectively in the tetrahedral clay. The bands at 469 and 692 cm^{-1} are due to the quartz impurity. The peak at 916 cm^{-1} corresponds to the bending vibration from the binding of the Al atoms to the hydroxyl group and the peak at 795 cm^{-1} results from Si-O-Al vibrations [278,279]. Fig. 3.2b shows the FT-IR spectra of DTP/K-10 which is similar to that of K-10 but the intensity of the K-

10 peaks has decreased which is most likely due to the well-dispersed loading of the catalyst on the support. Distinct peaks are seen in the DTP/K10 and all metal exchanged DTP/K-10 catalysts which arise from the characteristic Keggin structure of the DTP [152,280]. The band at 986 cm^{-1} is due to the terminal W=O vibration, 895 cm^{-1} to W-O-W vibration and 1082 cm^{-1} to the P-O stretching frequency in the central tetrahedra of the polyanion. The peaks at around 1630 and 3629 cm^{-1} depict -OH bending and stretching vibrations, respectively, which correspond to the presence of water in the DTP. All the catalysts show similar spectra which confirm the intactness of the Keggin structure after supporting metal exchanged DTP catalysts on K-10. Similar FT-IR spectra are shown by fresh and reused $Al_{0.66}$-DTP/K-10 which confirm the structural stability of the catalyst after third reuse.

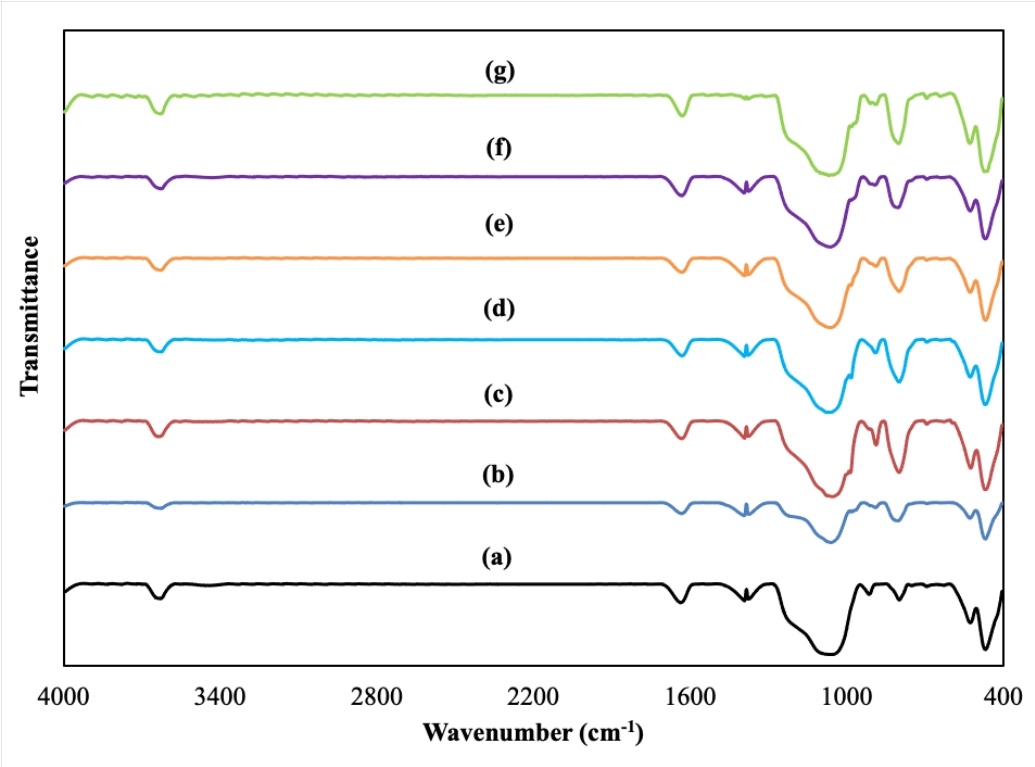

Figure 3.2 FTIR of catalysts (a) K-10 (b) DTP/K-10 (c) Cs_2-DTP/K-10 (d) Cu_1-DTP/K-10 (e) $Zr_{0.5}$-DTP/K-10 (f) $Al_{0.66}$-DTP/K-10 (g) Reused $Al_{0.66}$-DTP/K-10

3.3.1.3 NH_3-TPD

NH_3-TPD analysis of the synthesized catalysts was done from 100 to 650 ºC to analyze the acid strength of the catalysts (Figure 3.3 and 3.4). All the catalysts showed TPD peaks in the range of 100-300 °C which signifies the presence of weak acid sites in the catalysts [152]. Montmorillonite K-10 is an acid treated clay and thus possesses an acidity of its own [152,197]. The loading of DTP on K-10 increases the Bronsted acidity of DTP/K-10 catalyst. The substitution of the hydrogen ions in the DTP with the metal has been reported to cause a slight decrease in the acidity of the catalyst [152,197]. However, an increase in acidity was observed as valency of the

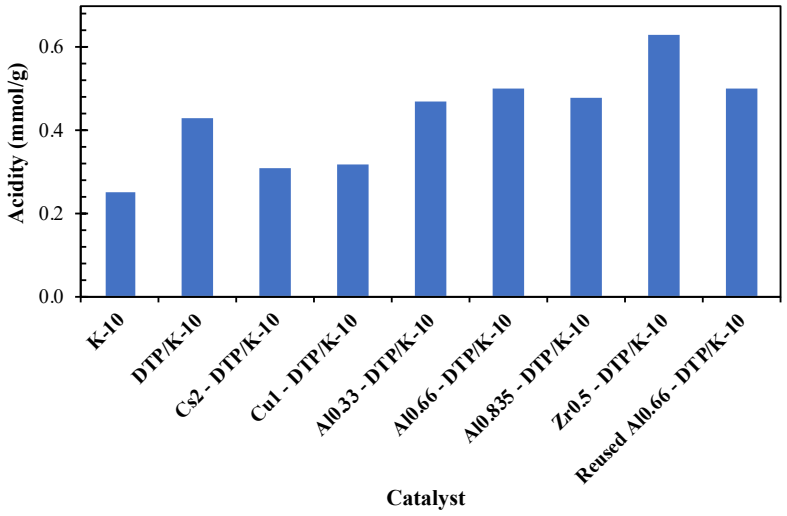

Figure 3.3 Acidity of the catalysts

substituted metal cations increased; Al- and Zr-substituted DTP showed higher acidity than the DTP/K-10 catalyst. This corroborates the findings in the literature [104,281].

Metallic aluminum possesses innate Lewis acidity [152]. $Al_{0.66}$-DTP/K-10 showed higher acidity as compared to $Al_{0.33}$-DTP/K-10 which could be due to an overall increase in Lewis and Bronsted acid sites in the catalyst. The replacement of further hydrogen with the Al metal ($Al_{0.835}$DTP/K-10) leads to a slight decrease in the catalyst acidity. This suggests that Bronsted

acidity of the DTP has an important role in the overall catalyst acidity. Negligible loss was observed in the acidity after reusing $Al_{0.66}$-DTP/K-10 catalyst.

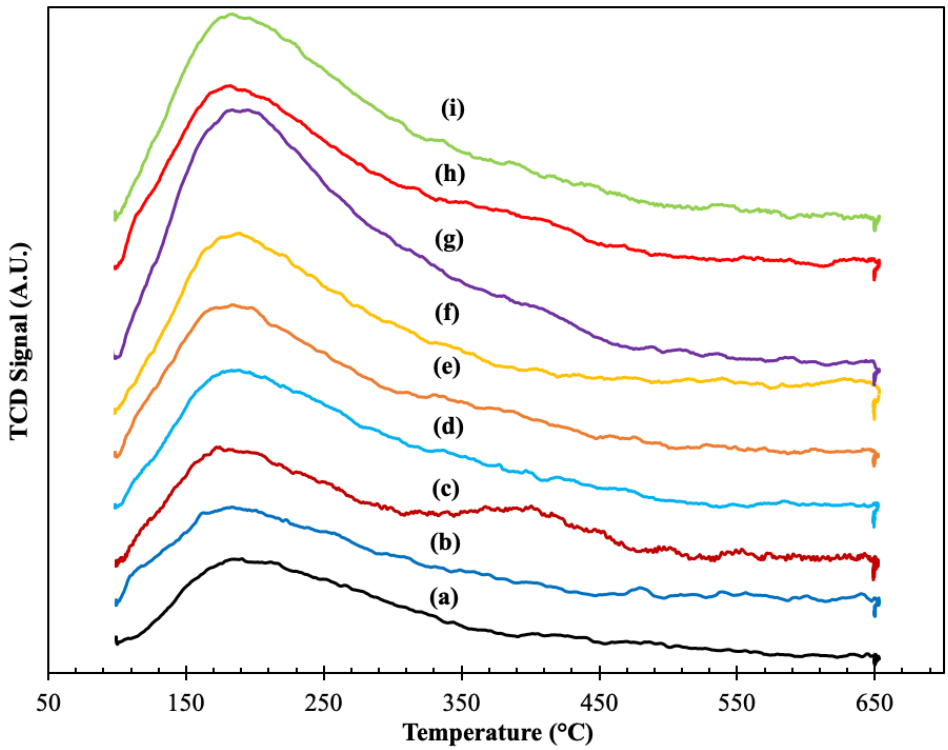

Figure 3.4 NH_3-TPD of catalysts (a) K-10 (b) DTP/K-10 (c) Cs_2-DTP/K-10 (d) Cu_1-DTP/K-10 (e) $Zr_{0.5}$-DTP/K-10 (f) $Al_{0.33}$-DTP/K-10 (g) $Al_{0.66}$-DTP/K-10 (h) $Al_{0.835}$-DTP/K-10 (i) Reused $Al_{0.66}$-DTP/K-10

3.3.1.4 Surface area and porosimetry analysis

The surface area and porosimetry data for fresh and reused Al-DTP-K10 was calculated by nitrogen adsorption-desorption isotherms (Figure 3.5a). The surface area and pore volume data for K10 support and DTP/K-10 have been well documented in the literature [152,197]. It has been reported that certain metals (Cs^+, Al^{3+}) substitution in DTP salt results in increased pore density and thereby, increased surface area of the catalyst as compared to the parent DTP

[152,197,204,282]. The catalyst shows type 1V adsorption-desorption isotherms with hysteresis loop of type H3, indicating mesoporous material [283].

Figure 3.5b further shows the dV/dlog(W) pore volume versus pore width, which clearly indicates no microporous volume and completely mesoporous nature of the fresh and reused catalyst. The BET surface area of fresh Al-DTP-K10 was found to be 226.4 m^2/g with pore

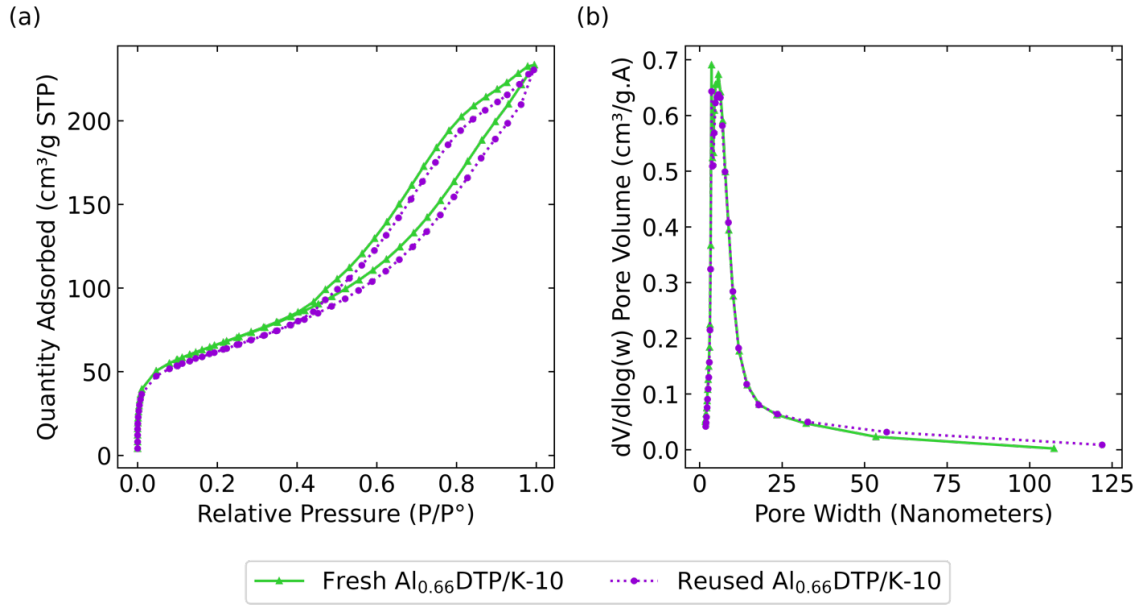

Figure 3.5 (a) N_2 adsorption-desorption isotherms of fresh and reused $Al_{0.66}$-DTP/K-10 catalyst **(b)** Pore volume vs pore size distribution of fresh and reused $Al_{0.66}$-DTP/K-10 catalyst

diameter and pore volume as 6.4 nm and 0.36 cm^3/g, respectively. The reusable catalyst showed minimal loss in surface area (213.2 m^2/g) and pore volume (0.35 cm^3/g) with slight increase in pore diameter (6.6 nm) after three reuses, signifying stable and reusable catalyst material.

3.3.1.5 SEM

The morphology of the $Al_{0.66}$-DTP/K-10, analyzed by SEM, is shown in Figure 3.6. The particles were found in agglomerates, as observed in the literature for Al and Cs metal substituted

DTP/K-10 catalysts [152,197,284]. The virgin and reused catalyst show similar morphology confirming the stability of the catalyst after reuse.

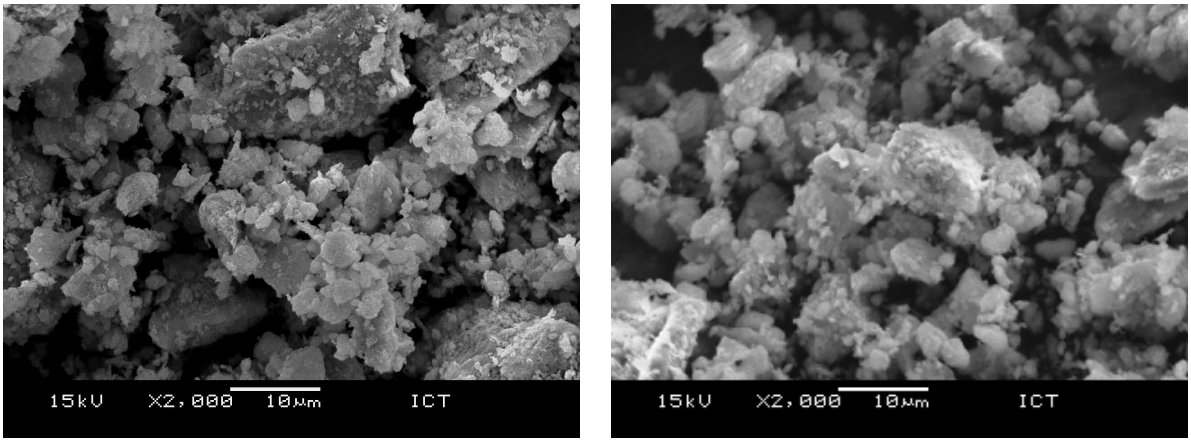

Figure 3.6 SEM images of (a) Fresh $Al_{0.66}$-DTP/K-10, (b) Reused $Al_{0.66}$-DTP/K-10

3.3.1.6 DSC-TGA

DSC-TGA analysis was done to determine the thermal stability of $Al_{0.66}$-DTP/K-10 catalyst. The Keggin structure of DTP decomposes at 465 °C which results in loss of its acidity [200].

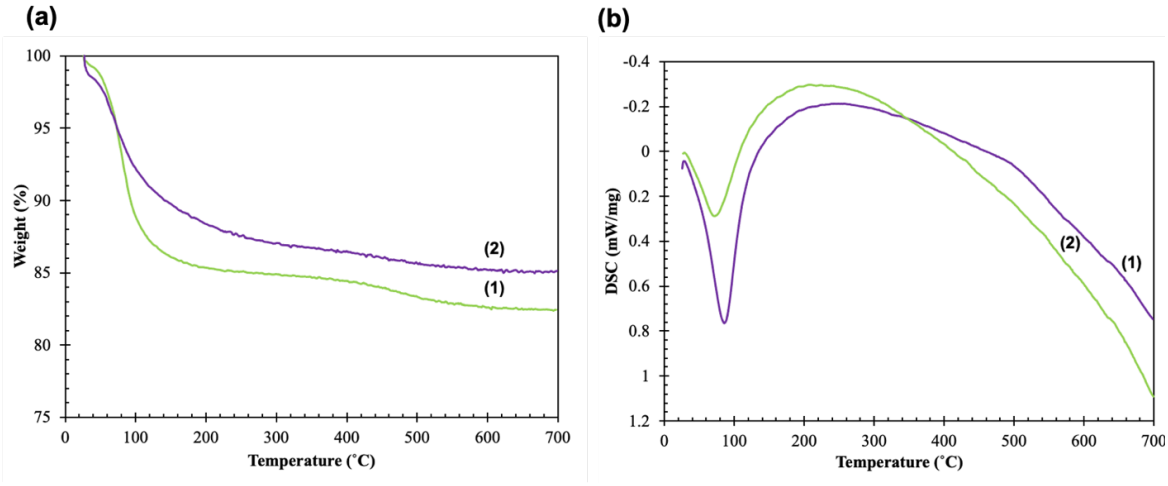

Figure 3.7 (a) DSC and (b) TGA analysis of catalysts (1) Fresh $Al_{0.66}$-DTP/K-10, (2) Reused $Al_{0.66}$-DTP/K-10

Exchanging the protons of DTP with metal cations and supporting it on inorganic support helps to enhance its thermal stability [199,285]. The DSC curves of fresh as well as reused $Al_{0.66}$-DTP/K-10 catalyst show an endothermic peak at around 75 and 85 °C, respectively (Figure 3.7a). This could be attributed to the loss of physisorbed and interlayer water molecules and also due to decomposition of hydroxide moieties in K-10 clay [152,286]. The TGA analysis of fresh and reused $Al_{0.66}$-DTP/K-10 catalyst showed a total weight loss of 15 and 18 %, respectively (Figure 3.7b). An initial weight loss of 12-15 % until 200 °C would result from the loss of adsorbed water, and subsequent weight loss of 3 % above 470 °C could be due to disintegration of structural -OH groups in the support. A lower weight loss until 700 °C means that the thermal stability of metal exchanged DTP/K-10 catalyst is higher, consistent with the literature [152,197].

3.3.2 Etherification of HMF to HEMF

The etherification of HMF with ethylene glycol was studied using different catalysts to selectively produce HEMF (Scheme 3.1) as compared to HMFA (Scheme 3.2). Ethylene glycol is used in excess to act as a reactant as well as solvent for the reaction. The effect of different reaction parameters on the conversion of the reactant and product selectivity were studied with HMF as a limiting reactant.

3.3.2.1 Catalyst screening

The etherification reaction of HMF with ethylene glycol was screened using various metal exchanged dodecatungstophosphoric acid catalysts (20 % w/w M_x-DTP/K-10) where metals (M) vary in valency from 1-4, i.e. Cs, Cu, Al, Zr and x represents the number of metal ions. For catalyst screening, x was initially taken to retain one hydrogen atom in the DTP. Thus, 20 % (w/w) Cs_2-DTP/K-10, Cu_1-DTP/K-10, $Al_{0.66}$-DTP/K-10 and $Zr_{0.5}$-DTP/K-10 were screened for their activity for the reaction. The catalyst activity was screened for 6 h under the control experimental

conditions mentioned in Section 2.4. All metal exchanged DTP/K-10 catalysts were found to have appreciable activity towards the reaction (Figure 3.8). HMF conversion was very low (15.7 %) with 97.5 % selectivity of HEMF when only K-10 support was used for the reaction. 20 % w/w DTP/K-10 showed high conversion for the reaction (95.1 %), but the selectivity was very low (50.7 %). This could be due to very high acidity of DTP which lead to degradation and polymerization reactions of HMF forming humins.

The order of M_x-DTP/K-10 catalysts conversion and selectivity towards HEMF was as follows: Cs_2-DTP/K-10 (74.1 %, 83.3 %), Cu_1-DTP/K-10 (75.9 %, 91.3 %), $Al_{0.66}$-DTP/K-10 (98.9 %, 96.6 %) and $Zr_{0.5}$-DTP/K-10 (96.6 %, 74.2 %). An increase in HMF conversion and HEMF selectivity was observed with increase in metal valency in case of Cs, Cu and Al substituted DTP/K-10. This effect could be correlated to the acidity of the catalysts as it was found to increase with metal valency (Figure 3.3). However, although $Zr_{0.5}$-DTP/K-10 possessed the highest acidity, it gave lower selectivity. This suggests that very high acidity of this catalyst might have led to HMF polymerization. All 20 % (w/w) M_x-DTP/K-10 catalysts except DTP/K-10 favored higher ether formation over acetal, thus making them truly chemo-selective. We have achieved almost complete conversion of HMF during the esterification reaction, which made the separation of product mixture of HEMF and HMFA easier by vacuum distillation.

Since, aluminum exchanged DTP/K-10 (20 % (w/w) $Al_{0.66}$-DTP/K-10) was found to give the best activity for the reaction as compared to other metals, different varieties of 20 % (w/w) Al_x-DTP/K-10 catalysts were prepared and screened for their activity to gain an insight into their role for this reaction. As mentioned previously, $Al_{0.33}$-DTP/K-10 and $Al_{0.835}$-DTP/K-10 were synthesized based on the retention of 2 and 0.5 hydrogen in DTP. $Al_{0.33}$-DTP/K-10 and $Al_{0.835}$-DTP/K-10 gave lower HMF conversion and HEMF selectivity which might be due to low acidity

as compared to $Al_{0.66}$-DTP/K-10 (Figure 3.3). Higher HEMF selectivity shown by $Al_{0.66}$-DTP/K-10 as compared to $Al_{0.33}$-DTP/K-10 could suggest the role of higher Lewis acidity due to Al metal favoring HEMF formation. Thus, 20 % (w/w) $Al_{0.66}$-DTP/K-10 was selected as the best catalyst for the reaction considering both the HMF conversion and selectivity towards the desired product. Hence, it was used in further experimental studies.

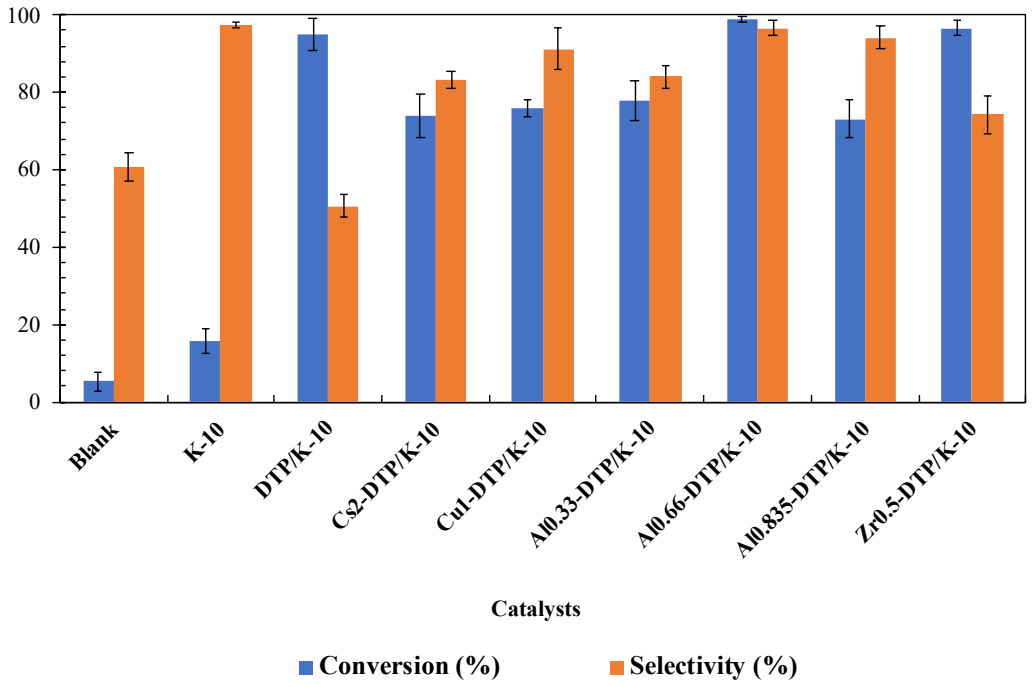

Figure 3.8 Effect of different catalysts on conversion of HMF and selectivity of HEMF. HMF:Ethylene glycol mole ratio: 1:30, Speed of agitation: 1000 rpm, Temperature: 100°C, Catalyst Loading: 0.03 g/cm^3, Total volume: 12 cm^3, Reaction time: 360 min.

3.3.2.2 Catalyst stability

The hot filtration method was used to test the stability and resistance to acid site leaching of the catalysts [197,277]. In this method, the catalyst was filtered after 30 min of reaction and reaction was allowed to extend without catalyst for the remaining time at the same control experimental conditions. The conversion of HMF was measured at the start as well as at the end of 30 min and 360 min reaction time (Figure A3.3). With DTP/K-10 as catalyst, the conversion

increased from 57.2 % (t = 30 min) to 92.8 % (t = 360 min). These results suggest that acidic DTP leached out from the K-10 support during the reaction and thus, it behaved as a strong homogenous acid catalyst. All M_x-DTP/K-10 catalysts were found to be resistant to leaching in the hot filtration test as they did not show significant change in HMF conversion after catalyst removal from the reaction (Figure A3.3). This is consistent with the results obtained in the literature with Cs-DTP/K10 catalysts [197]. Metal substituted DTP/K-10 catalysts are reported to immobilize the DTP on the catalyst efficiently by forming insoluble salts, which resist acid sites leaching making it a true heterogeneous catalyst [197,277]. Thus, M_x-DTP/K-10 catalysts were found to be stable and durable during the reaction.

3.3.2.3 Effect of speed of agitation

The effect of speed of agitation was studied in the range of 600-1000 rpm with experimental conditions maintained at HMF to ethylene glycol ratio of 1:30 (total volume = 12 cm^3), catalyst loading 0.03 g/cm^3 and temperature 100 ˚C (Figure 3.9). The conversion of HMF increased from 88.3 % to 96.9 % when the agitation speed is increased from 600 rpm to 1000 rpm respectively. However, not much appreciable increase in conversion was seen between 800 and 1000 rpm which signified the absence of external mass transfer resistance on the reaction. Thus, 1000 rpm was chosen as the speed of agitation for further studies.

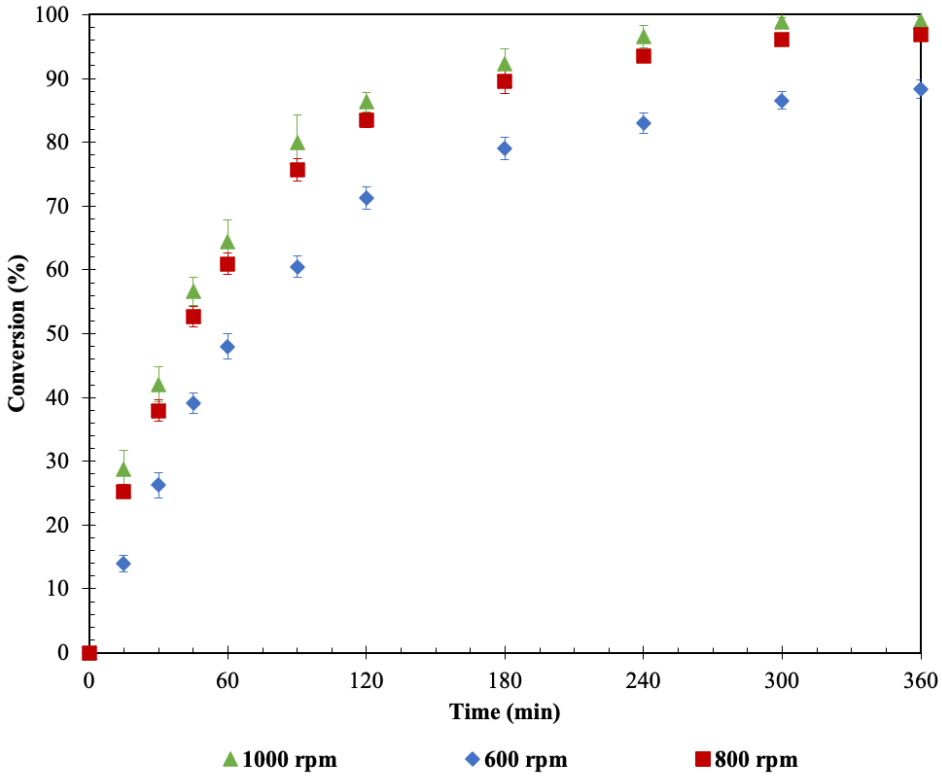

Figure 3.9 Effect of speed of agitation on conversion of HMF. HMF:Ethylene glycol mole ratio: 1:30, Temperature: 100°C, Catalyst Loading: 0.03 g/cm^3, Total volume: 12 cm^3, Reaction time: 360 min.

3.3.2.4 Effect of catalyst loading

The effect of catalyst loading was observed in the range of 0.02 to 0.04 g/cm^3 keeping the total volume constant in each case (Figure 3.10). The other variables were kept constant at the speed of agitation 1000 rpm, HMF to ethylene glycol ratio of 1:30 (total volume = 12 cm^3) and temperature 100 ˚C. There was a 12 % increase in conversion brought by the increase in number of catalytic active sites when the loading was increased from 0.02 to 0.03 g/cm^3. The final conversion did not show significant change when the catalyst loading was further increased from 0.03 to 0.04 g/cm^3. However, the initial rate of reaction was directly proportional to the catalyst loading (Fig. 3.10). Thus, 0.03 g/cm^3 was chosen as the optimum catalyst loading for further experiments.

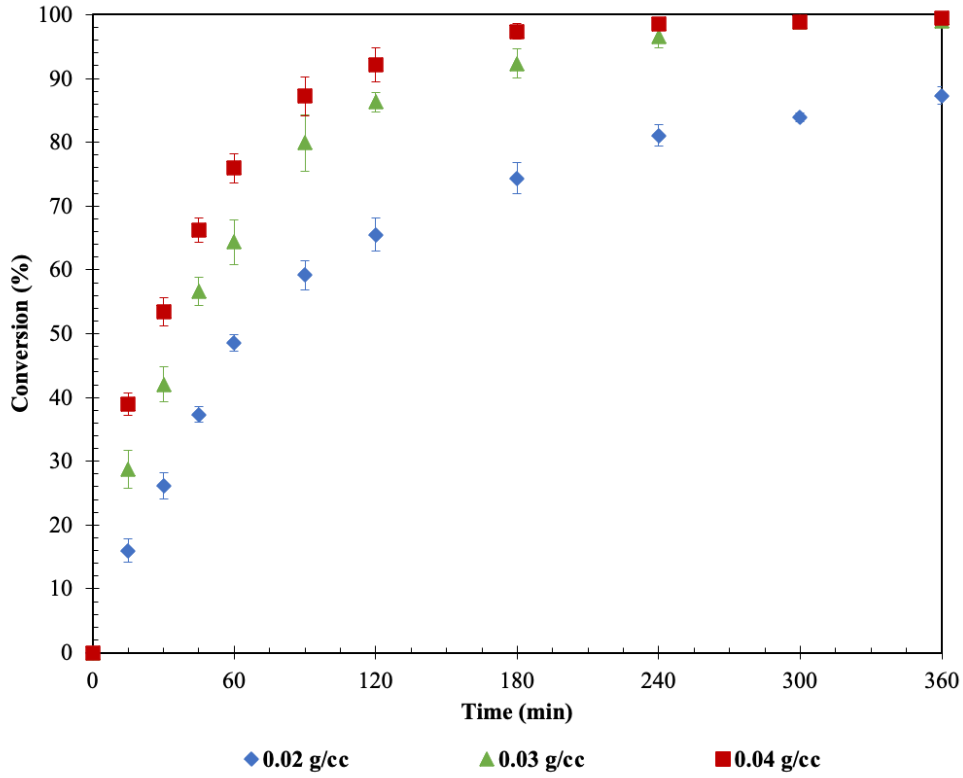

Figure 3.10 Effect of catalyst loading on conversion of HMF. HMF:Ethylene glycol mole ratio: 1:30, Speed of agitation: 1000 rpm, Temperature: 100°C, Total volume: 12 cm^3, Reaction time: 360 min.

3.3.2.5 Effect of mole ratio

The mole ratio of HMF: ethylene glycol was varied in the range of 1:10 to 1:40 keeping the total volume and the other variables constant (Figure 3.11). Increase in mole ratio from 1:10 to 1:30 resulted in increase in conversion from 76.5 % to 99.5 %. This means excess ethylene glycol is required for this reaction to get high conversion. Excess ethylene glycol as a solvent also makes the reaction mixture less viscous and dissolves the solid reactant HMF effectively. It would also solubilize the products making the catalytic active sites freely available for further reactant adsorption and surface reaction. However, further increase in mole ratio from 1:30 to 1:40 did not

show any appreciable difference in conversion. Thus, mole ratio of 1:30 (HMF: ethylene glycol) was taken as optimum for further reactions.

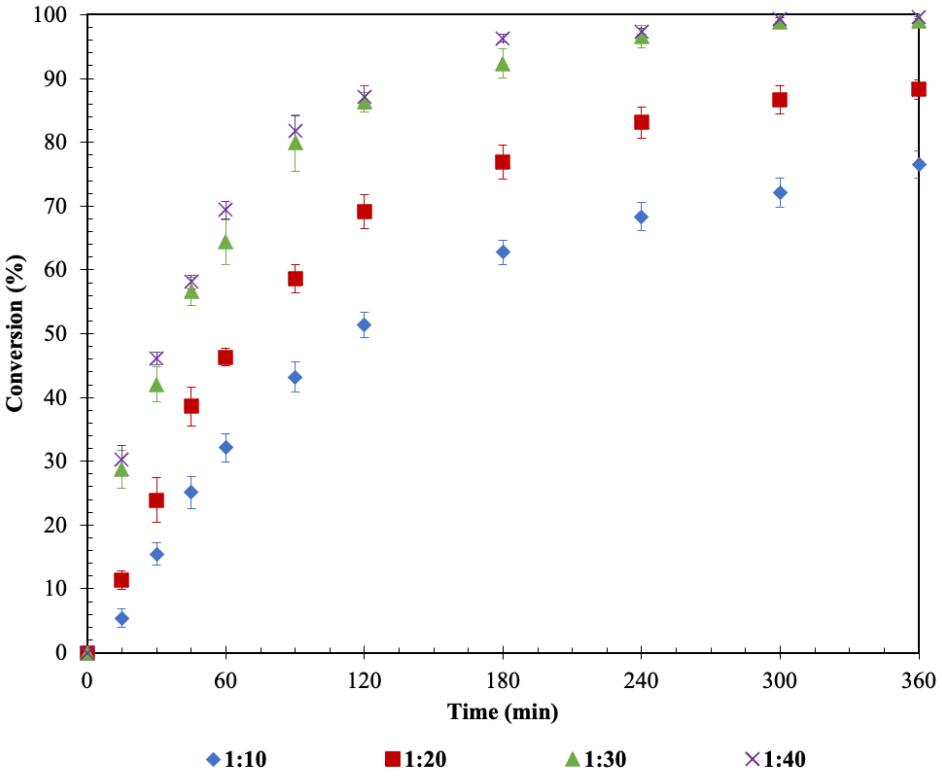

Figure 3.11 Effect of HMF to ethylene glycol mole ratio on conversion of HMF. Speed of agitation: 1000 rpm, Temperature: 100°C, Catalyst Loading: 0.03 g/cm^3, Total volume: 12 cm^3, Reaction time: 360 min.

3.3.2.6 Effect of temperature

The effect of temperature was studied in the range of 80 - 110 ˚C with the other reaction variables constant (Figure 3.12). The rate of the reaction and hence the conversion increased significantly with increase in temperature showing that the reaction is only kinetically controlled. Almost complete conversion of HMF (98.9 %) is achieved at 100 ˚C. Thus, 100 ˚C was chosen as

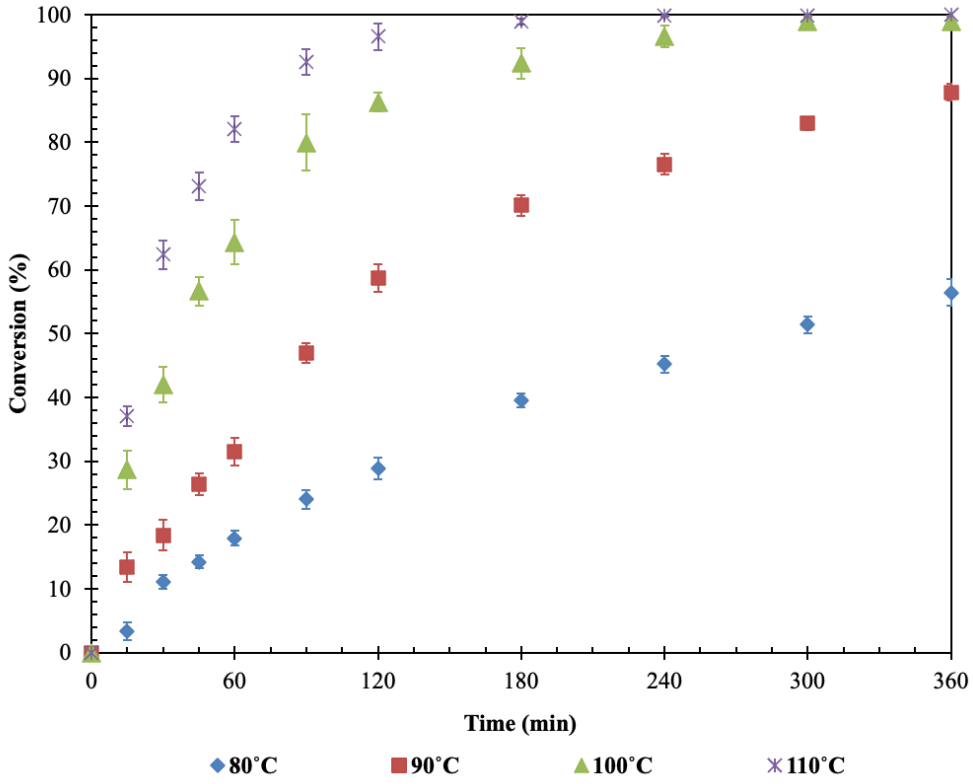

Figure 3.12 Effect of temperature on conversion of HMF. HMF:Ethylene glycol mole ratio: 1:30, Speed of agitation: 1000 rpm, Catalyst Loading: 0.03 g/cm^3, Total volume: 12 cm^3, Reaction time: 360 min.

optimum temperature for these reaction conditions. The initial rate data from the conversion of the reactant was used to deduce the kinetics of the system.

3.3.2.7 Reaction mechanism and kinetic modelling

The reaction mechanism for the etherification of HMF with ethylene glycol is shown in Scheme 3.3. HMF (A) and ethylene glycol (B) both adsorb on adjacent acid catalytic sites (S) of Al-DTP-K10 catalyst via oxygen. The nucleophilic attack of terminal hydroxyl group of ethylene glycol by lone pair electrons of oxygen on the electrophilic hydroxyl group of HMF results in the formation of 5-(2-hydroxyethoxymethyl)furfural (E) ether by removal of water molecule (F).

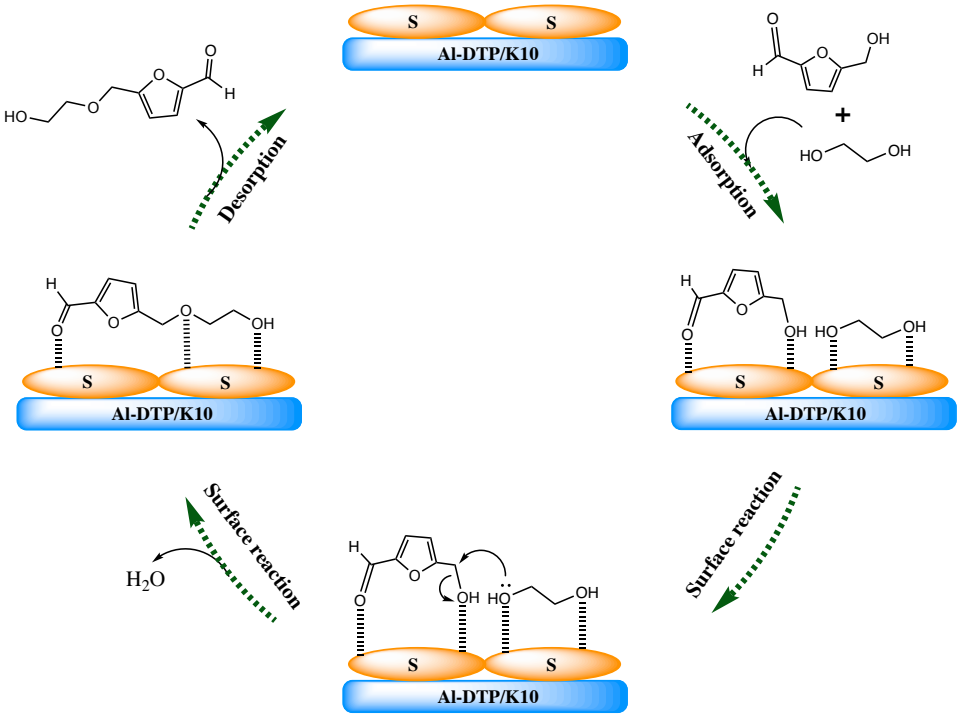

Scheme 3.3 Reaction mechanism for etherification of HMF to HEMF on catalytic acid site (S).

The kinetic model was derived using dual site LHHW mechanism. The detailed derivation is provided in Appendix. The surface reaction between chemisorbed HMF and ethylene glycol was assumed as the rate limiting step. For a fixed catalyst loading *w*, using the catalytic site balance and the concentration of adsorbed species from the adsorption-desorption step equilibrium, the rate of surface etherification reaction or the rate of decomposition of HMF can be derived as:

$$-r_A = \frac{-dC_A}{dt} = \frac{wk_S K_A C_A K_B C_B}{(1+K_A C_A+K_B C_B+K_E C_E+K_F C_F)^2} \tag{3.1}$$

Assuming the adsorption constants are very small ($K_i << 1$), equation (1) can be simplified as:

$$-r_A = \frac{-dC_A}{dt} = w\, k_S K_A C_A K_B C_B \tag{3.2}$$

Since, ethylene glycol (C_B) is in excess, the concentration can be assumed to remain constant throughout the reaction. Thus, the above equation can be reduced to a pseudo-first order rate equation (3.3), which can be integrated to get an equation (3.4) in terms of time and conversion as follows:

$$r_A = \frac{-dC_A}{dt} = wkC_AC_{B0} \quad \text{,where } k = k_S K_A K_B \tag{3.3}$$

$$-\ln(1 - X_A) = wkC_{B0}t\ , \quad \text{where } C_{B0} = 14.8\ mol/L \text{ and } w = 30\ g/L \tag{3.4}$$

The experimental HMF conversion versus time data recorded at different temperatures, keeping other parameters constant (Figure 3.13), was used to validate the predicted kinetic model. Figure 3.13 shows that the reaction follows a pseudo-first order reaction. The fit at all temperatures was found to be greater than 99%, suggesting that our assumptions are valid. The kinetic rate constants evaluated at different temperatures are given in Table 3.1. The activation energy of the reaction was calculated from the Arrhenius plot (Figure 3.14) and was found to be 21 kcal/mol.

Table 3.1 Kinetic rate constants and activation energy

Temperature (K)	**Rate constant, k*10^6 (L^2/mol/g/s)**	**Activation energy (kcal/mol)**
353	0.9 ± 0.03	21 ± 1.1
363	2.3 ± 0.05	
373	5.3 ± 0.16	
383	9.5 ± 0.15	

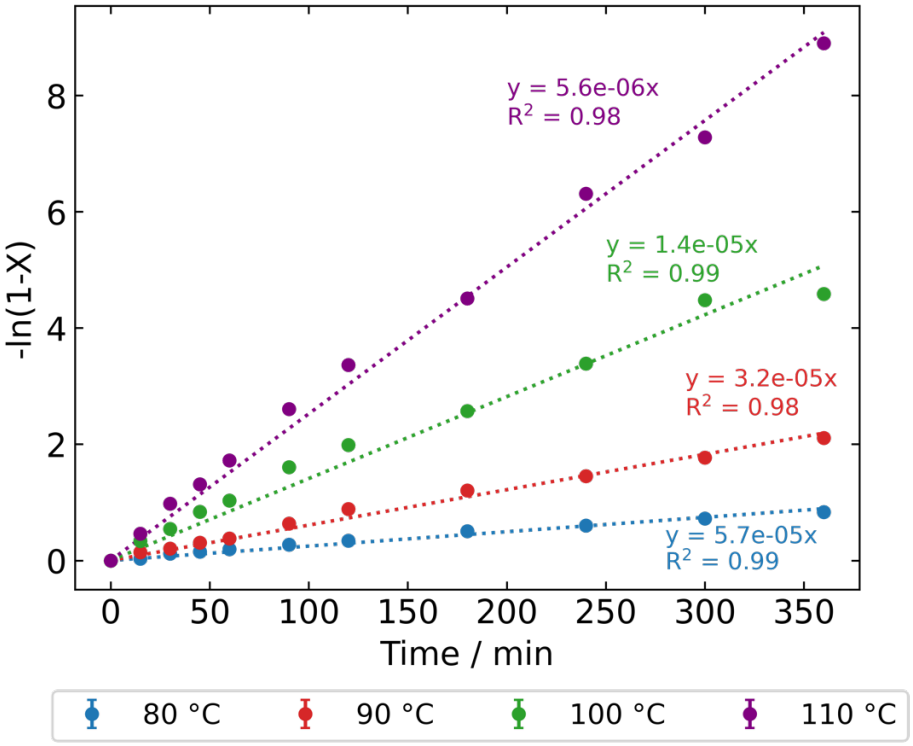

Figure 3.13 Plot of -ln(1-X) vs time

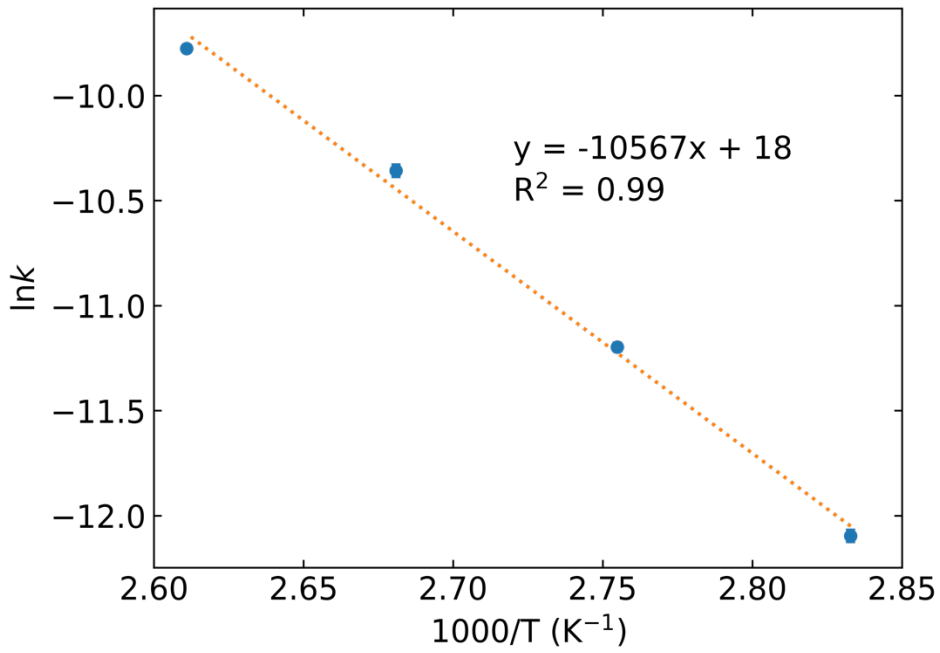

Figure 3.14 Arrhenius plot for etherification of HMF with kinetic rate constants (k) as a function of temperature (T).

3.3.2.8 Catalyst reusability

The catalyst was tested for reusability over three cycles (Figure 3.15). The catalyst was filtered at the end of reaction, and it was refluxed with methanol for 1 h to remove any adsorbed chemical compounds. It was dried at 120 °C for 12 h followed by calcination at 350 °C for 3 h. The catalyst loss during handling (0.03 g) was compensated with fresh catalyst in each experiment. The results shows that the catalyst maintains similar conversion of HMF for all cycles with only marginal loss in activity after third reuse (5.1 %). The catalyst maintained high selectivity of HEMF for all reusability cycles. After characterization, the spent catalyst showed similar structure with negligible loss in surface area, porosity. These results demonstrate the stability and reusability of the catalyst.

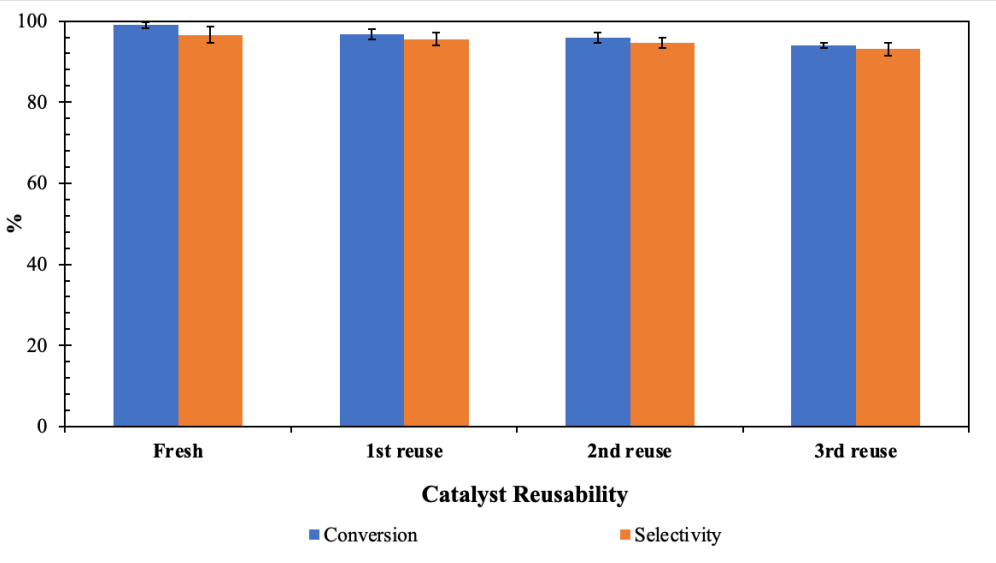

Figure 3.15 Effect of catalyst reusability on conversion of HMF and selectivity of HEMF. HMF:Ethylene glycol mole ratio: 1:30, Speed of agitation: 1000 rpm, Temperature: 100°C, Catalyst Loading: 0.03 g/cm^3, Total volume: 12 cm^3, Reaction time: 360 min.

3.4 Conclusion

Metal substituted dodecatungstophosphoric acid catalysts were found to be chemo-selective catalysts for the synthesis of HEMF by etherification of HMF with ethylene glycol. 20 % (w/w)

$Al_{0.66}$-DTP/K-10 was found to achieve the best activity for the reaction showing 98.9 % HMF conversion and 96.6 % selectivity of HEMF. The presence of Lewis acid sites in $Al_{0.66}$-DTP/K-10 balanced by Bronsted acidity of DTP favored the etherification reaction over acetalization. The metal substituted DTP/K10 catalysts were found to be resistant to acid site leaching. The optimized reaction conditions were as follows: speed of agitation of 1000 rpm, catalyst loading of 0.03 g/cm^3, HMF to ethylene glycol mole ratio of 1:30 and temperature of 100 ^{o}C. HMF conversion data at different temperatures were used to model the reaction kinetics by fitting to a first order rate law and activation energy was calculated as 21 kcal/mol. The fresh and reused catalyst was characterized, which indicated the structural, textural, porous, and surface characteristics were stable after reuse. The reusability studies showed that the catalyst was active and reusable with minimal loss in its activity.

Chapter 4

Zinc-Electrocatalyzed Hydrogenation of Furfural in Near-Neutral Electrolytes[3]

4.1 Introduction

Furfural can be valorized to FAL and MF by hydrogenation [22,59,101,287], which find applications in perfumery, polymer, pharmaceutical and fuel industries [8,101,106–110], as discussed in Chapter 1.

The furfural hydrogenation reactions are typically carried out in a vapor-phase reactor at high temperatures (90-500 °C) and pressures (0.1-2 MPa) using hydrogen gas in the presence of catalysts such as copper, copper chromite, iron, Cu/SiO_2, Cu/ZnO, Cu/C, bimetallic Pt-Sn, Cu-Cr, Cu-Co, $CuO/CeO_2/Al_2O_3$ etc. [219,288,297,289–296]. The studies report almost 98-100% conversion furfural [110,288,292,296] with 70-96% yield of FAL [288,289,297] and 90-98% yield of MF [110,292]. The storage and transportation of hydrogen gas required for these processes generates safety issues. Also, the catalysts such as chromium and solvents used for conventional furfural hydrogenation are toxic and environmentally hazardous [291,298]. Thus, there is a need to design reaction operating conditions that are mild and safe.

We aim to convert furfural to FAL and MF by ECH**,** as depicted by Scheme 4.1[101,106]. Furfural adsorbed on the metal catalyst electrode surface reacts with two moles of protons and electrons to give rise to hydrogenated product, FAL. FAL further hydrogenates to MF by consuming two protons and electrons with the removal of a water molecule. Dissolved protons may be partially regenerated at the anode, for example by water oxidation (1.12). The protons may adsorb on the surface of the metal catalyst by Volmer reaction (1.13). Protons are incorporated

[3]This work is published as M.S. Dhawan, G.D. Yadav, S. Calabrese Barton, Zinc-electrocatalyzed hydrogenation of furfural in near-neutral electrolytes, Sustain. Energy Fuels. 5 (2021) 2972–2984. doi:10.1039/D1SE00221J.

into the desired products – FAL and MF after the reaction, this results in atom economy of 100 %. Use of furfural, metal catalysis, water as a safe solvent and hydrogen source, and co-production of two value-added chemicals makes this ECH process satisfy green chemistry principles. These incude the use of renewable feedstocks, catalysis, less hazardous chemical synthesis, safer solvents and design for energy efficiency.

ECH reaction:

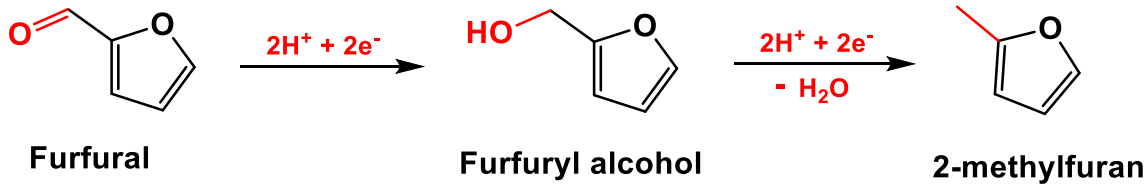

Scheme 4.1 ECH of furfural to FAL and methyl furan

The selectivity for ECH may be limited by HER, which consumes protons to produce H_2 gas making them less available for ECH, thereby lowering the FE of the system. Another side reaction is the dimerization of furfural radicals that are intermediate in FAL generation to produce hydrofuroin (Scheme 4.2) [108,109,173]. The choice of a metal catalyst that has high FE for ECH over both HER and dimerization helps to maximize FE of the reaction system. The formation of hydrogen, dimerization side products and unreacted furfural will lead to a >1 % E-factor of this process. High E-factor due to side products from furfural derivatives and unreacted furfural will be counted in the mole balance calculations.

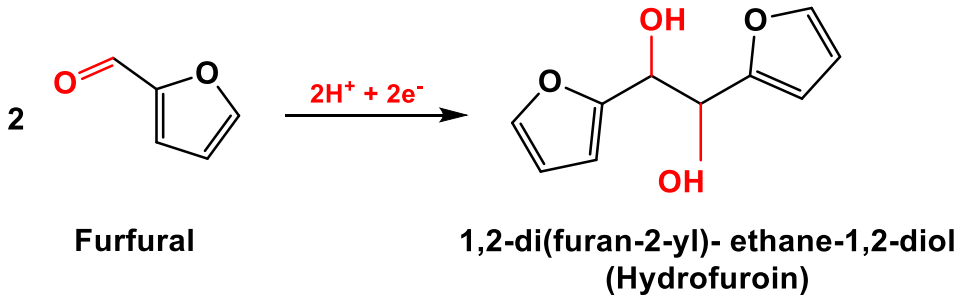

Scheme 4.2 Electrodimerization reaction of furfural to hydrofuroin [173]

There has been a number of reports of furfural ECH by various groups, who studied the impact of reaction conditions and electrode materials on the conversion, FE and product yields [107,111,299,300]. The literature for ECH of furfural has been mainly dominated by copper and nickel as a catalyst at various pH resulting in good reactant conversion and product yields [8,43,108,111,157,299]. Zhao et al. compared the reactivity of copper, nickel, lead and platinum for the ECH of furfural. Pure platinum gave the highest selectivity for FAL (99%), but the conversion was very low. Copper gave high conversion and low selectivity whereas nickel yielded low conversion and high selectivity in basic pH with higher onset potentials [216]. Thus, there is a need to find a catalyst that gives both higher conversions and selectivities for the ECH of furfural.

Apart from metal catalyst screening, the effect of pH on FE and product selectivities from ECH of furfural have been studied [108]. Li et al. achieved a good yield of FAL (63%) in 0.2 M ammonium chloride (pH 5) using nickel as a catalyst cathode with a electrochemical efficiency of 56% [101] whereas MF was reported to be formed at higher selectivities (~ 80%) at low acidic pH (~ 0.5) by Nilges et al. [100].

Similar findings were achieved by Jung et al. who studied the activity of bulk copper and compared it to higher surface area nano- and microcrystalline copper catalyst particles electrodeposited on copper itself [109,158]. The highest selectivity for FAL (25.1%) was obtained at pH 5 [109]. Thus, the main conclusion of these studies was that MF was formed at strongly acidic conditions (pH = 0.5) and FAL was a preferred product at pH of 5. Copper was found to promote FAL and MF formation over H_2 gas at less negative potentials, but the conversion was low. More negative potentials increased the conversion of furfural but at lower FE [109].

The applied potential may determine whether HER or ECH is favored [106,158,301]. In acidic pH, the onset potential for both ECH and HER are close, which leaves less room to modify the

kinetics of the reactions [106,158]. High starting concentrations of furfural (100 mM) have been shown to favor ECH over HER due to higher catalytic surface coverage and adsorption [101,106]. A further increase in initial furfural concentration to 200 mM has been reported to promote undesired electrodimerization reactions [106]. Higher electrolyte concentration has also been reported to favor ECH, higher conversion and product yield [109]. High electrolyte concentration provides high ionic conductivity, reducing potential drop across the cell.

It was also shown by Jung and Biddinger that furfural, FAL and MF degrade in acidic solutions by polymerization/oligomerization to give rise to humins [109]. Kim et al. used Raman spectroscopy to observe the acid-catalyzed polymerization of FAL in sulfuric acid at room temperature to conjugated diene and diketone species, which were also evident by color and viscosity changes of FAL within an hour [302]. Liu et al. studied the reactivity of various catalysts in basic carbonate buffer at pH 10, and the highest current efficiency of FAL (70%) was achieved with copper at –0.56 V/RHE. However, the reaction time of 10 h was required to achieve these results [303]. Thus, neutral or basic pH can be expected to avoid degradative side reactions and increase FE of furfural ECH.

Other catalysts such as gold [114], silver [159], palladium [230], rhodium [229] etc. have been reported for ECH in the literature but have not been used for ECH of furfural. Zinc has been reported to effectively catalyze CO_2 and HMF electroreduction with high Faradaic efficiencies [114,226,238]. Feng et al. observed an 18% increase in FE for the formation of ethylene from CO_2 after alloying copper catalyst with zinc and using it as a bimetallic catalyst [304]. HMF is a structural analog of furfural with an additional hydroxyl functional group present at the fifth carbon. Zinc exhibited exceptional catalytic activity for the reduction of HMF to 2,5-hexanedione with a FE of 72.4% and outperformed copper by 70% in terms of FE and selectivity to desired

product [114]. Many reports on chemical hydrogenation of furfural have been published using zinc oxide catalysts either as an active phase or as a support [110,288,289]. Thus, it was hypothesized that zinc catalyst could have good catalytic activity for the ECH of furfural.

In this work, the hydrogenation of furfural to FAL was carried out using various catalysts such as copper, nickel and zinc. This is the first-time zinc has been used as metal catalyst for the hydrogenation of furfural. The present work establishes zinc as catalyst that is selective for the ECH of furfural while inhibiting HER. The variables used to assess the activity of the catalyst were the applied potential, achieved current density, reactant conversion, yield and FE for the desired reaction products. Apart from these variables, the electrolyte and the pH, which determine the proton concentration in the solvent and thus affect the selectivity of the reaction and product formation have also been studied [106,109]. Preliminary tests to screen the activity of the catalyst under different pH conditions – acidic, basic and neutral were performed on catalyst wire using transient and steady-state voltammetric techniques such as cyclic voltammetry (CV) and staircase voltammetry (SV). The catalysts and electrolyte pH were screened on the basis of potential windows and the current density for the occurrence of desired ECH reaction and to avoid HER. The activity of the catalysts for the ECH was screened on the basis of FE, conversion and selectivity towards the desired products measured by potentiostatic electrolysis.

4.2 Materials and Methods

4.2.1 Chemicals

The following chemicals were obtained from reputed vendors and used without further purification: Furfural (99%, Sigma-Aldrich), FAL (FAL, 98%, Sigma-Aldrich) , MF (MF, 99%, 200 – 400 ppm BHT as stabilizer, Sigma-Aldrich), acetonitrile (ACN, 99.5%, Mallinckrodt Chemicals), p-xylene (≥ 99%, Sigma-Aldrich), sulfuric acid (H_2SO_4, 98%, EMD Chemicals),

sodium hydroxide (NaOH, Macron Fine Chemicals), sodium bicarbonate ($NaHCO_3$, 100.3%, J. T. Baker), sodium sulphate (Na_2SO_4, 99.6%, Fisher Chemical), ammonium chloride (NH_4Cl, ≥ 99.5%, Columbus Chemical Industries), sodium chloride (NaCl, ≥ 99%, Columbus Chemical Industries), sodium phosphate monobasic ($NaH_2PO_4.H_2O$, 99.7%, J. T. Baker), sodium phosphate dibasic ($Na_2HPO_4.7H_2O$, Jade Scientific). 0.5 M phosphate was prepared by mixing 0.37 M $Na_2HPO_4.7H_2O$ and 0.13 M $NaH_2PO_4.H_2O$. All the electrolytes were prepared in deionized water (≥ 18 MΩ cm, Thermo Scientific).

4.2.2 Electrodes

The metal wires used as working electrodes for the ECH of furfural are as follows: copper (1.2 mm diameter, 18 AWG, 99.9%, Arcor electronics), nickel (1.0 mm diameter, 99.98%, Alfa Aesar), zinc (1.0 mm diameter, 99.95%, Alfa Aesar). The catalyst wire electrodes were rubbed with sandpaper (800 grit (P2400), diameter = 6.5 μm, Buehler) to remove oxides, rinsed with ethanol and deionized water prior to be used for the reaction. The geometric surface area of the working electrode for cyclic and staircase voltammetry experiments was 1 cm^2 and that for electrolysis experiments was 5 cm^2. A reversible hydrogen electrode was used as a reference electrode (RE). It was made in-house using a Pt wire (0.5 mm dia., 99.95%, Thermo Fisher Scientific) in a one-end sealed glass tube. The RE tube was filled with working electrolyte before each experiment. Graphite rod, (2.5 cm diameter, Pine Research Instrumentation) was used as a counter electrode.

4.2.3 Electrochemical set-up

The reactions were conducted using a three-electrode system connected via a VSP Bio-logic SA potentiostat in a divided glass jacketed H-cell. The compliance voltage range of the potentiostat was 20 V. The anodic chamber contained 25 ml of desired electrolyte and the cathodic chamber contained 25 ml of 100 mM furfural in the same electrolyte. The anodic and cathodic compartment

was separated by Nafion 115 cation exchange membrane (Ion Power). Nafion 115 membranes were pretreated by boiling in 1M solutions of sulfuric acid, sodium sulphate or sodium hydroxide at 80 °C for 1 h depending on the pH to be used for electrolysis *i.e.* acidic, neutral, basic respectively. They were subsequently boiled in DI water at 80 °C for 1 h and stored in DI water thereafter. The on-center distance between the two compartments was measured as 5 cm. The pH of the electrolyte was measured prior to and following every reaction using a pH meter (Fisher Scientific, Accumet Basic AB15). The cathodic chamber was purged with nitrogen throughout the reaction to maintain oxygen-free conditions and to create a positive pressure inside for the removal of evolved gases and MF. MF was collected in a cold trap connected to the H-cell as it is volatile [109]. The cold trap was maintained at -15 ± 3 °C using 20 wt% NaCl and ice mixture in Dewar [100]. All reactions were carried out at 30 ± 0.1 °C. A rotation speed of 900 rpm was maintained using a magnetic stirrer in the cathode chamber.

4.2.4 Electrochemical techniques

CV was used for transient studies to analyze the onset potential and reduction peaks for copper, nickel and zinc electrodes in different pH electrolytes. The onset potential was recorded as the potential where the current reached 0.1 mA. CVs were acquired at a scan rate of 20 mV/sec with end potential as -1 V/RHE. The starting potential for CV was varied based on the open circuit potential of the electrode in the electrolyte, in order to record the onset potential.

SV was used as a steady-state technique to analyze the faradaic current density obtained with each electrode in different pH electrolytes while avoiding the background capacitive current to a greater extent as opposed to CV. For SV, a potential step of 100 mV was applied consecutively from -0.6 to -1 V/RHE with a halt at each potential for 1 min and then reversed to the initial potential to check steady state current density.

Potentiostatic electrolysis experiments were run using chronoamperometry at the desired potential for 2 h.

4.2.5 Analysis

During electrolysis, 0.2 ml of reaction samples were collected intermittently at specific time intervals up to 2h. Reaction analysis was performed with a Varian 450 gas chromatography system equipped with SolGel-Wax column (30m, 0.53 mm ID, 1 μm film thickness) using flame ionization detector and helium as carrier gas at 1 ml/min. The temperature program started at an initial temperature of 37 °C (held for 4 min) and then ramped at 10 °C/min to 90 °C (held for 3 min) followed by ramp at 10 °C/min to 150 °C and ramp at 30 °C/min to 230 °C (held for 2 min). The split ratio was 1:100. Injector and detector temperatures were set at 270 °C [305]. The furfural, FAL standards and reaction samples were prepared by ten-fold dilution with ACN containing p-xylene as internal standard. The diluted samples were filtered with a 0.22 μm syringe filter prior to injection on the column. MF standard was prepared in ACN, and cold trap sample was directly analyzed without any dilution. The unknown concentration in the reaction samples was calculated by comparing to the calibration curve prepared using the standard samples of furfural, FAL and MF.

Some diluted reaction samples were also analyzed by gas chromatography with mass spectrometry (GC-MS). We used a Shimadzu QP-5050A gas chromatograph equipped with Restek Rtx-1701 capillary column (60 m, 0.25 mm ID, 0.25 μm film thickness) coupled with an electron ionization mass spectrometer. The ionization energy was 80 eV and m/z values ranged from 40 to 400 [101]. The GC program started at 40 °C (held for 1 min) and then ramped at 3 °C/min to 121 °C followed by ramp at 8 °C/min to 270 °C (held for 1 min). Injector and detector temperatures were set at 270 °C. The mass spectrum of each chromatogram peak was identified by comparing

to the mass spectrum of the probable chemical compounds provided by the NIST library, based on similarity index.

It is possible for furfural to cross over through the Nafion membrane to the anode compartment, resulting in an error in our conversion calculations. We conducted crossover measurements to observe the concentration of furfural transferred to anode by permeation through the membrane. The concentration profile was fitted to an equation derived for the flux of furfural across the membrane which is proportional to the concentration gradient (Fig. A4.2). The fit demonstrated a membrane permeability to furfural of 1×10^{-6} cm^2 sec^{-1}. Based on this value, we estimate an error of less than 1% in our conversion estimates due to furfural crossover from cathode to anode during electrolysis.

4.2.6 Calculations

The conversion, yield and FE was calculated using the equations provided in Chapter 1. For calculation of Faradaic efficiency, the electron transfer coefficient for FAL and MF formation is 2 and 4, respectively.

4.2.7 Catalyst characterization

The surface morphology and elemental analysis of zinc wires and precipitates was obtained using scanning electron microscopy with energy dispersive X-ray spectroscopy (SEM/EDS, JEOL 6610LV). Dried wires were mounted on specimen stubs partially coated with a thin film of carbon tape. The wire portion not stuck to the carbon tape was analyzed. The precipitates were embedded in a cylinder stub with a hole for sample containment to avoid carbon taping as it would obscure any organic carbonaceous compound present in the precipitates. The samples were analyzed at low vacuum of 60 Pa and acceleration voltage of 10 kV.

4.3 Results and Discussion

4.3.1 Steady state voltammetry with zinc in different pH electrolytes

To study the catalytic activity of zinc catalyst for hydrogenation of furfural, we first conduct polarization studies of the zinc electrode in the presence and absence of furfural, and in different electrolytes. Figure 4.1 shows steady-state polarization curves of zinc wire in three 0.5 M electrolytes of widely varying pH: H_2SO_4 (pH = 0.5), NaOH (pH = 13.9), and $NaHCO_3$ (pH = 8.4), representing acidic, basic and neutral electrolytes. Dashed and bold lines indicate the potential-dependent current density in the absence and presence of 100 mM furfural, respectively.

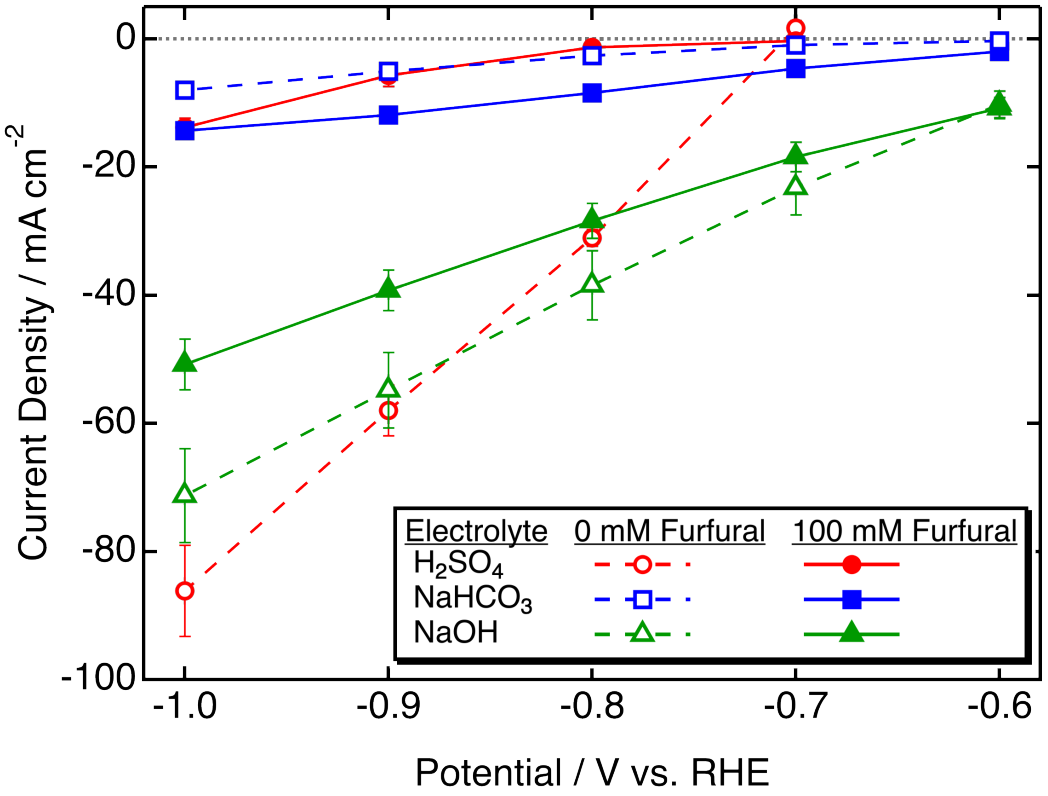

Figure 4.1 Furfural reduction and HER polarization curves obtained with zinc in electrolytes of varying pH.

With no oxygen or furfural present, only HER occurs on the catalyst in this potential range. The addition of furfural to the electrolyte leads to increased or decreased current density, depending on the dominance of ECH reaction and the effect of furfural on HER.

With zinc in acidic pH, the polarization curve was recorded from -0.7 to -1 V/RHE because of low onset potential (Table 4.1). There was a significant decrease in faradaic current density in the presence of furfural. This suggests that HER reaction was hindered, which could be due to the surface coverage of the electrode with furfural that would affect electron transfer to form H_2 gas. The low current density would still suggest less activity and slower kinetics of ECH in acidic pH. Additionally, in the absence of furfural, the linear potential dependence at zero current suggests a mixed reaction consisting of both HER and zinc oxidation.

In basic pH, there was a lesser decrease in current density after the addition of furfural as compared to acidic pH. Thus, we might expect ECH to have higher efficiency in basic electrolytes. In near-neutral pH electrolyte, 0.5 M $NaHCO_3$, at all studied potentials, an increase in current density was observed after the addition of furfural. This strongly suggests that ECH is a more dominant reaction in neutral pH electrolytes and higher efficiency of ECH may be achieved at these conditions.

Table 4.1 Onset potential of HER and ECH with zinc catalyst in different pH electrolytes

Electrolyte	**Onset Potential (V/RHE)**	
	HER	**ECH**
H_2SO_4	-0.69 ± 0.003	-0.69 ± -0.01
$NaHCO_3$	-0.5 ± 0.005	-0.56 ± 0.007
NaOH	-0.45 ± 0.001	-0.39 ± 0.002

Table 4.1 shows the onset potential of HER and ECH reactions with zinc at different pH, recorded from their respective cyclic voltammograms (Figure A4.3). In case of acidic pH, the onset

potential of HER and ECH was similar, thus the potential window cannot be altered to favor ECH over HER, and HER is the dominant reaction at low pH at all applied potentials.

In basic pH, the onset potential of ECH was less negative than HER, but decreased current density was observed after addition of furfural (Figure 4.1) suggesting that ECH selectivity would increase at less negative potentials. In near-neutral pH electrolyte, 0.5 M bicarbonate, although the onset potential of ECH was more negative than that of HER, higher current density in the presence of furfural (Figure 4.1) suggests higher selectivity toward ECH over HER.

Cyclic voltammograms obtained with zinc in the presence of furfural in different pH electrolytes show features due to various reactions involving metallic zinc (Figs. A4.3 and A4.4). These may include oxidation-reduction, dissolution to form zinc hydroxide, and hydrogenation of FAL to MF. In acidic electrolyte, zinc also shows additional onset peaks in the absence of furfural (Fig. A4.3). This could be due to high instability of zinc catalyst at acidic pH which leads to its oxidation and dissolution [162].

4.3.2 Steady state voltammetry with varying catalysts in near-neutral electrolyte

Steady-state polarization performed with zinc in bicarbonate were compared to well-studied metallic ECH catalysts, copper and nickel [8,101,106,109,303]. Steady state polarization curves obtained with these catalysts are shown in Figure 4.2.

With nickel, there was a decrease in current density after the addition of furfural, which indicates fast kinetics of HER over ECH. In contrast, both copper and zinc catalysts showed an increase in current density after the addition of furfural, with the increase with zinc being considerably greater as compared to copper at all potentials. At -0.7 V/RHE, the increase in current

density with zinc was around 398% as opposed to 61% with copper. Thus, zinc catalysis appears to be selective toward furfural ECH.

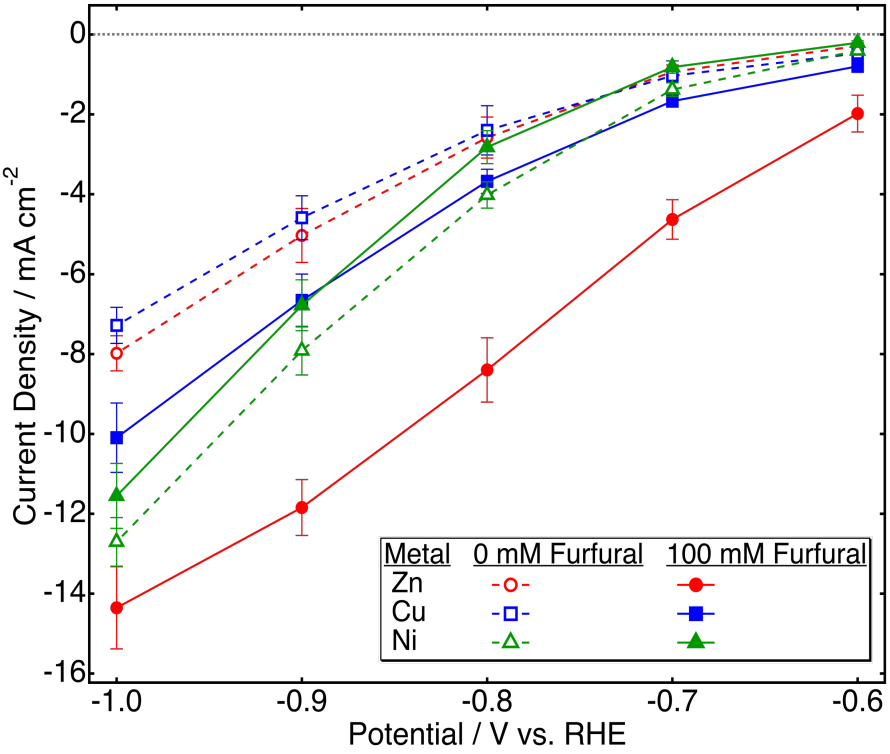

Figure 4.2 Furfural reduction and HER polarization curves obtained with different

Table 4.2 Onset potential of HER and ECH with different catalysts in 0.5 M bicarbonate.

Catalyst	**Onset Potential (V/RHE)**	
	HER	**ECH**
Copper	-0.31 ± 0.009	-0.29 ± -0.015
Zinc	-0.5 ± 0.005	-0.56 ± 0.007
Nickel	-0.24 ± 0.009	-0.45 ± 0.03

Table 4.2 shows ECH and HER onset potentials obtained by CV in $NaHCO_3$ with different catalysts. For the nickel catalyst, the onset potential for ECH was significantly more negative as compared to HER; thus, we might expect HER to be dominant over ECH at all potentials on nickel. The onset potentials of ECH and HER were close for both copper and zinc, suggesting competitive

kinetics for both reactions. No additional peaks were observed with copper or nickel catalysts in the absence or presence of furfural (Fig. A4.4).

4.3.3 Electrolysis with zinc in 0.5 M $NaHCO_3$ at -0.7 V/RHE

Figure 4.3a shows the variation of current density with time during a two-hour potentiostatic electrolysis of zinc in bicarbonate electrolyte at -0.7 V/RHE. The initial current density of ~22 mA/cm^2 increases for 3 minutes, reaching 26 mA/cm^2. This can be due to an initial period of activation which may involve slow adsorption of furfural on the electrode or reduction of any surface zinc oxides. After this period, the current density continuously decreases with time, reaching 1.3 mA/cm^2 after 120 minutes.

Typical gas chromatography (GC) of the reaction mixture containing furfural, FAL, and p-xylene (internal standard) are shown in Figure A4.1. Data are included for pre- and post-electrolysis along with the post electrolysis cold trap sample containing MF. GC results are interpreted as conversion, yield, and FE in Fig. 4.3b. A steep increase in conversion occurs during initial electrolysis. In contrast, the relatively small yield and FE of MF were assayed only at the end of electrolysis.

The initial furfural concentration of 100 mM has been well studied in the literature [101,106,109,111,158,303] allowing for direct comparison of results. After two hours, furfural conversion of 88% was obtained with 40% yield of FAL. Yield and FE of MF was obtained as 3.5% and 13%, respectively. The zinc-catalyzed reaction maintained nearly constant faradaic efficiency, varying from 72 to 77% throughout the reaction, a demonstration of high selectivity towards furfural ECH over HER.

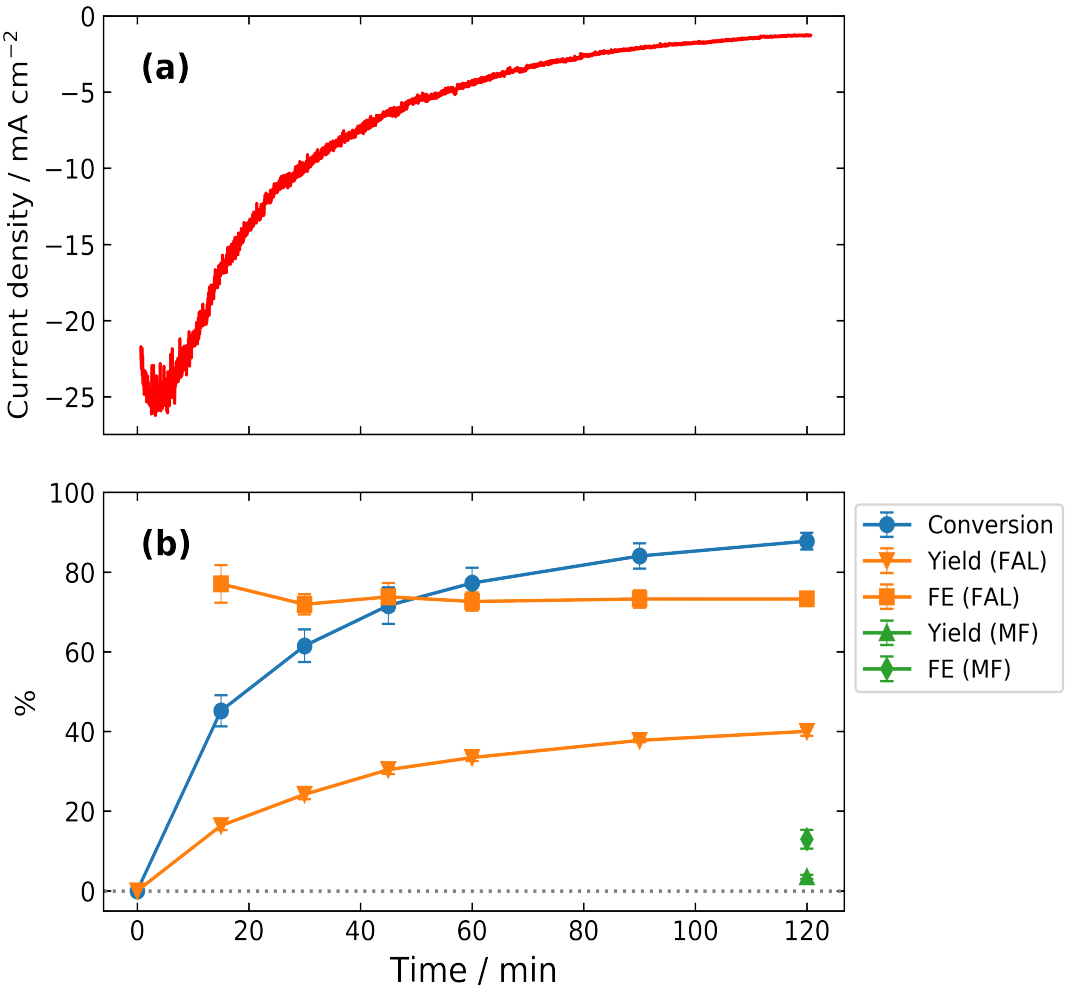

Figure 4.3 Potentiostatic electrolysis of furfural on zinc catalyst in 0.5 M $NaHCO_3$ at -0.7 V vs. RHE **a)** Chronoamperometry during electrolysis **(b)** Evolution of conversion, yield and FE of products.

4.3.4 Effect of electrolyte pH on the activity of zinc catalyst

Identifying the pH range that minimizes both HER and degradative side reactions can maximize product yield and FE for ECH. Potentiostatic electrolysis experiments were conducted in electrolytes of various pH using zinc catalyst, to observe the stability of furfural and its products at various pH. A high electrolyte concentration of 0.5 M was used for all the electrolytes, to minimize ionic resistance.

Electrolysis was performed -0.7 V/RHE for 2 h in 0.5 M electrolytes of the following composition and pH: sulfuric acid (H_2SO_4, pH = 0.5), sodium sulphate (Na_2SO_4, pH = 6), phosphate (Na_2HPO_4/NaH_2PO_4, pH = 7.4), sodium bicarbonate ($NaHCO_3$, pH = 8.4) and sodium hydroxide (NaOH, pH = 13.9).

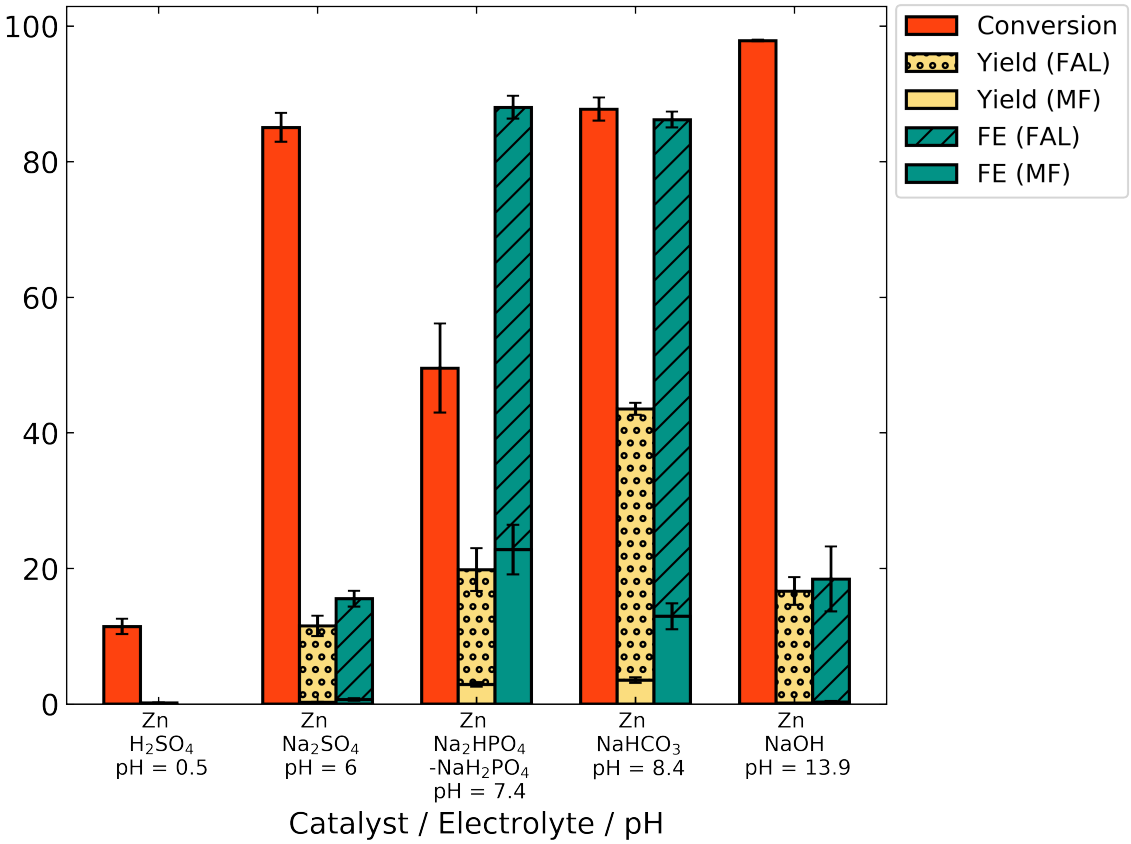

Figure 4.4 ECH electrolysis results with zinc catalyst at -0.7 V/RHE for 2 h in different pH electrolytes

Figure 4.4 shows the conversion of furfural and yield and FE of both FAL and MF after 2 h electrolysis at -0.7 V/RHE in different electrolytes. Yield and FE are displayed as stacked bars, to indicate the overall value as well as the contribution to furfuryl alcohol (FAL) and methyl furan (MF). The pH of the electrolyte significantly affected the product yield and FE. In acidic pH, the conversion of furfural after 2 h was only 11.5% which resulted in very low yields of MF (0.2%).

Such low conversion can be explained by higher proton concentration, favoring HER. No FAL product was observed in acid. However, the presence of MF, the hydrogenation product of FAL, suggests the degradation of FAL, possibly by resinification in acidic conditions [111]. MF may escape the degradation reaction in acidic electrolyte due to its lower aqueous solubility.

The open circuit potential of zinc in acid was measured as -0.61 ± 0.01 V/RHE (Figure A4.6). Thus, the observed current density obtained at -0.7 V was low (-0.25 ± 0.14 mA/cm^2) due to lower overpotential, leading to imprecise FE calculations. For this reason, FE values are not given for H_2SO_4 (pH 0.5) in Fig. 4.4.

In alkaline electrolyte (NaOH, pH 13.9), conversion was very high (98%). Still, yields of FAL and MF remain low at 16.5% and 0.1%, respectively. High conversion may result from minimal competition by HER. Low product yield, on the other hand, suggests that either furfural or the generated FAL degraded. Highly acidic and basic conditions have been reported to induce furfural polymerization reactions [109,302,306].

However, similar results were observed at pH 6 in Na_2SO_4 electrolyte, with high conversion (85%) and low yield (11.3% for FAL). This may indicate polymerization of furfural in neutral electrolyte as well. The buffer strength of the electrolyte may also play a role; pH measurements taken pre- and post-electrolysis show a significant pH shift for un-buffered Na_2SO_4 electrolyte (Fig. A4.6), suggesting that polymerization may take place at high pH.

An increase in yield and FE of products was observed as the pH was increased from 6 to 8 using buffered electrolytes. In 0.5 M phosphate (pH = 7.4) and bicarbonate (pH = 8.4) electrolytes, the yield of FAL was 17% and 40% for a conversion of 49.5% and 88%, respectively, which suggests reduced degradation and higher ECH efficiency in these electrolytes. Additionally, the highest FE for MF (23 %) was obtained in phosphate electrolyte (pH = 7.4).

The total FE obtained in phosphate electrolyte (88 %) was close to that obtained with bicarbonate electrolyte (86%). This suggests that a pH range of 7–9 could be optimum, to favor ECH over HER with minimal degradation. In our study, the highest FAL yield (40%) and FE (73%) were obtained in bicarbonate electrolyte at pH 8.4. As a control, a negligible change in furfural concentration (0.03 %) was observed over 2 h in bicarbonate electrolyte without any electrode (data not shown), which eliminates the possibility of non-electrochemical or autocatalytic polymerization reactions of furfural at pH 8.4. Thus, bicarbonate electrolyte (pH 8.4) was used for further studies.

In all the neutral pH range electrolytes, we observed that the pH of the reaction mixture increased during electrolysis. Cathode open-circuit potential (OCV) was also observed to shift to more negative potentials during electrolysis. We consider the change in OCV to be related to the increased pH, due to proton depletion. Figure A4.6 shows the change of pH and OCV during the two-hour ECH reaction in different pH electrolytes. Strong acidic H_2SO_4 (pH = 0.5) and basic NaOH (pH = 13.9) electrolytes did not show significant change in pH during the reaction because of low pKa and pKb values, respectively. H_2SO_4 (pH = 0.5) electrolyte also did not show significant change in OCV. However, the NaOH electrolyte did show a high change in OCV, possibly due to lower proton concentration. Among the neutral pH range electrolytes, Na_2SO_4 (pH = 6) showed the largest shift in both pH and OCV, which is expected as it is a non-buffered electrolyte.

ECH in buffered electrolytes (bicarbonate, phosphate) led to positive shifts in pH accompanied by negative shifts in OCV. We surmise that the lower magnitude of pH increase, and consequent OCV decrease, during ECH in these electrolytes is related to buffer capacity.

The buffer capacity of 0.5 M sodium bicarbonate and phosphate was calculated analytically using their respective equilibrium equations and disassociation constants and assuming electroneutrality (Figure A4.7). The resulting buffer capacity of phosphate (pH 7.4) was 0.27 M/pH and that of bicarbonate (pH 8.4) was 0.03 M/pH, largely due to the proximity of the nearest pKa (7.2 for phosphate, 6.4 for bicarbonate). The higher buffer capacity of phosphate explains its higher resistance to change in pH and hence, OCV.

4.3.5 Effect of applied potential on the activity of zinc catalyst in $NaHCO_3$

The activity of zinc in bicarbonate electrolyte was studied by potentiostatic electrolysis at the applied potentials of -0.6 and -0.7 V/RHE to determine the potential that would give the maximum conversion, yield and FE of the products (Figure 4.5). Less negative potentials, *i.e.* lower overpotential, is preferred to maximize energy efficiency. Potentiostatic electrolysis provides an

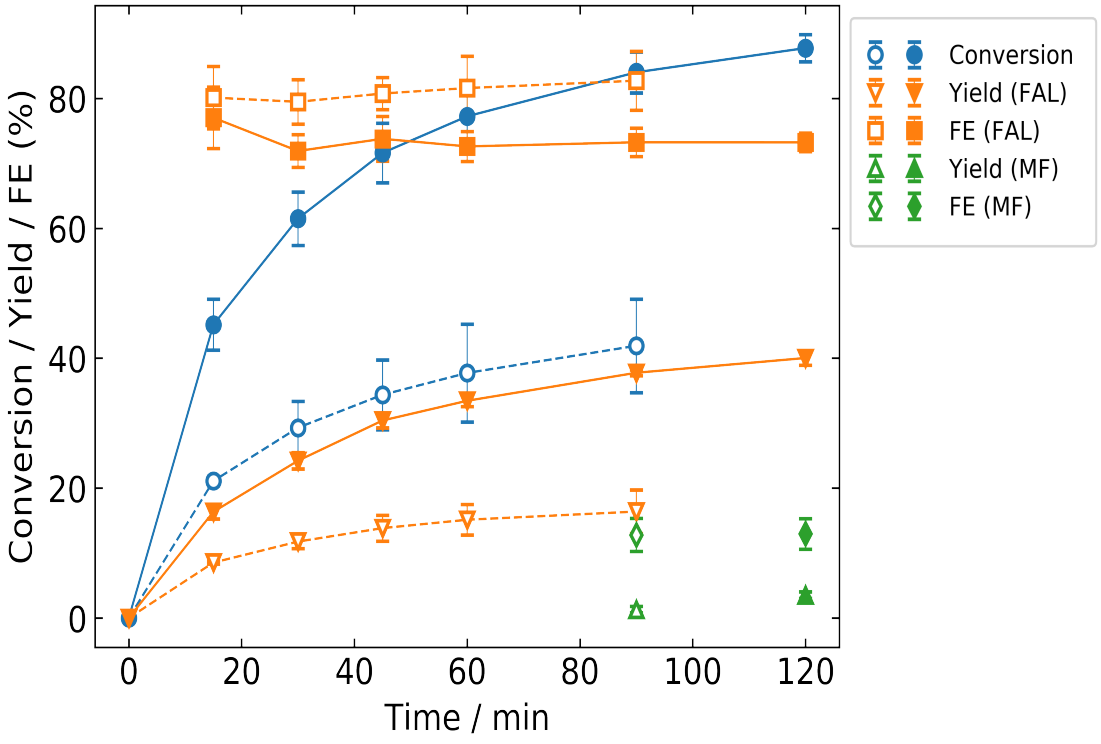

Figure 4.5 ECH electrolysis results with zinc catalyst in 0.5 M $NaHCO_3$ at different cathode potentials. Open symbols with dashed lines: -0.6 V vs. RHE. Closed symbols with solid lines: -0.7 V vs. RHE.

advantage over galvanostatic experiments in that the kinetics of the system can be studied with control over the potential, a significant thermodynamic driving force for the reaction.

As discussed previously, the open circuit potential of zinc during ECH in bicarbonate was observed to shift to more negative potentials as pH increases due to proton depletion (Fig. A4.6). Thus, potentiostatic electrolysis at -0.5 V/RHE would have resulted in positive oxidation currents over the course of 2 h resulting in the formation of zinc oxide or hydroxide on the catalyst cathode. Therefore, the potentiostatic electrolysis for ECH of furfural was performed at -0.6 V/RHE.

Even at -0.6 V/RHE, the current density became positive after 1.5 h of reaction. Thus, the reaction at -0.6 V/RHE was terminated after 1.5 h. Satisfactory conversion of furfural (41.9%) was obtained at -0.6 V/RHE potential with 16.4% and 1.3% yields of FAL and MF, respectively. The cell voltage when the ECH was conducted at -0.7 V/RHE was around 19 V, primarily due to the electrolyte resistance (data not shown). We did aim to carry out ECH at -0.8 V/RHE; however, the cell voltage exceeded the 20 V limit of our equipment. Thus, -0.7 V/RHE is the most negative potential reported here. The FE of MF remained almost the same at ~13% for both applied potentials, but the FE of FAL at -0.6 V/RHE (83%) was higher as compared -0.7 V/RHE (73%). Also, at both potentials, zinc maintains a nearly constant FE for FAL throughout the reaction. This suggests that zinc is an active catalyst for furfural ECH and does not degrade at these time scales. Higher conversion of furfural (88%) along with higher yield of FAL (40%) and MF (3.5%) were obtained at -0.7 V/RHE, so this potential was chosen for further studies.

4.3.6 Effect of different catalysts in $NaHCO_3$

After establishing the catalytic activity of zinc for the ECH of furfural at -0.7 V/RHE in 0.5 M bicarbonate (pH = 8.4), it was compared to the electrolytic activity of copper and nickel catalyst under the same reaction conditions (Figure 4.6). It was found that the catalyst had a tremendous effect on the reactant conversion, product yield and FE of the reaction. The main product was FAL in all the cases and MF was formed with low yields. Nickel catalysis resulted in 9% yield of FAL with FE of 18%. The highest yield and FE of MF was obtained with nickel catalyst as 5.7% and 20% respectively, indicating that nickel is more selective to MF formation in bicarbonate electrolyte as compared to copper and zinc. The yield of both the desired products was tremendously low on copper but the FE was fair (13.5% (FAL) and 18% (MF)). The highest reactant conversion for furfural (88%) and FE for FAL (73%) was obtained with zinc as a catalyst.

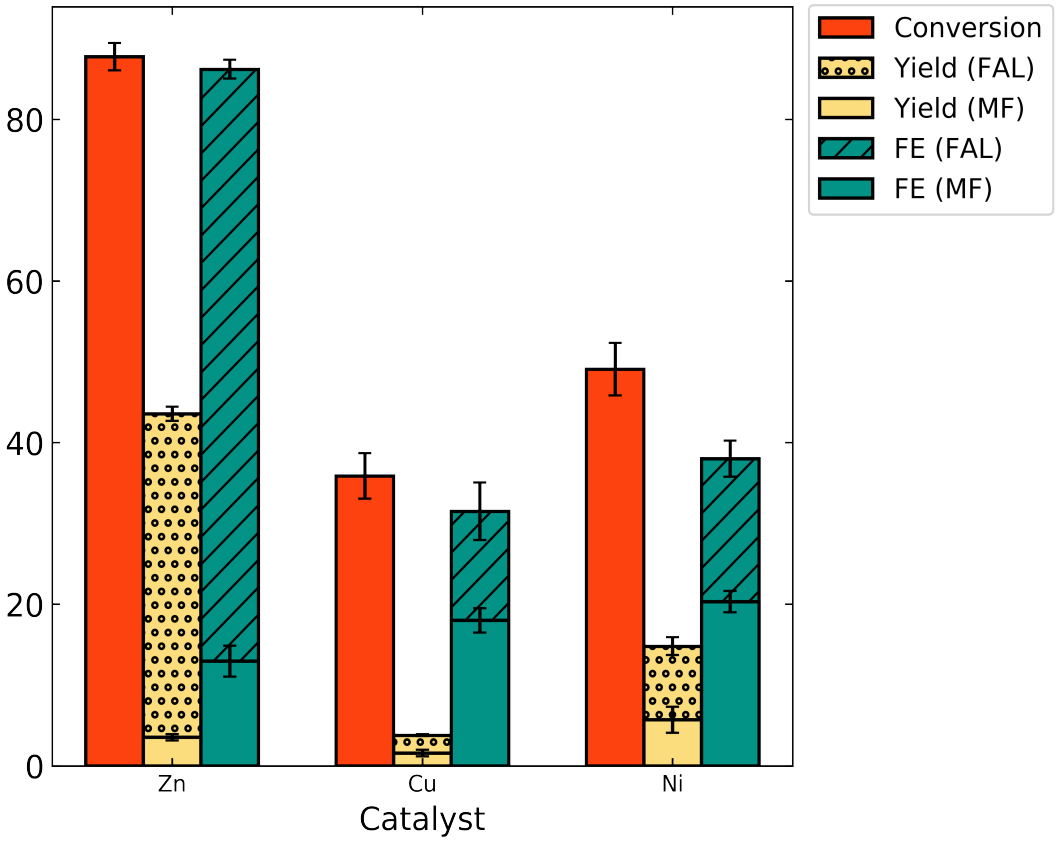

Figure 4.6 ECH electrolysis results with different catalysts in 0.5 M $NaHCO_3$ at -0.7 V/RHE.

To our knowledge, this is the highest FE of FAL that has been reported. Zinc was highly selective towards the formation of FAL, with 40% yield as compared to 3.5% yield of MF. This result is consistent with observations made by Jung and Biddinger in mildly acidic electrolyte where copper catalyst was more selective to FAL production as compared to MF [109].

The results obtained with zinc were also compared to the results obtained in the literature with copper and nickel catalyst. The plots of the activity of zinc catalyst compared to copper and nickel catalyst at varying pH in literature based on conversion, yield and FE of products are given in the Appendix (Figure A4.8). Higher conversions have been observed in the literature at acidic and basic pH (Fig. A4.8a) [8,101,106,109,111,158]. We have obtained 88% conversion with zinc at pH of 8.4 which is comparable to copper and nickel at a broader pH range (Fig. A4.8a). Yield and FE for MF have been observed to decrease with increase in pH in literature (Fig. A4.8d, A4.8e) [101,106,109,158]. In the neutral pH range, the highest FE for MF was obtained with zinc at 23% in phosphate (pH 8.4). The nickel catalyst achieved an MF yield of 5.7% at pH of 8.4, nearly same as that obtained at pH 1 (6%) [101]. The yields of FAL with zinc, copper and nickel were low at pH 8.4 as compared to the literature (Fig. A4.8b) [101,109,111]. However, FE of FAL with zinc at pH 8.4 was high as compared to literature results for all catalysts at varying pH (Fig. A4.8c) [8,101,106,109,111,158,303]. This signifies that zinc favors ECH over HER and suggests that a mechanistic role of zinc favors hydrogen transfer to furfural making it less available for H_2 formation.

For all catalysts, the yield of all products is less than the conversion of furfural, and the mole balance is not 100%; thus, there are side products formed during furfural ECH. GC-MS analysis of the reaction mixture revealed the presence of multiple side products formed during ECH. A GC chromatogram of the reaction mixture containing furfural, furfuryl alcohol, p-xylene (internal

standard) along with the side product peaks is provided in Appendix (Figure A4.9). In the figure, six side product peaks appear at high retention time (42-44 min). The mass spectra of each peak was obtained and compared to chemical compounds returned by the NIST library, based on similarity index (SI). All side product peaks generated same probable products, varying in similarity indices (Table A4.1). The most common match was alpha-furoin, with a SI of 80+ for all side product peaks.

A representative mass spectrum of peak at retention time 43.72 min is given in Figure A4.10. Based on GC-MS data, the side products formed during ECH are alpha-furoin (1,2-di-2-furanyl-2-hydroxyethanone) [307], hydrofuroin (1,2-di-2-furanyl-ethane-1,2-diol), 4-methyl-5-(2-methyl-2-propenyl)-2(5H)-furanone [308] and 1-(2-furanyl)-3-methyl-3-butene-1,2-diol. It is suspected that alpha-furoin and hydrofuroin are the primary side products that could be formed by electro-dimerization. 4-methyl-5-(2-methyl-2-propenyl)-2(5H)-furanone could be formed by ring opening and fragmentation of hydrofuroin. The formation of 1-(2-furanyl)-3-methyl-3-butene-1,2-diol during ECH is less likely.

Similar side reactions have been extensively investigated in the literature, where for example the formation of a pinacol product (hydrofuroin) has been identified, which occurs via coupling of furfuryl radicals formed after the first electron transfer process [100,106]. Such radical coupling inhibits subsequent electron transfer and formation of desired products (FAL and MF). The higher FE for FAL with zinc suggests that the second electron transfer required for the hydrogenation of furfuryl radicals is more facile for zinc as compared to electrodimerization. This also reflects the significant variation in catalytic specificity among the electrode materials.

4.3.7 Catalyst Characterization

Precipitates were observed on the electrode surface during electrolysis with zinc in the presence of furfural. The precipitates detached from the electrode and loosely settled at the bottom of the H-cell. Additionally, a mass loss of 0.8 ± 0.08% zinc catalyst was observed after ECH electrolysis. No precipitates or mass loss were observed during ECH electrolysis with copper and nickel catalyst. Additionally, no precipitates or mass loss was observed in Zn wire during a control electrolysis experiment with no furfural present at the same reaction conditions. This indicates that the formation of precipitates on zinc surface is observed only during electrolysis in the presence of furfural, even at negative potential. Similarly, Roylance and Choi observed roughening of Zn surface in SEM analysis after electrochemical HMF reduction at -0.9 V/RHE, which was attributed to surface restructuring due to the interactions between the Zn surface and HMF [114]. Furfural radical or hydroxyl anions formed during the ECH reaction may stabilize the oxidized form of zinc, leading to increased zinc dissolution and subsequent precipitation as zinc oxides [173,303]. Furfural has also been reported to act as stabilizing agent by forming an ion pair with the cationic species due to lone pair of electrons on carbonyl oxygen [220]. There is some question of whether the dissolved zinc participates in the ECH reaction.

A control experiment wherein the zinc electrode was polarized to -0.7 V/RHE in bicarbonate electrolyte (pH = 8.4) in the absence of furfural showed a lesser increase in pH (0.6) as compared to that during ECH (1.6, Fig. A4.6) over 2 h. This could be due to increased proton consumption as indicated by higher charge transfer during ECH as compared to HER [303].

Metallic zinc is known to easily oxidize in the presence of air and aqueous alkaline electrolytes [162,226,228]. Zinc passivates in aqueous bicarbonate solutions by formation of a zinc oxide surface layer with partial dissolution to form zinc hydroxide [309]. Zincate ion formation has also

been observed in zinc-air cells [310]. Thus, we expect these precipitates to comprise zinc oxides or hydroxides.

Surface composition of the pre- and post-electrolysis zinc wire along with zinc precipitates were analyzed by scanning electron microscopy with energy dispersive X-ray spectroscopy (SEM/EDS). The SEM images and EDS spectra are shown in Appendix Figures 4.7 and A4.5, respectively. Clean zinc wire yielded a surface composition of 91.6 wt% zinc with minor carbon (6 wt%) and oxide content (2.5 wt%, Table 3). The surface content of the post-electrolysis wire was 27.8 wt% zinc, 19.6 wt% sodium and 39.6 wt% oxygen. A 7 wt% increase in carbon content was observed in all post-electrolysis samples, which could be due to adsorbed organic compounds from the ECH reaction, contributing to electrode poisoning.

SEM images of the post-electrolysis catalyst wire showed particles of triangular morphology surrounded by agglomerated fine particles (Fig. 4.7b). EDS of one triangular particle was compared to that of the agglomerated particles. The triangular particle displayed almost equal zinc and oxygen content, of 36.3 wt% and 37.3 wt% respectively. This may be interpreted as zincate ($Zn(OH)_4^{2-}$), based on theoretical wt%. The agglomerated particles on post-electrolysis zinc wire contained 27.3 % zinc and 39.6 wt% oxygen, which is still close to the theoretical wt% and is therefore likely zincate as well. In comparison, precipitates showed higher zinc content (57.4 wt%)

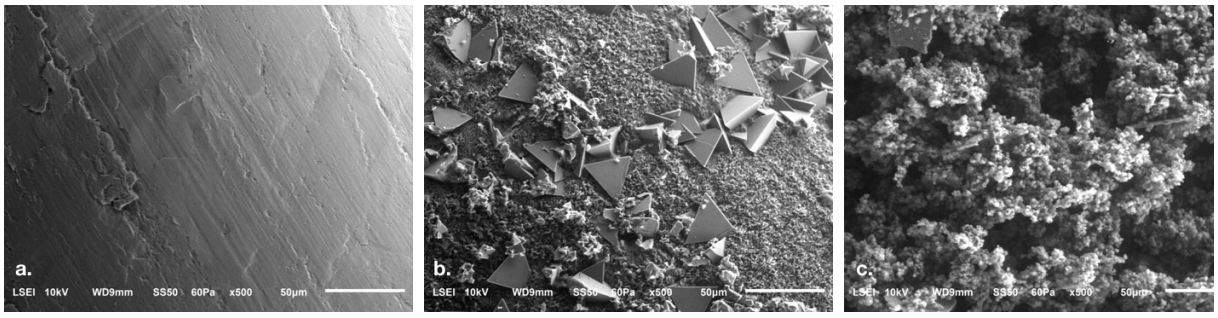

Figure 4.7 SEM images of the (a) pre-electrolysis zinc wire (b) post-electrolysis zinc wire (c) Zinc precipitates.

with 30.6 wt% oxygen and minor traces of sodium (4.7 wt%). This result suggests that the precipitate is primarily zinc hydroxide (based on theoretical wt%).

Table 4.3 Catalyst content (wt%) of Pre- and Post-Electrolysis zinc wire, and precipitates

Element	Pre-electrolysis	Post-electrolysis			Precipitates
		Overall	Triangle Particle	Agglomerated Particle	
Zinc	91.6	27.8	36.3	27.3	57.4
Sodium	-	19.6	15.7	21.1	4.7
Oxygen	2.5	39.6	37.3	39.6	30.6
Carbon	6	13	10.6	12	7.3

The high activity of zinc for ECH over HER implies that there could be a mechanistic role of adhered oxidized zinc precipitates that favors hydrogen transfer to furfural making it less available for H_2 formation. The high concentration of zincate ions in the vicinity of electrode surface as compared to bulk solution leads to their deposition on electrode surface [311]. At saturated concentrations, soluble zincate ions precipitate out as insoluble zinc oxide [310,312]. Burch et al. reported that zinc oxide catalyst acted as a reservoir for atomic hydrogen and promoted hydrogen spillover towards copper to catalyze methanol synthesis from H_2 and CO_2 [313]. The presence of oxidized layer on the zinc metal surface has been proposed to enable stabilization of adsorbed intermediates, thus promoting higher product selectivity [165].

Based on the above discussion, Figure A4.11 shows a proposed mechanism, wherein zinc oxides provide adsorption sites for protons, which gets reduced to adsorbed hydrogen on the zinc metal by Volmer reaction (Eq. 1.13). Zinc is an oxophilic metal that promotes carbonylic aldehyde group coordination of organic compound on its surface [60,61]. Thus, furfural could adsorb on metallic zinc. Zinc is reported to form a loose passive zinc oxides layer on the surface at alkaline pH [309,310], which could facilitate proton association with electronegative oxygen. From there, hydrogen may adsorb to the metal surface, and react with adsorbed furfural to produce FAL and MF. The remaining steps shown for hydrogenation to FAL, and MF are based on the literature for

chemical hydrogenation of furfural to FAL and MF [15,24]. There is still a question of whether both furfural and hydrogen adsorb on zinc oxides, which requires further mechanistic investigation. Thus, there is scope for further studies to fully elucidate the electrocatalysis of ECH by oxidized zinc.

4.3.8 Kinetic Analysis

In principle, potentiostatic electrolysis enables chronological data to be fit to kinetic models, which is more difficult in the case of constant-current data. Initial time-dependent furfural concentration data for different catalysts and varying potential in bicarbonate electrolyte was fitted to a first order rate law using a nonlinear least squares procedure. As shown in Figure 8, the first-order model does not fit the data over the entire period of electrolysis. This is likely due to catalyst surface modification or poisoning by reaction byproducts, which is consistent with the presence of increased carbon content after electrolysis, as observed by EDS (Table 3). Instead, we took the initial reaction rate by fitting the first order model to the initial data points, between 0 and 30 min.

The experimental and fitted concentration profiles are given in Figure 4.8. The fit was found to be good, with an R^2 value of varying from 89 - 97%, for different cases. The highest rate constant for ECH of furfural was obtained for zinc catalyst at -0.7 V/RHE as 0.42 /h.cm^2 (Table 4.4). As expected, the rate constant of zinc at -0.7 V/RHE was over 60% higher than zinc at -0.6 V/RHE.

Table 4.4 Rate constants for ECH of furfural in 0.5 M $NaHCO_3$.

Catalyst	Potential (V/RHE)	k (1/h.cm^2)	R^2
Zinc	-0.6	0.15 ± 0.01	0.93
Zinc	-0.7	0.42 ± 0.02	0.97
Copper		0.13 ± 0.01	0.89
Nickel		0.19 ± 0.02	0.90

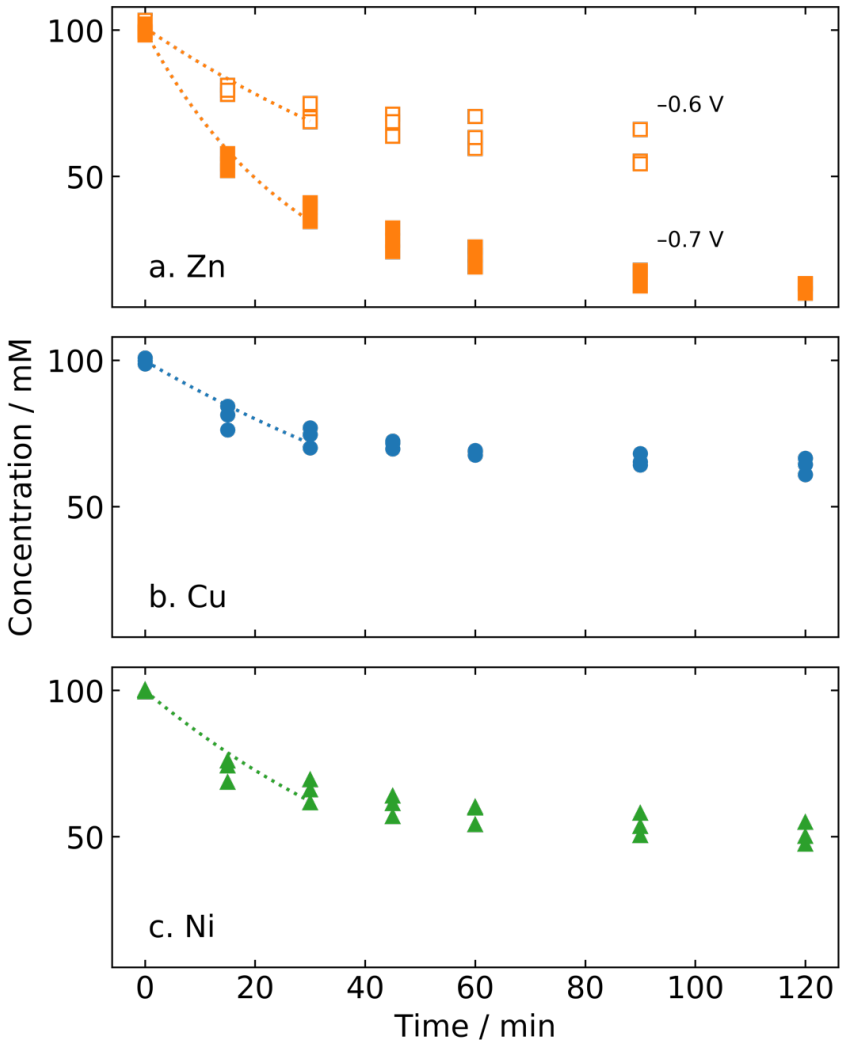

Figure 4.8 Experimental furfural concentration profiles during electrolysis in 0.5 M $NaHCO_3$ with (a) Zinc catalyst at -0.6 and -0.7 V vs. RHE; (b) Copper catalyst at -0.7 V vs. RHE; (c) Nickel catalyst at -0.7 V vs. RHE. Curves represent fitting of initial reaction rate (0–30 min) to a first order rate law.

The rate constant for copper and nickel were found to be similar. As seen in Figure 4.6, the activity of copper and nickel in terms of conversion of furfural did not show significant difference. The rate constant of zinc at -0.7 V/RHE was found around 55% higher than copper and nickel. By this measure, therefore, zinc is comparatively better catalyst for ECH of furfural.

4.4 Conclusion

Electrochemical hydrogenation of furfural to FAL and MF was studied using various catalysts in multiple electrolytes of varying pH. The nature of the electrode material and electrolyte pH immensely affected the conversion, yield and FE to the desired products. Higher product yield and FE was obtained at pH 7.4 to 8.4 as compared to acidic and basic pH. FAL yield was high at high pH with MF formed at lower yields. Although, the yields of FAL and MF were low on copper and nickel, the FE was appreciable. The highest yield of MF was achieved with nickel as a catalyst.

The best activity was achieved using zinc as a catalyst on the basis 88% conversion, 40% yield and 73% FE of FAL in 0.5 M bicarbonate electrolyte for potentiostatic electrolysis at -0.7 V/RHE over 2 h. The total FE for ECH of furfural was obtained as 86% with zinc catalyst in bicarbonate electrolyte (pH = 8.4), which suggests that HER was restricted. The total FE of products obtained with zinc in phosphate (pH = 7.4) were close to those in bicarbonate (pH = 8.4). This emphasizes the role of proton concentration in neutral pH range electrolytes to inhibit HER, polymerization and electrodimerization reactions. Additionally, dissolution of zinc during electrolysis, only in the presence of furfural, suggests participation of dissolved zinc in the hydrogenation mechanism. Further investigations on the reaction mechanism for the role of zinc or oxidized zinc for ECH of furfural will help gain better insight into the reason for high activity of zinc for this reaction.

Chapter 5

Supported Zinc Nanoparticle Catalysts for Electrocatalytic Hydrogenation of Furfural

5.1 Introduction

As discussed in Chapter 4, Zn was found to have good activity for the ECH of furfural with higher FE for FAL and MF in 0.5 M $NaHCO_3$ electrolyte at -0.7 V/RHE. However, the yield of desired products was low based on the fractional conversion of furfural. Some side products, including electrodimerization products, were formed during ECH of furfural as identified by GC-MS. Thus, a way to increase the yield and selectivity is desired while maintaining higher conversion and FE.

Supported zinc nanoparticle catalysts can help to achieve higher conversion and rate of reaction as compared to bare metal due to high surface area to volume ratio. There have been few reports on the ECH of furfural wherein nanoparticle catalysts supported on a conducting surface such as activated carbon fiber (ACF) or on the bulk metal itself has led to enhanced catalytic activity, due to high exposed surface area compared to bare metal electrodes [158,216]. Zhao et al. compared the activity of impregnated and electrodeposited 3% Pt/ACF with the bulk Pt for the ECH of furfural [216]. The bulk Pt as well as the synthesized nanoparticle catalyst maintained the same selectivity to furfuryl alcohol (99 %) but there was ~75% increase in both conversion and FE of furfural ECH with the use of impregnated 3% Pt/ACF catalyst as compared to bulk Pt. The higher activity of the impregnated 3% Pt/ACF catalyst was attributed to high Pt surface area of 4 m^2/g and particle size of 2 nm. However, the total surface area of dispersed 3% Pt/ACF catalyst of 1862 m^2/g came largely from the blank ACF (2398 m^2/g).

Higher rate could also aid in increasing the reaction rate for the conversion of intermediate radicals in ECH of furfural to FAL and MF instead of forming dimerized furfural product,

depending on catalyst selectivity. Hence, it can be expected that higher conversion can be achieved using zinc nanoparticles. However, increased surface area could also lead to increase in production of hydrogen by-product by HER, which needs to be minimized. Bare zinc was found to be selective toward FAL and MF formation as compared to HER in previous studies, so we might expect zinc metal nanoparticles to maintain the same or higher FE as with bare zinc.

Jung et al. studied the activity of bulk copper and compared it to higher surface area nano- and microcrystalline copper catalyst particles electrodeposited on copper itself [158]. Higher furfural conversion was observed with electrodeposited Cu/Cu catalysts but the FE of FAL decreased at all the studied potentials of -0.5, -0.65 and -0.8 V/RHE. Nanocrystalline Cu/Cu showed ~ 20 % increase in FE of MF at -0.5 V/RHE as compared to bare Cu, but the FE decreased at -0.65 and -0.8 V/RHE. Overall, the bare as well as the electrodeposited Cu/Cu catalysts maintained high FE for ECH over HER. At near onset potentials for ECH, nanocrystalline Cu/Cu showed 2.4 times higher production rate of FA+MF as compared to bare Cu. At -0.8 V/RHE, FAL and MF production yields increased by 40 and 20 μmol/cm^2, respectively with electrodeposited copper catalysts [158] (Figure 5.1). The results for improved catalytic activity were attributed to surface roughness, and not to particle size or crystal structure. However, with increased surface roughness of micro- and nano-crystalline Cu/Cu, the increase in production rate and FE of hydrogen gas was much higher as compared to the desired products, FAL and MF. Thus, it is required to synthesize a nanoparticle catalyst that is more efficient to FAL and MF production by ECH as compared to HER.

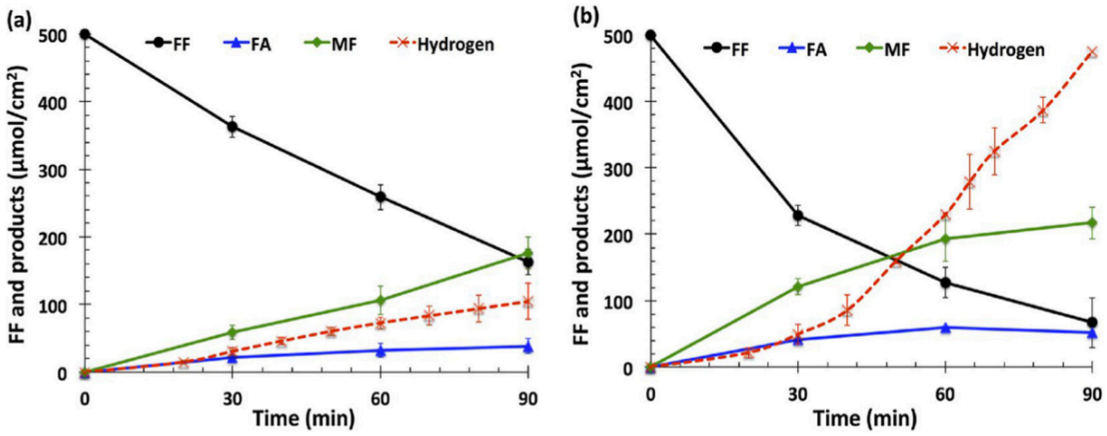

Figure 5.1 Consumption of FF, cumulative production of FA and MF from ECH of FF, and competitive H2 production from HER as a function of time at −0.8 V with (a) bare Cu and (b) Cu/Cu-400 nm (Reproduced from [158])

Zinc oxide catalysts have been used as an active phase, dopant or as a support for chemical hydrogenation of furfural [110,288,289,314–316]. Increasing the elemental ratio of Zn in the Cu:Zn:Cr:Zr catalyst lead to an increase in conversion during chemical hydrogenation of furfural to FAL [288]. The increased activity of zinc oxide catalyst has been mainly attributed to its role as a support enhancing catalyst nanoparticle dispersion, metal-support interactions, and porosity exposing more active sites [289,314,315]. Dong et al. characterized Cu/ZnO catalyst by NH_3-TPD and identified medium acidic sites in the catalyst, which might have resulted from ZnO support and could have an effect on achieving high FAL selectivity [110].

As discussed in Chapter 4, during electrolysis for the ECH of furfural with bare Zn as a metal catalyst, we observed oxidized zinc species on the metal wire after the reaction. At near neutral and basic pH, the oxidation of zinc is inevitable even at reducing potentials. Thus, the superficial zinc metal nanoparticle layer would be expected to oxidize to zinc oxide in-situ during the ECH reaction. Surface zinc oxide formed during the ECH of furfural was proposed to enable proton adsorption and hydrogen transfer to Zn metal nanoparticle for furfural hydrogenation, which would be advantageous for the reaction(Figure A4.11). Zinc and zinc oxide catalysts have been

extensively used for CO_2 reduction reactions (CO2RR) to CO, wherein nanostructured metal catalysts have helped to achieve better product selectivity as compared to bulk metal electrodes [165,226,228,238]. The majority of the work on zinc catalysis for CO2RR has focused on electrodeposition as an efficient method to produce zinc metal nanoparticles with different morphologies, such as porous zinc [226,227], dendritic zinc [228], hexagonal Zn [165], etc. Bulk zinc metal itself has generally been used to support zinc nanoparticles [165,226–228,238]. Details on the synthesis of zinc nanoparticle catalysts by electrodeposition were discussed in Chapter 1.

These electrodeposited nanostructured zinc catalysts have exhibited high activity for CO2RR over bulk Zn due to their high surface area, nanoscale morphology, prevalence of surface zinc oxide species and crystalline structure [165,226–228,238]. Electrodeposited porous and dendritic zinc catalysts show higher current densities and FE for CO2RR to CO than bulk zinc foil [227,228]. This suggested that the kinetics of CO2RR over porous electrodeposited Zn were higher than HER as well as CO2RR on bulk Zn foil. It was also reported that high surface area and morphology of zinc had an impact on the FE and product selectivity [227]. Higher activity of porous Zn for CO2RR was also reported to be related to the concentration of ZnO species on the catalyst [226]. The reduced ZnO catalysts were found to exhibit enhanced CO production rates at lower overpotential as compared to bulk Zn foil [226]. Won et al. found that rough Zn (101) facets arising from hexagonal Zn (h-Zn) exhibited higher selectivity and lower reduction potential for CO formation over smooth bulk Zn (002) facets, achieving 60 % higher FE for CO formation at -0.95 V/RHE than bulk Zn foil [165].

Thus, we think that zinc nanoparticles can help to achieve higher yield, selectivity of FAL and MF due to high surface area, roughness and varied crystalline structure as compared to bare zinc. Also, higher conversion and similar FE for ECH of furfural could be achieved at a lower

overpotential when nanoparticle catalysts are used because of the increase in the number of catalytic active sites. Thus, ECH of furfural using supported Zn nanoparticle catalysts has been studied using the pH conditions optimized for bare Zn metal, as described in Chapter 4. This allowed us to directly compare the results with electrodeposited Zn to bare Zn in terms of current density at a given potential, conversion, yield and FE for FAL and MF.

5.2 Experimental methods

5.2.1 Chemicals

The following chemicals were procured from reputed vendors: zinc chloride (≥ 98 %, Sigma Aldrich), hydrochloric acid (HCl, 12.1 M, 36.5-38 %, EMD Chemicals). The rest of the chemicals: furfural, FAL, MF, ACN, p-xylene, $NaHCO_3$, Na_2SO_4 were used as described in Chapter 4. All the electrolytes were prepared in deionized water (≥ 18 MΩ cm, Ward's Science). All the chemicals were used per se without any further purification.

5.2.2 Electrodes

Bare zinc metal wire was used as a substrate/support for electrodeposition of zinc metal nanoparticles. It was pre-treated prior to use in each experiment by rubbing with sandpaper to remove surface oxides followed by rinsing with ethanol and DI water. The geometric surface area of the bare zinc substrate was chosen as 1 cm^2 for voltammetry and 5 cm^2 for electrolysis experiments, which allowed direct comparison to previous work results with bare Zn wire (Chapter 4).

For electrodeposition experiments, silver-silver chloride (Ag-AgCl) and 25 cm^2 carbon paper (5 cm length, 5cm breadth, Toray) were used as reference and counter electrode, respectively. For electrolysis experiments, a reversible hydrogen electrode and graphite rod were used as reference and counter electrode, respectively, as detailed in Chapter 4.

5.2.3 Experimental setup

The electrodeposition experiment was conducted using a three-electrode system connected via a VSP Bio-logic SA potentiostat. 150 ml of 0.2 M zinc chloride solution (pH = 6.2 ± 0.06) was used as a precursor for zinc metal nanoparticle synthesis. 0.2 M zinc chloride solution was found to be colloidal, which could be due to the formation of zinc oxychlorate species [317]. Zinc chloride was completely dissolved by adding 40 μL of hydrochloric acid, which resulted in solution pH of 4.5 ± 0.2. The reaction was maintained at 50 ± 3 °C temperature and 900 rpm rotation speed using a hot plate, with the temperature monitored using a thermocouple. The on-center distance between the working and counter electrode was measured as 0.5 ± 0.1 cm. Electrolyte pH was measured pre- and post-electrodeposition using a pH meter (Fisher Scientific, Accumet Basic AB15). The solution was purged with nitrogen during the synthesis experiment to maintain oxygen-free conditions that would help in achieving zinc metal formation avoiding oxides. The experimental set-up used for electrolysis is the same as described in Chapter 4.

5.2.4 Electrochemical techniques

Transient experiments (CV and SV) were performed to analyze faradaic current density with and without furfural to test the dominance of ECH of furfural as compared to HER with electrodeposited Zn/Zn catalyst. CV and SV test conditions were as described in Chapter 4, and thus the results were directly compared to bare Zn wire for HER and ECH. Potentiostatic electrolysis was performed at -0.6 V/RHE for 2 h in 0.5 M $NaHCO_3$ electrolyte with the electrodeposited catalyst, as experiments at -0.7 V/RHE were not possible due to a compliance voltage limit of the instrument (20 V). Thus, electrolysis results with bare zinc wire at -0.6 V/RHE under same conditions were used for comparison (Chapter 4).

5.2.5 Reaction analysis

The progress of furfural ECH reaction during electrolysis was analyzed using gas chromatography, the details of which are highlighted in Chapter 4.

5.2.6 Catalyst characterization

The Zn nanoparticle catalyst was characterized before and after ECH of furfural electrolysis to analyze catalyst composition, morphological stability and zinc oxidation state. Characterization results can help in determining probable catalytic active sites to elucidate reaction mechanism. SEM/EDS was conducted to study the morphology and chemical composition of the synthesized Zn nanoparticles using the procedure described in Chapter 4. The crystalline structure of the synthesized zinc particle catalyst was examined using X-ray diffraction (XRD) using a Bruker Davinci D8 Advance Diffractometer. For XRD analysis, Cu Kα radiation (wavelength = 1.54 A°) at 40 kV and 40 mA. Measurements were taken in steps of 0.02º and 18.2s step time from 2θ = 5–110º. Surface area and porosity analysis of the zinc nanoparticles was done by N_2 physisorption at -196 °C on Micromeritics ASAP instrument, Micromeritics, USA. Before the analysis, the samples were degassed under vacuum at 100 °C for 4 h to remove any adsorbed species.

5.3 Results and Discussion

Zn nanoparticle catalysts were synthesized by electrodeposition and characterized by SEM, EDS, XRD and BET to verify desired metallic phase, determine morphology and surface area. Preliminary electrochemical studies to test the performance and selectivity electro-deposited zinc in the potential range of -0.6 to -1 V/RHE were done using CV and SV. The activity of zinc nanoparticle catalyst for ECH was screened on the basis of FE, conversion and selectivity towards the desired products measured by potentiostatic electrolysis. All the results were compared to activity of bare zinc at the same experimental conditions.

5.3.1 Catalyst synthesis

Zinc metal nanoparticles were electrodeposited galvanostatically on bare zinc wire from zinc chloride solution using current density of -20 mA/cm^2 for a total synthesis time of 3 h [165]. Depending on the geometric surface of the bare substrate zinc wire electrode during electrodeposition, the yields of deposited zinc varied. For 1 cm^2 wire, the yield was 0.065 ± 0.002 g for a charge transfer of -216.2 C/cm^2, corresponding to a FE of 88.2 ± 2.3 %. For 5 cm^2 wire, the yield of deposited zinc was found as 0.23 ± 0.01 g for a charge transfer of -1080 C/cm^2, which resulted in a FE of 62.3 ± 2.4 %. The variation in FE of the electrodeposition could be due the mass transfer effects for a 1cm^2 straight wire as compared to 5 cm^2 spiral wire. Figure 5.2 shows a representative potential vs time profile during the electrodeposition synthesis on 5 cm^2 wire with the potential varying from -1.15 V/Ag-AgCl to -1.1 V/Ag-AgCl until the end of synthesis. At the end of experiment, electrodeposited Zn metal particles supported on bare Zn wire were gently washed with DI water and ethanol. The catalyst was vacuum dried at 80 °C for 12 h, to avoid any air oxidation. The as-dried electrodeposited wires were used for experiments.

In order to achieve higher yield of deposited nanoparticles to perform characterization, electrodeposition experiment with 5 cm^2 was scaled up keeping the current density same as -20 mA/cm^2 but experiment extended to 5 h. The yield obtained under such experimental conditions was 0.41 ± 0.04 g for a charge transfer of -1800 C/cm^2, which resulted in a FE of 65.6 ± 5.6 %. The washed and dried Zn metal particles obtained from electrodeposition were scraped off from the wire and used for characterization to make sure that there is no background signal from the zinc wire substrate in analysis.

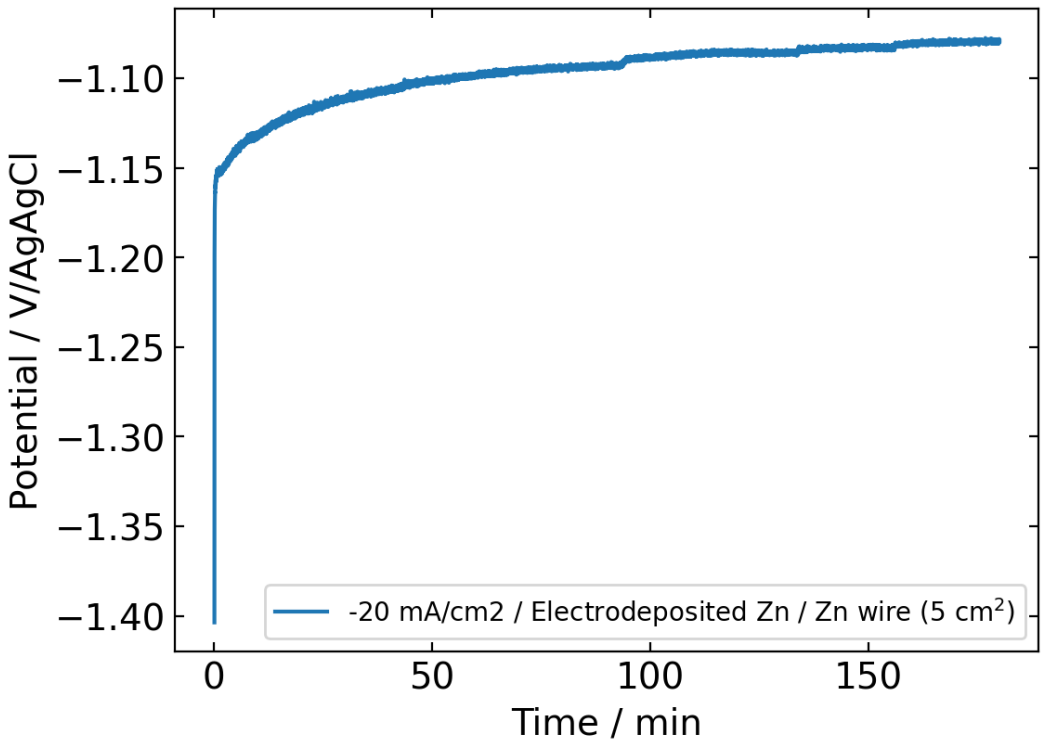

Figure 5.2 Variation of potential with time during zinc catalyst electrodeposition

For the purpose of characterization comparison, in order to determine the effect of zinc precursor for electrodeposition, we also synthesized zinc particles using 0.05 M zinc nitrate solution by applying multistep potentials at -1 and -2.5 V/Ag-AgCl each at 3 sec over the period of 90 cycles [227]. This process was scaled up for XRD analysis by conducting potentiostatic deposition at -1.95 V/Ag-AgCl for 3 h to obtain 0.6 g of catalyst with 54 % FE. The particles derived from nitrate precursor did not remain strongly adherent to the substrate and thus, could not be used for electrochemical measurements.

5.3.2 SEM-EDS

Electrodeposited zinc particles synthesized from zinc chloride and zinc nitrate precursors were analyzed by SEM/EDS to determine resulting differences in morphology and composition (Figure 5.3 and 5.4). SEM analysis revealed the presence of fibrous morphology of zinc nanoparticles obtained from zinc chloride precursor (Figure 5.3a). The particles also show high amount of

macroporosity. Zinc particles obtained from zinc nitrate precursor showed agglomerated particles with little porosity (Figure 5.3b).

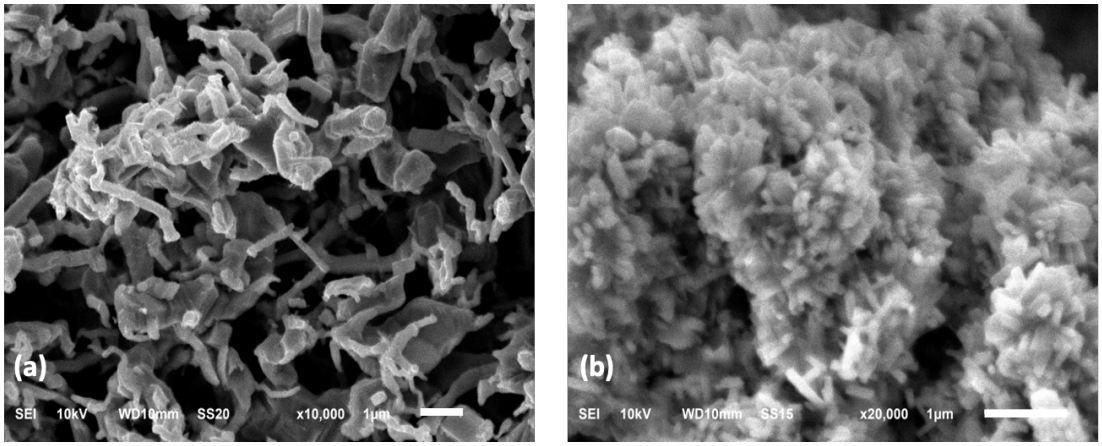

Figure 5.3 SEM images of electrodeposited zinc particles obtained using (a) zinc chloride, (b) zinc nitrate precursors

EDS analysis of zinc nanoparticles derived using zinc chloride precursor showed surface elemental composition of 97 wt% zinc and 3 wt% oxygen (Figure 5.4). Interestingly, the particles obtained from zinc nitrate precursor contained 84 % zinc and 16 % oxygen content, which is close

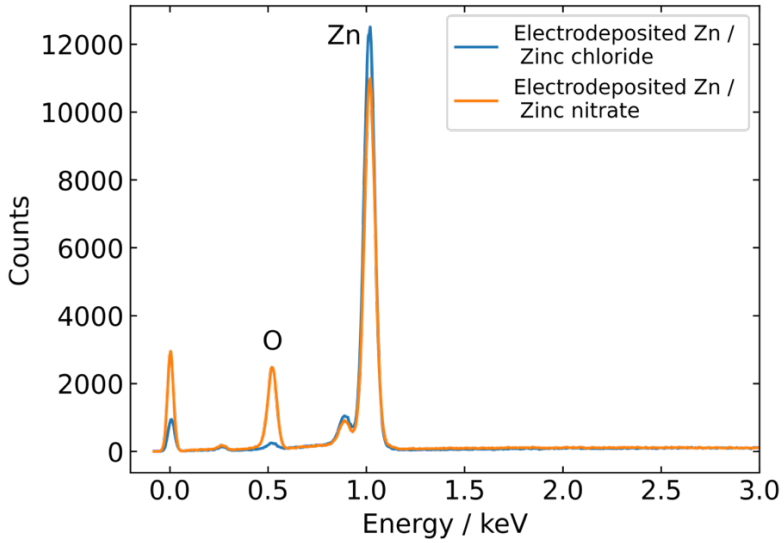

Figure 5.4 EDS spectra of electrodeposited zinc particles from zinc chloride and zinc nitrate precursors

to theoretical weight percentages of these metals in zinc oxide material (Zn (80 %) and O (19 %)). This signifies that nearly pure zinc metal nanoparticles can be obtained by electro-deposition from zinc chloride.

5.3.3 XRD

XRD spectra of electrodeposited zinc nanoparticles was recorded and compared to the reference zinc metal (JCPDS 00-04-0831) as well zinc oxide compound (JCPDS 01-082-9744) from the database (Figure 5.5). The spectral peaks at 2θ positions confirm that the crystalline structure of electrodeposited zinc nanoparticles obtained from zinc chloride matches that of pure zinc metal. Both the standard zinc metal and electrodeposited zinc nanoparticles from zinc chloride show the following peaks at 2θ values corresponding to lattice indices as: 36.2° (002), 38.9° (100), 43.2° (101), 54.3° (102), 70° (110), 70.6° (110), 77° (004), 82.1° (112), 86.5° (201), 89.9° (104), 94.9° (202), 109.1° (203). The peak at 11.2° is unidentified and could be related to some impurity. It was observed that in the electrodeposited zinc catalyst, the intensity of the peak at 2θ value of 43.2°, which corresponds to (101) facet has increased considerably as compared to standard zinc metal. This increase in (101) facet in electrodeposited zinc as compared to bulk zinc has also been observed by Won et al. [165]. Average crystallite size of the nanoparticles was calculated using the Scherrer equation and found to be 92 nm.

XRD spectra of chloride derived electrodeposited zinc nanoparticles contain all the peaks shown by zinc metal and does not contain additional peaks corresponding to zinc oxide. However, spectral peaks from electrodeposited zinc made from zinc nitrate precursor correspond to all the peaks found in the standard zinc oxide compound. This confirms that electrodeposition from zinc chloride precursor produces zinc metal and that from zinc nitrate yields zinc oxide. This also

suggests that 3 wt% oxygen found in the EDS analysis of chloride derived zinc particles would be due to surface adsorbed oxygen.

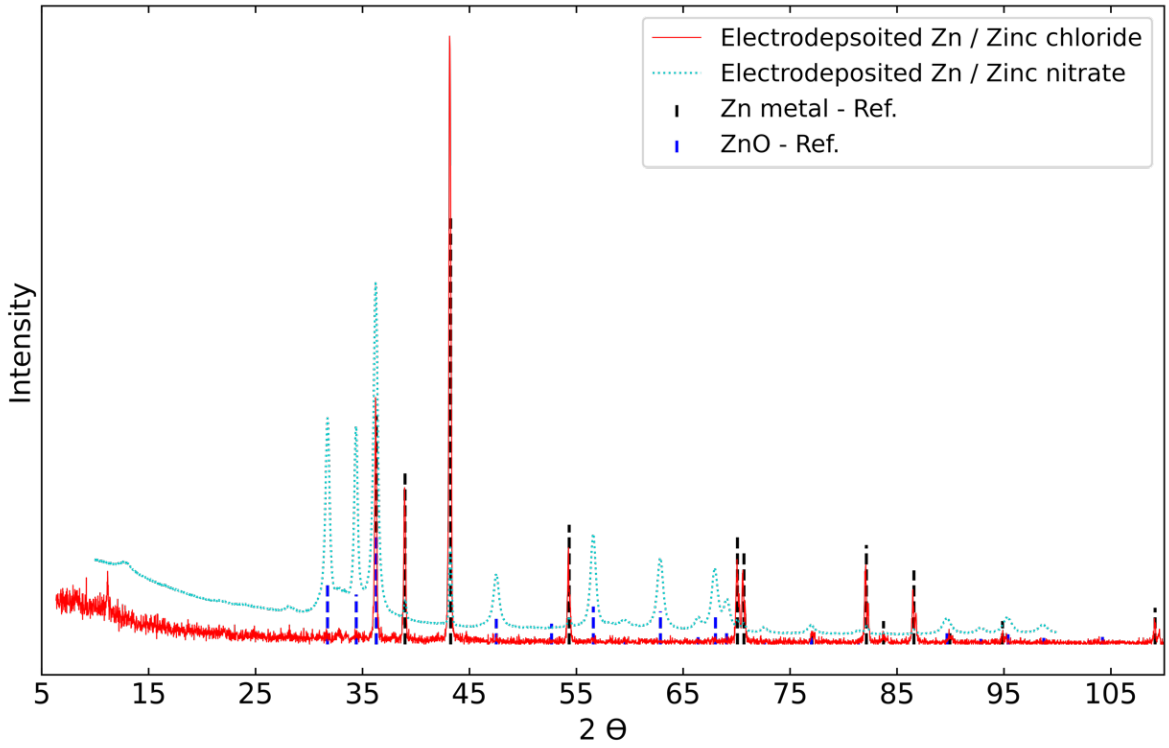

Figure 5.5 XRD spectra of electrodeposited zinc nanoparticles and reference zinc metal, zinc oxide compound from reference library

5.3.4 BET

BET surface area and pore size analysis of the catalyst was measured by nitrogen adsorption-desorption isotherms. The BET surface area of the catalyst was found to be 5.4 m^2/g with average pore size and pore volume as 16.5 nm and 0.02 cm^3/g, respectively. The catalyst exhibited type V isotherm with hysteresis loop of type H3 which signifies plate-like particle aggregates [5] (Figure 5.6). In terms of surface area of electrodeposited zinc as 5.4 m^2/g, considering the electrochemical roughness of bare zinc as 1, the roughness factor, can be calculated as 5.4.

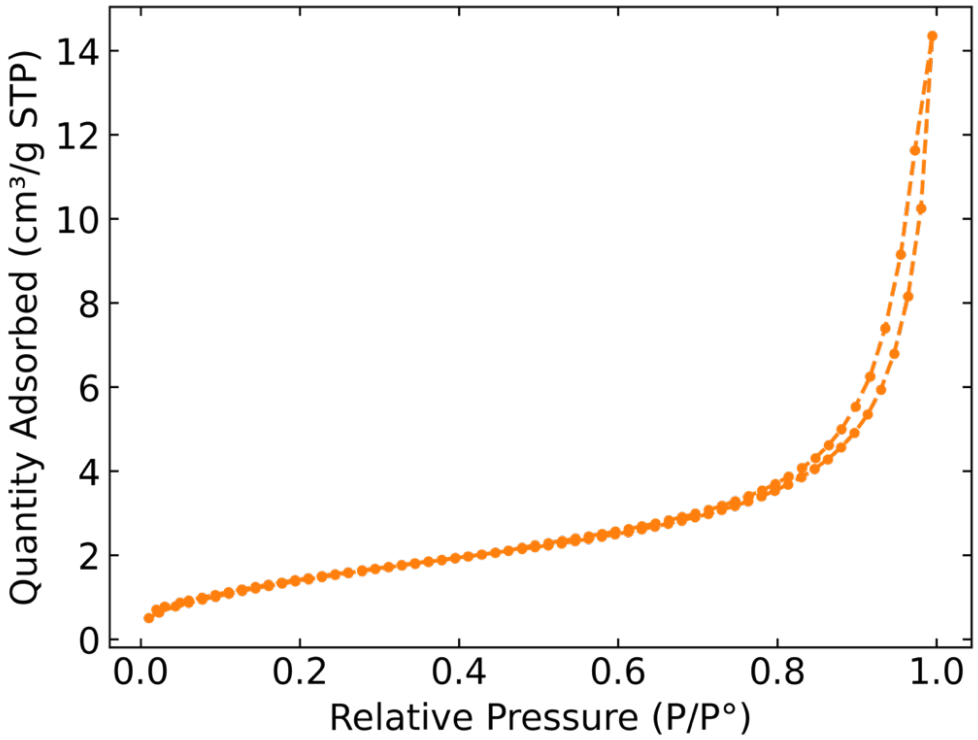

Figure 5.6 N_2 adsorption-desorption isotherm of electrodeposited zinc catalyst

5.3.5 Cyclic and steady state voltammetry

Preliminary tests to compare the electrochemical response of bare zinc with respect to electrodeposited zinc were performed using CV and steady state voltammetry (SV). Voltammetry data for bare zinc wire are the same as discussed in Chapter 4. CVs with electrodeposited zinc (Figure 5.7) in the presence of furfural showed similar rough peaks as with bare zinc (Figure A4.4), which could be due to zinc metal oxidation-reduction, even at negative potentials. They may also correspond to furfural and FAL hydrogenation to FAL and MF, respectively. Increased current densities with electrodeposited zinc catalyst for ECH and HER in comparison to bare zinc in CVs is similar to that obtained in steady state polarization curves, as discussed further (Figure 5.8).

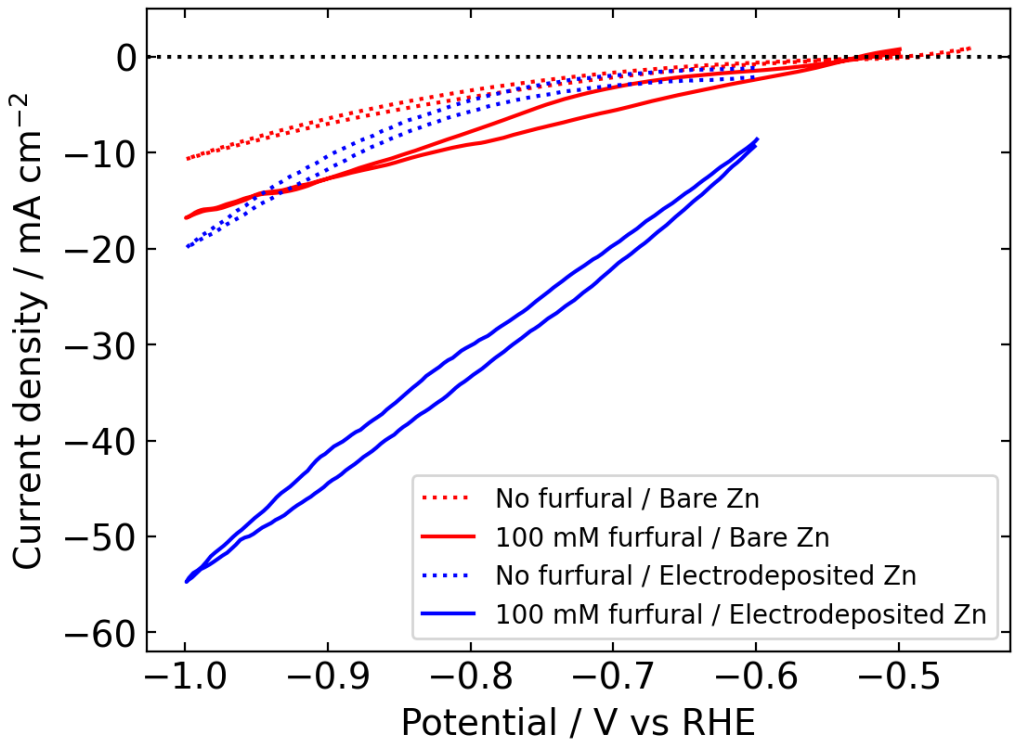

Figure 5.7 CV showing furfural ECH, and HER polarization curves obtained with bare and electrodeposited zinc catalysts in 0.5 M $NaHCO_3$

Figure 5.8 shows steady state polarization curves recorded in 0.5 M $NaHCO_3$ electrolyte in the absence and presence of 100 mM furfural, depicted by dashed and bold lines, respectively. With bare zinc, a higher current density was observed with the presence of furfural, which suggested ECH as a more dominant reaction as compared to HER. It was observed that the rate of HER nearly doubled with electrodeposited zinc as compared to bare zinc. This can be expected due to increase in surface area and roughness of the electrodeposited zinc catalyst. A very high increase in current density was observed after the addition of furfural which suggests a higher rate of ECH as compared to HER and thus, selectivity. In the presence of furfural, the current density obtained with electrodeposited zinc is nearly three times higher as compared to bare zinc at all studied potentials. However, based on roughness factor, we would expect nearly five times increased current density with electrodeposited zinc, which indicates mass transfer resistance during the

reaction. Additionally, the increase in current density after the addition of furfural is much higher in case of electrodeposited zinc catalyst as compared to bare zinc. At potential of -0.6 V/RHE in presence of furfural, ~350 % increase in current density is recorded with electrodeposited zinc as compared to bare zinc. This suggests that higher activity and selectivity for ECH of furfural can be expected with the electrodeposited zinc catalyst at these conditions.

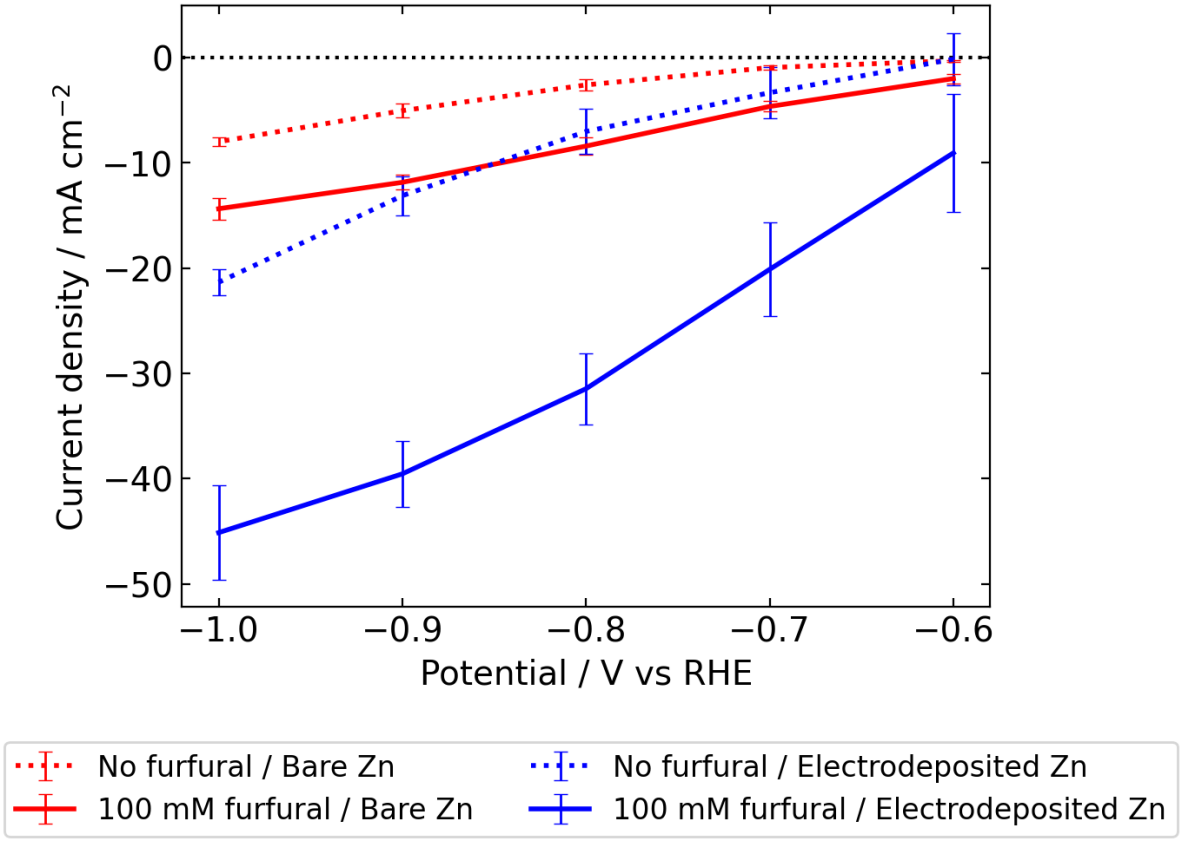

Figure 5.8 Furfural reduction and HER polarization curves obtained with bare and electrodeposited zinc catalysts in 0.5 M $NaHCO_3$

5.3.6 Electrolysis

Figure 5.9 shows the current density verses time profile at 0.6 V/RHE for bare and electrodeposited zinc catalyst during 2 h potentiostatic electrolysis in sodium bicarbonate electrolyte. It was observed that with the electrodeposited zinc catalyst, the current density starts at -36 mA/cm^2, much higher than the bare zinc, but decays quickly with time reaching -18 mA/cm^2 by 2 min, which is almost the same current density as for the bare zinc. Also, a period of increased initial current density that was attributed to furfural adsorption during furfural electrolysis with bare zinc (Figure 4.3), was not observed with electrodeposited zinc. This indicates that the rate of decay was much higher than the rate of furfural adsorption. After 2 min, although the current density decreased with time, at all-time points, the electrodeposited zinc maintains a higher reduction current throughout the 2 h electrolysis. Electrolysis on bare zinc was found to zero

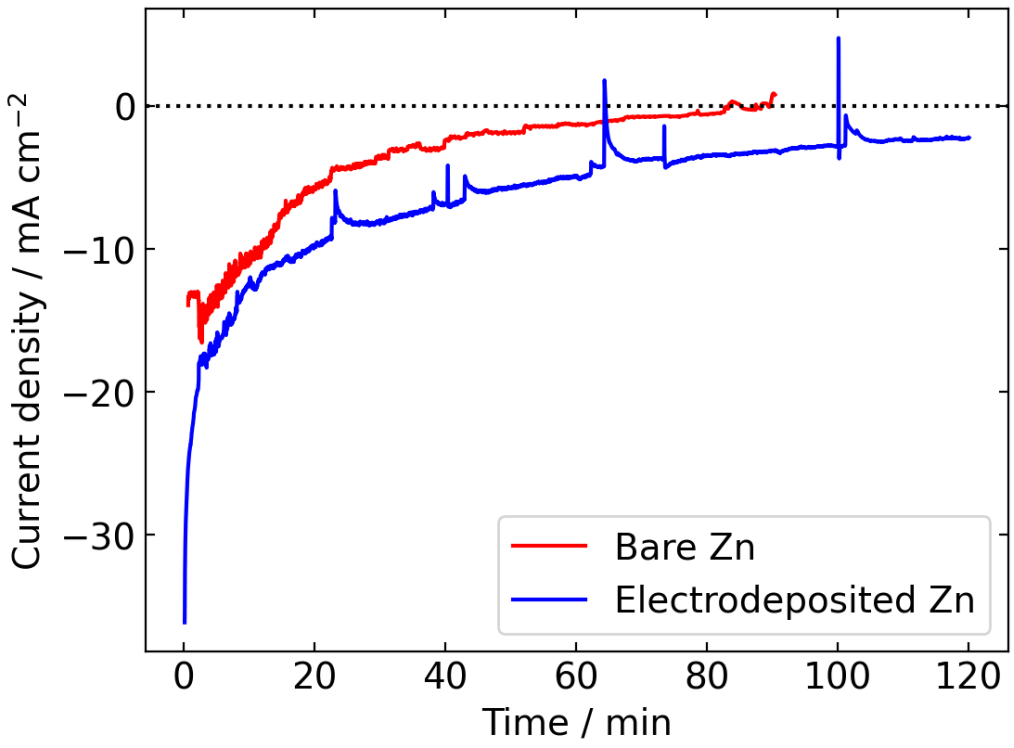

Figure 5.9 Chronoamperometry during potentiostatic electrolysis of furfural on bare and electrodeposited zinc catalyst in 0.5 M $NaHCO_3$ at -0.6 V vs. RHE

current after 1.5 h after electrolysis. Thus, it suggests that the electrodeposited zinc catalyst can maintain stable furfural reduction activity for a longer period as compared to bare zinc.

We did not observe any mass loss of electrodeposited zinc due to oxidation over the electrolysis as compared to 0.5 ± 0.2 % % loss with bare zinc wire. Instead, we observed a mass gain of 0.06 %, which could be due to oxide formation and bicarbonate salt adsorption from electrolyte. Also, no precipitates were observed. This suggests that despite surface oxidation to zinc oxide, the particles did not convert to zinc hydroxide precipitates, which further confirms the stability of electrodeposited zinc nanoparticles.

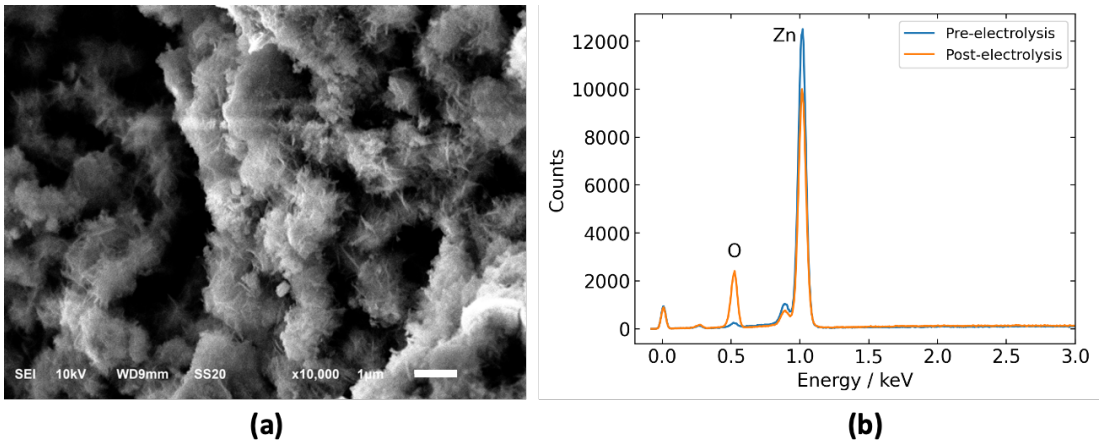

Figure 5.10 (a) SEM image of post-electrolysis electrodeposited zinc particles, (b) EDS spectra of pre- and post-electrolysis electrodeposited zinc particles

Surface oxide formation of post-electrolysis zinc particles was also analyzed by SEM-EDS. SEM images of the post-electrolysis zinc catalyst showed that fibrous morphology was lost but it still shows porous material (Figure 5.10a). It could be due to some surface reconstruction during electrolysis. Also, interestingly, EDS analysis of the used zinc catalyst showed surface content of 79 % zinc and 21 % oxygen, which corresponds to the theoretical weight percentage of these elements in zinc oxide compound (Figure 5.10b). Thus, it can be concluded that zinc metal oxidizes

during electrolysis which leads to change in surface morphology. It also suggests that zinc oxide could possibly have a role in reaction mechanism.

Figure 5.11 shows the variation of conversion, yield and FE as a function of time during the electrolysis. Figure 5.12 shows the final conversion, yield and FE obtained with bare and electrodeposited zinc. Since the results of electrolysis with bare zinc were acquired only over 1.5 h, the results with electrodeposited zinc were compared at that time point. MF yield, selectivity and FE were compared with 2 h samples since it is measured only at end of electrolysis (Figure 5.12). After 1.5 h, electrodeposited zinc catalyst (45.7 %) did not show an appreciable increase in

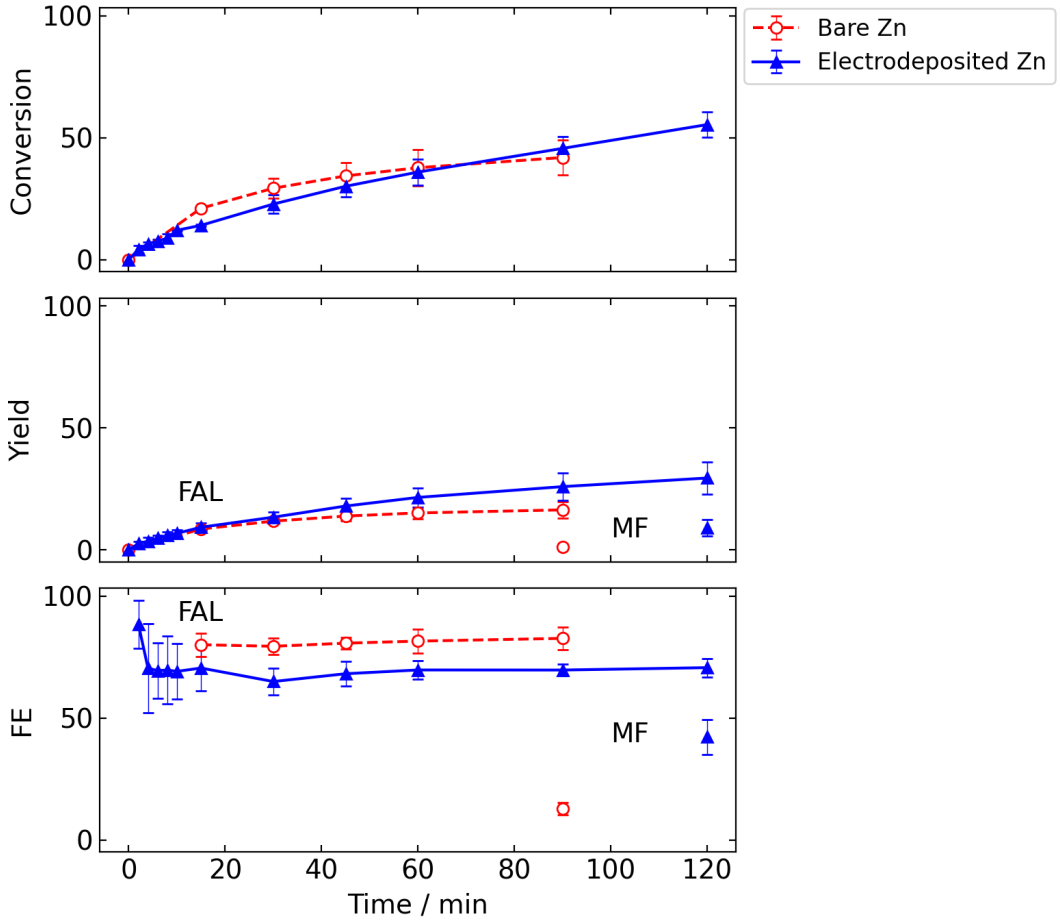

Figure 5.11 Evolution of conversion, yield and FE during potentiostatic electrolysis of furfural on bare and electrodeposited zinc catalyst in 0.5 M $NaHCO_3$ at -0.6 V vs. RHE

conversion as compared to bare zinc (42 %). This could be related to rapid decay in current density observed during electrolysis.

Interestingly, the yield of the desired products, FAL (26 %) and MF (9 % after 2 h) were higher as compared to bare zinc (FAL, 16.4 % and MF, 1.3 %). Increased yield with electrodeposited zinc can be attributed to the increase in surface roughness of the electrodeposited zinc, as has been observed by Jung et al. [158].

The FE of FAL (69.7 %) was found decreased as compared to bare zinc (82.7 %), but the FE of MF increased (42 %). Lower FE of FAL with electrodeposited zinc could indicate that it favored further conversion of FAL to MF rather than going to dimerized products. However, total FE of FAL and MF products was calculated as 112 %, a FE value higher than 100 % indicates imprecise

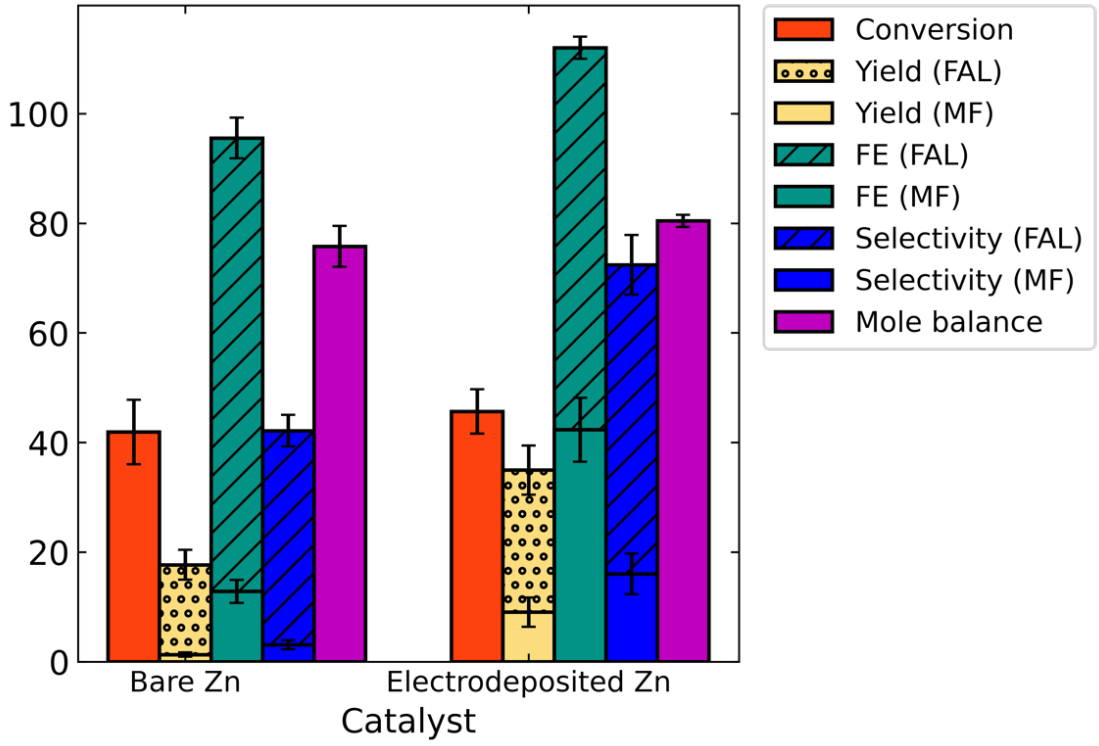

Figure 5.12 ECH electrolysis results with bare and electrodeposited zinc catalyst in 0.5 M $NaHCO_3$ at -0.6 V/RHE after 1.5 h

calculations or non-electrochemical side reactions. These results further need to be verified by

using internal standard calibration method to quantify methyl furan concentration. Electrodeposited zinc maintains nearly constant FE throughout the reaction, alike bare zinc, which further proves the efficiency of zinc as a catalyst for ECH of furfural over HER. This might also indicate the stability of the catalyst performance, despite surface oxidation, over 2 h electrolysis.

Also, with electrodeposited zinc, selectivity of FAL and MF was recorded as 56.4 % and 16 %, which are considerably higher than bare zinc (FAL, 39 % and MF, 3.1 %) (Figure 5.12). This would suggest that the electrodeposited zinc was more selective to FAL, and MF as compared to electro-dimerized products. It is also possible that variation in crystalline structure of electrodeposited zinc, marked by increase (101) facets as compared to bare zinc has a role in increased selectivity to FAL and MF formation, as has been observed by Won et al. for selectivity to CO formation compared to HER [165]. Higher selectivity was further indicated by mole balance, which closed at 80 % for electrodeposited zinc as opposed to 76 % with bare zinc (Figure 5.12).

Thus, overall higher conversion, yield, selectivity, FE and mole balance was observed with electrodeposited zinc at -0.6 V vs. RHE in 0.5 M $NaHCO_3$. These results can be attributed to high surface area and roughness as well as to varied crystalline structure of the electrodeposited zinc, which might have increased rate of FAL formation and FAL conversion to MF, making them more selective to ECH than electrodimerization.

5.4 Conclusion

Electrocatalytic hydrogenation of furfural to FAL and MF was studied with electrodeposited zinc catalysts and its activity was compared to bare zinc at -0.6 V vs. RHE in 0.5 M $NaHCO_3$. Zinc particle catalysts were synthesized by electrodeposition using 0.2 M zinc chloride as precursor on bare zinc foil at -20 mA/cm_2 at 50 C. The nanoparticles were found to be of fibrous morphology

with elemental composition as 97 wt% zinc with the remainder oxygen. XRD confirmed the crystalline structure of the zinc metal nanoparticles. The catalyst possessed surface area of 5.4 m^2/g.

Steady state polarization curves indicated that higher current density and thus, more selectivity to ECH could be achieved with electrodeposited zinc catalyst as compared to HER and ECH with bare zinc. During potentiostatic electrolysis at -0.6 V/RHE, a higher and stable ECH reduction current density was obtained with electrodeposited zinc catalyst. Higher conversion (46 %), yield (FAL (26 %) and MF (9 %)) and FE (FAL (69 %) and MF (42 %)) was observed with electrodeposited zinc catalyst as compared to bare zinc. Higher selectivity to FAL, MF and mole balance during the reaction indicated that electrodeposited zinc was more selective to ECH as compared to electrodimerization. No zinc dissolution was observed but surface analysis of post-electrodeposited zinc nanoparticles showed the presence of zinc oxide. Further investigations on the role of zinc oxide catalysts for electrolysis can help in understanding reaction mechanism.

Chapter 6

Summary and Future Work

Work presented in this thesis is motivated by the need to investigate various pathways of biomass valorization, which offers a sustainable alternative to produce fuels and chemicals as compared to fossil resources to meet increased consumer energy demands, control CO_2 emissions in the so-called net zero economy, lower environmental footprint, and achieve carbon neutrality in the coming years. In the entire thesis, principles of green chemistry have been applied, including waste prevention (low E-factor), high atom economy, catalysis, use of renewable feedstocks, less hazardous chemical synthesis, safer solvents and design for energy efficiency. The conversion of triglyceride (vegetable oil) and cellulose/sugar derived feedstocks (furfural and HMF), was studied using heterogeneous chemo- and electro-catalytic selective synthesis methods to obtain value-added and industrially important chemicals for the polymer, perfumery, pharmaceutical and fuel industries.

To achieve desired reactions, various acid/base/metal catalysts were synthesized and screened for their activity based on conversion, yield, selectivity and Faradaic efficiency. In each chapter, a systematic evaluation of the effects of various reaction parameters on the catalytic activity and reaction rate was conducted to achieve the optimum experimental conditions to maximize catalytic activity. The catalysts were synthesized and characterized before and after the reaction to understand stability and reusability.

In Chapters 2, 4 and 5, two value added chemicals were simultaneously obtained from a single one pot cascade reaction, which aids in process intensification. Thus, overall this work provides new insights into catalyst and materials synthesis, careful evaluation of reaction conditions and

their optimization via observed effect on reaction based on conversion, yield, selectivity and Faradaic efficiency in order to design a successful biomass valorization reaction system.

Chapter 2 focusses on the study of chemical interesterification of soybean oil triglycerides with methyl acetate to co-produce valuable fuel, biodiesel and fuel additive, triacetin. Calcined Mg-Al hydrotalcite (Mg:Al mole ratio – 3:1) was found as the best catalyst for achieving 95.5 % conversion of soybean oil triglycerides in 4 h and yielding 5.3 % selectivity of triacetin along with the value-added intermediates - monoacetindiglycerides and diacetinmonoglycerides, produced with a selectivity of 46 % and 48.7 %, respectively. The optimum reaction conditions were found at an oil to methyl acetate mole ratio of 1:50, catalyst loading of 0.04 g/cm^3 and a temperature of 200 $^{\circ}C$. The catalysts were fully characterized before and after the reaction, and were found to possess high surface area with both basic and acidic sites. The concentration profiles of the reactants, intermediates and products obtained at different temperatures were used to obtain the kinetic rate constants and the activation energy of each parallel step was evaluated. Reusability studies showed that the catalyst was stable and reusable up to three cycles.

Overall, interesterification of triglycerides was found as a good alternative as compared to transesterification, to yield a higher value-added compound, triacetin, as a co-product instead of the already abundant commodity, glycerol. To further pursue this area, higher triacetin selectivity should be targeted at by driving conversion of intermediates towards end products. This can be achieved by using a catalyst that has a higher basicity (combined with intermediate acidity) as compared to the calcined Mg-Al hydrotalcite. Also, since higher temperatures favoured triacetin selectivity, reactors that can withstand temperatures higher than 200 $^{\circ}C$, for example fixed bed continuous reactors, can be used [76]. After successfully achieving higher triacetin selectivity combined with already achieved high triglyceride conversion and biodiesel yield, waste soybean

oil can be used as the feedstock with the optimized catalyst and reaction conditions, in order to make the triglyceride interesterification process more economical [63,318].

In Chapter 3, we explored the formation of an AMF fuel additive, 5-(2-hydroxyethoxy-methyl)furfural (HEMF) by etherification of bio-based platform chemical, HMF with ethylene glycol at high conversion and selectivity. Chemo-selective catalyst was desired to selectively synthesize HEMF instead of the acetalized product, 5-hydroxymethylfurfural ethylene acetal (HMFA). Metal substituted dodecatungstophosphoric acid supported on K-10 clay (M_x-DTP/K-10) catalysts were found to serve the purpose. The highest activity was achieved with 20 % (w/w) $Al_{0.66}$-DTP/K-10 as a catalyst yielding 98.9 % conversion of HMF with 96.6 % selectivity to HEMF. High selective to HEMF is attributed to the combined activity of Lewis and Bronsted acid sites in the Al substituted DTP/K10 catalyst. The effect of reaction variables was studied, and the optimum conditions were found to be speed of agitation of 1000 rpm, catalyst loading of 0.03 g/cm^3, HMF to ethylene glycol mole ratio of 1:30 and a temperature of 100 ^oC. The catalysts were characterized by various techniques and were found to be mesoporous with high surface area and acidity. Catalyst was found to be stable and reusable up to three cycles with resistance to acid site leaching. The reaction was kinetically controlled, and activation energy was calculated as 21 kcal/mol. Almost complete HMF conversion and high etherification selectivity yielded nearly pure HEMF product, which could be separated by vacuum distillation. Thus, this work provided a green and efficient way for upgrading HMF to valuable fuel with minimal downstream processing.

This study can be further followed up establishing the characteristic fuel properties of HEMF such as cetane number, octane number, viscosity, cloud point etc., which are not available in the literature. This can be done by using the methods developed in the literature for the testing of fuel additives: 5-methoxymethyl furfural and 5-ethoxymethyl furfural, which are monohydroxy

alcohol derived HMF ethers [319,320]. It would also be worthwhile to find a catalyst that does not produce acetalized product, HMFA and thus, is completely selective to etherification reaction. Also, different di- and tri-hydroxy alcohols can be used to produce high molecular weight branched AMFs, which might result in better blending and fuel properties as compared to other ethers [38,138].

Chapter 3 transitions this thesis towards electrocatalysis, where we studied zinc metal as a novel electrocatalyst for potentiostatic ECH of furfural to furfuryl alcohol (FAL) and 2-methylfuran (MF), products having applications in pharmaceutical, polymer and fuel industries. The activity of zinc was compared to other well-known catalysts, copper and nickel. The effect of electrolyte pH was studied, and it was found that electrolysis in near-neutral electrolyte (pH 6 to 8) showed increased yields and FE as compared to acidic and alkaline conditions. This result is attributed to optimum proton concentration in neutral electrolytes that restricts HER while minimizing side reactions. At neutral pH, the reaction was more selective towards FAL formation than MF. The best activity of zinc catalyst was obtained with 0.5 M sodium bicarbonate ($NaHCO_3$) electrolyte (pH = 8.4) at -0.7 V/RHE, yielding 73% FE for FAL and 86% FE overall. At these experimental conditions, higher conversion, yield and FE of desired products, FAL and MF were achieved with zinc as compared to copper and nickel catalyst. To the best of our knowledge, this is the highest FE for FAL that has been reported to date. Oxidized zinc species were found on the electrode following furfural electrolysis, which were suspected to be involved in possible reaction mechanism favouring proton transfer to furfural contributing to high activity of zinc for ECH.

Lastly, based on motivation of zinc as an efficient catalyst from Chapter 4, in Chapter 5, we studied the activity of zinc metal nanoparticles for furfural ECH, comparing it to our previous results with bare zinc. This work was done to achieve higher current density, furfural conversion,

and higher yield of FAL, MF with high surface area zinc metal nanoparticles. It was also desired to minimize furfural dimerization reactions, which reduce the selectivity to FAL, MF, and can further help to increase the FE of the furfural ECH reaction.

It was envisaged that post-electrolytic characterization will aid in elucidating reaction mechanism. Zinc metal nanoparticles were synthesized on zinc wire as substrate by electrodeposition using 0.2 M zinc chloride as precursor at -20 mA/cm^2 for 5 h at 50° C. SEM-EDS analysis revealed the presence of fibrous morphology of zinc particles with elemental composition of zinc in the material as 97 wt% and remainder oxygen. Steady state polarization curves depicted that in the presence of furfural, electrodeposited zinc obtained nearly three times higher current density as compared to bare zinc, with over 350 % increased current density at -0.6 V/RHE. Also, the relative increase in current density for ECH as compared to HER was much higher with electrodeposited zinc, which confirms their higher dominance to ECH as compared to bare zinc. Electrolysis results further confirmed that electrodeposited zinc catalyst obtained a higher conversion (46 %), yield (FAL (26 %) and MF (9 %)) and FE (FAL (69 %) and MF (42 %)) of desired products than the bare zinc. Higher selectivity and mole balance was achieved with electrodeposited zinc catalyst which indicates its selectivity to ECH as opposed to electrodimerization. Surface zinc oxide formation was observed on post-electrolysis zinc particles, which might play a role in reaction mechanism.

We believe that many novel and interesting contributions can be made to the work on ECH of furfural by finding efficient ways to quantify the intermediate radicals formed during the ECH reaction, which will be helpful in devising a reaction mechanism. For examples, spectroscopic methods to test intermediate radical and dimerized product formation, which have been identified in the literature [321], can be calibrated to calculate product concentration based on peak intensity.

It is also desired to test the activity of dissolved zinc for furfural ECH reaction. This might be achieved by using zinc salt-based electrolyte with a working electrode which does not have any activity for furfural ECH, to specifically test dissolved zinc catalysis. A more extensive empirical investigation that tests activity of zinc oxide as compared to metallic zinc will also aid in understanding the active species and role of zinc in the ECH reaction. For example, zinc precursors that result in strongly adherent zinc oxide particles deposition on a substrate or anodized zinc can be used as an electrode for furfural ECH reaction and the results can be compared to zinc metal activity [226,322]. At last, this process can be scaled up employing higher surface area zinc nanoparticle catalysts in a continuous electrolyzer to obtain high product yields and conversion efficiency. This system may also be applicable to ECH of other aldehydes, such as benzaldehyde, cinnamaldehyde to produce valuable products [321,323]. Zinc catalysis for ECH can also be extended to hydrogenation of aldehydes or ketones present in bio-oil for its upgrading and stabilization [47].

In summary, this work provides a guide to selective design of catalysts and chemicals by reaction engineering and process optimization. It significantly contributes to understanding of various catalytic biomass conversion processes to synthesize value-added fuels and chemicals with industrial applications. By way of biomass valorization, it adds value to the existing field of green chemistry for the design of processes using renewable feedstocks and catalysis. The results obtained in this thesis would be helpful in further process intensification of studied biomass conversion processes.

APPENDICES

APPENDIX A

Reaction Analysis, GC-MS spectra of products and concentration profiles

Reaction analysis

Triglycerides (T), monoacetindiglycerides (MA), diacetinmonoglycerides (DA), fatty acid methyl esters (F) and triacetin (TA) possess no conjugate structure and thus show poor UV absorption. Thus, UV detector was used at a very low UV wavelength of 205 nm. The gradient method of elution was used for analysis by passing different ratios of methanol and isopropyl alcohol-hexane (5:4, v/v) (Table A2.1). This method of analysis was adopted from the literature and a similar chromatogram was obtained [267]. The different fractions of mobile phase during the 21 min run could create a mixture of polar and non-polar mobile phase in the column. The time with high polar mobile phase could help in elution of slightly polar compounds – F, TA and DA and moderately non-polar mobile phase will help in elution of MA and T. The chromatogram of the reaction mixture based on this HPLC method is shown in Figure A2.1.

Table A2.1. Gradient method of elution of Methanol and isopropyl alcohol-hexane 5:4 (v/v)

Time (min)	A: Methanol; B: Isopropyl alcohol-hexane 5:4 (v/v)	
0	A = 100 %	B = 0 %
10	A = 50 %	B = 50 %
16	A = 50 %	B = 50 %
21	A = 100 %	B = 0 %

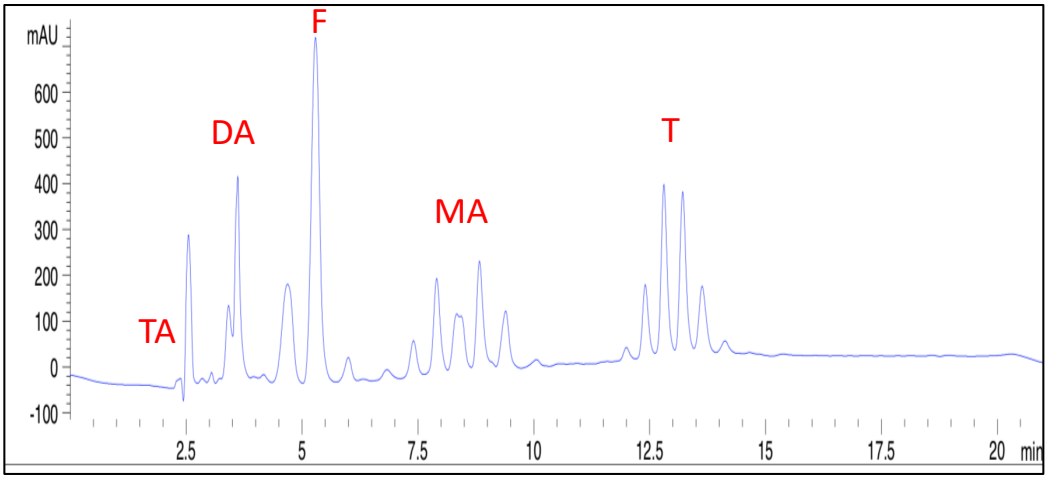

Figure A2.1 HPLC Chromatogram of a reaction mixture (Triglycerides (T), monoacetindiglycerides (MA), diacetinmonoglycerides (DA), fatty acid methyl esters (F) and triacetin (TA))

The total area under the peaks of soybean oil triglyceride (T), fatty acid methyl esters (F), monoacetindiglycerides (MA), diacetinmonoglycerides (DA) were used to calculate concentrations of these species based on the differential rate equations and mole balance equation as follows:

The net rate of consumption of methyl acetate (M) by three parallel reactions is given by the following equation:

$$-r_M = -\frac{dC_M}{dt} = w.\{(k_1 C_M C_T + k_2 C_M C_{MA} + k_3 C_M C_{DA}) - (k_1{}' C_F C_{MA} + k_2{}' C_F C_{DA} + k_3{}' C_F C_{TA})\} \quad (1)$$

The rate of consumption of triglycerides (T) and the rates of formation of fatty acid methyl esters (FAME, biodiesel) (F), monoacetindiglyceride (MA) and diacetin-monoglyceride (DA), triacetin (TA) are as follows:

$$-r_T = -\frac{dC_T}{dt} = w.(k_1 C_M C_T - k_1{}' C_F C_{MA}) \quad (2)$$

$$r_{MA} = \frac{dC_{MA}}{dt} = w.(k_1 C_M C_T - k_1{}' C_F C_{MA} - k_2 C_M C_{MA} + k_2{}' C_F C_{DA}) \quad (3)$$

$$r_F = \frac{dC_F}{dt} = w.(k_1 C_M C_T - k_1{}' C_F C_{MA} + k_2 C_M C_{MA} - k_2{}' C_F C_{MA} + k_3 C_M C_{DA} - k_3{}' C_F C_{TA}) \quad (4)$$

$$r_{DA} = \frac{dC_{DA}}{dt} = w.(k_2 C_M C_{MA} - k_2{}' C_F C_{DA} - k_3 C_M C_{DA} + k_3{}' C_F C_{TA}) \quad (5)$$

$$r_{TA} = \frac{dC_{TA}}{dt} = w.(k_3 C_M C_{DA} - k_3{}' C_F C_{TA}) \quad (6)$$

At time t=0

$$C_T = C_{T_0} \quad C_M = C_{M_0}$$
$$C_F = 0 \quad C_{MA} = 0 \quad C_{DA} = 0 \quad C_{TA} = 0$$

At any time t, the following holds:1 mole of T reacts with 3 moles of M and leads to formation of 3 moles of F, 1 mol of each of MA, DA and TA

The total material balance states the following:

$$C_T = C_{T_0}(1 - X_T) \tag{7}$$

$$C_M = C_{M_0} - X_F C_{T_0} = C_{T_0}\left(\frac{C_{M_0}}{C_{T_0}} - X_F\right) = C_{T_0}(R - X_F) \tag{8}$$

Converting differential equations into difference equations for all species:

$$\Delta C = C(t) - C_0$$

Manipulate equations 1 through 6 by addition or subtraction to get all rate terns on LHS and others on RHS to make them zero.

Subtracting equation (4) from equation (1) gives the following:

$$-r_M = -\frac{dC_M}{dt} = w.\{(k_1 C_M C_T + k_2 C_M C_{MA} + k_3 C_M C_{DA}) - (k_1{}' C_F C_{MA} + k_2{}' C_F C_{DA} + k_3{}' C_F C_{TA})\} \tag{9}$$

$$r_F = \frac{dC_F}{dt} = w.(k_1 C_M C_T - k_1{}' C_F C_{MA} + k_2 C_M C_{MA} - k_2{}' C_F C_{MA} + k_3 C_M C_{DA} - k_3{}' C_F C_{TA}) \tag{10}$$

That it:

$$-\frac{dC_M}{wdt} - \frac{dC_F}{wdt} = (k_1 C_M C_T + k_2 C_M C_{MA} + k_3 C_M C_{DA}) - (k_1{}' C_F C_{MA} + k_2{}' C_F C_{DA} + k_3{}' C_F C_{TA}) - (k_1 C_M C_T - k_1{}' C_F C_{MA} + k_2 C_M C_{MA} - k_2{}' C_F C_{MA} + k_3 C_M C_{DA} - k_3{}' C_F C_{TA}) = 0 \tag{11}$$

So,

$$-dC_M - dC_F = 0$$
$$-\Delta C_M - \Delta C_F = 0$$
$$-C_M + C_{M_0} - C_F + C_{F_0} = 0$$
$$C_{M_0} + C_{F_0} = C_M + C_F$$

Since,

$$C_{F_0} = 0$$

$$C_{M_0} = C_M + C_F \tag{12}$$

Equation 12 holds at any time t.

Similarly, we can connect other concentrations by manipulating other equations.

Similarly,

$$-r_T = -\frac{dC_T}{dt} = w.(k_1 C_M C_T - k_1{}' C_F C_{MA}) \tag{13}$$

Similarly, subtract equations 3, 5 and 6 from equation 2 to get:

$$-\frac{dC_T}{dt} - \frac{dC_{MA}}{dt} - \frac{dC_{DA}}{dt} - \frac{dC_{TA}}{dt} = 0 \tag{14}$$

$$-dC_T - dC_{MA} - dC_{DA} - dC_{TA} = 0 \tag{15}$$

$$-\Delta C_T - \Delta C_{MA} - \Delta C_{DA} - \Delta C_{TA} = 0 \tag{16}$$

Since the initial concentrations of mono-, di- and triacetins are zero. The following holds

$$C_{T_0} = C_T + C_{MA} + C_{DA} + C_{TA} \tag{17}$$

Equation 17 also hold at all times.

Using equation 17 we can write,

$$C_{T0} - C_T = C_{MA} + C_{DA} + C_{TA}$$

$$1 = \frac{C_{MA}}{C_{T0} - C_T} + \frac{C_{DA}}{C_{T0} - C_T} + \frac{C_{TA}}{C_{T0} - C_T}$$

$$1 = S_{MA} + S_{DA} + S_{TA}$$

$$S_i = \frac{C_i}{C_{TO} - C_T} \tag{18}$$

Here, *i* refers to MA, DA or TA.

Thus, the concentrations of MA, DA, TA can calculated using equation:

$$C_i = S_i * (C_{TO} - C_T) \tag{19}$$

The concentration of T can be calculated using equation 7.

Since 1 mole of T can produce 3 moles of F, 1 mole of MA can produce 2 moles of F and 1 mole of DA can produce 1 mole of F, the concentration of F can be calculated as:

$$C_F = 3 * C_T - 2 * C_{DA} - C_{MA} \quad (20)$$

The rate equations and the concentrations can be solved using Python to get rate constants as discussed in Chapter 2 (Section 2.3.2.6).

Gas chromatography-mass spectra of products

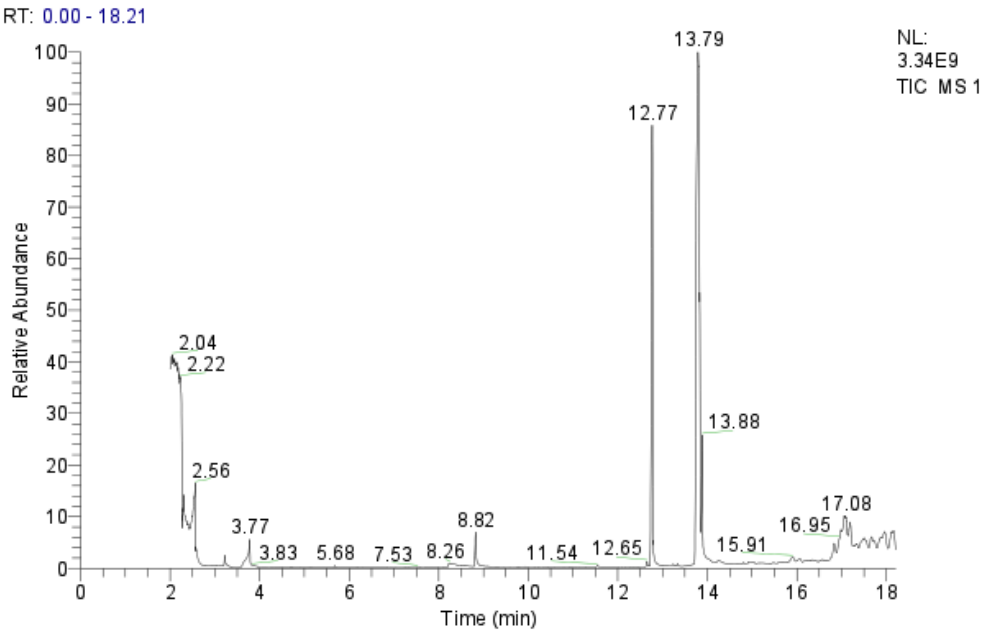

Figure A2.2 Gas chromatography-mass spectra of the reaction mixture

➢ Biodiesel (FAMEs)

- Methyl palmitate

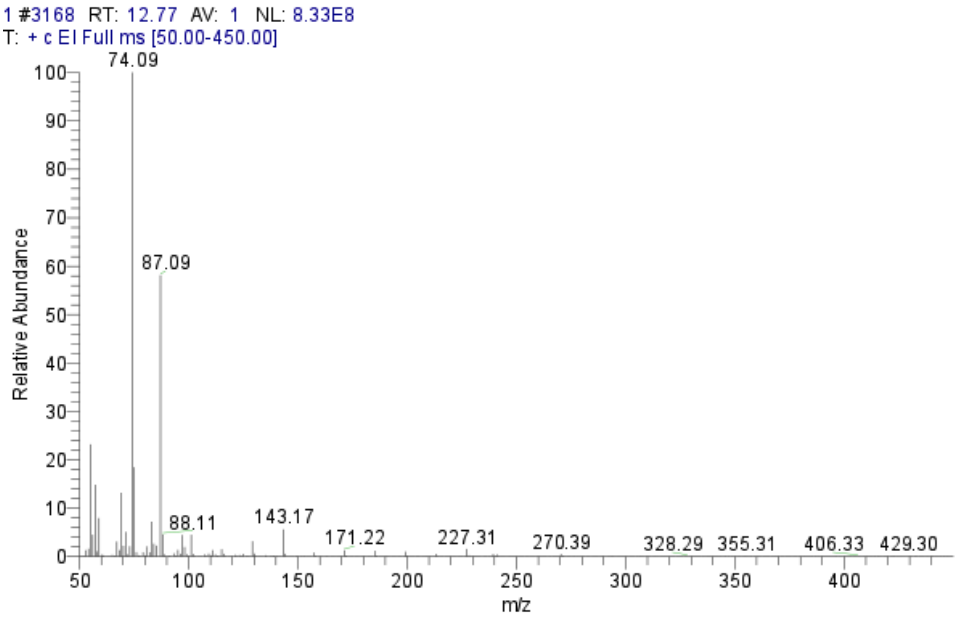

Figure A2.3 Gas chromatography-mass spectra of methyl palmitate

- Methyl linoleate

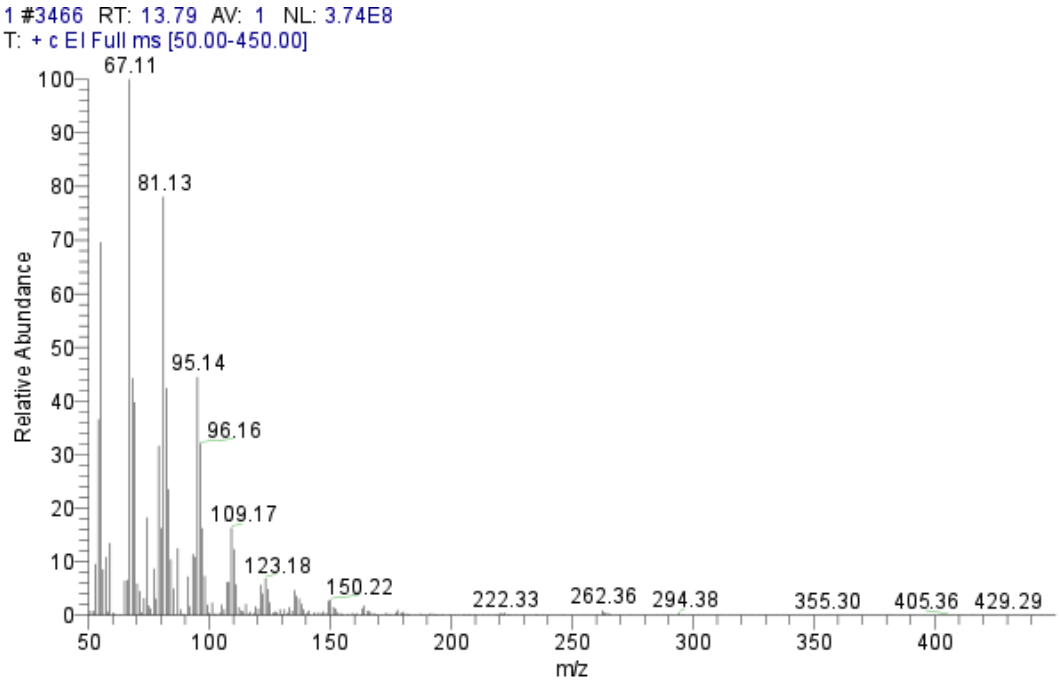

Figure A2.4 Gas chromatography-mass spectra of methyl linoleate

- Methyl oleate

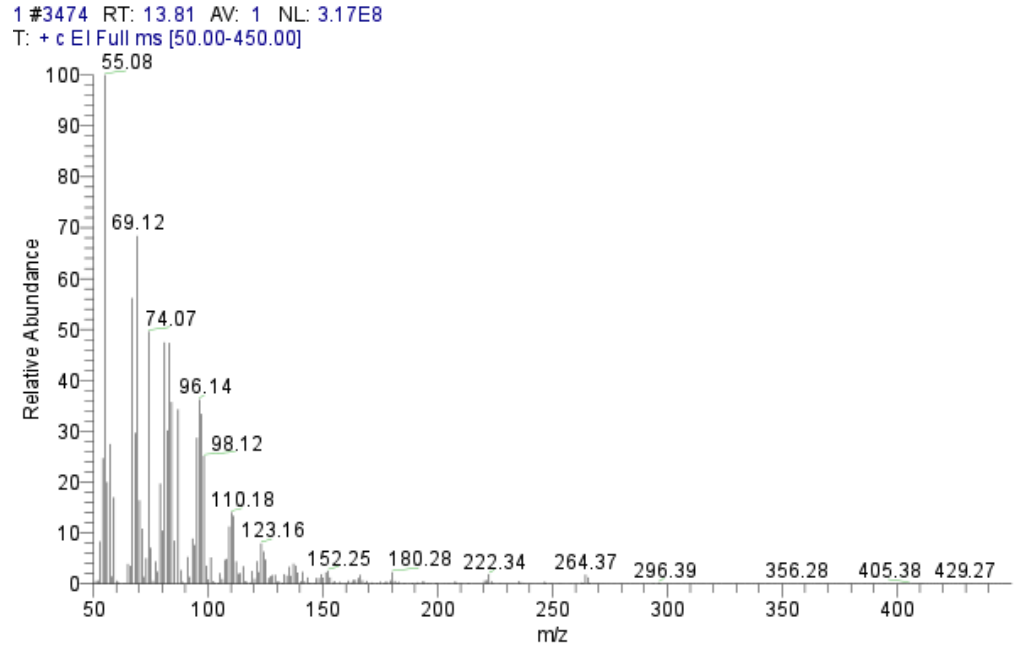

Figure A2.5 Gas chromatography-mass spectra of methyl oleate

- Methyl stearate

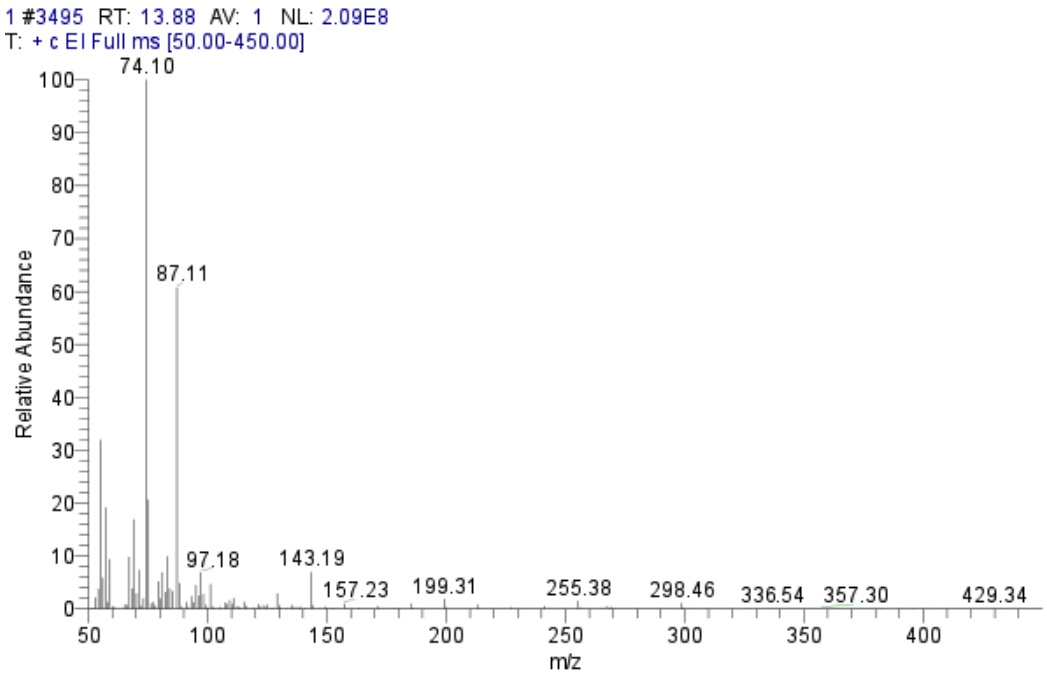

Figure A2.6 Gas chromatography-mass spectra of methyl stearate

➢ Triacetin

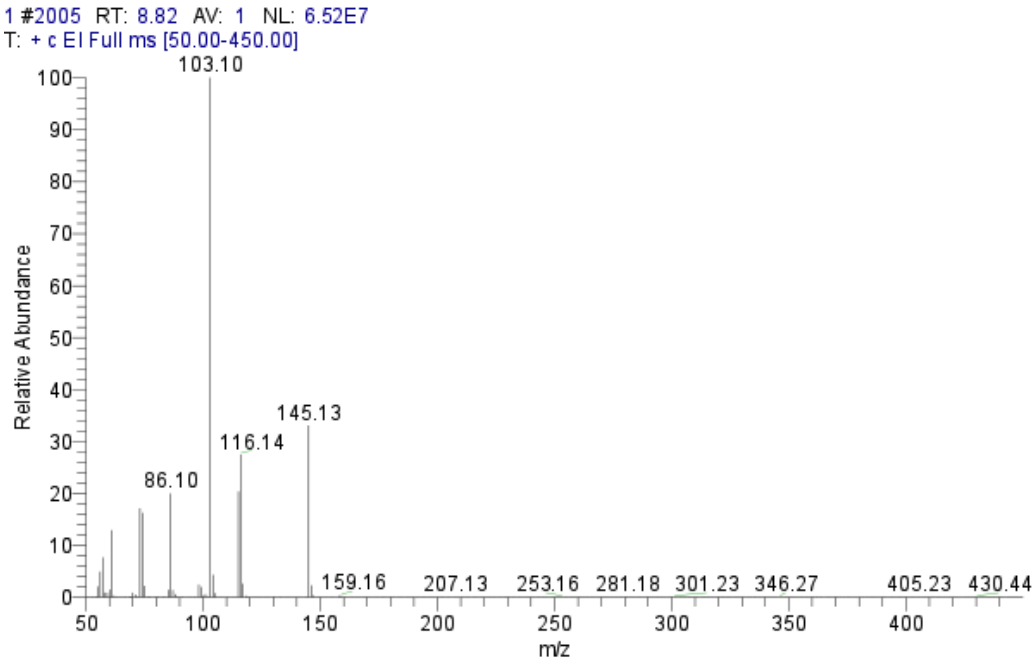

Figure A2.7 Gas chromatography-mass spectra of triacetin

Concentration profile at different temperatures

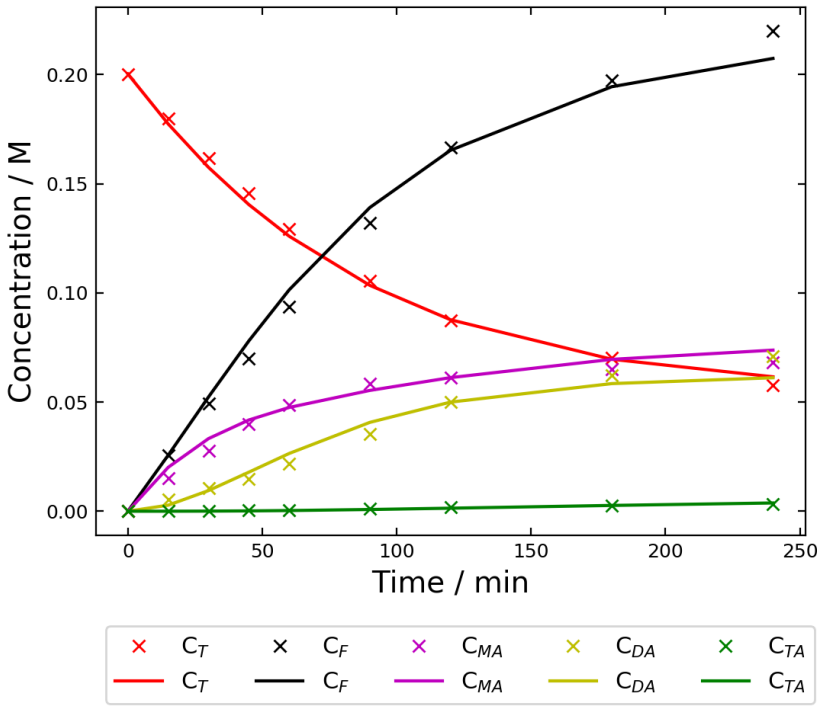

(a)

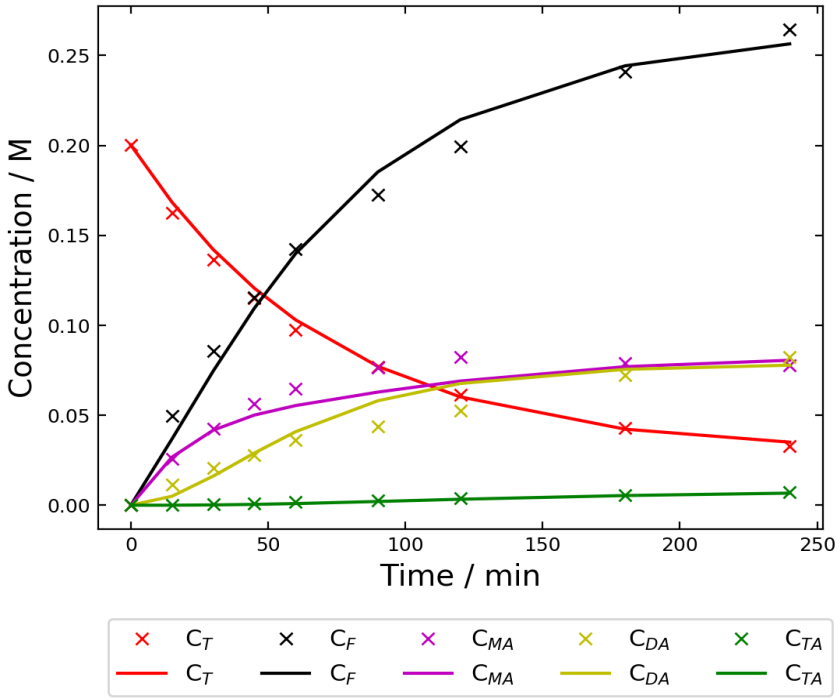

(b)

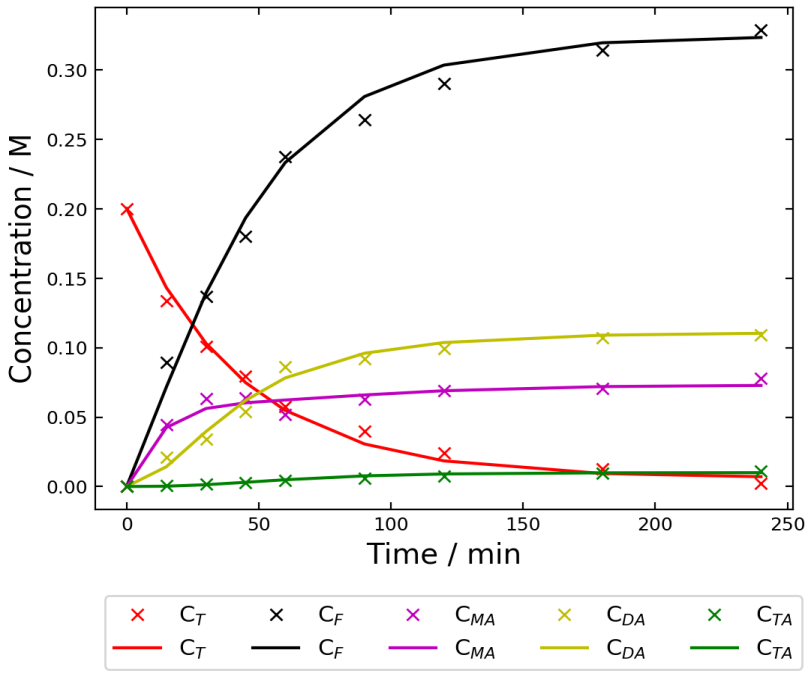

(c)

Figure A2.8 Experimental (x) and fitted (—) concentration (C) profile of soybean oil triglycerides (T), fatty acid methyl esters (F), monoacetindiglycerides (MA), diacetinmonoglycerides (DA) and triacetin (TA) as a function of time at temperature (a) 180 °C, (b) 190 °C, (b) 210 °C. Soybean oil: 7.0 g, soybean oil:methyl acetate mole ratio: 1:50, speed of agitation: 1000 rpm, catalyst loading: 0.04 g/cm^3, total volume 40 cm^3, reaction time 240 min.

APPENDIX B

HPLC Analysis, Catalyst stability and Kinetic modelling

HPLC chromatogram of the reaction mixture

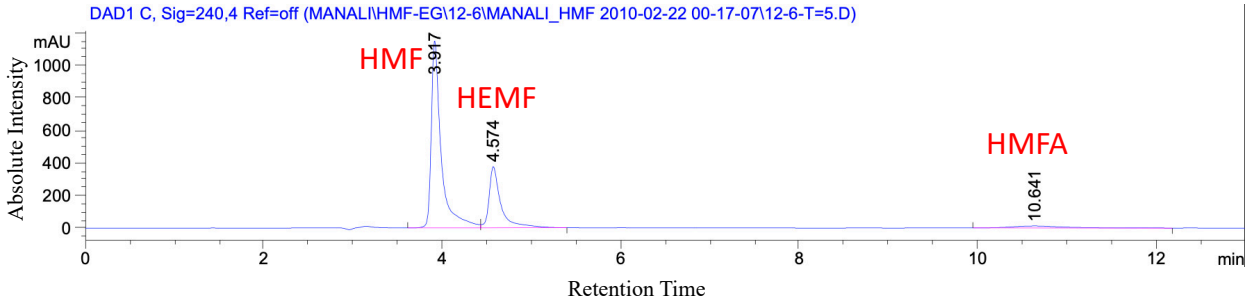

Figure A3.1 GC chromatogram of reaction mixture containing 5-hydroxymethylfurfural (HMF), 5-(2-hydroxyethoxymethyl)furfural (HEMF), 5-hydroxymethylfurfural ethylene acetal (HMFA).

Liquid chromatography-mass spectra of products

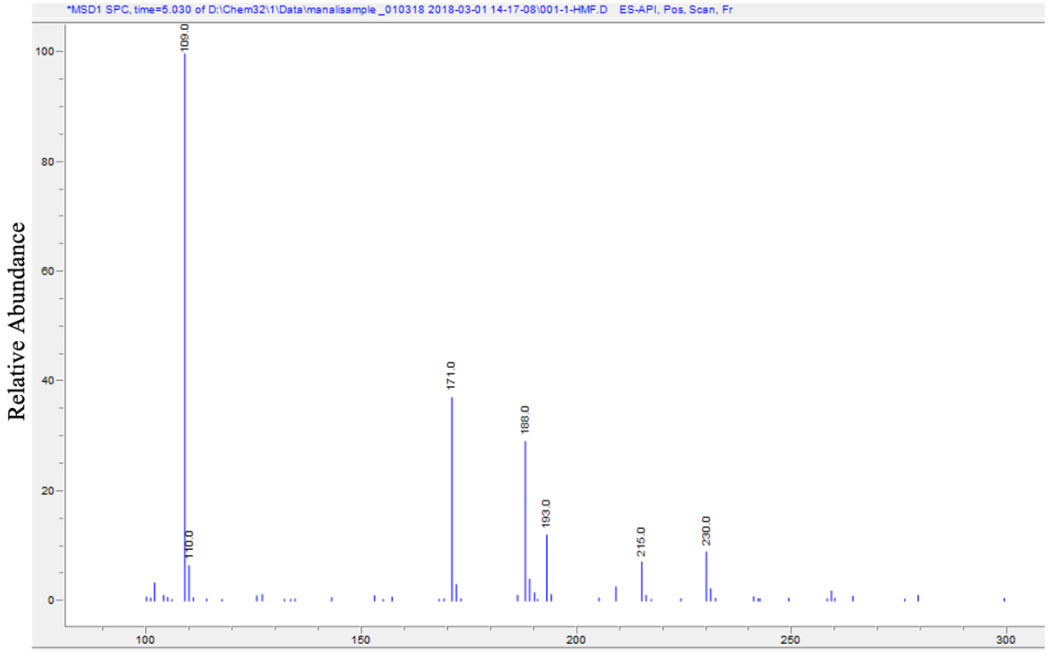

Figure A3.2 HPLC-MS spectra of synthesized 5-(2-Hydroxyethoxymethyl)furfural (HEMF)

Catalyst stability tests by hot filtration method

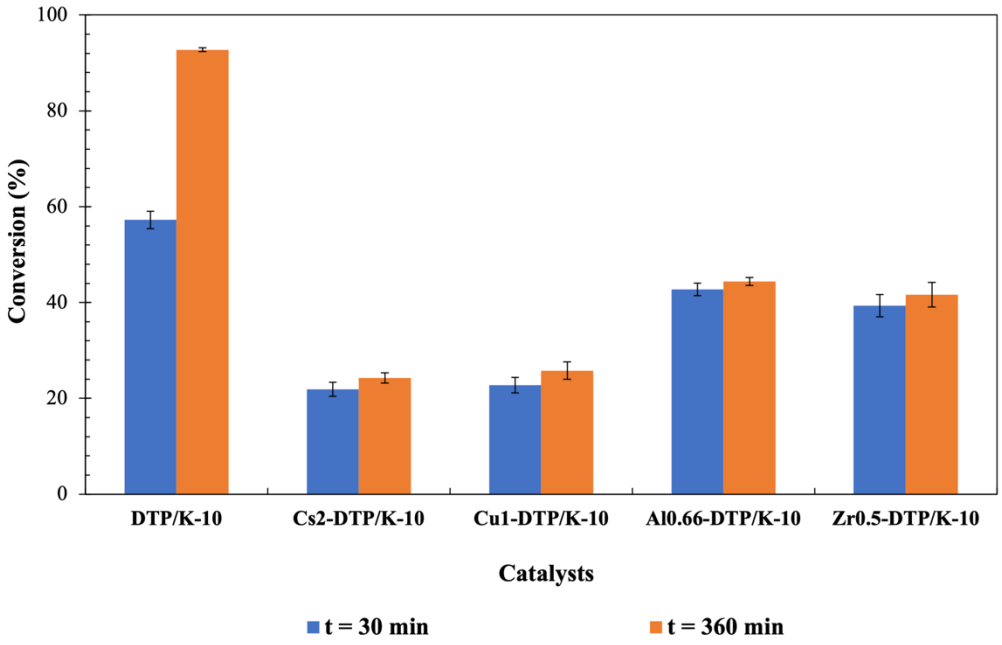

Figure A3.3 Catalyst stability test to check the conversion of HMF after 30 and 360 min reaction time. HMF:Ethylene glycol mole ratio: 1:30, Speed of agitation: 1000 rpm, Temperature: 100°C, Catalyst Loading: 0.03 g/cm^3, Total volume: 12 cm^3, Reaction time: 360 min.

Kinetic model

The kinetic model was derived using a dual site LHHW mechanism [141]. The detailed derivation is provided below:

Adsorption (Molecular):

Adsorption of A on vacant acid sites:

$$A + S \Leftrightarrow AS \quad (1)$$

Adsorption of B on vacant acid sites:

$$B + S \Leftrightarrow BS \quad (2)$$

The adsorption rates of A and B are given by:

$$r_{AD} = k_A \left(C_A C_S - \frac{C_{AS}}{K_A} \right) \tag{3}$$

$$r_{BD} = k_B \left(C_B C_S - \frac{C_{BS}}{K_B} \right) \tag{4}$$

Surface reaction:

The surface reaction of adsorbed species AS and BS to form products, ES and DS is given by:

$$AS + BS \Longrightarrow ES + DS \tag{5}$$

The rate of surface reaction is given by:

$$r_S = k_S C_{AS} C_{BS} \tag{6}$$

Desorption (Molecular):

Desorption of E:

$$E + S \Leftrightarrow ES \tag{7}$$

Desorption of F:

$$F + S \Leftrightarrow FS \tag{8}$$

The desorption rates of E and D are given by:

$$r_{ED} = k_E \left(C_E C_S - \frac{C_{ES}}{K_E} \right) \tag{9}$$

$$r_{FD} = k_F \left(C_F C_S - \frac{C_{FS}}{K_F} \right) \tag{10}$$

Site Balance:

The total concentration of catalytic active sites is given by:

$$C_T = C_S + C_{AS} + C_{BS} + C_{ES} + C_{FS} \tag{11}$$

Assuming that the surface reaction is rate limiting and the adsorption and desorption steps are in equilibrium, we can determine the concentration of adsorbed species from equations (3), (4), (9) and (10) as:

$$C_{AS} = K_A C_A C_S \quad (12)$$

$$C_{BS} = K_B C_B C_S \quad (13)$$

$$C_{ES} = K_E C_E C_S \quad (14)$$

$$C_{FS} = K_F C_F C_S \quad (15)$$

Substituting equations 12-15 in equation 11,

$$C_T = C_S + K_A C_A C_S + K_B C_B C_S + K_E C_E C_S + K_F C_F C_S \quad (11)$$

$$C_S = \frac{C_T}{(1+K_A C_A+K_B C_B+K_E C_E+K_F C_F)} \quad (12)$$

The rate of reaction of A is given as:

$$-r_A = \frac{-dC_A}{dt} = r_S = k_S C_{AS} C_{BS} \quad (13)$$

Substituting equations 12-15 in equation 6, we get:

$$-r_A = \frac{-dC_A}{dt} = r_S = k_S K_A C_A K_B C_B C_S^2 \quad (14)$$

Substituting (12) in (14), we get:

$$-r_A = \frac{-dC_A}{dt} = \frac{k_S K_A C_A K_B C_B C_T^2}{(1+K_A C_A+K_B C_B+K_E C_E+K_F C_F)^2} \quad (15)$$

If w is the catalyst loading, then,

$$-r_A = \frac{-dC_A}{dt} = \frac{k_S K_A C_A K_B C_B w}{(1+K_A C_A+K_B C_B+K_E C_E+K_F C_F)^2} \quad (16)$$

Assuming the adsorption constants (K_i<<<1), we get

$$-r_A = \frac{-dC_A}{dt} = w\, k_S K_A C_A K_B C_B \quad (17)$$

Since, ethylene glycol (C_B) is in excess, the concentration can be assumed to remain constant throughout the reaction, which gives:

$$r_A = \frac{-dC_A}{dt} = wkC_A C_{B0} \quad \text{, where, } k = k_S K_A K_B \quad (18)$$

Integrating above equation, we get:

$$\ln\left(\frac{C_{A0}}{C_A}\right) = wkC_{B0}t$$

Using $C_A = C_{A0}(1 - X_A)$,

$$-\ln(1 - X_A) = wkC_{B0}t \tag{19}$$

The experimental conversion versus time data recorded at different temperatures, keeping other parameters constant can be used to validate the predicted kinetic model by equation 19.

APPENDIX C

GC, GC-MS analysis, Cyclic voltammograms, Buffer capacity, Open circuit potential vs pH tests, EDS Spectra and Literature comparison of results

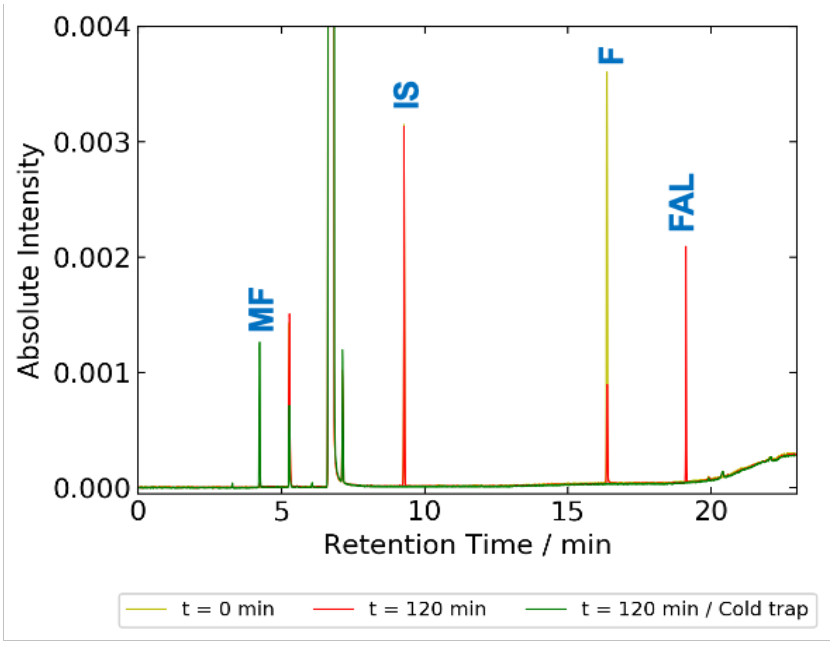

Figure A4.1 GC chromatogram of reaction mixture containing furfural (F); furfuryl alcohol (FAL), 2-methylfuran (MF), p-xylene (internal standard, IS)

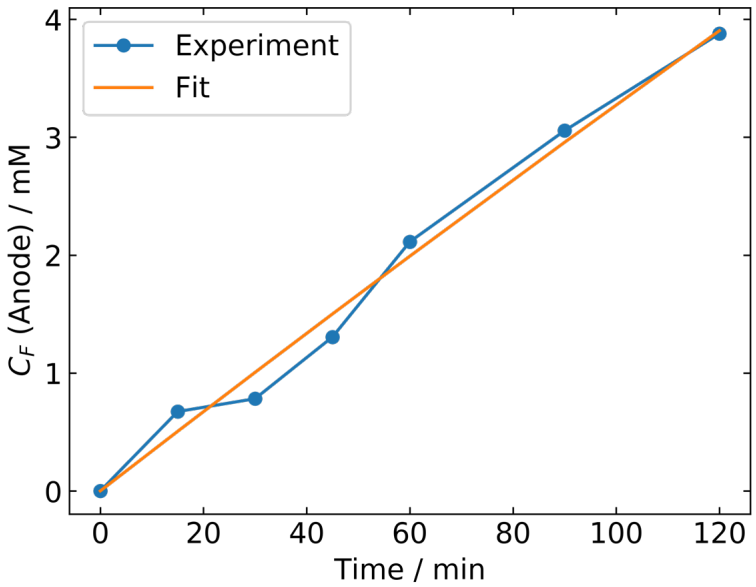

Figure A4.2 Experimental (Exp.) and fitted (Fit) concentration profile of furfural in anode chamber after permeation

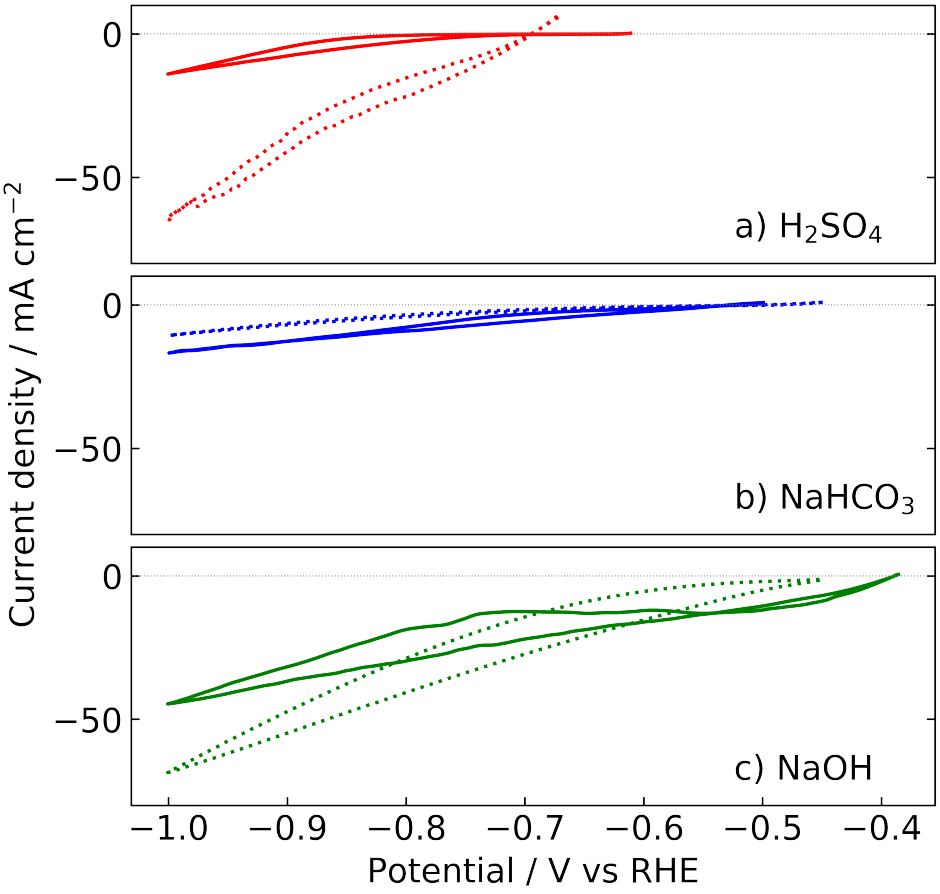

Figure A4.3 CV showing polarization curves obtained with zinc at different pH (dashed lines = No furfural, bold lines = 100 mM furfural)

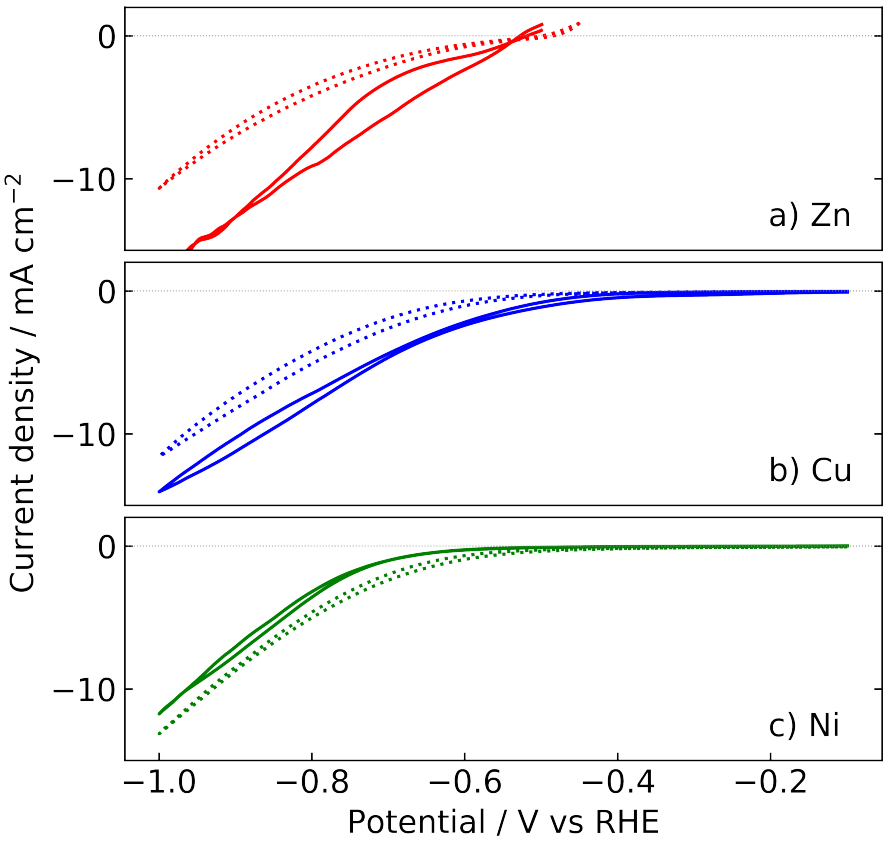

Figure A4.4 CV showing polarization curves obtained with different catalysts in 0.5 M $NaHCO_3$ (dashed lines = No furfural, bold lines = 100 mM furfural)

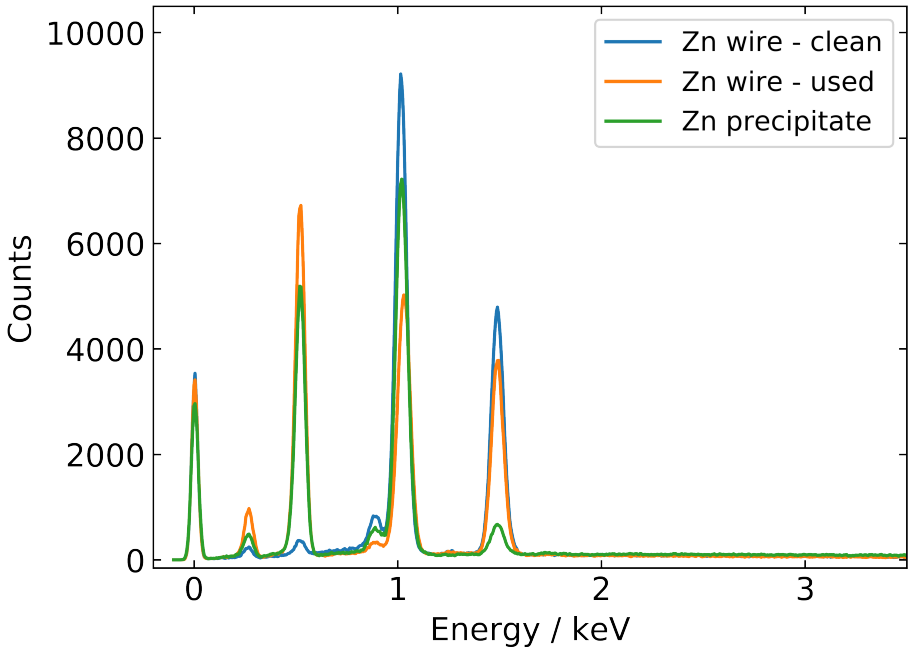

Figure A4.5 EDS spectra of the clean zinc wire, used zinc wire and zinc precipitates

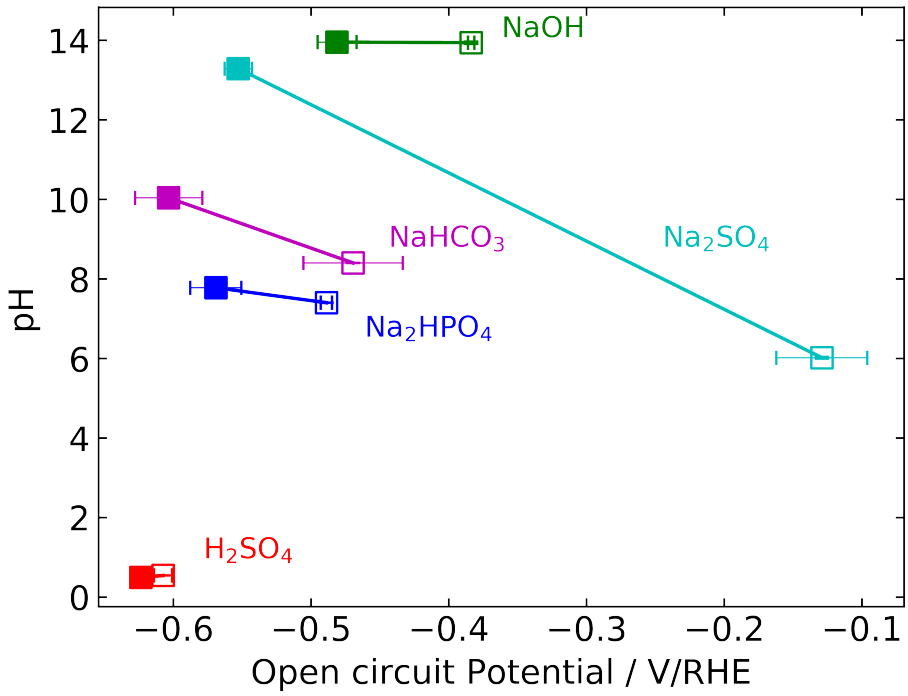

Figure A4.6 Change in electrolyte pH and Open Circuit potential during two-hour ECH electrolysis. Closed symbols: initial conditions; Open symbols: final conditions.

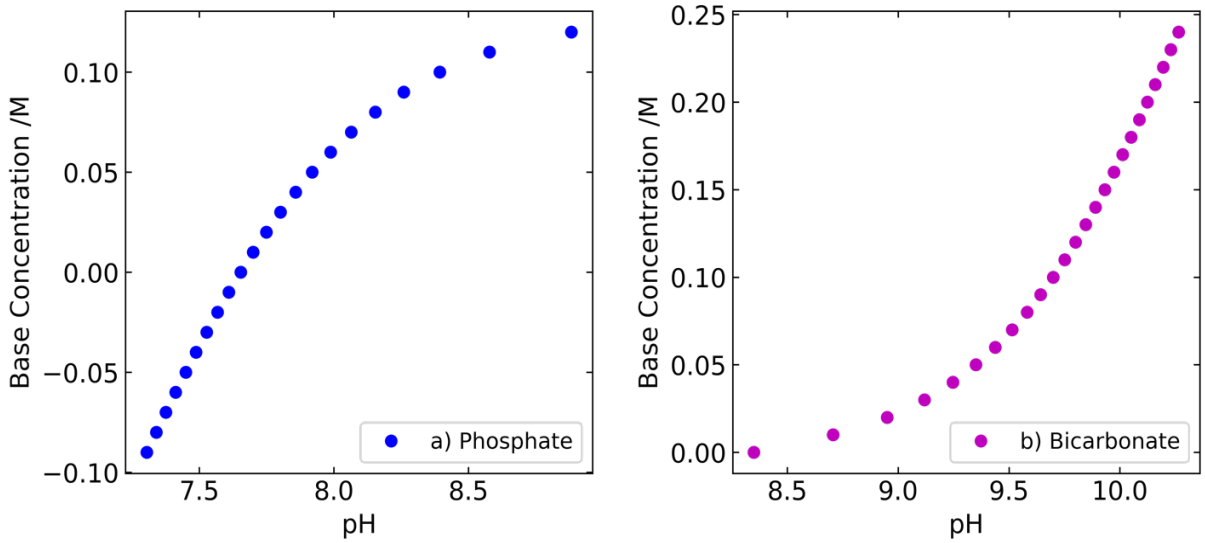

Figure A4.7 pH as a function of base concentration for a) Phosphate buffer b) Sodium bicarbonate buffer

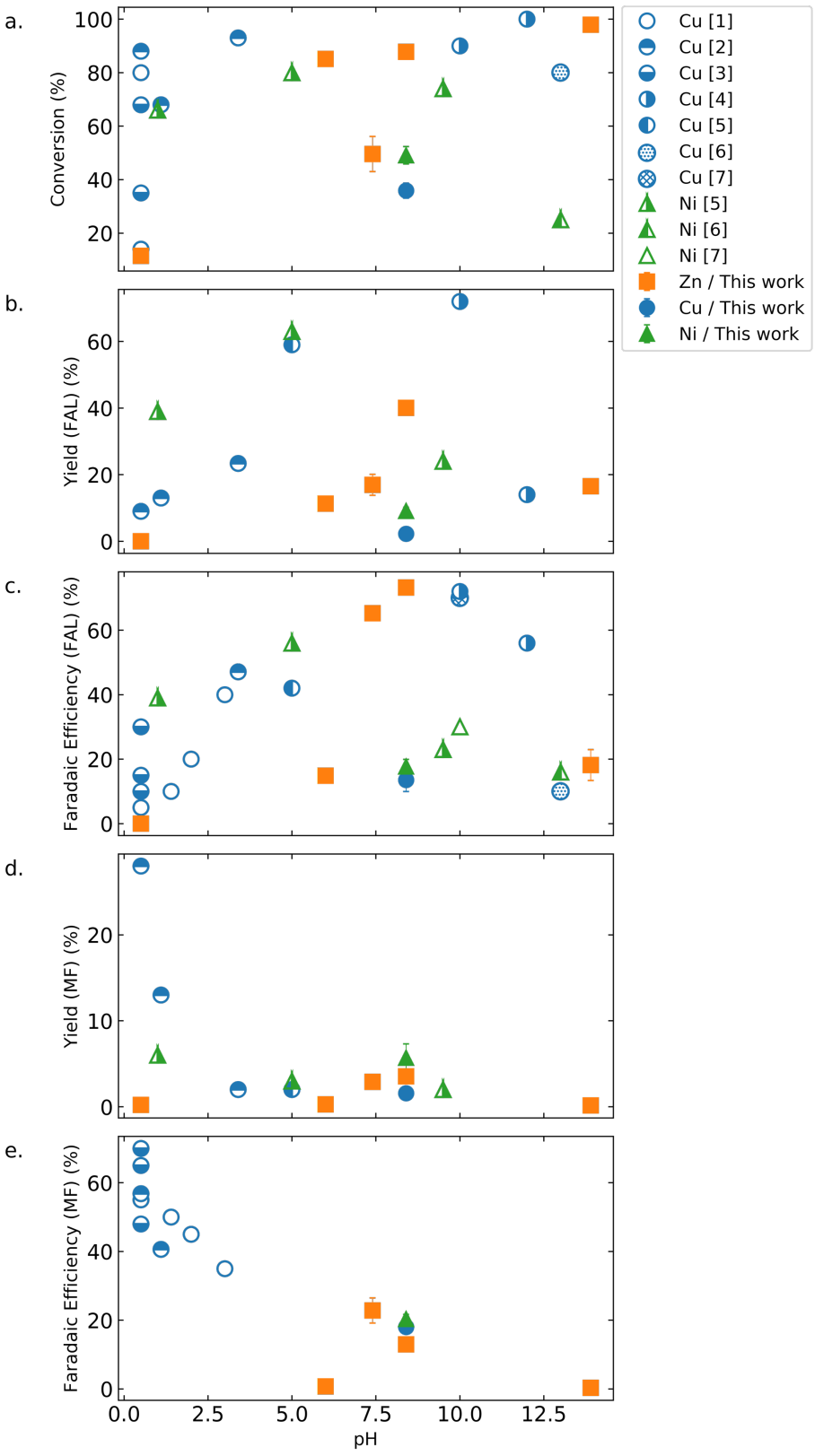

Figure A4.8 Variation of **(a).** Conversion of furfural, **(b).** Yield of FAL, **(c).** FE of FAL, **(d).** Yield of MF, **(e).** FE of MF with electrolyte pH (Literature vs this work)

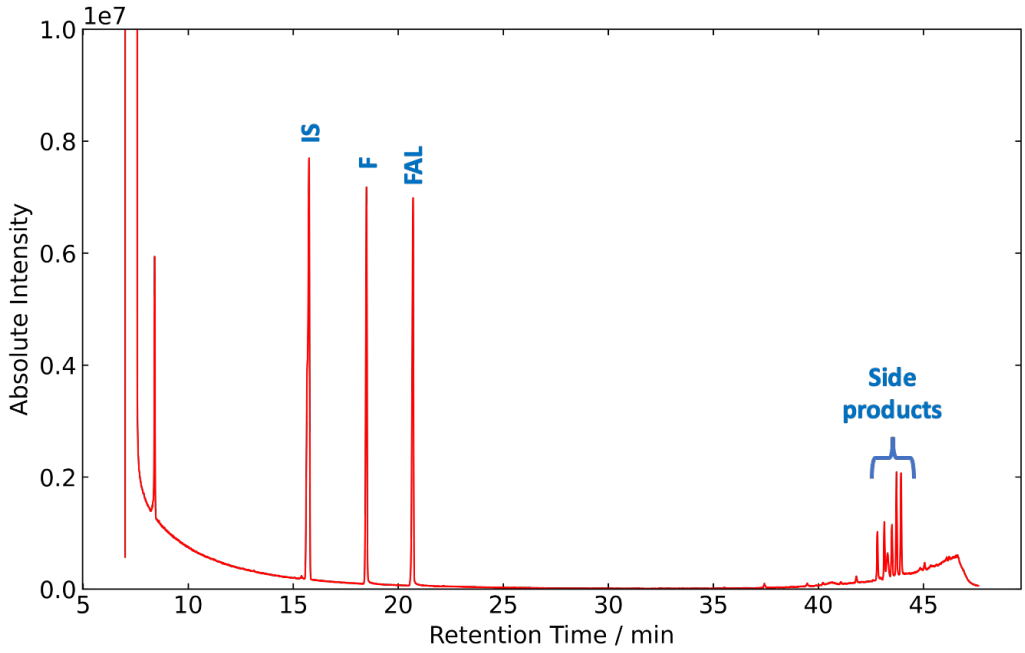

Figure A4.9 GC chromatogram of reaction mixture containing furfural (F); furfural alcohol (FAL), p-xylene (internal standard, IS) and side products (alpha-furoin (Ethanone,1,2-di-2-furanyl-2-hydroxy); hydrofuroin (1,2-Ethanediol, 1,2-di-2-furanyl-); 4-methyl-5-(2-methyl-2-propenyl)-2(5H)-furanone and 1-(2-furanyl)-3-methyl-butene-1,2-diol [cold trap sample containing MF not analyzed by GC-MS].

Table A4.1 Similarity indices of probable chemical compounds at respective peak retention times in GC chromatogram [Fig. A4.9]

		Similarity Index of Chemical Products			
		alpha-furoin	**Hydrofuroin**	**4-methyl-5-(2-methyl-2-propenyl)-2(5H)-furanone**	**1-(2-furanyl)-3-methyl-butene-1,2-diol**
Retention Time / min	**42.8**	87	-	88	89
	43.1	87	-	89	-
	43.3	80	-	-	-
	43.5	83	82	-	-
	43.7	82	84	85	82
	43.9	82	85	85	

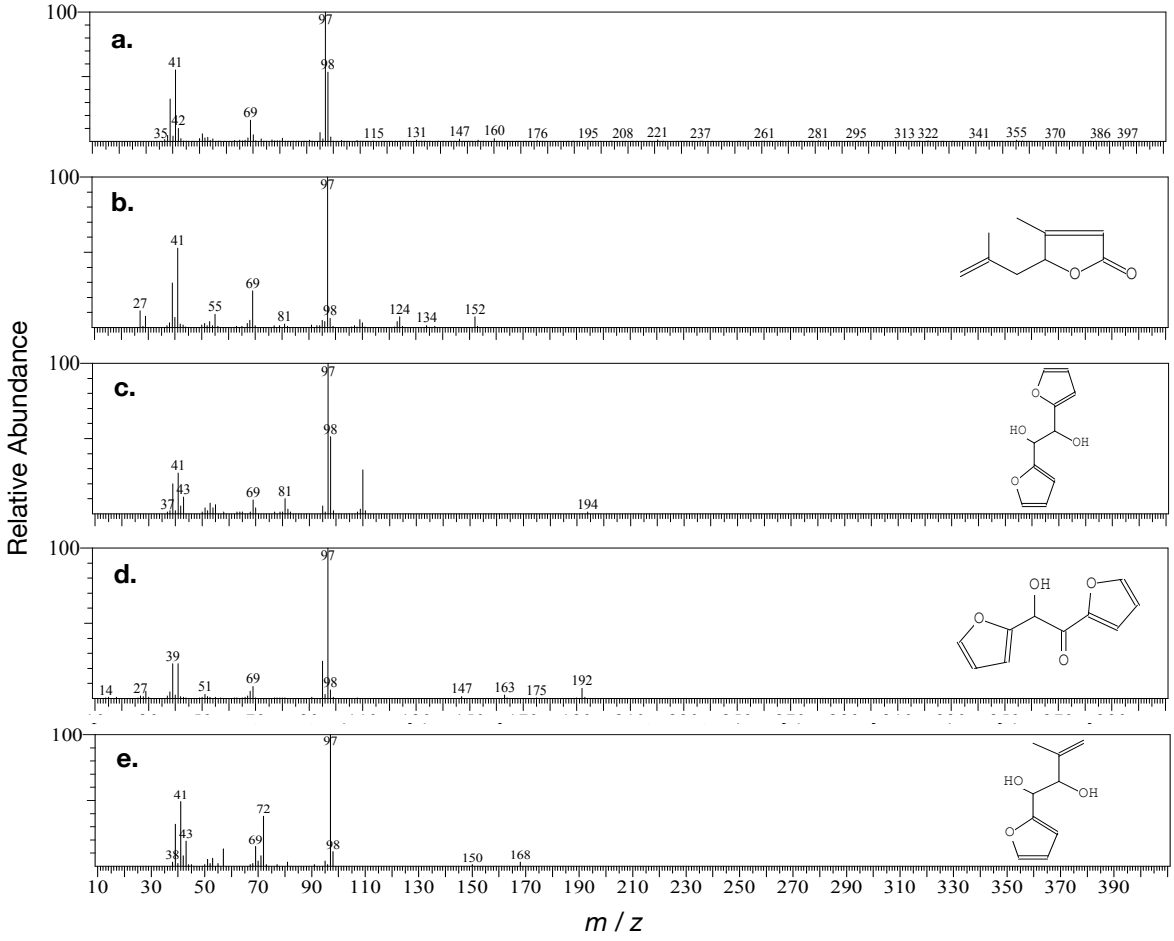

Figure A4.10 GC Mass spectra with probable chemical side products. (a) Mass spectrum of GC peak at 43.7 min retention time. Reference mass spectrum for (b) 4-methyl-5-(2-methyl-2-propenyl)-2(5H)-furanone; (c) hydrofuroin; (d) alpha-furoin; (e) 1-(2-furanyl)-3-methyl-butene-1,2-diol

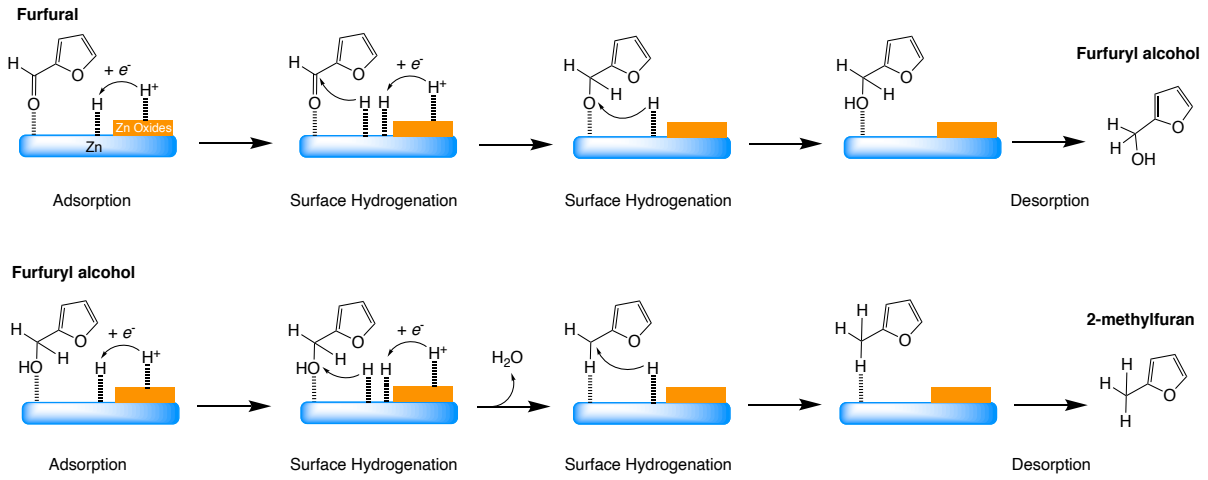

Figure A4.11 Proposed mechanism for ECH of furfural

References

[1] X.H. Chadderdon, D.J. Chadderdon, J.E. Matthiesen, Y. Qiu, J.M. Carraher, J.P. Tessonnickeler, W. Li, Mechanisms of Furfural Reduction on Catalyst Electrodes: Distinguishing Pathways for Selective Hydrogenation of Bioderived Oxygenates, J. Am. Chem. Soc. 139 (2017) 14120–14128. doi:10.1021/jacs.7b06331.

[2] S. Jung, E.J. Biddinger, Electrocatalytic Hydrogenation and Hydrogenolysis of Furfural and the Impact of Homogeneous Side Reactions of Furanic Compounds in Acidic Electrolytes, ACS Sustain. Chem. Eng. 4 (2016) 6500–6508. doi:10.1021/acssuschemeng.6b01314.

[3] S. Jung, A.N. Karaiskakis, E.J. Biddinger, Enhanced activity for electrochemical hydrogenation and hydrogenolysis of furfural to biofuel using electrodeposited Cu catalysts, Catal. Today. 323 (2019) 26–34. doi:10.1016/j.cattod.2018.09.011.

[4] P. Parpot, A.P. Bettencourt, G. Chamoulaud, K.B. Kokoh, E.M. Belgsir, Electrochemical investigations of the oxidation-reduction of furfural in aqueous medium - Application to electrosynthesis, Electrochim. Acta. 49 (2004) 397–403. doi:10.1016/j.electacta.2003.08.021.

[5] Z. Li, S. Kelkar, C.H. Lam, K. Luczek, J.E. Jackson, D.J. Miller, C.M. Saffron, Aqueous electrocatalytic hydrogenation of furfural using a sacrificial anode, Electrochim. Acta. 64 (2012) 87–93. doi:10.1016/j.electacta.2011.12.105.

[6] B. Zhao, M. Chen, Q. Guo, Y. Fu, Electrocatalytic hydrogenation of furfural to furfuryl alcohol using platinum supported on activated carbon fibers, Electrochim. Acta. 135 (2014) 139–146. doi:10.1016/j.electacta.2014.04.164.

[7] L. Liu, H. Liu, W. Huang, Y. He, W. Zhang, C. Wang, H. Lin, Mechanism and kinetics of the electrocatalytic hydrogenation of furfural to furfuryl alcohol, J. Electroanal. Chem. 804 (2017) 248–253. doi:10.1016/j.jelechem.2017.09.021.

BIBLIOGRAPHY

BIBLIOGRAPHY

[1] United States Census Bureau, U.S. and World Population Clock, (n.d.). http://www.census.gov/popclock/ (accessed May 22, 2021).

[2] U.S. Energy Information Administration, International Energy Outlook 2019, (n.d.). https://www.eia.gov/pressroom/releases/press465.php (accessed May 22, 2021).

[3] BP Statistical Review of World Energy 2020, (n.d.). https://www.bp.com/en/global/corporate/energy-economics/statistical-review-of-world-energy.html (accessed May 22, 2021).

[4] S. Solomon, G.-K. Plattner, R. Knutti, P. Friedlingstein, Irreversible climate change due to carbon dioxide emissions, Proc. Natl. Acad. Sci. 106 (2009) 1704–1709. doi:10.1073/pnas.0812721106.

[5] A. Narayanan, K. Mets, M. Strobbe, C. Develder, Feasibility of 100% renewable energy-based electricity production for cities with storage and flexibility, Renew. Energy. 134 (2019) 698–709. doi:10.1016/j.renene.2018.11.049.

[6] S.R. Bull, Renewable energy today and tomorrow, Proc. IEEE. 89 (2001) 1216–1226. doi:10.1109/5.940290.

[7] N.L. Panwar, S.C. Kaushik, S. Kothari, Role of renewable energy sources in environmental protection: A review, Renew. Sustain. Energy Rev. 15 (2011) 1513–1524. doi:10.1016/j.rser.2010.11.037.

[8] B. Zhao, M. Chen, Q. Guo, Y. Fu, Electrocatalytic hydrogenation of furfural to furfuryl alcohol using platinum supported on activated carbon fibers, Electrochim. Acta. 135 (2014) 139–146. doi:10.1016/j.electacta.2014.04.164.

[9] R.A. Sheldon, Utilisation of biomass for sustainable fuels and chemicals: Molecules, methods and metrics, Catal. Today. 167 (2011) 3–13. doi:10.1016/j.cattod.2010.10.100.

[10] J. Clark, F. Deswarte, Introduction to Chemicals from Biomass, Wiley, 2015. doi:10.1002/9781118714478.

[11] R.A. Sheldon, Green and sustainable manufacture of chemicals from biomass: state of the art, Green Chem. 16 (2014) 950–963. doi:10.1039/C3GC41935E.

[12] F. Cherubini, The biorefinery concept: Using biomass instead of oil for producing energy and chemicals, Energy Convers. Manag. 51 (2010) 1412–1421. doi:10.1016/j.enconman.2010.01.015.

[13] D. Kim, K. Lee, K.Y. Park, Upgrading the characteristics of biochar from cellulose, lignin, and xylan for solid biofuel production from biomass by hydrothermal carbonization, J. Ind. Eng. Chem. 42 (2016) 95–100. doi:10.1016/j.jiec.2016.07.037.

[14] C.-H. Zhou, X. Xia, C.-X. Lin, D.-S. Tong, J. Beltramini, Catalytic conversion of lignocellulosic biomass to fine chemicals and fuels, Chem. Soc. Rev. 40 (2011) 5588. doi:10.1039/c1cs15124j.

[15] V.G. Yadav, G.D. Yadav, S.C. Patankar, The production of fuels and chemicals in the new world: critical analysis of the choice between crude oil and biomass vis-à-vis sustainability and the environment, Clean Technol. Environ. Policy. 22 (2020) 1757–1774. doi:10.1007/s10098-020-01945-5.

[16] T.J. Collins, Green Chemistry, Macmillan Encycl. Chem. Vol. 2, Simon Schuster Macmillan, New York. (1997) 691–697.

[17] P.T. Anastas, L.B. Bartlett, M.M. Kirchhoff, T.C. Williamson, The role of catalysis in the design, development, and implementation of green chemistry, Catal. Today. 55 (2000) 11–22. doi:10.1016/S0920-5861(99)00222-9.

[18] E. Farnetti, R. Di Monte, J. Kapser, Homogeneous and Heterogeneous Catalysis, in: Inorg. Bio-Inorganic Chem., 1999: pp. 50–86.

[19] B.M. Upton, A.M. Kasko, Strategies for the Conversion of Lignin to High-Value Polymeric Materials: Review and Perspective, Chem. Rev. 116 (2016) 2275–2306. doi:10.1021/acs.chemrev.5b00345.

[20] S. Yaman, Pyrolysis of biomass to produce fuels and chemical feedstocks, Energy Convers. Manag. 45 (2004) 651–671. doi:10.1016/S0196-8904(03)00177-8.

[21] S.-Y. No, Application of hydrotreated vegetable oil from triglyceride based biomass to CI engines – A review, Fuel. 115 (2014) 88–96. doi:10.1016/j.fuel.2013.07.001.

[22] C. Chatterjee, F. Pong, A. Sen, Chemical conversion pathways for carbohydrates, Green Chem. 17 (2015) 40–71. doi:10.1039/C4GC01062K.

[23] X. Li, P. Jia, T. Wang, Furfural: A Promising Platform Compound for Sustainable Production of C4 and C5 Chemicals, ACS Catal. 6 (2016) 7621–7640. doi:10.1021/acscatal.6b01838.

[24] S.N. Naik, V. V. Goud, P.K. Rout, A.K. Dalai, Production of first and second generation biofuels: A comprehensive review, Renew. Sustain. Energy Rev. 14 (2010) 578–597. doi:10.1016/j.rser.2009.10.003.

[25] F. Karaosmanoglu, Vegetable Oil Fuels: A Review, Energy Sources. 21 (1999) 221–231. doi:10.1080/00908319950014858.

[26] D.P. Ho, H.H. Ngo, W. Guo, A mini review on renewable sources for biofuel, Bioresour. Technol. 169 (2014) 742–749. doi:10.1016/j.biortech.2014.07.022.

[27] A.W. Go, P.L. Tran Nguyen, L.H. Huynh, Y.-T. Liu, S. Sutanto, Y.-H. Ju, Catalyst free esterification of fatty acids with methanol under subcritical condition, Energy. 70 (2014)

393–400. doi:10.1016/j.energy.2014.04.013.

[28] A. Sharma, S.P. Chaurasia, A.K. Dalai, Enzymatic hydrolysis of cod liver oil for the fatty acids production, Catal. Today. 207 (2013) 93–100. doi:https://doi.org/10.1016/j.cattod.2012.05.006.

[29] M.S. Dhawan, G.D. Yadav, Insight into a catalytic process for simultaneous production of biodiesel and glycerol carbonate from triglycerides, Catal. Today. 309 (2018) 161–171. doi:10.1016/j.cattod.2017.08.020.

[30] M.S. Dhawan, S.C. Barton, G.D. Yadav, Interesterification of triglycerides with methyl acetate for the co-production biodiesel and triacetin using hydrotalcite as a heterogenous base catalyst, Catal. Today. 375 (2021) 101–111. doi:10.1016/j.cattod.2020.07.056.

[31] A. Casas, M.J. Ramos, Á. Pérez, Methanol-enhanced chemical interesterification of sunflower oil with methyl acetate, Fuel. 106 (2013) 869–872. doi:10.1016/j.fuel.2012.11.037.

[32] S. Sankaranarayanan, C.A. Antonyraj, S. Kannan, Transesterification of edible, non-edible and used cooking oils for biodiesel production using calcined layered double hydroxides as reusable base catalysts, Bioresour. Technol. 109 (2012) 57–62. doi:10.1016/j.biortech.2012.01.022.

[33] R.E.H. Sims, W. Mabee, J.N. Saddler, M. Taylor, An overview of second generation biofuel technologies, Bioresour. Technol. 101 (2010) 1570–1580. doi:10.1016/j.biortech.2009.11.046.

[34] M.P. Pandey, C.S. Kim, Lignin Depolymerization and Conversion: A Review of Thermochemical Methods, Chem. Eng. Technol. 34 (2011) 29–41. doi:10.1002/ceat.201000270.

[35] X. Zhou, M.W. Nolte, B.H. Shanks, L.J. Broadbelt, Experimental and Mechanistic Modeling of Fast Pyrolysis of Neat Glucose-Based Carbohydrates. 2. Validation and Evaluation of the Mechanistic Model, Ind. Eng. Chem. Res. 53 (2014) 13290–13301. doi:10.1021/ie502260q.

[36] Z. Li, M. Garedew, C.H. Lam, J.E. Jackson, D.J. Miller, C.M. Saffron, Mild electrocatalytic hydrogenation and hydrodeoxygenation of bio-oil derived phenolic compounds using ruthenium supported on activated carbon cloth, Green Chem. 14 (2012) 2540–2549. doi:10.1039/c2gc35552c.

[37] A. Corma, S. Iborra, A. Velty, Chemical Routes for the Transformation of Biomass into Chemicals, Chem. Rev. 107 (2007) 2411–2502. doi:10.1021/cr050989d.

[38] L. Hu, L. Lin, Z. Wu, S. Zhou, S. Liu, Recent advances in catalytic transformation of biomass-derived 5-hydroxymethylfurfural into the innovative fuels and chemicals, Renew. Sustain. Energy Rev. 74 (2017) 230–257. doi:10.1016/j.rser.2017.02.042.

[39] H. Wang, M. Tucker, Y. Ji, Recent Development in Chemical Depolymerization of Lignin: A Review, J. Appl. Chem. 2013 (2013) 1–9. doi:10.1155/2013/838645.

[40] P. Varanasi, P. Singh, M. Auer, P.D. Adams, B.A. Simmons, S. Singh, Survey of renewable chemicals produced from lignocellulosic biomass during ionic liquid pretreatment, Biotechnol. Biofuels. 6 (2013) 1. doi:10.1186/1754-6834-6-14.

[41] A.R. Go, Y. Lee, Y.H. Kim, S. Park, J. Choi, J. Lee, S.O. Han, S.W. Kim, C. Park, Enzymatic coproduction of biodiesel and glycerol carbonate from soybean oil in solvent-free system, Enzyme Microb. Technol. 53 (2013) 154–158. doi:10.1016/j.enzmictec.2013.02.016.

[42] E.M. Usai, E. Gualdi, V. Solinas, E. Battistel, Simultaneous enzymatic synthesis of FAME and triacetyl glycerol from triglycerides and methyl acetate, Bioresour. Technol. 101 (2010) 7707–7712. doi:10.1016/j.biortech.2010.05.044.

[43] Y. Kwon, K.J.P. Schouten, J.C. Van Der Waal, E. De Jong, M.T.M. Koper, Electrocatalytic Conversion of Furanic Compounds, ACS Catal. 6 (2016) 6704–6717. doi:10.1021/acscatal.6b01861.

[44] K.R. Vuyyuru, P. Strasser, Oxidation of biomass derived 5-hydroxymethylfurfural using heterogeneous and electrochemical catalysis, Catal. Today. 195 (2012) 144–154. doi:10.1016/j.cattod.2012.05.008.

[45] S. Alipour, H. Omidvarborna, D.-S. Kim, A review on synthesis of alkoxymethyl furfural, a biofuel candidate, Renew. Sustain. Energy Rev. 71 (2017) 908–926. doi:10.1016/j.rser.2016.12.118.

[46] Z. Ilham, S. Saka, Two-step supercritical dimethyl carbonate method for biodiesel production from Jatropha curcas oil, Bioresour. Technol. 101 (2010) 2735–2740. doi:10.1016/j.biortech.2009.10.053.

[47] Z. Li, S. Kelkar, L. Raycraft, M. Garedew, J.E. Jackson, D.J. Miller, C.M. Saffron, A mild approach for bio-oil stabilization and upgrading: electrocatalytic hydrogenation using ruthenium supported on activated carbon cloth, Green Chem. 16 (2014) 844–852. doi:10.1039/C3GC42303D.

[48] V.S. Sikarwar, M. Zhao, P.S. Fennell, N. Shah, E.J. Anthony, Progress in biofuel production from gasification, Prog. Energy Combust. Sci. 61 (2017) 189–248. doi:10.1016/j.pecs.2017.04.001.

[49] G. Bozzano, F. Manenti, Efficient methanol synthesis: Perspectives, technologies and optimization strategies, Prog. Energy Combust. Sci. 56 (2016) 71–105. doi:10.1016/j.pecs.2016.06.001.

[50] T. Werpy, G. Petersen, Top Value Added Chemicals from Biomass: Volume I -- Results of Screening for Potential Candidates from Sugars and Synthesis Gas, Golden, CO (United States), 2004. doi:10.2172/15008859.

[51] J.J. Bozell, G.R. Petersen, Technology development for the production of biobased products from biorefinery carbohydrates—the US Department of Energy's "Top 10" revisited, Green Chem. 12 (2010) 539. doi:10.1039/b922014c.

[52] S. Choi, C.W. Song, J.H. Shin, S.Y. Lee, Biorefineries for the production of top building block chemicals and their derivatives, Metab. Eng. 28 (2015) 223–239. doi:10.1016/j.ymben.2014.12.007.

[53] E. De Jong, H. Stichnothe, G. Bell, H. Jorgensen, Bio-Based Chemicals: A 2020 Update, 2020. https://task42.ieabioenergy.com/wp-content/uploads/sites/10/2020/02/Bio-based-chemicals-a-2020-update-final-200213.pdf.

[54] C. Delhomme, D. Weuster-Botz, F.E. Kühn, Succinic acid from renewable resources as a C 4 building-block chemical—a review of the catalytic possibilities in aqueous media, Green Chem. 11 (2009) 13–26. doi:10.1039/B810684C.

[55] R. Narayan, Biobased & Biodegradable Plastics: Rationale, Drivers, and Technology Exemplars, in: ACS Symp. Ser., 2012: pp. 13–31. doi:10.1021/bk-2012-1114.ch002.

[56] J. Zhang, J. Li, S.-B. Wu, Y. Liu, Advances in the Catalytic Production and Utilization of Sorbitol, Ind. Eng. Chem. Res. 52 (2013) 11799–11815. doi:10.1021/ie4011854.

[57] A. Mukherjee, M.-J. Dumont, V. Raghavan, Review: Sustainable production of hydroxymethylfurfural and levulinic acid: Challenges and opportunities, Biomass and Bioenergy. 72 (2015) 143–183. doi:10.1016/j.biombioe.2014.11.007.

[58] M.S. Dhawan, G.D. Yadav, S. Calabrese Barton, Zinc-electrocatalyzed hydrogenation of furfural in near-neutral electrolytes, Sustain. Energy Fuels. 5 (2021) 2972–2984. doi:10.1039/D1SE00221J.

[59] S.K. Green, J. Lee, H.J. Kim, G.A. Tompsett, W.B. Kim, G.W. Huber, The electrocatalytic hydrogenation of furanic compounds in a continuous electrocatalytic membrane reactor, Green Chem. 15 (2013) 1869. doi:10.1039/c3gc00090g.

[60] B.H. Shanks, P.L. Keeling, Bioprivileged molecules: creating value from biomass, Green Chem. 19 (2017) 3177–3185. doi:10.1039/C7GC00296C.

[61] L.M. Lopez, B.H. Shanks, L.J. Broadbelt, Identification of bioprivileged molecules: expansion of a computational approach to broader molecular space, Mol. Syst. Des. Eng. 6 (2021) 445–460. doi:10.1039/D1ME00013F.

[62] F. Ma, M.A. Hanna, Biodiesel production: a review1Journal Series #12109, Agricultural Research Division, Institute of Agriculture and Natural Resources, University of Nebraska–Lincoln.1, Bioresour. Technol. 70 (1999) 1–15. doi:10.1016/S0960-8524(99)00025-5.

[63] M.K. Lam, K.T. Lee, A.R. Mohamed, Homogeneous, heterogeneous and enzymatic catalysis for transesterification of high free fatty acid oil (waste cooking oil) to biodiesel:

A review, Biotechnol. Adv. 28 (2010) 500–518. doi:10.1016/j.biotechadv.2010.03.002.

[64] S.J. Clark, L. Wagner, M.D. Schrock, P.G. Piennaar, Methyl and ethyl soybean esters as renewable fuels for diesel engines, J. Am. Oil Chem. Soc. 61 (1984) 1632–1638. doi:10.1007/BF02541648.

[65] P.R. Muniyappa, S.C. Brammer, H. Noureddini, Improved conversion of plant oils and animal fats into biodiesel and co-product, Bioresour. Technol. 56 (1996) 19–24. doi:10.1016/0960-8524(95)00178-6.

[66] K. Sivaramakrishnan, P. Ravikumar, Determination of cetane number of biodiesel and it's influence on physical properties, ARPN J. Eng. Appl. Sci. 7 (2012) 205–211.

[67] S. V Ranganathan, S.L. Narasimhan, K. Muthukumar, An overview of enzymatic production of biodiesel, Bioresour. Technol. 99 (2008) 3975–3981. doi:Doi 10.1016/J.Biortech.2007.04.060.

[68] D.Y.C. Leung, X. Wu, M.K.H. Leung, A review on biodiesel production using catalyzed transesterification, Appl. Energy. 87 (2010) 1083–1095. doi:10.1016/j.apenergy.2009.10.006.

[69] J.M. Marchetti, V.U. Miguel, A.F. Errazu, Possible methods for biodiesel production, Renew. Sustain. Energy Rev. 11 (2007) 1300–1311. doi:10.1016/j.rser.2005.08.006.

[70] C.C.C.M. Silva, N.F.P. Ribeiro, M.M.V.M. Souza, D.A.G. Aranda, Biodiesel production from soybean oil and methanol using hydrotalcites as catalyst, Fuel Process. Technol. 91 (2010) 205–210. doi:10.1016/j.fuproc.2009.09.019.

[71] V.V. Bokade, G.D. Yadav, Synthesis of Bio-Diesel and Bio-Lubricant by Transesterification of Vegetable Oil with Lower and Higher Alcohols Over Heteropolyacids Supported by Clay (K-10), Process Saf. Environ. Prot. 85 (2007) 372–377. doi:10.1205/psep06073.

[72] S. Saka, D. Kusdiana, Biodiesel fuel from rapeseed oil as prepared in supercritical methanol, Fuel. 80 (2001) 225–231. doi:10.1016/S0016-2361(00)00083-1.

[73] M. Çetinkaya, F. Karaosmanoğlu, Optimization of Base-Catalyzed Transesterification Reaction of Used Cooking Oil, Energy & Fuels. 18 (2004) 1888–1895. doi:10.1021/ef049891c.

[74] W. Xie, H. Peng, L. Chen, Calcined Mg-Al hydrotalcites as solid base catalysts for methanolysis of soybean oil, J. Mol. Catal. A Chem. 246 (2006) 24–32. doi:10.1016/j.molcata.2005.10.008.

[75] J.F.P. Gomes, J.F.B. Puna, L.M. Gon??alves, J.C.M. Bordado, Study on the use of MgAl hydrotalcites as solid heterogeneous catalysts for biodiesel production, Energy. 36 (2011) 6770–6778. doi:10.1016/j.energy.2011.10.024.

[76] S. Furuta, H. Matsuhashi, K. Arata, Biodiesel fuel production with solid superacid catalysis in fixed bed reactor under atmospheric pressure, Catal. Commun. 5 (2004) 721–723. doi:10.1016/j.catcom.2004.09.001.

[77] M. Ayoub, A.Z. Abdullah, Critical review on the current scenario and significance of crude glycerol resulting from biodiesel industry towards more sustainable renewable energy industry, Renew. Sustain. Energy Rev. 16 (2012) 2671–2686. doi:10.1016/j.rser.2012.01.054.

[78] A.B. Leoneti, V. Aragão-Leoneti, S.V.W.B. de Oliveira, Glycerol as a by-product of biodiesel production in Brazil: Alternatives for the use of unrefined glycerol, Renew. Energy. 45 (2012) 138–145. doi:10.1016/j.renene.2012.02.032.

[79] C.A.G. Quispe, C.J.R. Coronado, J.A. Carvalho, Glycerol: Production, consumption, prices, characterization and new trends in combustion, Renew. Sustain. Energy Rev. 27 (2013) 475–493. doi:10.1016/j.rser.2013.06.017.

[80] N.M. Kosamia, M. Samavi, B.K. Uprety, S.K. Rakshit, Valorization of Biodiesel Byproduct Crude Glycerol for the Production of Bioenergy and Biochemicals, Catalysts. 10 (2020) 609. doi:10.3390/catal10060609.

[81] S. Veluturla, N. Archna, D. Subba Rao, N. Hezil, I.S. Indraja, S. Spoorthi, Catalytic valorization of raw glycerol derived from biodiesel: a review, Biofuels. 9 (2018) 305–314. doi:10.1080/17597269.2016.1266234.

[82] M. Checa, S. Nogales-Delgado, V. Montes, J.M. Encinar, Recent Advances in Glycerol Catalytic Valorization: A Review, Catalysts. 10 (2020) 1279. doi:10.3390/catal10111279.

[83] S.C. Kim, Y.H. Kim, H. Lee, D.Y. Yoon, B.K. Song, Lipase-catalyzed synthesis of glycerol carbonate from renewable glycerol and dimethyl carbonate through transesterification, J. Mol. Catal. B Enzym. 49 (2007) 75–78. doi:10.1016/j.molcatb.2007.08.007.

[84] F.S.H. Simanjuntak, T.K. Kim, S.D. Lee, B.S. Ahn, H.S. Kim, H. Lee, CaO-catalyzed synthesis of glycerol carbonate from glycerol and dimethyl carbonate: Isolation and characterization of an active Ca species, Appl. Catal. A Gen. 401 (2011) 220–225. doi:10.1016/j.apcata.2011.05.024.

[85] M.J. Climent, A. Corma, P. De Frutos, S. Iborra, M. Noy, A. Velty, P. Concepción, Chemicals from biomass: Synthesis of glycerol carbonate by transesterification and carbonylation with urea with hydrotalcite catalysts. The role of acid-base pairs, J. Catal. 269 (2010) 140–149. doi:10.1016/j.jcat.2009.11.001.

[86] M. Malyaadri, K. Jagadeeswaraiah, P.S. Sai Prasad, N. Lingaiah, Synthesis of glycerol carbonate by transesterification of glycerol with dimethyl carbonate over Mg/Al/Zr catalysts, Appl. Catal. A Gen. 401 (2011) 153–157. doi:10.1016/j.apcata.2011.05.011.

[87] K.T. Tan, K.T. Lee, A.R. Mohamed, Optimization of supercritical dimethyl carbonate

(SCDMC) technology for the production of biodiesel and value-added glycerol carbonate, Fuel. 89 (2010) 3833–3839. doi:10.1016/j.fuel.2010.07.010.

[88] G.D. Yadav, P.A. Chandan, A green process for glycerol valorization to glycerol carbonate over heterogeneous hydrotalcite catalyst, Catal. Today. 237 (2014) 47–53. doi:10.1016/j.cattod.2014.01.043.

[89] M.O. Sonnati, S. Amigoni, E.P. Taffin de Givenchy, T. Darmanin, O. Choulet, F. Guittard, Glycerol carbonate as a versatile building block for tomorrow: synthesis, reactivity, properties and applications, Green Chem. 15 (2013) 283–306. doi:10.1039/C2GC36525A.

[90] Z. Ilham, S. Saka, Optimization of supercritical dimethyl carbonate method for biodiesel production, Fuel. 97 (2012) 670–677. doi:10.1016/j.fuel.2012.02.066.

[91] B.M. Panchal, S.B. Dhoot, S.A. Deshmukh, M.R. Sharma, M.S. Kachole, Production of DMC-BioD from Pongamia pinnata seed oil using dimethyl carbonate, Fuel. 109 (2013) 201–205. doi:10.1016/j.fuel.2012.12.052.

[92] F.A. Dawodu, O.O. Ayodele, J. Xin, S. Zhang, Dimethyl carbonate mediated production of biodiesel at different reaction temperatures, Renew. Energy. 68 (2014) 581–587. doi:10.1016/j.renene.2014.02.036.

[93] J.A. Melero, R. van Grieken, G. Morales, M. Paniagua, Acidic Mesoporous Silica for the Acetylation of Glycerol: Synthesis of Bioadditives to Petrol Fuel, Energy & Fuels. 21 (2007) 1782–1791. doi:10.1021/ef060647q.

[94] G. Morales, M. Paniagua, J.A. Melero, G. Vicente, C. Ochoa, Sulfonic acid-functionalized catalysts for the valorization of glycerol via transesterification with methyl acetate, Ind. Eng. Chem. Res. (2011). doi:10.1021/ie102357c.

[95] J. Keogh, M.S. Tiwari, H. Manyar, Esterification of Glycerol with Acetic Acid Using Nitrogen-Based Brønsted-Acidic Ionic Liquids, Ind. Eng. Chem. Res. 58 (2019) 17235–17243. doi:10.1021/acs.iecr.9b01223.

[96] Z. Sustere, V. Kampars, Chemical Interesterification of the Rapeseed Oil with Methyl Acetate in the Presence of Potassium tert-Butoxide in tert-Butanol, Int. J. Eng. Tech. Res. 3 (2015) 226–232. https://www.erpublication.org/published_paper/IJETR033244.pdf.

[97] A. Casas, M.J. Ramos, Á. Pérez, Kinetics of chemical interesterification of sunflower oil with methyl acetate for biodiesel and triacetin production, Chem. Eng. J. 171 (2011) 1324–1332. doi:10.1016/j.cej.2011.05.037.

[98] S. Saka, Y. Isayama, Z. Ilham, X. Jiayu, New process for catalyst-free biodiesel production using subcritical acetic acid and supercritical methanol, Fuel. 89 (2010) 1442–1446. doi:10.1016/j.fuel.2009.10.018.

[99] P. Roffia, P. Calini, S. Tonti, Methyl acetate: by-product in the terephthalic acid

production process. Mechanisms and rates of formation and decomposition in oxidation, Ind. Eng. Chem. Res. 27 (1988) 765–770. doi:10.1021/ie00077a008.

[100] P. Nilges, U. Schröder, Electrochemistry for biofuel generation: production of furans by electrocatalytic hydrogenation of furfurals, Energy Environ. Sci. 6 (2013) 2925. doi:10.1039/c3ee41857j.

[101] Z. Li, S. Kelkar, C.H. Lam, K. Luczek, J.E. Jackson, D.J. Miller, C.M. Saffron, Aqueous electrocatalytic hydrogenation of furfural using a sacrificial anode, Electrochim. Acta. 64 (2012) 87–93. doi:10.1016/j.electacta.2011.12.105.

[102] M.J. Climent, A. Corma, S. Iborra, Conversion of biomass platform molecules into fuel additives and liquid hydrocarbon fuels, Green Chem. 16 (2014) 516. doi:10.1039/c3gc41492b.

[103] J.C. Serrano-Ruiz, R. Luque, A. Sepúlveda-Escribano, Transformations of biomass-derived platform molecules: from high added-value chemicals to fuels via aqueous-phase processing, Chem. Soc. Rev. 40 (2011) 5266. doi:10.1039/c1cs15131b.

[104] R.S. Malkar, H. Daly, C. Hardacre, G.D. Yadav, Novelty of iron-exchanged heteropolyacid encapsulated inside ZIF-8 as an active and superior catalyst in the esterification of furfuryl alcohol and acetic acid, React. Chem. Eng. 4 (2019) 1790–1802. doi:10.1039/c9re00167k.

[105] P. Bhaumik, P.L. Dhepe, Solid acid catalyzed synthesis of furans from carbohydrates, Catal. Rev. 58 (2016) 36–112. doi:10.1080/01614940.2015.1099894.

[106] X.H. Chadderdon, D.J. Chadderdon, J.E. Matthiesen, Y. Qiu, J.M. Carraher, J.P. Tessonnier, W. Li, Mechanisms of Furfural Reduction on Metal Electrodes: Distinguishing Pathways for Selective Hydrogenation of Bioderived Oxygenates, J. Am. Chem. Soc. 139 (2017) 14120–14128. doi:10.1021/jacs.7b06331.

[107] F. Wang, M. Xu, L. Wei, Y. Wei, Y. Hu, W. Fang, C.G. Zhu, Fabrication of La-doped TiO2Film Electrode and investigation of its electrocatalytic activity for furfural reduction, Electrochim. Acta. 153 (2015) 170–174. doi:10.1016/j.electacta.2014.11.203.

[108] Y. Cao, T. Noël, Efficient Electrocatalytic Reduction of Furfural to Furfuryl Alcohol in a Microchannel Flow Reactor, Org. Process Res. Dev. 23 (2019) 403–408. doi:10.1021/acs.oprd.8b00428.

[109] S. Jung, E.J. Biddinger, Electrocatalytic Hydrogenation and Hydrogenolysis of Furfural and the Impact of Homogeneous Side Reactions of Furanic Compounds in Acidic Electrolytes, ACS Sustain. Chem. Eng. 4 (2016) 6500–6508. doi:10.1021/acssuschemeng.6b01314.

[110] F. Dong, Y. Zhu, H. Zheng, Y. Zhu, X. Li, Y. Li, Cr-free Cu-catalysts for the selective hydrogenation of biomass-derived furfural to 2-methylfuran: The synergistic effect of metal and acid sites, J. Mol. Catal. A Chem. 398 (2015) 140–148.

doi:10.1016/j.molcata.2014.12.001.

[111] P. Parpot, A.P. Bettencourt, G. Chamoulaud, K.B. Kokoh, E.M. Belgsir, Electrochemical investigations of the oxidation-reduction of furfural in aqueous medium - Application to electrosynthesis, Electrochim. Acta. 49 (2004) 397–403. doi:10.1016/j.electacta.2003.08.021.

[112] A.A. Rosatella, S.P. Simeonov, R.F.M. Frade, C.A.M. Afonso, 5-Hydroxymethylfurfural (HMF) as a building block platform: Biological properties, synthesis and synthetic applications, Green Chem. 13 (2011) 754. doi:10.1039/c0gc00401d.

[113] J.M.R. Gallo, D.M. Alonso, M.A. Mellmer, J.A. Dumesic, Production and upgrading of 5-hydroxymethylfurfural using heterogeneous catalysts and biomass-derived solvents, Green Chem. 15 (2013) 85–90. doi:10.1039/C2GC36536G.

[114] J.J. Roylance, K.-S. Choi, Electrochemical reductive biomass conversion: direct conversion of 5-hydroxymethylfurfural (HMF) to 2,5-hexanedione (HD) via reductive ring-opening, Green Chem. 18 (2016) 2956–2960. doi:10.1039/C6GC00533K.

[115] W. Guo, H. Liu, S. Zhang, H. Han, H. Liu, T. Jiang, B. Han, T. Wu, Efficient hydrogenolysis of 5-hydroxymethylfurfural to 2,5-dimethylfuran over a cobalt and copper bimetallic catalyst on N-graphene-modified Al 2 O 3, Green Chem. 18 (2016) 6222–6228. doi:10.1039/C6GC02630C.

[116] A. Villa, M. Schiavoni, S. Campisi, G.M. Veith, L. Prati, Pd-modified Au on Carbon as an Effective and Durable Catalyst for the Direct Oxidation of HMF to 2,5-Furandicarboxylic Acid, ChemSusChem. 6 (2013) 609–612. doi:10.1002/cssc.201200778.

[117] R.S. Malkar, H. Daly, C. Hardacre, G.D. Yadav, Aldol Condensation of 5-Hydroxymethylfurfural to Fuel Precursor over Novel Aluminum Exchanged-DTP@ZIF-8, ACS Sustain. Chem. Eng. 7 (2019) 16215–16224. doi:10.1021/acssuschemeng.9b02939.

[118] I. Delidovich, P.J.C. Hausoul, L. Deng, R. Pfützenreuter, M. Rose, R. Palkovits, Alternative Monomers Based on Lignocellulose and Their Use for Polymer Production, Chem. Rev. 116 (2016) 1540–1599. doi:10.1021/acs.chemrev.5b00354.

[119] G.D. Yadav, A.R. Yadav, Synthesis of ethyl levulinate as fuel additives using heterogeneous solid superacidic catalysts: Efficacy and kinetic modeling, Chem. Eng. J. 243 (2014) 556–563. doi:10.1016/j.cej.2014.01.013.

[120] S. Kang, J. Fu, G. Zhang, From lignocellulosic biomass to levulinic acid: A review on acid-catalyzed hydrolysis, Renew. Sustain. Energy Rev. 94 (2018) 340–362. doi:10.1016/j.rser.2018.06.016.

[121] M. Balakrishnan, E.R. Sacia, A.T. Bell, Etherification and reductive etherification of 5-(hydroxymethyl)furfural: 5-(alkoxymethyl)furfurals and 2,5-bis(alkoxymethyl)furans as potential bio-diesel candidates, Green Chem. 14 (2012) 1626. doi:10.1039/c2gc35102a.

[122] M. Chidambaram, A.T. Bell, A two-step approach for the catalytic conversion of glucose to 2,5-dimethylfuran in ionic liquids, Green Chem. 12 (2010) 1253. doi:10.1039/c004343e.

[123] L. Hu, X. Tang, J. Xu, Z. Wu, L. Lin, S. Liu, Selective Transformation of 5-Hydroxymethylfurfural into the Liquid Fuel 2,5-Dimethylfuran over Carbon-Supported Ruthenium, Ind. Eng. Chem. Res. 53 (2014) 3056–3064. doi:10.1021/ie404441a.

[124] J. Jae, W. Zheng, R.F. Lobo, D.G. Vlachos, Production of Dimethylfuran from Hydroxymethylfurfural through Catalytic Transfer Hydrogenation with Ruthenium Supported on Carbon, ChemSusChem. 6 (2013) 1158–1162. doi:10.1002/cssc.201300288.

[125] D. Song, S. An, B. Lu, Y. Guo, J. Leng, Arylsulfonic acid functionalized hollow mesoporous carbon spheres for efficient conversion of levulinic acid or furfuryl alcohol to ethyl levulinate, Appl. Catal. B Environ. 179 (2015) 445–457. doi:10.1016/j.apcatb.2015.05.047.

[126] B. Girisuta, L.P.B.M. Janssen, H.J. Heeres, A kinetic study on the decomposition of 5-hydroxymethylfurfural into levulinic acid, Green Chem. 8 (2006) 701. doi:10.1039/b518176c.

[127] Z. Zhang, K. Deng, Recent Advances in the Catalytic Synthesis of 2,5-Furandicarboxylic Acid and Its Derivatives, ACS Catal. 5 (2015) 6529–6544. doi:10.1021/acscatal.5b01491.

[128] B. Liu, Y. Ren, Z. Zhang, Aerobic oxidation of 5-hydroxymethylfurfural into 2,5-furandicarboxylic acid in water under mild conditions, Green Chem. 17 (2015) 1610–1617. doi:10.1039/C4GC02019G.

[129] E.R. Sacia, M. Balakrishnan, A.T. Bell, Biomass conversion to diesel via the etherification of furanyl alcohols catalyzed by Amberlyst-15, J. Catal. 313 (2014) 70–79. doi:10.1016/j.jcat.2014.02.012.

[130] L. Hu, J. Xu, S. Zhou, A. He, X. Tang, L. Lin, J. Xu, Y. Zhao, Catalytic Advances in the Production and Application of Biomass-Derived 2,5-Dihydroxymethylfuran, ACS Catal. (2018) 2959–2980. doi:10.1021/acscatal.7b03530.

[131] D. Sun, S. Chiba, Y. Yamada, S. Sato, Vapor-phase intramolecular aldol condensation of 2,5-hexanedione to 3-methylcyclopent-2-enone over ZrO2-supported Li2O catalyst, Catal. Commun. 92 (2017) 105–108. doi:10.1016/j.catcom.2017.01.010.

[132] M. Besson, P. Gallezot, C. Pinel, Conversion of biomass into chemicals over metal catalysts, Chem. Rev. 114 (2014) 1827–1870. doi:10.1021/cr4002269.

[133] Z. Yuan, Z. Zhang, J. Zheng, J. Lin, Efficient synthesis of promising liquid fuels 5-ethoxymethylfurfural from carbohydrates, Fuel. 150 (2015) 236–242. doi:10.1016/j.fuel.2015.02.020.

[134] P. Che, F. Lu, J. Zhang, Y. Huang, X. Nie, J. Gao, J. Xu, Catalytic selective etherification

of hydroxyl groups in 5-hydroxymethylfurfural over H4SiW12O40/MCM-41 nanospheres for liquid fuel production, Bioresour. Technol. 119 (2012) 433–436. doi:10.1016/j.biortech.2012.06.001.

[135] S. Wang, Z. Zhang, B. Liu, J. Li, Silica coated magnetic Fe3O4 nanoparticles supported phosphotungstic acid: a novel environmentally friendly catalyst for the synthesis of 5-ethoxymethylfurfural from 5-hydroxymethylfurfural and fructose, Catal. Sci. Technol. 3 (2013) 2104. doi:10.1039/c3cy00223c.

[136] G.A. Kraus, T. Guney, A direct synthesis of 5-alkoxymethylfurfural ethers from fructose via sulfonic acid-functionalized ionic liquids, Green Chem. 14 (2012) 1593. doi:10.1039/c2gc35175g.

[137] L. Bing, Z. Zhang, K. Deng, Efficient One-Pot Synthesis of 5-(Ethoxymethyl)furfural from Fructose Catalyzed by a Novel Solid Catalyst, Ind. Eng. Chem. Res. 51 (2012) 15331–15336. doi:10.1021/ie3020445.

[138] K.S. Arias, M.J. Climent, A. Corma, S. Iborra, Biomass-Derived Chemicals: Synthesis of Biodegradable Surfactant Ether Molecules from Hydroxymethylfurfural, ChemSusChem. 7 (2014) 210–220. doi:10.1002/cssc.201300531.

[139] V. Cottier, Louis; Descotes, Gerard; Nigay, Henri; Parron, Jean-Claude; Gregoire, Photo-oxygenation des derives de l'hydroxymethyl-5 furfural-2, Bull. Soc. Chim. Fr. 5 (1986) 844 – 850.

[140] G.J.M. Gruter, Hydroxymethylfurfural ethers from sugars and di- and triols, EP2033958 A1, 2009.

[141] S.H. Fogler, Essentials of Chemical Reaction Engineering, 2nd ed., Pearson, 2017.

[142] R. Schlögl, Heterogeneous Catalysis, Angew. Chemie Int. Ed. 54 (2015) 3465–3520. doi:10.1002/anie.201410738.

[143] A. Corma, H. Garcia, Crossing the Borders Between Homogeneous and Heterogeneous Catalysis: Developing Recoverable and Reusable Catalytic Systems, Top. Catal. 48 (2008) 8–31. doi:10.1007/s11244-008-9056-5.

[144] K. Tanabe, Industrial application of solid acid–base catalysts, Appl. Catal. A Gen. 181 (1999) 399–434. doi:10.1016/S0926-860X(98)00397-4.

[145] L. Xin, Electrocatalytic Processing of Renewable Biomass-Derived Compounds for Production of Chemicals , Fuels and Electricity, (2014).

[146] J.O. Bockris, H. Wroblowa, Electrocatalysis, J. Electroanal. Chem. 7 (1964) 428–451. doi:10.1016/0022-0728(64)80123-6.

[147] Z.W. Seh, J. Kibsgaard, C.F. Dickens, I. Chorkendorff, J.K. Nørskov, T.F. Jaramillo, Combining theory and experiment in electrocatalysis: Insights into materials design,

Science (80-.). 355 (2017) eaad4998. doi:10.1126/science.aad4998.

[148] R. Ameta, M.S. Solanki, S. Benjamin, S.C. Ameta, Photocatalysis, in: S.C. Ameta, R.B.T.-A.O.P. for W.W.T. Ameta (Eds.), Adv. Oxid. Process. Waste Water Treat., Elsevier, 2018: pp. 135–175. doi:10.1016/B978-0-12-810499-6.00006-1.

[149] A. Schmid, J.S. Dordick, B. Hauer, A. Kiener, M. Wubbolts, B. Witholt, Industrial biocatalysis today and tomorrow, Nature. 409 (2001) 258–268. doi:10.1038/35051736.

[150] A. Dutta, J.A. Schaidle, D. Humbird, F.G. Baddour, A. Sahir, Conceptual Process Design and Techno-Economic Assessment of Ex Situ Catalytic Fast Pyrolysis of Biomass: A Fixed Bed Reactor Implementation Scenario for Future Feasibility, Top. Catal. 59 (2016) 2–18. doi:10.1007/s11244-015-0500-z.

[151] M.P. Gimeno, J. Soler, J. Herguido, M. Menéndez, Counteracting Catalyst Deactivation in Methane Aromatization with a Two Zone Fluidized Bed Reactor, Ind. Eng. Chem. Res. 49 (2010) 996–1000. doi:10.1021/ie900682y.

[152] M.S. Tiwari, G.D. Yadav, Novel aluminium exchanged dodecatungstophosphoric acid supported on K-10 clay as catalyst: benzoylation of diphenyloxide with benzoic anhydride, RSC Adv. 6 (2016) 49091–49100. doi:10.1039/C6RA05379C.

[153] S.L. Bhanawase, G.D. Yadav, Activity and selectivity of different base catalysts in synthesis of guaifenesin from guaiacol and glycidol of biomass origin, Catal. Today. (2017). doi:10.1016/j.cattod.2016.12.008.

[154] G. Horányi, Heterogeneous catalysis and electrocatalysis, Catal. Today. 19 (1994) 285–311. doi:10.1016/0920-5861(94)80188-6.

[155] J.O. Bockris, S. Srinivasan, Fuel Cells: Their Electrochemistry, New York: McGraw-Hill, 1969.

[156] N. Jiang, X. Liu, J. Dong, B. You, X. Liu, Y. Sun, Electrocatalysis of Furfural Oxidation Coupled with H_2 Evolution via Nickel-Based Electrocatalysts in Water, ChemNanoMat. 3 (2017) 491–495. doi:10.1002/cnma.201700076.

[157] X. Zhang, M. Han, G. Liu, G. Wang, Y. Zhang, H. Zhang, H. Zhao, Simultaneously high-rate furfural hydrogenation and oxidation upgrading on nanostructured transition metal phosphides through electrocatalytic conversion at ambient conditions, Appl. Catal. B Environ. 244 (2019) 899–908. doi:10.1016/j.apcatb.2018.12.025.

[158] S. Jung, A.N. Karaiskakis, E.J. Biddinger, Enhanced activity for electrochemical hydrogenation and hydrogenolysis of furfural to biofuel using electrodeposited Cu catalysts, Catal. Today. 323 (2019) 26–34. doi:10.1016/j.cattod.2018.09.011.

[159] J.J. Roylance, T.W. Kim, K.S. Choi, Efficient and Selective Electrochemical and Photoelectrochemical Reduction of 5-Hydroxymethylfurfural to 2,5-Bis(hydroxymethyl)furan using Water as the Hydrogen Source, ACS Catal. 6 (2016)

1840–1847. doi:10.1021/acscatal.5b02586.

[160] D.J. Chadderdon, L. Xin, J. Qi, Y. Qiu, P. Krishna, K.L. More, W. Li, Electrocatalytic oxidation of 5-hydroxymethylfurfural to 2,5-furandicarboxylic acid on supported Au and Pd bimetallic nanoparticles, Green Chem. 16 (2014) 3778–3786. doi:10.1039/C4GC00401A.

[161] S. Jung, E.J. Biddinger, Controlling Competitive Side Reactions in the Electrochemical Upgrading of Furfural to Biofuel, Energy Technol. 6 (2018) 1370–1379. doi:10.1002/ente.201800216.

[162] T.F. Fuller, J.N. Harb, Electrochemical Engineering, 1st ed., 2018 John Wiley & Sons, Inc, 2018.

[163] E. Roduner, Selected fundamentals of catalysis and electrocatalysis in energy conversion reactions—A tutorial, Catal. Today. 309 (2018) 263–268. doi:10.1016/j.cattod.2017.05.091.

[164] C. Gumeci, Z. Li, D.J. Casadonte, C. Korzeniewski, Pt-Ni Nanoparticles for Oxygen Reduction Prepared by a Sonochemical Method, J. Electrochem. Soc. 159 (2012) F35–F41. doi:10.1149/2.029203jes.

[165] D.H. Won, H. Shin, J. Koh, J. Chung, H.S. Lee, H. Kim, S.I. Woo, Highly Efficient, Selective, and Stable CO 2 Electroreduction on a Hexagonal Zn Catalyst, Angew. Chemie Int. Ed. 55 (2016) 9297–9300. doi:10.1002/anie.201602888.

[166] A. Roy, D. Hursán, K. Artyushkova, P. Atanassov, C. Janáky, A. Serov, Nanostructured metal-N-C electrocatalysts for CO2 reduction and hydrogen evolution reactions, Appl. Catal. B Environ. 232 (2018) 512–520. doi:10.1016/j.apcatb.2018.03.093.

[167] M. Grotheer, R.C. Alkire, R. Varjian, V. Srinivasan, J.W. Weidner, Industrial Electrolysis and Electrochemical Engineering, Electrochem. Soc. Interface. 15 (2006) 52–54. doi:10.1149/2.F15061IF.

[168] G.G. Botte, Electrochemical Manufacturing in the Chemical Industry, Interface Mag. 23 (2014) 49–55. doi:10.1149/2.F04143if.

[169] C.A.C. Sequeira, D.M.F. Santos, Electrochemical routes for industrial synthesis, J. Braz. Chem. Soc. 20 (2009) 387–406. doi:10.1590/S0103-50532009000300002.

[170] D. Tountian, A. Brisach-Wittmeyer, P. Nkeng, G. Poillerat, H. Ménard, Effect of support conductivity of catalytic powder on electrocatalytic hydrogenation of phenol, J. Appl. Electrochem. 39 (2009) 411–419. doi:10.1007/s10800-008-9686-0.

[171] a Bard, L. Faulkner, Allen J. Bard and Larry R. Faulkner, Electrochemical Methods: Fundamentals and Applications, New York: Wiley, 2001, 2002. doi:10.1023/A:1021637209564.

[172] L.M. Torres, A.F. Gil, L. Galicia, I. González, Understanding the Difference between Inner- and Outer-Sphere Mechanisms: An Electrochemical Experiment, J. Chem. Educ. 73 (1996) 808. doi:10.1021/ed073p808.

[173] L. Nadjo, J.M. Saveant, Dimerization, disproportionation and e.c.e. mechanisms in the reduction of aromatic carbonyl compounds in alkaline media, J. Electroanal. Chem. 33 (1971) 419–451. doi:10.1016/S0022-0728(71)80127-4.

[174] F.-X. Felpin, E. Fouquet, Heterogeneous Multifunctional Catalysts for Tandem Processes: An Approach toward Sustainability, ChemSusChem. 1 (2008) 718–724. doi:10.1002/cssc.200800110.

[175] M. Zhao, K. Deng, L. He, Y. Liu, G. Li, H. Zhao, Z. Tang, Core–Shell Palladium Nanoparticle@Metal–Organic Frameworks as Multifunctional Catalysts for Cascade Reactions, J. Am. Chem. Soc. 136 (2014) 1738–1741. doi:10.1021/ja411468e.

[176] M.J. Climent, A. Corma, S. Iborra, Heterogeneous Catalysts for the One-Pot Synthesis of Chemicals and Fine Chemicals, Chem. Rev. 111 (2011) 1072–1133. doi:10.1021/cr1002084.

[177] Y. Zhang, C. Huang, L. Mi, Metal–organic frameworks as acid- and/or base-functionalized catalysts for tandem reactions, Dalt. Trans. 49 (2020) 14723–14730. doi:10.1039/D0DT03025B.

[178] M. Tao, Dan Zhang, H. Guan, G. Huang, X. Wang, Designation of highly efficient catalysts for one pot conversion of glycerol to lactic acid, Sci. Rep. 6 (2016) 29840. doi:10.1038/srep29840.

[179] Y. Yuan, S. Adimi, T. Thomas, J. Wang, H. Guo, J. Chen, J.P. Attfield, F.J. DiSalvo, M. Yang, Co3Mo3N—An efficient multifunctional electrocatalyst, Innov. 2 (2021) 100096. doi:10.1016/j.xinn.2021.100096.

[180] Y. Zhu, X. Cui, H. Liu, Z. Guo, Y. Dang, Z. Fan, Z. Zhang, W. Hu, Tandem catalysis in electrochemical CO2 reduction reaction, Nano Res. 12 (2021). doi:10.1007/s12274-021-3448-2.

[181] H. Hattori, Solid base catalysts: generation of basic sites and application to organic synthesis, Appl. Catal. A Gen. 222 (2001) 247–259. doi:10.1016/S0926-860X(01)00839-0.

[182] Y. Ono, Solid base catalysts for the synthesis of fine chemicals, J. Catal. 216 (2003) 406–415. doi:10.1016/S0021-9517(02)00120-3.

[183] H. Hattori, Heterogeneous Basic Catalysis, Chem. Rev. 95 (1995) 537–558. doi:10.1021/cr00035a005.

[184] D. Kwon, J.Y. Kang, S. An, I. Yang, J.C. Jung, Tuning the base properties of Mg–Al hydrotalcite catalysts using their memory effect, J. Energy Chem. 46 (2020) 229–236.

doi:10.1016/j.jechem.2019.11.013.

[185] H. Hattori, Solid base catalysts: fundamentals and their applications in organic reactions, Appl. Catal. A Gen. 504 (2015) 103–109. doi:10.1016/j.apcata.2014.10.060.

[186] D.-W. Lee, Y.-M. Park, K.-Y. Lee, Heterogeneous Base Catalysts for Transesterification in Biodiesel Synthesis, Catal. Surv. from Asia. 13 (2009) 63–77. doi:10.1007/s10563-009-9068-6.

[187] T. Jose, J. Ftouni, P.C.A. Bruijnincx, Structured hydroxyapatite composites as efficient solid base catalysts for condensation reactions, Catal. Sci. Technol. 11 (2021) 3428–3436. doi:10.1039/D1CY00102G.

[188] T.C. Keller, S. Isabettini, D. Verboekend, E.G. Rodrigues, J. Pérez-Ramírez, Hierarchical high-silica zeolites as superior base catalysts, Chem. Sci. 5 (2014) 677–684. doi:10.1039/C3SC51937F.

[189] F. Cavani, F. Trifirò, A. Vaccari, Hydrotalcite-type anionic clays: Preparation, properties and applications., Catal. Today. 11 (1991) 173–301. doi:10.1016/0920-5861(91)80068-K.

[190] S.S. Shafiei, M. Solati-Hashjin, H. Rahim-Zadeh, A. Samadikuchaksaraei, Synthesis and characterisation of nanocrystalline Ca–Al layered double hydroxide {[Ca 2 Al(OH) 6]NO 3 .nH 2 O}: in vitro study, Adv. Appl. Ceram. 112 (2013) 59–65. doi:10.1179/1743676112Y.0000000045.

[191] T. Baskaran, J. Christopher, A. Sakthivel, Progress on layered hydrotalcite (HT) materials as potential support and catalytic materials, RSC Adv. 5 (2015) 98853–98875. doi:10.1039/C5RA19909C.

[192] J.C.A.A. Roelofs, J.A. van Bokhoven, A.J. van Dillen, J.W. Geus, K.P. de Jong, The Thermal Decomposition of Mg-Al Hydrotalcites: Effects of Interlayer Anions and Characteristics of the Final Structure, Chem. - A Eur. J. 8 (2002) 5571–5579. doi:10.1002/1521-3765(20021216)8:24<5571::AID-CHEM5571>3.0.CO;2-R.

[193] K. Wilson, A.F. Lee, Rational design of heterogeneous catalysts for biodiesel synthesis, Catal. Sci. Technol. 2 (2012) 884. doi:10.1039/c2cy20038d.

[194] S. Bhanawase, G. Yadav, Hydrotalcite as Active and Selective Catalyst for Synthesis of Dehydrozingerone from Vanillin and Acetone: Effect of Catalyst Composition and Calcination Temperature on Activity and Selectivity, Curr. Catal. (2016). doi:10.2174/2211544705666161123122411.

[195] P. Gupta, S. Paul, Solid acids: Green alternatives for acid catalysis, Catal. Today. 236 (2014) 153–170. doi:10.1016/j.cattod.2014.04.010.

[196] A. Corma, H. García, Lewis Acids: From Conventional Homogeneous to Green Homogeneous and Heterogeneous Catalysis, Chem. Rev. 103 (2003) 4307–4366. doi:10.1021/cr030680z.

[197] M.S. Tiwari, G.D. Yadav, Kinetics of Friedel-Crafts benzoylation of veratrole with benzoic anhydride using Cs2.5H0.5PW12O40/K-10 solid acid catalyst, Chem. Eng. J. 266 (2015) 64–73. doi:10.1016/j.cej.2014.12.043.

[198] G.D. Yadav, N. Kirthivasan, Single-pot synthesis of methyl tert-butyl ether from tert-butyl alcohol and methanol: dodecatungstophosphoric acid supported on clay as an efficient catalyst, J. Chem. Soc. Chem. Commun. (1995) 203. doi:10.1039/c39950000203.

[199] G.D. Yadav, Synergism of Clay and Heteropoly Acids as Nano-Catalysts for the Development of Green Processes with Potential Industrial Applications, Catal. Surv. from Asia. 9 (2005) 117–137. doi:10.1007/s10563-005-5997-x.

[200] I. V. Kozhevnikov, Catalysis by heteropoly acids and multicomponent polyoxometalates in liquid-phase reactions, Chem. Rev. 98 (1998) 171–198. doi:10.1021/cr960400y.

[201] F. Cavani, Heteropolycompound-based catalysts:, Catal. Today. 41 (1998) 73–86. doi:10.1016/S0920-5861(98)00039-X.

[202] G.D. Yadav, N.S. Asthana, V.S. Kamble, Friedel–Crafts benzoylation of p-xylene over clay supported catalysts: novelty of cesium substituted dodecatungstophosphoric acid on K-10 clay, Appl. Catal. A Gen. 240 (2003) 53–69. doi:10.1016/S0926-860X(02)00418-0.

[203] I. V Kozhevnikov, K.I. Matveev, N.M. Emanuel, Russian Chemical Reviews, Nature. 188 (1960) 453–453. doi:10.1038/188453d0.

[204] K. Narasimharao, D.R. Brown, A.F. Lee, A.D. Newman, P.F. Siril, S.J. Tavener, K. Wilson, Structure-activity relations in Cs-doped heteropolyacid catalysts for biodiesel production, J. Catal. 248 (2007) 226–234. doi:10.1016/j.jcat.2007.02.016.

[205] G.D. Yadav, V.V. Bokade, Novelties of heteropoly acid supported on clay: etherification of phenethyl alcohol with alkanols, Appl. Catal. A Gen. 147 (1996) 299–323. doi:10.1016/S0926-860X(96)00206-2.

[206] V. V. Bokade, G.D. Yadav, Dodecatungstophosphoric Acid Supported on Acidic Clay Catalyst for Disproportionation of Ethylbenzene in the Presence of C 8 Aromatics, Ind. Eng. Chem. Res. 51 (2012) 1209–1217. doi:10.1021/ie202298e.

[207] C. Ramesh Kumar, K.T.V. Rao, P.S. Sai Prasad, N. Lingaiah, Tin exchanged heteropoly tungstate: An efficient catalyst for benzylation of arenes with benzyl alcohol, J. Mol. Catal. A Chem. 337 (2011) 17–24. doi:10.1016/j.molcata.2011.01.008.

[208] K. Shimizu, H. Furukawa, N. Kobayashi, Y. Itaya, A. Satsuma, Effects of Brønsted and Lewis acidities on activity and selectivity of heteropolyacid-based catalysts for hydrolysis of cellobiose and cellulose, Green Chem. 11 (2009) 1627. doi:10.1039/b913737h.

[209] A.K. Ghosh, J.B. Moffat, Acidity of heteropoly compounds, J. Catal. 101 (1986) 238–245. doi:10.1016/0021-9517(86)90249-6.

[210] K. Shimizu, K. Niimi, A. Satsuma, Polyvalent-metal salts of heteropolyacid as efficient heterogeneous catalysts for Friedel–Crafts acylation of arenes with carboxylic acids, Catal. Commun. 9 (2008) 980–983. doi:10.1016/j.catcom.2007.09.030.

[211] X. Jin, T. Fang, J. Wang, M. Liu, S. Pan, B. Subramaniam, J. Shen, C. Yang, R. V. Chaudhari, Nanostructured Metal Catalysts for Selective Hydrogenation and Oxidation of Cellulosic Biomass to Chemicals, Chem. Rec. 19 (2019) 1952–1994. doi:10.1002/tcr.201800144.

[212] Z. Guo, B. Liu, Q. Zhang, W. Deng, Y. Wang, Y. Yang, Recent advances in heterogeneous selective oxidation catalysis for sustainable chemistry, Chem. Soc. Rev. 43 (2014) 3480. doi:10.1039/c3cs60282f.

[213] C. Parmeggiani, F. Cardona, Transition metal based catalysts in the aerobic oxidation of alcohols, Green Chem. 14 (2012) 547. doi:10.1039/c2gc16344f.

[214] S.E. Davis, L.R. Houk, E.C. Tamargo, A.K. Datye, R.J. Davis, Oxidation of 5-hydroxymethylfurfural over supported Pt, Pd and Au catalysts, Catal. Today. 160 (2011) 55–60. doi:10.1016/j.cattod.2010.06.004.

[215] M. Hudlicky, Reductions in organic chemistry, 1984. https://linkinghub.elsevier.com/retrieve/pii/0160932785900560.

[216] B. Zhao, M. Chen, Q. Guo, Y. Fu, Electrocatalytic hydrogenation of furfural to furfuryl alcohol using platinum supported on activated carbon fibers, Electrochim. Acta. 135 (2014) 139–146. doi:10.1016/j.electacta.2014.04.164.

[217] K.J. Carroll, T. Burger, L. Langenegger, S. Chavez, S.T. Hunt, Y. Román-Leshkov, F.R. Brushett, Electrocatalytic Hydrogenation of Oxygenates using Earth-Abundant Transition-Metal Nanoparticles under Mild Conditions, ChemSusChem. (2016) 1904–1910. doi:10.1002/cssc.201600290.

[218] C.M. Mulero, A. Sáez, J. Iniesta, V. Montiel, An alternative to hydrogenation processes. Electrocatalytic hydrogenation of benzophenone, Beilstein J. Org. Chem. 14 (2018) 537–546. doi:10.3762/bjoc.14.40.

[219] S. Srivastava, G.C. Jadeja, J. Parikh, Copper-cobalt catalyzed liquid phase hydrogenation of furfural to 2-methylfuran: An optimization, kinetics and reaction mechanism study, Chem. Eng. Res. Des. 132 (2018) 313–324. doi:10.1016/j.cherd.2018.01.031.

[220] R. Lakra, M.S. Kiran, P.S. Korrapati, Furfural mediated synthesis of silver nanoparticles for photocatalytic reduction of hexavalent chromium, Environ. Technol. Innov. 21 (2021) 101348. doi:10.1016/j.eti.2020.101348.

[221] T. YOSHINO, Surface characteristics and activities of plate-type Raney nickel catalyst, J. Catal. 118 (1989) 436–442. doi:10.1016/0021-9517(89)90330-8.

[222] R. Kothandaraman, V. Nallathambi, K. Artyushkova, S.C. Barton, Non-precious oxygen

reduction catalysts prepared by high-pressure pyrolysis for low-temperature fuel cells, Appl. Catal. B Environ. 92 (2009) 209–216. doi:10.1016/j.apcatb.2009.07.005.

[223] S. Ganesan, N. Leonard, S.C. Barton, Impact of transition metal on nitrogen retention and activity of iron-nitrogen-carbon oxygen reduction catalysts, Phys. Chem. Chem. Phys. 16 (2014) 4576–4585. doi:10.1039/c3cp54751e.

[224] T. Asset, S.T. Garcia, S. Herrera, N. Andersen, Y. Chen, E.J. Peterson, I. Matanovic, K. Artyushkova, J. Lee, S.D. Minteer, S. Dai, X. Pan, K. Chavan, S. Calabrese Barton, P. Atanassov, Investigating the Nature of the Active Sites for the CO 2 Reduction Reaction on Carbon-Based Electrocatalysts, ACS Catal. 9 (2019) 7668–7678. doi:10.1021/acscatal.9b01513.

[225] W. Ju, A. Bagger, X. Wang, Y. Tsai, F. Luo, T. Möller, H. Wang, J. Rossmeisl, A.S. Varela, P. Strasser, Unraveling Mechanistic Reaction Pathways of the Electrochemical CO 2 Reduction on Fe–N–C Single-Site Catalysts, ACS Energy Lett. 4 (2019) 1663–1671. doi:10.1021/acsenergylett.9b01049.

[226] D.L.T. Nguyen, M.S. Jee, D.H. Won, H. Jung, H.S. Oh, B.K. Min, Y.J. Hwang, Selective CO2 Reduction on Zinc Electrocatalyst: The Effect of Zinc Oxidation State Induced by Pretreatment Environment, ACS Sustain. Chem. Eng. 5 (2017) 11377–11386. doi:10.1021/acssuschemeng.7b02460.

[227] Y. Lu, B. Han, C. Tian, J. Wu, D. Geng, D. Wang, Efficient electrocatalytic reduction of CO2 to CO on an electrodeposited Zn porous network, Electrochem. Commun. 97 (2018) 87–90. doi:10.1016/j.elecom.2018.11.002.

[228] J. Rosen, G.S. Hutchings, Q. Lu, R. V. Forest, A. Moore, F. Jiao, Electrodeposited Zn Dendrites with Enhanced CO Selectivity for Electrocatalytic CO2 Reduction, ACS Catal. 5 (2015) 4586–4591. doi:10.1021/acscatal.5b00922.

[229] Y. Song, O.Y. Gutiérrez, J. Herranz, J.A. Lercher, Aqueous phase electrocatalysis and thermal catalysis for the hydrogenation of phenol at mild conditions, Appl. Catal. B Environ. 182 (2016) 236–246. doi:10.1016/j.apcatb.2015.09.027.

[230] A.M. Polcaro, S. Palmas, S. Dernini, Role of Catalyst Characteristics in Electrocatalytic Hydrogenation: Reduction of Benzaldehyde and Acetophenone on Carbon Felt/Pd Electrodes, Ind. Eng. Chem. Res. 32 (1993) 1315–1322. doi:10.1021/ie00019a005.

[231] J.M. Friedrich, C. Ponce-de-León, G.W. Reade, F.C. Walsh, Reticulated vitreous carbon as an electrode material, J. Electroanal. Chem. (2004). doi:10.1016/j.jelechem.2003.07.019.

[232] W. Xue, Q. Zhou, F. Li, B.S. Ondon, Zeolitic imidazolate framework-8 (ZIF-8) as robust catalyst for oxygen reduction reaction in microbial fuel cells, J. Power Sources. 423 (2019) 9–17. doi:10.1016/j.jpowsour.2019.03.017.

[233] L. Shang, H. Yu, X. Huang, T. Bian, R. Shi, Y. Zhao, G.I.N. Waterhouse, L.Z. Wu, C.H.

Tung, T. Zhang, Well-Dispersed ZIF-Derived Co,N-Co-doped Carbon Nanoframes through Mesoporous-Silica-Protected Calcination as Efficient Oxygen Reduction Electrocatalysts, Adv. Mater. 28 (2016) 1668–1674. doi:10.1002/adma.201505045.

[234] Z. Li, M. Shao, L. Zhou, Q. Yang, C. Zhang, M. Wei, D.G. Evans, X. Duan, Carbon-based electrocatalyst derived from bimetallic metal-organic framework arrays for high performance oxygen reduction, Nano Energy. 25 (2016) 100–109. doi:10.1016/j.nanoen.2016.04.041.

[235] X. Chen, K. Shen, J. Chen, B. Huang, D. Ding, L. Zhang, Y. Li, Rational design of hollow N/Co-doped carbon spheres from bimetal-ZIFs for high-efficiency electrocatalysis, Chem. Eng. J. 330 (2017) 736–745. doi:10.1016/j.cej.2017.08.024.

[236] M. Wu, X. Hu, C. Li, J. Li, H. Zhou, X. Zhang, R. Liu, Encapsulation of metal precursor within ZIFs for bimetallic N-doped carbon electrocatalyst with enhanced oxygen reduction, Int. J. Hydrogen Energy. 43 (2018) 14701–14709. doi:10.1016/j.ijhydene.2018.05.160.

[237] Y. Wang, P. Hou, Z. Wang, P. Kang, Zinc Imidazolate Metal–Organic Frameworks (ZIF-8) for Electrochemical Reduction of CO2 to CO, ChemPhysChem. 18 (2017) 3142–3147. doi:10.1002/cphc.201700716.

[238] H.S. Jeon, I. Sinev, F. Scholten, N.J. Divins, I. Zegkinoglou, L. Pielsticker, B.R. Cuenya, Operando Evolution of the Structure and Oxidation State of Size-Controlled Zn Nanoparticles during CO2 Electroreduction, J. Am. Chem. Soc. 140 (2018) 9383–9386. doi:10.1021/jacs.8b05258.

[239] R.Y. Wang, D.W. Kirk, G.X. Zhang, Effects of Deposition Conditions on the Morphology of Zinc Deposits from Alkaline Zincate Solutions, J. Electrochem. Soc. (2006). doi:10.1149/1.2186037.

[240] T. Zhang, H. Zhong, Y. Qiu, X. Li, H. Zhang, Zn electrode with a layer of nanoparticles for selective electroreduction of CO 2 to formate in aqueous solutions, J. Mater. Chem. A. 4 (2016) 16670–16676. doi:10.1039/C6TA07000K.

[241] Q.H. Low, N.W.X. Loo, F. Calle-Vallejo, B.S. Yeo, Enhanced Electroreduction of Carbon Dioxide to Methanol Using Zinc Dendrites Pulse-Deposited on Silver Foam, Angew. Chemie Int. Ed. 58 (2019) 2256–2260. doi:10.1002/anie.201810991.

[242] G. Trejo, R. Ortega B., Y. Meas, P. Ozil, E. Chainet, B. Nguyen, Nucleation and Growth of Zinc from Chloride Concentrated Solutions, J. Electrochem. Soc. 145 (1998) 4090–4097. doi:10.1149/1.1838919.

[243] M. Pölzler, A.H. Whitehead, B. Gollas, A Study of Zinc Electrodeposition From Zinc Chloride: Choline Chloride: Ethylene Glycol, ECS Trans. 25 (2019) 43–55. doi:10.1149/1.3378972.

[244] D.S. Baik, D.J. Fray, Electrodeposition of zinc from high acid zinc chloride solutions, J.

Appl. Electrochem. 31 (2001) 1141–1147. doi:10.1023/A:1012290132379.

[245] G. Panzeri, D. Muller, A. Accogli, E. Gibertini, E. Mauri, F. Rossi, L. Nobili, L. Magagnin, Zinc electrodeposition from a chloride-free non-aqueous solution based on ethylene glycol and acetate salts, Electrochim. Acta. 296 (2019) 465–472. doi:10.1016/j.electacta.2018.11.060.

[246] P.T. Vasudevan, M. Briggs, Biodiesel production - Current state of the art and challenges, J. Ind. Microbiol. Biotechnol. 35 (2008) 421–430. http://ovidsp.ovid.com/ovidweb.cgi?T=JS&PAGE=reference&D=emed8&NEWS=N&AN=2008186102.

[247] Monthly Biodiesel Production Report, (2018). http://www.eia.gov/biofuels/biodiesel/production/ (accessed December 21, 2018).

[248] Q.M. Viana, M.B. Viana, E.A.F. Vasconcelos, S.T. Santaella, R.C. Leitão, Fermentative H2 production from residual glycerol: a review, Biotechnol. Lett. 36 (2014) 1381–1390. doi:10.1007/s10529-014-1507-4.

[249] J. Bonet, J. Costa, R. Sire, J.-M. Reneaume, A.E. Pleşu, V. Pleşu, G. Bozga, Revalorization of glycerol: Comestible oil from biodiesel synthesis, Food Bioprod. Process. 87 (2009) 171–178. doi:10.1016/j.fbp.2009.06.003.

[250] A. Casas, J.R. Ruiz, M.J. Ramos, A. Pérez, Effects of Triacetin on Biodiesel Quality, Energy & Fuels. 24 (2010) 4481–4489. doi:10.1021/ef100406b.

[251] A. Casas, M.J. Ramos, Á. Pérez, New trends in biodiesel production: Chemical interesterification of sunflower oil with methyl acetate, Biomass and Bioenergy. 35 (2011) 1702–1709. doi:10.1016/j.biombioe.2011.01.003.

[252] A. Casas, M.J. Ramos, Á. Pérez, Product Separation after Chemical Interesterification of Vegetable Oils with Methyl Acetate. Part I: Vapor–Liquid Equilibrium, Ind. Eng. Chem. Res. 51 (2012) 8087–8094. doi:10.1021/ie3007903.

[253] A. Casas, M.J. Ramos, Á. Pérez, Product Separation after Chemical Interesterification of Vegetable Oils with Methyl Acetate. Part II: Liquid–Liquid Equilibrium, Ind. Eng. Chem. Res. 51 (2012) 10201–10206. doi:10.1021/ie300791g.

[254] W. Du, Y. Xu, D. Liu, J. Zeng, Comparative study on lipase-catalyzed transformation of soybean oil for biodiesel production with different acyl acceptors, J. Mol. Catal. B Enzym. 30 (2004) 125–129. doi:10.1016/j.molcatb.2004.04.004.

[255] Y. Xu, W. Du, D. Liu, J. Zeng, A novel enzymatic route for biodiesel production from renewable oils in a solvent-free medium., Biotechnol. Lett. 25 (2003) 1239–41. doi:10.1023/A:1025065209983.

[256] N. Ognjanovic, D. Bezbradica, Z. Knezevic-Jugovic, Enzymatic conversion of sunflower oil to biodiesel in a solvent-free system: Process optimization and the immobilized system

stability, Bioresour. Technol. 100 (2009) 5146–5154. doi:10.1016/j.biortech.2009.05.068.

[257] Y. Xu, W. Du, D. Liu, Study on the kinetics of enzymatic interesterification of triglycerides for biodiesel production with methyl acetate as the acyl acceptor, J. Mol. Catal. B Enzym. 32 (2005) 241–245. doi:10.1016/j.molcatb.2004.12.013.

[258] P. Campanelli, M. Banchero, L. Manna, Synthesis of biodiesel from edible, non-edible and waste cooking oils via supercritical methyl acetate transesterification, Fuel. 89 (2010) 3675–3682. doi:10.1016/j.fuel.2010.07.033.

[259] K.T. Tan, K.T. Lee, A.R. Mohamed, Prospects of non-catalytic supercritical methyl acetate process in biodiesel production, Fuel Process. Technol. 92 (2011) 1905–1909. doi:10.1016/j.fuproc.2011.05.009.

[260] S. Saka, Y. Isayama, A new process for catalyst-free production of biodiesel using supercritical methyl acetate, Fuel. 88 (2009) 1307–1313. doi:10.1016/j.fuel.2008.12.028.

[261] E.A.N. Simonetti, G.P. Thim, G.G. Cortez, Ca-Al Hydrotalcites as Catalysts for Methanolysis and Ethanolysis of Soybean Oil, Mod. Res. Catal. 03 (2014) 117–127. doi:10.4236/mrc.2014.34015.

[262] L. Gao, G. Teng, G. Xiao, R. Wei, Biodiesel from palm oil via loading KF/Ca-Al hydrotalcite catalyst, Biomass and Bioenergy. 34 (2010) 1283–1288. doi:10.1016/j.biombioe.2010.03.023.

[263] C.S. Castro, L.C.F. Garcia, J.M. Assaf, The enhanced activity of Ca/MgAl mixed oxide for transesterification, Fuel Process. Technol. 125 (2014) 73–78. doi:10.1016/j.fuproc.2014.03.024.

[264] M.J. Climent, A. Corma, S. Iborra, A. Velty, Activated hydrotalcites as catalysts for the synthesis of chalcones of pharmaceutical interest, J. Catal. 221 (2004) 474–482. doi:10.1016/j.jcat.2003.09.012.

[265] S.L. Bhanawase, G.D. Yadav, Green Synthesis of Vanillyl Mandelic Acid (Sodium Salt) from Guaiacol and Sodium Glyoxylate over Novel Silica Encapsulated Magnesium Hydroxide, ACS Sustain. Chem. Eng. (2016). doi:10.1021/acssuschemeng.5b01219.

[266] G.D. Yadav, P. Aduri, Aldol condensation of benzaldehyde with heptanal to jasminaldehyde over novel Mg-Al mixed oxide on hexagonal mesoporous silica, J. Mol. Catal. A Chem. (2012). doi:10.1016/j.molcata.2011.12.008.

[267] M.S. Carvalho, M.A. Mendonça, D.M.M. Pinho, I.S. Resck, P.A.Z. Suarez, Chromatographic analyses of fatty acid methyl esters by HPLC-UV and GC-FID, J. Braz. Chem. Soc. 23 (2012) 763–769. doi:10.1590/S0103-50532012000400023.

[268] scipy.integrate.solve_ivp, (2019). https://docs.scipy.org/doc/scipy/reference/generated/scipy.integrate.solve_ivp.html (accessed May 14, 2020).

[269] L.E. Revell, B.E. Williamson, Why are some reactions slower at higher temperatures?, J. Chem. Educ. (2013). doi:10.1021/ed400086w.

[270] F. Yang, S. Zhang, Z.C. Zhang, J. Mao, S. Li, J. Yin, J. Zhou, A biodiesel additive: etherification of 5-hydroxymethylfurfural with isobutene to tert-butoxymethylfurfural, Catal. Sci. Technol. 5 (2015) 4602–4612. doi:10.1039/C5CY00750J.

[271] J. Luo, J. Yu, R.J. Gorte, E. Mahmoud, D.G. Vlachos, M.A. Smith, The effect of oxide acidity on HMF etherification, Catal. Sci. Technol. 4 (2014) 3074–3081. doi:10.1039/C4CY00563E.

[272] M. Bicker, D. Kaiser, L. Ott, H. Vogel, Dehydration of d-fructose to hydroxymethylfurfural in sub- and supercritical fluids, J. Supercrit. Fluids. 36 (2005) 118–126. doi:10.1016/j.supflu.2005.04.004.

[273] H. Zhu, Q. Cao, C. Li, X. Mu, Acidic resin-catalysed conversion of fructose into furan derivatives in low boiling point solvents, Carbohydr. Res. 346 (2011) 2016–2018. doi:10.1016/j.carres.2011.05.026.

[274] S. Kanai, I. Nagahara, Y. Kita, K. Kamata, M. Hara, A bifunctional cerium phosphate catalyst for chemoselective acetalization, Chem. Sci. 8 (2017) 3146–3153. doi:10.1039/c6sc05642c.

[275] Shagufta, I. Ahmad, R. Dhar, Sulfonic Acid-Functionalized Solid Acid Catalyst in Esterification and Transesterification Reactions, Catal. Surv. from Asia. 21 (2017) 53–69. doi:10.1007/s10563-017-9226-1.

[276] S.N. Mudliar, K.V. Padoley, P. Bhatt, M. Sureshkumar, S.K. Lokhande, R.A. Pandey, A.N. Vaidya, Pyridine biodegradation in a novel rotating rope bioreactor, Bioresour. Technol. 99 (2008) 1044–1051. doi:10.1016/j.biortech.2007.02.039.

[277] A.B. Gawade, M.S. Tiwari, G.D. Yadav, Biobased Green Process: Selective Hydrogenation of 5-Hydroxymethylfurfural to 2,5-Dimethyl Furan under Mild Conditions Using Pd-Cs2.5H0.5PW12O40/K-10 Clay, ACS Sustain. Chem. Eng. 4 (2016) 4113–4123. doi:10.1021/acssuschemeng.6b00426.

[278] G.D. Yadav, N.S. Asthana, Kinetics and mechanism of selective monoacylation of mesitylene, Ind. Eng. Chem. Res. 41 (2002) 5565–5575. doi:10.1021/ie020152y.

[279] F.F. Wang, J. Liu, H. Li, C.L. Liu, R.Z. Yang, W.S. Dong, Conversion of cellulose to lactic acid catalyzed by erbium-exchanged montmorillonite K10, Green Chem. 17 (2015) 2455–2463. doi:10.1039/c4gc02131b.

[280] G.D. Yadav, A.R. Yadav, Solid Acid Catalyzed Solventless Highly Selective , Effective and Reusable Method for Synthesis of 1 , 4-dioxanol Using Glycerol and Cyclohexanone, Int. Rev. Chem. Eng. 4 (2012) 608–617.

[281] L. Méndez, R. Torviso, L. Pizzio, M. Blanco, 2-Methoxynaphthalene acylation using

aluminum or copper salts of tungstophosphoric and tungstosilicic acids as catalysts, Catal. Today. 173 (2011) 32–37. doi:10.1016/j.cattod.2011.03.028.

[282] S.N. Basahel, N.S. Ahmed, K. Narasimharao, M. Mokhtar, Simple and efficient protocol for synthesis of pyrido[1,2-a]pyrimidin-4-one derivatives over solid heteropolyacid catalysts, RSC Adv. 6 (2016) 11921–11932. doi:10.1039/c5ra22180c.

[283] M. Kruk, M. Jaroniec, Gas Adsorption Characterization of Ordered Organic−Inorganic Nanocomposite Materials, Chem. Mater. 13 (2001) 3169–3183. doi:10.1021/cm0101069.

[284] G.D. Yadav, P.S. Surve, Regioselective ring opening reaction of epichlorohydrin with acetic acid to 3-chloro-2-hydroxypropyl acetate over cesium modified heteropolyacid on clay support, Appl. Catal. A Gen. 468 (2013) 112–119. doi:10.1016/j.apcata.2013.08.003.

[285] S.K. Bhorodwaj, D.K. Dutta, Heteropoly acid supported modified Montmorillonite clay: An effective catalyst for the esterification of acetic acid with sec-butanol, Appl. Catal. A Gen. 378 (2010) 221–226. doi:10.1016/j.apcata.2010.02.026.

[286] O.S. Ahmed, D.K. Dutta, In situ generation of metal clusters in interlamellar spacing of montmorillonite clay and their thermal behaviour, Thermochim. Acta. 395 (2002) 209–216. doi:10.1016/S0040-6031(02)00215-0.

[287] J.B. Binder, R.T. Raines, Simple Chemical Transformation of Lignocellulosic Biomass into Furans for Fuels and Chemicals, J. Am. Chem. Soc. 131 (2009) 1979–1985. doi:10.1021/ja808537j.

[288] R. V. Sharma, U. Das, R. Sammynaiken, A.K. Dalai, Liquid phase chemo-selective catalytic hydrogenation of furfural to furfuryl alcohol, Appl. Catal. A Gen. 454 (2013) 127–136. doi:10.1016/j.apcata.2012.12.010.

[289] C.P. Jiménez-Gómez, J.A. Cecilia, D. Durán-Martín, R. Moreno-Tost, J. Santamaría-González, J. Mérida-Robles, R. Mariscal, P. Maireles-Torres, Gas-phase hydrogenation of furfural to furfuryl alcohol over Cu/ZnO catalysts, J. Catal. 336 (2016) 107–115. doi:10.1016/j.jcat.2016.01.012.

[290] J. Yang, H.-Y. Zheng, Y.-L. Zhu, G.-W. Zhao, C.-H. Zhang, B.-T. Teng, H.-W. Xiang, Y. Li, Effects of calcination temperature on performance of Cu–Zn–Al catalyst for synthesizing γ-butyrolactone and 2-methylfuran through the coupling of dehydrogenation and hydrogenation, Catal. Commun. 5 (2004) 505–510. doi:10.1016/j.catcom.2004.06.005.

[291] R.S. Rao, R. Terry, K. Baker, M. Albert Vannice, Furfural hydrogenation over carbon-supported copper, Catal. Letters. 60 (1999) 51–57. doi:10.1023/A:1019090520407.

[292] J. Lessard, J.-F. Morin, J.-F. Wehrung, D. Magnin, E. Chornet, High Yield Conversion of Residual Pentoses into Furfural via Zeolite Catalysis and Catalytic Hydrogenation of Furfural to 2-Methylfuran, Top. Catal. 53 (2010) 1231–1234. doi:10.1007/s11244-010-9568-7.

[293] A.B. Merlo, V. Vetere, J.F. Ruggera, M.L. Casella, Bimetallic PtSn catalyst for the selective hydrogenation of furfural to furfuryl alcohol in liquid-phase, Catal. Commun. 10 (2009) 1665–1669. doi:10.1016/j.catcom.2009.05.005.

[294] P.D. Vaidya, V. V Mahajani, Kinetics of Liquid-Phase Hydrogenation of Furfuraldehyde to Furfuryl Alcohol over a Pt/C Catalyst, Ind. Eng. Chem. Res. 42 (2003) 3881–3885. doi:10.1021/ie030055k.

[295] S. Sitthisa, T. Sooknoi, Y. Ma, P.B. Balbuena, D.E. Resasco, Kinetics and mechanism of hydrogenation of furfural on Cu/SiO2 catalysts, J. Catal. 277 (2011) 1–13. doi:10.1016/j.jcat.2010.10.005.

[296] X. Yang, Q. Meng, G. Ding, Y. Wang, H. Chen, Y. lei Zhu, Y.W. Li, Construction of novel Cu/ZnO-Al2O3 composites for furfural hydrogenation: The role of Al components, Appl. Catal. A Gen. 561 (2018) 78–86. doi:10.1016/j.apcata.2018.04.005.

[297] M.A. Jackson, M.G. White, R.T. Haasch, S.C. Peterson, J.A. Blackburn, Hydrogenation of furfural at the dynamic Cu surface of CuOCeO2/Al2O3 in a vapor phase packed bed reactor, Mol. Catal. 445 (2018) 124–132. doi:10.1016/j.mcat.2017.11.023.

[298] M.M. Villaverde, N.M. Bertero, T.F. Garetto, A.J. Marchi, Selective liquid-phase hydrogenation of furfural to furfuryl alcohol over Cu-based catalysts, Catal. Today. 213 (2013) 87–92. doi:10.1016/j.cattod.2013.02.031.

[299] G. Chamoulaud, D. Floner, C. Moinet, C. Lamy, E.M. Belgsir, Biomass conversion II: Simultaneous electrosyntheses of furoic acid and furfuryl alcohol on modified graphite felt electrodes, Electrochim. Acta. 46 (2001) 2757–2760. doi:10.1016/S0013-4686(01)00507-2.

[300] D. Chu, Y. Hou, J. He, M. Xu, Y. Wang, S. Wang, J. Wang, L. Zha, Nano TiO2 film electrode for electrocatalytic reduction of furfural in ionic liquids, J. Nanoparticle Res. 11 (2009) 1805–1809. doi:10.1007/s11051-009-9610-5.

[301] S. Jung, E.J. Biddinger, Electrocatalytic Hydrogenation and Hydrogenolysis of Furfural and the Impact of Homogeneous Side Reactions of Furanic Compounds in Acidic Electrolytes, ACS Sustain. Chem. Eng. 4 (2016) 6500–6508. doi:10.1021/acssuschemeng.6b01314.

[302] T. Kim, R.S. Assary, C.L. Marshall, D.J. Gosztola, L.A. Curtiss, P.C. Stair, Acid-Catalyzed Furfuryl Alcohol Polymerization: Characterizations of Molecular Structure and Thermodynamic Properties, ChemCatChem. 3 (2011) 1451–1458. doi:10.1002/cctc.201100098.

[303] L. Liu, H. Liu, W. Huang, Y. He, W. Zhang, C. Wang, H. Lin, Mechanism and kinetics of the electrocatalytic hydrogenation of furfural to furfuryl alcohol, J. Electroanal. Chem. 804 (2017) 248–253. doi:10.1016/j.jelechem.2017.09.021.

[304] Y. Feng, Z. Li, H. Liu, C. Dong, J. Wang, S.A. Kulinich, X. Du, Laser-Prepared CuZn

Alloy Catalyst for Selective Electrochemical Reduction of CO 2 to Ethylene, Langmuir. 34 (2018) 13544–13549. doi:10.1021/acs.langmuir.8b02837.

[305] I. Nezam, L. Peereboom, D.J. Miller, Continuous condensed-phase ethanol conversion to higher alcohols: Experimental results and techno-economic analysis, J. Clean. Prod. 209 (2019) 1365–1375. doi:10.1016/j.jclepro.2018.10.276.

[306] N.S. Gould, H. Landfield, B. Dinkelacker, C. Brady, X. Yang, B. Xu, Selectivity Control in Catalytic Reductive Amination of Furfural to Furfurylamine on Supported Catalysts, ChemCatChem. 12 (2020) 2106–2115. doi:10.1002/cctc.201901662.

[307] NIST MS number: 228113, NIST Chemistry WebBook, NIST Standard Reference Database 69, National Institute of Standards and Technology, (n.d.). https://webbook.nist.gov/cgi/cbook.cgi?ID=C552863&Units=SI&Mask=200#Mass-Spec (accessed January 4, 2021).

[308] NIST MS number: 151114, NIST Chemistry WebBook, NIST Standard Reference Database 69, National Institute of Standards and Technology, (n.d.). https://webbook.nist.gov/cgi/cbook.cgi?ID=C89902249&Units=SI&Mask=200#Mass-Spec (accessed January 4, 2021).

[309] H. Kaesche, The passivity of zinc in aqueous solutions of sodium carbonate and sodium bicarbonate, Electrochim. Acta. 9 (1964) 383–394. doi:10.1016/0013-4686(64)80044-X.

[310] S.C. Barton, A.C. West, Electrodissolution of Zinc at the Limiting Current, J. Electrochem. Soc. 148 (2001) A490. doi:10.1149/1.1365141.

[311] J. Yi, P. Liang, X. Liu, K. Wu, Y. Liu, Y. Wang, Y. Xia, J. Zhang, Challenges, mitigation strategies and perspectives in development of zinc-electrode materials and fabrication for rechargeable zinc-air batteries, Energy Environ. Sci. 11 (2018) 3075–3095. doi:10.1039/c8ee01991f.

[312] W. Yu, W. Shang, X. Xiao, P. Tan, B. Chen, Z. Wu, H. Xu, M. Ni, Achieving a stable zinc electrode with ultralong cycle life by implementing a flowing electrolyte, J. Power Sources. 453 (2020) 227856. doi:10.1016/j.jpowsour.2020.227856.

[313] R. Burch, S.E. Golunski, M.S. Spencer, The role of copper and zinc oxide in methanol synthesis catalysts, J. Chem. Soc. Faraday Trans. 86 (1990) 2683. doi:10.1039/ft9908602683.

[314] J. Zhang, D. Wu, Aqueous phase catalytic hydrogenation of furfural to furfuryl alcohol over in-situ synthesized Cu–Zn/SiO2 catalysts, Mater. Chem. Phys. 260 (2021) 124152. doi:10.1016/j.matchemphys.2020.124152.

[315] S. Li, Y. Fan, C. Wu, C. Zhuang, Y. Wang, X. Li, J. Zhao, Z. Zheng, Selective Hydrogenation of Furfural over the Co-Based Catalyst: A Subtle Synergy with Ni and Zn Dopants, ACS Appl. Mater. Interfaces. 13 (2021) 8507–8517. doi:10.1021/acsami.1c01436.

[316] X. Yang, H. Chen, Q. Meng, H. Zheng, Y. Zhu, Y.W. Li, Insights into influence of nanoparticle size and metal–support interactions of Cu/ZnO catalysts on activity for furfural hydrogenation, Catal. Sci. Technol. 7 (2017) 5625–5634. doi:10.1039/C7CY01284E.

[317] J. C., B. L. Deg. Peacock, Some Observations on the dissolving of zinc chloride and several suggested solvents, J. Am. Pharm. Assoc. (1918) 689–697.

[318] G.L. Maddikeri, A.B. Pandit, P.R. Gogate, Ultrasound assisted interesterification of waste cooking oil and methyl acetate for biodiesel and triacetin production, Fuel Process. Technol. 116 (2013) 241–249. doi:10.1016/j.fuproc.2013.07.004.

[319] M.J. Murphy, J.D. Taylor, R.L. Mccormick, Compendium of Experimental Cetane Number Data, Natl. Renew. Energy Lab. (2004) 1–48. http://www.nrel.gov/vehiclesandfuels/pdfs/sr368051.pdf.

[320] H. Omidvarborna, A. Kumar, D.S. Kim, Variation of diesel soot characteristics by different types and blends of biodiesel in a laboratory combustion chamber, Sci. Total Environ. 544 (2016) 450–459. doi:10.1016/j.scitotenv.2015.11.076.

[321] J. Anibal, B. Xu, Electroreductive C-C Coupling of Furfural and Benzaldehyde on Cu and Pb Surfaces, ACS Catal. 10 (2020) 11643–11653. doi:10.1021/acscatal.0c03110.

[322] D.O. Miles, P.J. Cameron, D. Mattia, Hierarchical 3D ZnO nanowire structures via fast anodization of zinc, J. Mater. Chem. A. 3 (2015) 17569–17577. doi:10.1039/C5TA03578C.

[323] S.S. Mohire, G.D. Yadav, Selective Synthesis of Hydrocinnamaldehyde over Bimetallic Ni–Cu Nanocatalyst Supported on Graphene Oxide, Ind. Eng. Chem. Res. 57 (2018) 9083–9093. doi:10.1021/acs.iecr.8b00957.

[324] M.K. Pasha, L. Dai, D. Liu, W. Du, M. Guo, Biodiesel production with enzymatic technology: progress and perspectives, Biofuels, Bioprod. Biorefining. (2021) bbb.2236. doi:10.1002/bbb.2236.

[325] S. Trasatti, Work function, electronegativity, and electrochemical behaviour of metals, J. Electroanal. Chem. Interfacial Electrochem. 39 (1972) 163–184. doi:10.1016/S0022-0728(72)80485-6.